

UNIVERSITY OF SÃO PAULO  
POLYTECHNIC SCHOOL

POURIA BAHRAMI ATAABADI

**AXIAL IMPACT ON CARBON FIBER TUBES: NUMERICAL AND EXPERIMENTAL  
STUDY**

São Paulo

2019



POURIA BAHRAMI ATAABADI

**AXIAL IMPACT ON CARBON FIBER TUBES: NUMERICAL AND EXPERIMENTAL  
STUDY**

Thesis submitted to the Polytechnic School  
of the University of São Paulo in fulfillment  
of the requirements for the degree of Doctor  
of Science.

São Paulo

2019

POURIA BAHRAMI ATAABADI

**AXIAL IMPACT ON CARBON FIBER TUBES: NUMERICAL AND EXPERIMENTAL  
STUDY**

Thesis submitted to the Polytechnic School  
of the University of São Paulo in fulfillment  
of the requirements for the degree of Doctor  
of Science.

Concentration area: Mechanical  
engineering, project and fabrication

Supervisor: Prof. Dr. Marcílio Alves

São Paulo

2019

Autorizo a reprodução e divulgação total ou parcial deste trabalho, por qualquer meio convencional ou eletrônico, para fins de estudo e pesquisa, desde que citada a fonte.

Este exemplar foi revisado e corrigido em relação à versão original, sob responsabilidade única do autor e com a anuência de seu orientador.

São Paulo, \_\_\_\_\_ de \_\_\_\_\_ de \_\_\_\_\_

Assinatura do autor: \_\_\_\_\_

Assinatura do orientador: \_\_\_\_\_

#### Catálogo-na-publicação

Ataabadi Bahrami, Pouria  
AXIAL IMPACT ON CARBON FIBER TUBES: NUMERICAL AND  
EXPERIMENTAL STUDY / P. Ataabadi Bahrami -- versão corr. -- São Paulo,  
2019.  
192 p.

Tese (Doutorado) - Escola Politécnica da Universidade de São Paulo.  
Departamento de Engenharia Mecânica.

1.CFRPs 2.Tubular absorber 3.Crashworthiness 4.Experimental tests  
5.Finite element analysis I.Universidade de São Paulo. Escola Politécnica.  
Departamento de Engenharia Mecânica II.t.

**Dedicated to my lovely family**

## **ACKNOWLEDGMENT**

I would like to thank my supervisor, Marcílio Alves, for his support, guidance, and patience.

Thanks to Prof. Dora Karagiozova for her unwavering guidance and efforts about this research project, especially in chapters three and four.

Thanks to the GMSIE staff, Henrique Ramos, for his technical supports and friendship.

I would like to thank to my lovely family; Fazlallah, Farideh, Roya, and Mostafa, for their love and support.



## ABSTRACT

Ataabadi, B.P. **Axial impact on carbon fiber tubes: Numerical and experimental study**. 2019. 192p. Ph.D. Thesis – School of Engineering of the University of São Paulo, São Paulo, 2019.

Carbon Fiber-Reinforced Plastics, CFRPs, have been widely used in the industry due to their high specific strength and stiffness ratios as well as good crushing performance when used as energy absorbers. Here, an experimental characterization of the crushing mechanism of tubular carbon fiber/epoxy absorbers is described in details, side by side with a finite element, FE, simulation of these components under compression. In the experimental study, CFRP tubes with two different stacking sequences, cross-ply and angle-ply, underwent axial quasi-static and impact in order to investigate possible effects of loading rate, stacking sequence and cross-section shape on the energy absorption capacity of the tubes. The experimental results were used to support the development of the finite element model of the composite parts under axial impact. Using Abaqus/Explicit code, a multi-layer model of laminated tube was conceived. Concentric layers of conventional shell element (S4R), in contrast to the extensive use of continuum elements, were adopted. A simple tying technique based on Continuum Damage Mechanics (CDM) was used to tie adjacent composite layers. The implementation of this bonding technique is more straightforward when comparing with the cohesive zone modes, requiring fewer mechanical properties as input. The results obtained from the numerical model agreed well with the experimental campaign, encouraging the use of the advanced finite element model developed here.

Keywords: CFRPs; Tubular absorber; Crashworthiness; Experimental tests; Finite element analysis.

## Resumo

Ataabadi, B.P. **Impacto axial em tubos de fibra de carbono: Estudo numérico e experimental**. 2019. 192p. Tese (Doutorado) – Escola Politécnica da Universidade de São Paulo, São Paulo, 2019.

Componentes de fibra de carbono, CFRPs, têm sido amplamente utilizados na indústria devido às suas altas taxas de resistência e rigidez específicas, bem como ao bom desempenho de esmagamento quando usados como absorvedores de energia. Aqui, uma caracterização experimental do mecanismo de esmagamento de absorvedores tubulares de fibra de carbono / epóxi é descrita em detalhes, lado a lado com a simulação via elementos finitos desses componentes sob compressão. No estudo experimental, os tubos CFRP com duas seqüências de empilhamento diferentes, camada cruzada e camada angular, foram submetidos a carregamentos quase estático e de impacto axiais a fim de investigar possíveis efeitos da taxa de carregamento, seqüência de empilhamento e forma da seção transversal na absorção de energia dos tubos. Os resultados experimentais foram utilizados para apoiar o desenvolvimento do modelo de elementos finitos das peças compostas sob impacto axial. Utilizando o código Abaqus / Explicit, foi concebido um modelo multicamada de tubo laminado. Camadas concêntricas do elemento de casca convencional (S4R), em contraste com o uso extensivo de elementos contínuos, foram adotadas. Uma técnica simples, baseada na Mecânica do Dano do Continuum (CDM), foi usada para unir as camadas compostas adjacentes. A implementação desta técnica de ligação é mais direta quando comparada com os modos de zona coesa, exigindo menos propriedades mecânicas como entrada. Os resultados obtidos no modelo numérico concordaram bem com a campanha experimental, incentivando o uso do modelo avançado de elementos finitos aqui desenvolvido.

Palavras-chave: CFRPs; Absorvedor tubular; Crashworthiness; Testes experimentais; Análise de elementos finitos.

## List of Figures

Figure 1.1 - Brazil traffic death toll from 2006 to 2015.	1
Figure 1.2 - The relationship between total automobile weight and design parameters.	2
Figure 1.3 - Crumple zone concept in automobile.	3
Figure 1.4 - Tubular energy absorbers in Tesla model 3.	3
Figure 2.1 - Undesired reversible elastic energy conversion; (a) Kinetic energy of the car is being restored in the form of the elastic strain; (b) Energy absorber is reaccelerating the car by recovering its restored elastic energy.	9
Figure 2.2 - Force-displacement curve for an ideal kinetic energy absorber.	10
Figure 2.3 - The characteristic feature of progressive folding; (a) Folds generation and propagation along the tube wall; (b) Typical force-displacement curve of a tube made of ductile materials.	12
Figure 2.4 - The progressive crushing mode; (a) Typical tube deformation; (b) Typical force-displacement curve of composite tubes under compressive load.	14
Figure 2.5 - Typical values of SEA for some materials.	15
Figure 2.6 - Two examples of carbon-reinforced composite frontal energy-absorber; (a) The 7.5 kg energy absorber of Lotus Elis; (b) Conical frontal energy absorbers of McLaren SLR.	16
Figure 2.7 - Lay-up definition of laminated composite made of unidirectional laminae.	17
Figure 2.8 - Some failure modes in laminated components; (a) Inter-laminar (delamination); (b) Intra-laminar failure modes of unidirectional lamina under uniaxial tension and compression.	18
Figure 2.9 - Cut-view of a tube with external chamfer being impacted by an impactor.	19
Figure 2.10 - Fragmentation failure mode; (a) Schematic features of fragmentation failure mode in tube wall;(b) Some features of fragmentation failure mode in the wall of a cross-ply, $[0/90]_n$ , tube under compression.	21
Figure 2.11 - Splaying mode; (a) Schematic features of splaying mode: (b) Some features of splaying failure mode in the wall of a cross-ply, $[0/90]_n$ , tube under compression.	22
Figure 2.12 - Brittle fracturing modes; (a) Schematic features of brittle fracturing mode in the tube's wall; (b) Some features of brittle fracturing mode in the wall of a cross-ply, $[0/90]_n$ , tube under compression.	23
Figure 2.13 - Effective parameters on the energy absorption of composite tubes.	25
Figure 2.14 - Effect of ply orientation on lamina bending (outer layers); Left: tube has an outermost layer with $\pm 45^\circ$ orientation respect to loading direction; Right: tube has an outermost layer with $0^\circ$ orientation respect to the loading direction.	27
Figure 2.15 - Carbon fiber orientation and distribution in the tube's wall.	28

## List of Figures

Figure 2.16 - Effect of material calibration on the crushing behavior of carbon-reinforced components under the axial impact.	33
Figure 2.17 - An example of force-displacement and failure mode predicted by a single-layer approach of axial crushing on CFRP tube specimen.	34
Figure 2.18 - Multi-layer model of the laminated component, including intra- and inter-layer modeling.	36
Figure 2.19 - Force-displacement and failure mode of tubes using multi-layer (shell element) in LS-Dyna.	39
Figure 2.20 - Force-displacement and failure mode of square tubes using multi-layer (shell element) in LS-Dyna.	39
Figure 2.21 - Force-displacement and failure mode of circular tubes with using multi-layer (shell element for CFRP) in Abaqus.	40
Figure 2.22 - Force-displacement and failure mode of circular tubes with using multi-layer (the solid element for CFRP) in Abaqus (implemented a material subroutine).	40
Figure 2.23 - Some subterfuges have been incorporated in multi-layer (with shell) in order to have a better splaying mode and axial splitting of the outermost layer in circular tubes under axial impact.	41
Figure 2.24 - Debris wedge in the crush front.	43
Figure 2.25 - Two types of crush initiator in FE simulation; (a) Plug initiator; (b) External chamfer..	43
Figure 2.26 - Conventional versus continuum shell element.	46
Figure 2.27 - The bilinear response of an element based on PFA.	48
Figure 2.28 - Fracture modes in interface.	51
Figure 2.29 - Few cohesive traction-separation curves in the literature; (a) Bilinear, (b) Perfectly plastic, (c) Exponential, (d) Trapezoidal.	51
Figure 2.30 - Inter-laminar fracture toughness characterization tests (a) double Cantilever Beam (DCB) (b) Four points bend end-notched flexure test (4ENF) and (c) Mixed-mode bending (MMB) tests.	53
Figure 3.1 - Geometry and coordinate system definitions; (a) Global curvilinear coordinate system ( $x,y,z$ ) of the laminated tube and the tensile test sample cut from the circular tube; (b) Local lamina coordinate system.	58
Figure 3.2 - Shear test fixture; (a) Double V-notch ring specimens undergoing shear loading at notched area; (b) Different parts of the shear fixture.	63
Figure 3.3 - Technical drawing of the shear fixture; (a) Top-view and general arrangement; (b) Semi-circular cap; (c) Half cylinder and its holes (dimensions in mm).	64

## List of Figures

- Figure 3.4 - Double V-notched specimens and projected sketch view of the notched area. 65
- Figure 3.5 - Shear stress-deformation curves for double V-notched ring specimens; (a) Cross-ply sample; (b) Angle-ply samples with 5 mm gauge length,  $L_G$ . 66
- Figure 3.6 - Carpet plot for in-plane shear modulus and strength of  $[0_m/90_n/(\pm 45)_p]_s$  carbon/epoxy laminates (AS4/3501-6); (a) Normalized shear strength of laminate; (b) Normalized shear modulus of the laminate. 67
- Figure 3.7 - Shear strain distribution and development within the notched gauge area, Test#1, cross-ply sample. 68
- Figure 3.8 - Shear strain distribution and development within the notch gauge area, Test#2, angle-ply sample. 69
- Figure 3.9 - Failure mode inspection of the cross-ply specimen; (a) Back double V-notch failure mode; (b) Front double V-notched failure mode; (c) Typical acceptable failure mode for  $[0/90]_{ns}$  laminate composites. 70
- Figure 3.10 - Failure mode inspection of the angle-ply specimen; (a) Front view of V-notch failure mode; (b) Back view of double V-notch failure mode. 71
- Figure 3.11- Axial tensile test description; (a) Principal axes of equivalent orthotropic material on the cross-ply laminate tube; (b) Axial tensile test specimen; (c) Test setup. 72
- Figure 3.12 - Axial tensile test results for the cross-ply specimen; (a) Stress-strain curve; (b) Partial stress-strain curve to measure the elastic modulus; (c) Hoop strain-axial strain curve to measure the Poisson's ratio. 72
- Figure 3.13 - The failure modes of carbon fiber samples under tensile tests; (a) Front view of failed samples; (b) Side-view of failed samples. 74
- Figure 3.14 - Lateral compression of the ring to calculate elastic modulus in hoop direction; (a) Cross-ply ring between platens of the machine; (b) The variation of calculated hoop elastic modulus versus the deflection of machine's cross-head 76
- Figure 4.1 - The specimens; (a) Schematic presentation of specimens; (b) Some full tube specimens; (c) C-section specimens glued to the base. 84
- Figure 4.2 - Experimental test procedure; (a) Quasi-static test, (1) Quasi-static setup, (2) Full tube under compression and (3) C-shape specimen under compression; (b) Dynamic test, Schematic of the drop hammer test setup. 86
- Figure 4.3 - Damage mechanism of different layers in angle-ply specimens; (a) Time-lapse of deformation of each layer of C-shape specimen; (b) Cut-view of full tube specimen after quasi-static compression; (c) Cut-view of full tube specimen after dynamic impact; (d) Schematic of fracture mechanism. 92
- Figure 4.4 - Crushed zone views of angle-ply specimens; (a) Full tube specimen after quasi-static compression; (b) Full tube specimen after dynamic compression, dynamic set#2; (c) C-shape specimen after quasi-static compression. 93

## List of Figures

Figure 4.5 - Damage mechanism of different layers in cross-ply specimens; (a) Sequential deformation of each layer of the C-shape specimen, (I: fragmentation mode, II: splaying mode and III: brittle fracturing); (b) Cut-view of full tube specimen after quasi-static test; (c) Cut-view of full tube specimen after impact; (d) Schematic presentation of failure modes.	96
Figure 4.6 - Top view of crushed zones of cross-ply specimens; (a) Full tube after quasi-static compression; (b) Full tube specimen after impact, dynamic set#2; (c) C-shape specimen after quasi-static compression.	98
Figure 4.7 - Effect of axial splitting of outermost 0° layer on the energy absorption capacity of cross-ply specimen; (a) Test description, (1) Before removing the outermost layer strips, (2) After removing the outermost layer's strips and (3) Further specimen's compression with removed outermost layer; (b) Force-displacement curve and results.	100
Figure 4.8 - Typical crushing behavior of angle-ply and cross-ply specimens under quasi-static compression; (a) Stress-displacement curves of full tube specimens; (b) Force-displacement curves of C-shape tubes with 60° external chamfer.	103
Figure 4.9 - Typical force-displacement curve of angle-ply specimens with 45° chamfer under different dynamic conditions.	104
Figure 4.10 - Force-displacement curves for dynamic set#1; (a) Cross-ply [0/90...] specimens; (b) Angle-ply [±45/0...] specimens.	105
Figure 4.11 - Force-displacement curves for dynamic set#2; (a) Cross-ply [0/90...] specimens; (b) Angle-ply [±45/0...] specimens.	106
Figure 4.12 - Typical stress variation curves of angle-ply [±45/0...] and cross-ply [0/90...] specimens under dynamic compression.	107
Figure 4.13 - Comparison between force-displacement curves of specimens under quasi-static compression and axial impact; (a) Angle-ply specimens, [±45/0...]; (b) Cross-ply specimens, [0/90].	108
Figure 4.14 - Comparison between the average stresses of specimens under quasi-static compression and axial impact.	109
Figure 4.15 - The comparison between SEA values under different loading rates and conditions.	110
Figure 5.1 - A general overview of the multi-layer approach in the present study.	114
Figure 5.2 - Progressive failure analysis flowchart.	115
Figure 5.3 - A unidirectional lamina and its local coordinate system.	116
Figure 5.4 - The typical bilinear response of composite material.	117
Figure 5.5 - Equivalent stress-displacement curve for a fiber-reinforced material in Abaqus progressive failure analysis.	121
Figure 5.6 - Evolution of damage variable for a specific failure mode.	122

## List of Figures

Figure 5.7 - Equivalent stress-displacement curve and fracture energy.	122
Figure 5.8 - Effect of fracture energy in the fiber direction on the stress-strain curve of a single S4R element under axial tension, parallel to the fiber direction.	124
Figure 5.9 - Typical traction-separation response including linear elastic, damage initiation and material degradation.	126
Figure 5.10 - Using solid resin with isotropic behavior to represent the interface between composite laminae.	128
Figure 5.11 - Typical stress-strain curve for elastic-plastic behavior.	130
Figure 6.1 - The 'dog-bone' sample for tensile test simulations; (a) Cross-plyed tensile sample; (b) Angle-ply tensile sample.	132
Figure 6.2 - Axial tensile load vs. displacement curve for cross-ply 'dog-bone' FE models with different global mesh size.	135
Figure 6.3 - Cross-ply specimens just before and after failure under tensile load.	136
Figure 6.4 - Angle-ply specimens just before and after failure under tensile load.	136
Figure 6.5 - Effect of fracture energies (fiber direction) on the load-bearing capacity of cross-ply laminate under uniaxial tension.	137
Figure 6.6 - Effect of fracture energies (fiber direction) on the load-bearing capacity of angle-ply laminate under uniaxial tension.	137
Figure 6.7 - The discretized model of the double V-notch shear sample.	138
Figure 6.8 - Shear stress-displacement curve of a cross-plyed double V-notch shear specimen.	139
Figure 6.9 - Shear stress distribution in layers with different fiber orientation; (a) The layer having fibers in the y-direction; (b) The layer having fibers in the x-direction.	139
Figure 6.10 - A quarter model of tube under axial impact.	140
Figure 6.11 - Effect of mesh size on the crushing force of cross-ply tube specimen	142
Figure 6.12 - Force-displacement curves of the cross-ply tube under dynamic impact condition #1; Simulation vs. experiment.	143
Figure 6.13 - Fracture morphology of cross-ply specimen after axial dynamic impact (for numerical results (shell thickness render is ON).	144
Figure 6.14 - Bending and damaging mechanism of layers with different fiber orientation; (a) 0° layers (fibers parallel to the tube axis); (b) 90° layers (fibers in the hoop direction).	145
Figure 6.15 - Deformation of each layer of the angle-ply specimen under the dynamic impact (shell thickness render is ON).	147

## List of Figures

Figure 6.16 - Compression between damage morphology for experimental and numerical axial impact on the angle-ply specimen (side-view).	147
Figure 6.17 - Compression between damage morphology for experimental and numerical axial impact on the angle-ply specimen (top-view).	148
Figure 6.18 - The force-displacement curve for angle-ply specimen under axial impact.	148
Figure 6.19 - The force-displacement curve for cross-ply specimen under axial impact.	149
Figure 6.20 - Damage morphology for cross-ply tube simulation with cohesive element.	150

## List of Tables

Table 2.1. Comparison between Metallic and composite materials.	15
Table 2.2 - Summary of failure modes of composite materials Hull (Hull 1991).	24
Table 2.3 - Effect of fiber orientation and fiber distribution through the tube's wall on the crushing behavior of carbon fiber-epoxy tubes under different loading rate (Hull 1991).	28
Table 2.4 - Examples of single-layer laminated specimens under axial compression.	34
Table 2.5. Example of recent multi-layer modeling approach of tubular absorbers under axial impact.	37
Table 2.6 - Comparison between some popular failure theories for composite materials (Daniel et al. 2006).	49
Table 3.1 - Description of laminated tubes.	61
Table 3.2 - Nominal mechanical properties of UD carbon fiber/epoxy prepregs, provided by the manufacturer.	61
Table 3.3 - Comparison between measured shear properties by using the proposed fixture and calculated shear properties using carpet plot in Figure 3.6.	67
Table 3.4 - Measured tensile properties of laminate specimens, x-direction tensile test.	71
Table 3.5 - Prediction of laminate mechanical properties to check the test results.	71
Table 3.6 - Elastic modulus in the tube's circumferential direction by applying a diametrical load on a ring.	74
Table 3.7 - Prediction of laminate elastic modulus in hoop direction by using classical laminate theory and Hart Smith 10% rule.	75
Table 3.8 - Comparison between reverse calculated UD lamina mechanical properties and nominal properties provided by the tube manufacturer.	75
Table 3.9 - Prediction of the angle-ply laminate mechanical properties.	76
Table 3.10 - Predicted failure tensile strength of UD carbon/epoxy material.	78
Table 4.1. A general overview of specimens under investigation.	82
Table 4.2 - Test results at quasi-static compression (0.5 mm/min).	84
Table 4.3 - Test results for dynamic set#1, striker mass equals to 102 kg.	85
Table 4.4 -. Test results for dynamic set#2, striker mass equals to 102 kg.	86
Table 4.5 - Test results for dynamic set#3, striker mass equals to 205 kg.	86
Table 4.6 - Test results for dynamic set#4, striker mass equals to 48.60 kg.	87

## List of Tables

Table 5.1 - Required in-plane material properties to represent the undamaged response of the model for fiber-reinforced materials in Abaqus.	120
Table 5.2 - Required fracture energies in the progressive failure analysis of fiber-reinforced composite in Abaqus.	123
Table 5.3 - A general overview of the material model for epoxy resin in the present thesis.	131
Table 6.1- Mechanical properties of the resin plies and UD carbon fiber/epoxy prepregs, from testing on non-standard specimens extracted from CFRP tubes.	129
Table 6.2 - Description of FE models of the cross-piled tube to check the resin response and different ply to represent the stacking sequence.	142
Table 6.3 - Description of FE models of the angle-ply specimen tube.	146

## Table of contents

1	<b>Introduction</b>	1
1.1	Objectives	4
1.2	Thesis overview	6
2	<b>Composite material and crashworthiness: Crushing mechanism and literature review</b>	8
2.1	Characteristics response of kinetic energy absorbers	8
2.1.1	Stable and consistent deformation behavior	8
2.1.2	Inelastic energy dissipation	8
2.1.3	Constant and restricted crushing force and long stroke	9
2.2	Energy absorption mechanisms of tubular components	11
2.2.1	Progressive folding mode	11
2.2.2	Progressive crushing of composite tubes	13
2.3	Material and crashworthiness	14
2.4	Progressive crushing modes of laminated composite tubes	17
2.4.1	Fragmentation mode	20
2.4.2	Splaying mode and brittle fracturing	21
2.5	Effective parameters on crushing mode and energy absorption of tubular composite absorbers	24
2.5.1	Effects of stacking sequence and ply orientation on crush performance of laminated tubes	26
2.5.2	Loading rate effects on crashworthiness of composite tubes	29
2.5.3	Effect of tube geometry	30
2.6	Methods to predict the crushing performance of tubular composite components	31
2.6.1	Finite element simulation of axial impact on tubes	31
2.6.2	Approaches to model axial tubular laminated absorber	32
2.6.3	Conventional shell and continuum shell elements in Abaqus	45
2.4	Intra-laminar modeling of composite plies: Overview of the progressive failure analysis of fiber-reinforced composites	46
2.8	Interface modeling	50
2.9	Summary	53
3	<b>In-plane material characterization of UD lamina</b>	55

## Table of contents

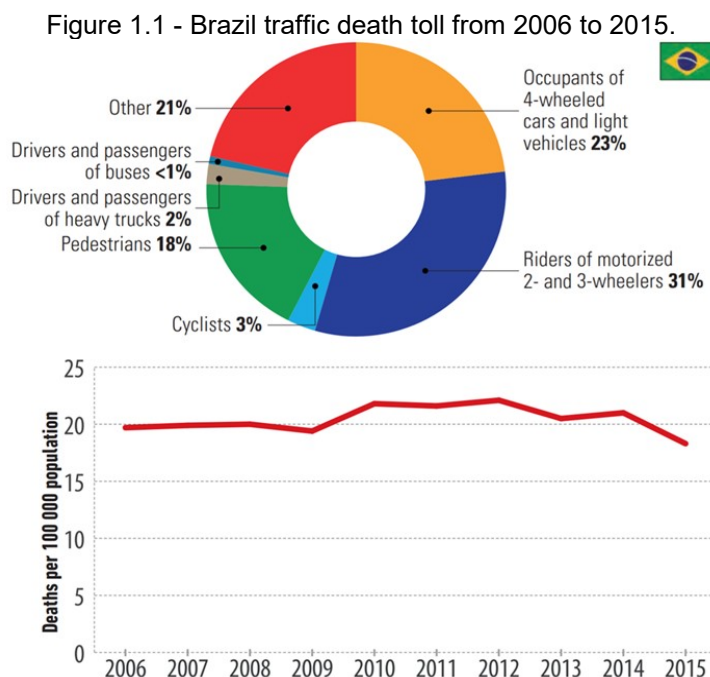
3.1	Deriving lamina in-plane properties from testing on the laminated samples	55
3.2	Laminate to lamina relations	57
3.2.1	Geometry and coordinate systems	57
3.2.2	Constitutive relations of a laminate shell	58
3.3	Finding the mechanical properties of tubular non-standard laminate specimens cut from tubes	60
3.3.1	In-plane shear test on ring-shaped specimens and proposed shear test fixture	61
3.3.2	Axial tensile test on the non-flat laminate specimen	70
3.3.3	Measuring the elastic modulus in hoop direction, $E_y$ , by using a tubular specimen	73
3.4	Calculating the UD lamina properties from measured mechanical properties of the multidirectional laminated tubes	75
3.5	Summary	78
4	<b>Experimental axial impact on CFRP tubes</b>	79
4.1	Experimental procedure	80
4.2	Results	84
4.3	Discussion	87
4.3.1	Damage modes of angle-ply tube specimens, [ $\pm 45/0\dots$ ]	87
4.3.2	The damage mode of cross-plyed specimens, [ $0/90\dots$ ]	90
4.3.3	Effect of the axial splitting of outermost $0^\circ$ layer on crushing behavior of cross-ply specimens	96
4.3.4	Force-displacement characteristics	98
4.3.4.1	Typical force-displacement response, quasi-static tests	98
4.3.4.2	Typical force-displacement response, impact tests	101
4.3.4.3	Dynamic effects on the force-displacement curves	104
4.3.5	SEA Value	106
4.3.6	Effects of the loading rate	107
4.4	Summary	108
5	<b>Description of the multi-layer FE model</b>	110
5.1	Intra- and inter-laminar modeling in the literature	110

## Table of contents

5.2	General description of the proposed multi-layer model of laminated specimens	112
5.3	In-plane Progressive failure analysis of fiber-reinforced composites in Abaqus	115
5.4	Inter-lamina modeling: resin plies	125
5.4.1	Inter-lamina modeling: Cohesive Element	
5.4.2	Inter-lamina modeling: Isotropic resin plies	127
5.5	Summary	131
6	<b>Finite element simulation and results</b>	132
6.1	Numerical simulations: Tensile and shear tests	132
6.2	Numerical simulations: Axial impact on CFRP tubes	140
6.2.1	General description of FE model of axial impact on CFRP tubes	140
6.3	Simulation results for cross-ply specimen under axial impact	141
6.3.1	Effect of mesh size on average crushing force	141
6.4	Results	142
6.4.1	Force-displacement and fracture morphology for cross-ply tube under axial impact	142
6.4.2	Simulation results for the angle-ply specimen under axial impact	145
6.4.3	Simulation results for models with cohesive element	149
6.5	Summary	150
7	<b>Conclusion</b>	152
	<b>References</b>	155
	<b>Appendices</b>	162

## 1 Introduction

Road traffic accidents have been the eighth underlying cause of death for all age groups and the first leading cause of death for children and young people. Currently, more people lost their lives due to road accidents rather than because of AIDS and diarrheal diseases (World Health Organization, 2018). Figure 1.1 shows the trend of road traffic deaths in Brazil. Unfortunately, around 40 thousand people (car's occupants are responsible for 23%) in Brazil, and 1.35 million people had lost their lives around the world yearly. Several strategies, including improvement in automotive crashworthiness and road safety, education, tightening the maximum speed limit, and stricter control on drivers' alcohol usage, have been implemented to reduce the road catastrophic deaths. Despite fulfilling all these measures, the roads traffic death toll still has been reported extremely high (World Health Organization, 2018).

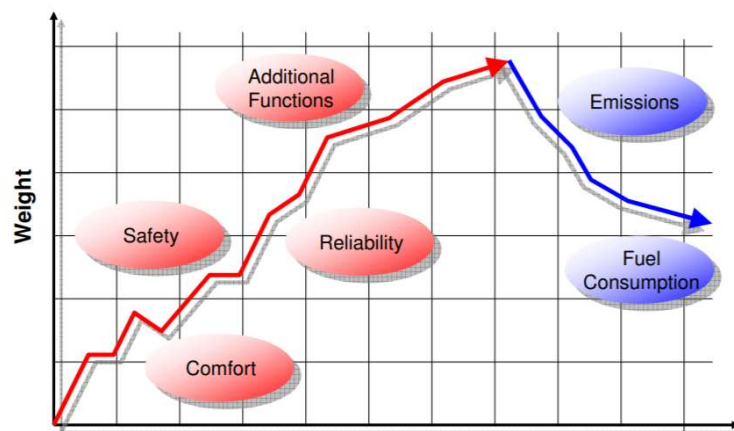


Source: (World Health Organization, 2018).

Besides crash safety, the automotive industry has been faced with growing concerns about environmental issues and the price of fossil fuels. Figure 1.2 shows that the total automobile weight is directly proportional to the reliability, comfort, safety, and additional functions provided in it. Regarding safety, it is obvious that in a frontal

crash of two cars, the occupants of the heavier car will experience lower deceleration. On the contrary, fuel consumption and emissions are inversely proportional to the total weight of the vehicle. These days the awareness of people about the environmental issue and air pollution is increasing; thus, the need for fuel-efficient vehicles is dramatically growing. The main emphasis is on minimizing CO<sub>2</sub> emissions. Several research studies in the literature showed that each 100 kg weight reduction of the personal car would reduce fuel consumption by 0.4 liters per 100 km (Marathe 2013).

Figure 1.2 - The relationship between total automobile weight and design parameters.



Source: (Sills 2008)

Therefore, sustainable mobility<sup>1</sup> has become a top policy of the major automakers. According to such a policy, besides improving the structural crashworthiness<sup>2</sup> of automobile, like introducing frontal and rear crumple zones, as presented in Figure 1.3, automakers have replaced unnecessarily heavy metallic parts with better and improved metals or those composite materials having high specific strength and stiffness ratios. Composite materials are lighter and present better energy absorption response based on biological thresholds of the human body (Jacob et al. 2002).

Although all parts and components in the crumple zones will absorb the kinetic energy of impact, specific parts called 'energy absorber' are designed to absorb a significant portion of kinetic energy thereby improve the crashworthiness of the

<sup>1</sup> Sustainable mobility means 'making vehicles that meet customer needs and expectations, while also being safe, sustainable and better for the environment' based on Toyota sustainable mobility.

<sup>2</sup> Crashworthiness is the ability of a structure to protect its occupants during an impact event.

vehicles. In the automotive industry, energy absorbers have been traditionally manufactured from metals like steel; Figure 1.4 shows the metallic tubular energy absorbers of Tesla model 3. These metallic components unnecessarily increase the total vehicle weight since have no more functions except during an accident. Tubular parts as a simplified model of automobile energy absorber have received extensive attention to be replaced by composite materials like CFRPs<sup>1</sup> (Jacob et al. 2002). Despite comprehensive studies, revealing the superior Specific Energy Absorption, *SEA*<sup>2</sup> and more similar deceleration behavior of composites materials to an ideal energy absorber, the application of carbon fiber-reinforced composites in the automotive industry have been limited to few research projects, like TECABS<sup>3</sup>, and luxury sports cars.

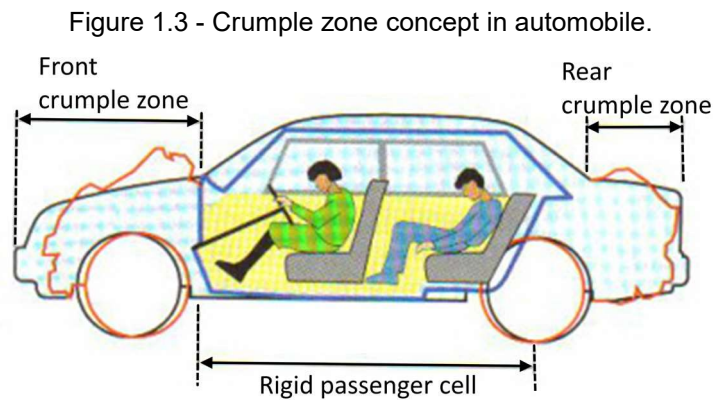
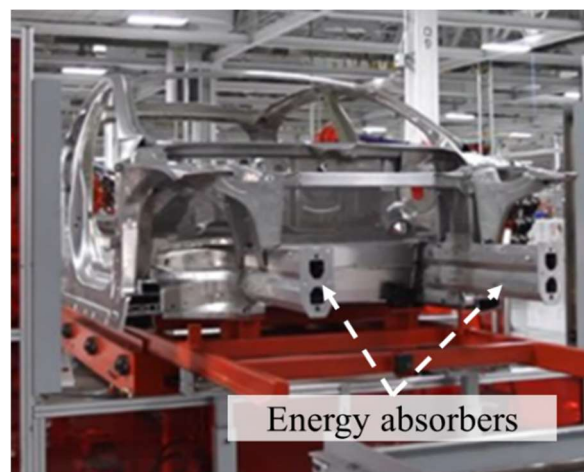


Figure 1.4 - Tubular energy absorbers in Tesla model 3.



Source: Tesla youtube channel.

<sup>1</sup> Carbon Fiber Reinforced Plastics.

<sup>2</sup> *SEA* is equal to absorbed energy per unit mass of damaged part of the absorber.

<sup>3</sup> Technologies for carbon fiber reinforced modular automotive body structures project.

Replacing ductile and isotropic materials by composite ones has been a challenging issue among engineers due to anisotropy, brittleness, and less understood dynamic behaviors of composite materials. Generally, these complex behaviors make the analysis of composite materials more complicated and even more expensive<sup>1</sup>. Due to several extrinsic and intrinsic parameters affecting composite behavior; such as constituents properties, reinforcement type, stacking sequence ..., several physical coupons and prototypes should be tested experimentally in order to develop a new composite part. Thus, in the past, the application of composites, or plastics, had been limited to secondary components.

Recently, relative improvements in composite modeling module of FE commercial packages have made the design procedure less expensive, by reducing the required experimental tests. Thus in some application like the aerospace industry using composite materials instead of metallic ones become economically justifiable. Reliable finite element model enables the engineers to utilize composite materials in primary components (load-bearing components) more confidently.

## 1.1 Objectives

Although several individual researchers and groups have investigated the crashworthiness of composite structures, the literature requires to be further enriched by both numerical and experimental contributions. Also, having a more reliable FE model and a better understanding of the crushing behavior of composite structure along with developing less expensive composite manufacturing methods, will make composite materials to be more competitive in the automotive industry. Based on this demand, the present thesis aims to;

- Enrich the literature with further experimental results on the energy absorption performance of close and open tubular laminated components made of carbon fiber epoxy material.

---

<sup>1</sup> Generally composite materials are themselves more expensive than conventional metallic materials. In the absence of a reliable analytical or numerical method, the design and development of composite components is highly depends on experimental tests. Thus several physical prototypes are required and the design process would be even more expensive. It is roughly true that cost is the major barrier against wide application of composite materials in some industries like automotive industry.

- Provide useful methods for doing material characterization of laminated composites by using non-standard tests and specimens. The outcomes will be helpful for quality control of tubular components and material characterization, while standard flat coupons are not available.
- Develop a numerical model of dynamic impact on laminated tubes using Abaqus/Explicit code. The model should be able to predict both force-displacement and crushing modes of different layers with different fiber orientations.

The following tasks will be done to accomplish the above objectives.

- Characterize the crushing performance of CFRP tubes with emphasis on the effect of following parameters.
  - Cross-section, by comparing crush performance of close and open (C-shaped) components
  - Loading rate, by comparing the quasi-static and dynamic axial impact on tubes
  - Stacking sequence, by comparing the energy absorption of two distinct stacking sequences, namely cross-ply and angle-ply.
  - Different input energies under axial impact, a wide range of loading rate from quasi-static test to dynamic impact will be considered.
- Material characterization to find lamina in-plane properties with the following features;
  - Experimental tests on laminated specimens and classical laminate theory will be utilized to derive the mechanical properties of unidirectional lamina
  - The samples will be cut from the laminated CFRP tubes

- The shear test will be done by introducing a new shear test fixture for ring-shaped specimens.
- The finite element model capable of predicting both the force-displacement curve and crushing modes will have the following characteristics;
  - FE model of the laminated tube will be a multi-layer of conventional shell element in Abaqus/Explicit code. Thus, it will be able to model both intra-laminar and inter-laminar failure modes.
  - Instead of using a cohesive zone model, a continuum damage model with bulk properties of epoxy resin will be used to model interface behavior of laminated tubes as a breakable tie interaction.
- The FE model will be validated using experimental tests on tubular carbon fiber specimens.

## **1.2 Thesis overview**

Each chapter of the present thesis has its relevant introduction and brief literature review; however, chapter 2 will provide a comprehensive review of the previous publications relevant to the scopes of the present research project. The crushing mechanisms of tubes under axial compressive load, the contradictory reported issues on crushing and energy absorption of composite materials, significant parameters on the response of composite tubes under the crushing condition and popular methodologies will be highlighted.

Chapter 3 will address the in-plane mechanical properties characterization of unidirectional CFRP lamina by using a theoretical-experimental approach. Experimental and required theoretical formulations, specimen's preparation, and a new shear test fixture for ring-shaped composite materials will be addressed here.

Chapter 4 is devoted to the energy absorption characterization of tubular CFRP components under axial compression. The outcomes will be used to validate the finite element model in the next chapter.

Chapters 5 and 6 contain the proposed finite element model and results of the dynamic axial impact on the CFRP tubes. The conclusion will be presented in chapter 7.

## **2 Composite material and crashworthiness: Crushing mechanism and literature review**

In this chapter, the characteristic behavior of an ideal kinetic energy absorber is introduced. Then damaging mechanisms of metallic and composite tubular absorbers under axial compression will be reviewed, including failure modes and significant parameters. Through comparing the ideal absorber and energy dissipation mechanisms of composite and metallic materials, the reasons for the superiority of composite materials in crashworthy design is revealed. The last part of this chapter reviews the methods to predict the crushing behavior of laminated composites with emphasis on finite element simulation.

### **2.1 Characteristics response of kinetic energy absorbers**

Energy absorber structures can be found in different shape, size, and material in many industries and their products; such as packaging, aerospace, and automotive industries. Depending on what object must be protected, the design procedure of an energy absorber should follow specific criteria. However, some essential characteristics must be considered to select the proper structure/material type for an energy absorber. Besides cost-effective and lightweight issues, some of these characteristics are explained briefly in the next subsections as explained by Lu (Lu and Yu 2003).

#### **2.1.1 Stable and consistent deformation behavior**

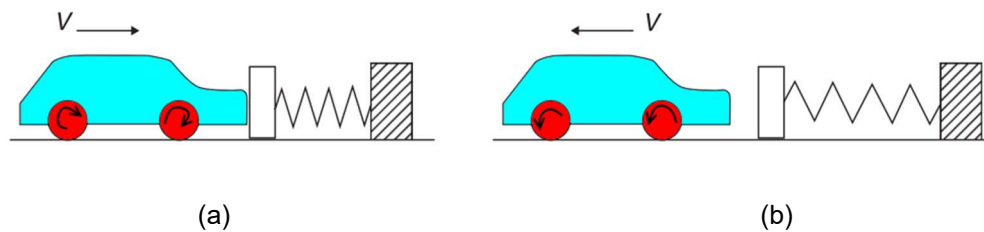
An energy absorber is likely to experience highly random loading conditions, such as loading direction, magnitude, and loading rate. Thus damaging behavior of an energy absorber (structurally and materially) should be insensitive to different loading conditions. Therefore, repeatable and consistent deformation mode is desired for an energy absorber.

#### **2.1.2 Inelastic energy dissipation**

An energy absorber should be capable of converting the main portion of input kinetic energy in plastic deformation, brittle fracturing, friction, and elastic strain.

Elastic conversion of kinetic energy is not desired in all application, such as automobile crashworthiness, because this restored energy can be released and reaccelerate the automobile immediately after deceleration, as shown in Figure 2.1. Plastic deformation and brittle fracture in metallic materials and polymeric composites are two main energy dissipation mechanisms with extensive practical applications.

Figure 2.1 - Undesired reversible elastic energy conversion; (a) Kinetic energy of the car is being restored in the form of the elastic strain; (b) Energy absorber is reaccelerating the car by recovering its restored elastic energy.



Source: (Lu and Yu 2003).

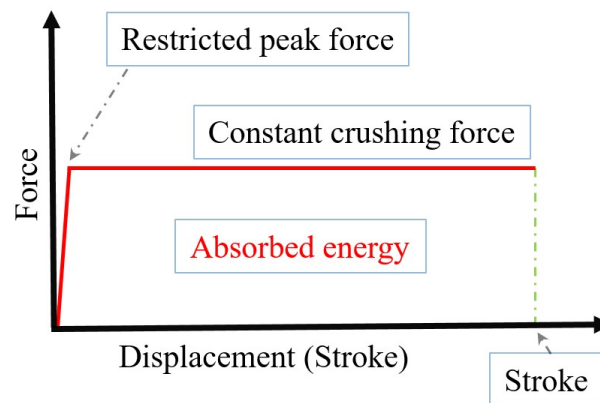
### 2.1.3 Constant and restricted crushing force and long stroke

Based on the injury tolerance of the human body during an accident, several characteristic behaviors have been considered for an ideal energy absorber to avoid head and chest injuries during the vehicle decelerating, even when there is no hard contact on the head and chest parts (Ambrasio, Pereira, and Silva 1997; Lu and Yu 2003).

The force-displacement (or acceleration profile) of an energy-absorber is a useful tool to investigate (judge) the effectiveness of its performance. Figure 2.2 shows the force-displacement curve of an ideal absorber. The passengers and automobile experience the same deceleration; Thus, during the accident, the crushing force (acceleration) should be restricted to a threshold based on the human body

tolerance<sup>1</sup>. However, the crushing force/ the stroke both should be high/ long<sup>2</sup> enough to absorb the input kinetic energy as much as possible, since the area under the force-displacement curve equals the absorbed energy. Having a constant decelerating profile decreases the chance of permanent head damage and injury<sup>3</sup>.

Figure 2.2 - Force-displacement curve for an ideal kinetic energy absorber.



Source: The author.

Thus the characteristics of a suitable structure/material for energy absorption applications in the automotive industry could be summarized as follows (Jacob et al. 2002; Lu and Yu 2003).

- Being competitive in price (cost-effectiveness)

---

<sup>1</sup> For example, the upper bound of the deceleration is 80g during a time period greater than 3 milliseconds in order to avoid head injuries, based on Euro NCAP [European NCAP Assessment Protocol – Adult Occupant Protection, Version 6.0, July 2013].

<sup>2</sup> The longer the crushed stroke, the longer the impact duration,  $\Delta t$ . Thus lower deceleration will be experienced by the passengers.

$$a(t) = \frac{0 - V_0}{\Delta t}$$

<sup>3</sup> For example, for a given initial velocity ( $V_0$ ) of impact, the Gadd Severity Index, GSI, becomes a minimum if the deceleration  $a(t)$  during impact remains constant.

$$GSI \equiv \int_0^T a(t)^{2.5} dt < 1000, \text{ The } GSI \text{ for head injury.}$$

- Complying with weight reduction strategies in the automotive industry (lightweight features)
- Constant and restricted crushing force (imposed by human body thresholds)
- Providing long enough deformation ('buying distance with time')
- Irreversible energy absorption mechanisms (energy dissipation)

In the next section, energy absorption mechanisms of tubular absorber under axial loading are presented. Then different crushing modes in composite tubes and the most effective parameters on the performance of composite absorber are explained briefly.

## **2.2 Energy absorption mechanisms of tubular components**

The amount of absorbed energy during impact is highly related to failure modes and crushing mechanisms of the absorber. Knowing the effective failure modes is essential to control the behavior of an absorber through selecting proper material and structural shape. A tube under axial compression can fail by catastrophic failure modes or progressive failure modes (Hull 1991). In the crashworthy design, the progressive failure modes are desired since the peak load is limited and the amount of absorbed energy is higher than when catastrophic failure modes occur (Hull 1991; Mamalis et al. 1998).

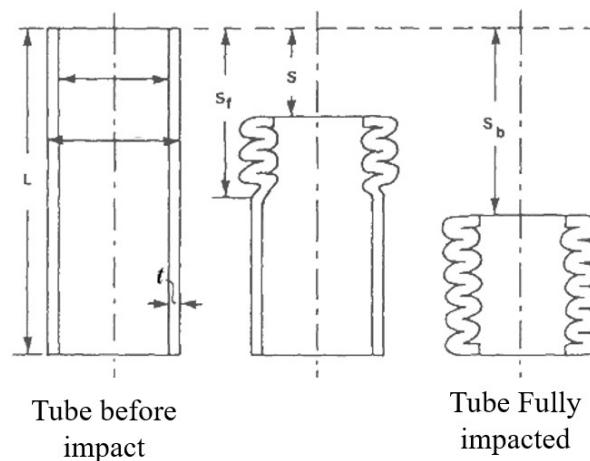
Depending on constituents properties of the absorber, progressive failure modes can be classified by progressive folding and progressive crushing. The former can be observed in ductile materials and the latter is more likely to occur in brittle plyometric composite material like carbon fiber and glass fiber embedded in a thermosetting resin.

### **2.2.1 Progressive folding mode**

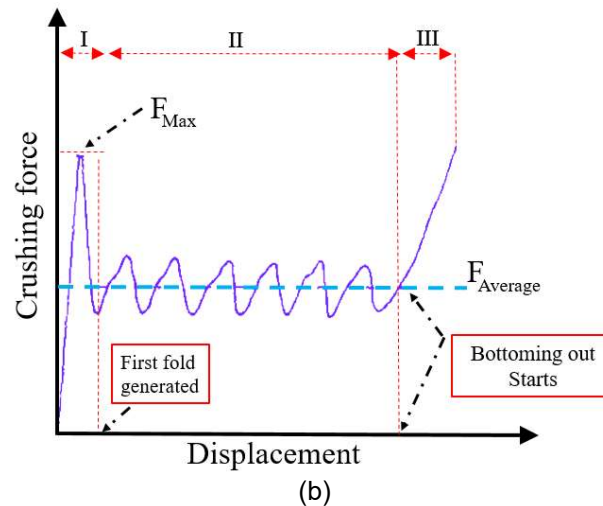
Metallic tubes (made of steel or aluminum), which are materially isotropic and ductile, collapse by progressive plastic folding (Hull 1991). Few composite materials such as Kevlar fiber (Scueser and L.E 1987) and even glass fiber composites at high-temperature condition can also fail by progressive folding modes. The characteristic features of progressive folding are depicted in Figure 2.3.

The typical force-displacement curve of progressive folding can be divided into three distinct phases. In phase I, the compressive force,  $F$ , increases suddenly and reaches a maximum value,  $F_{max}$ . A folded region is initiated at one end of the tube by local buckling and one complete fold has formed after a specific displacement. In phase II, the force fluctuates about an average value due to plastic deformation and hinge formation subsequently a series of folds form successively in the tube. Phase III is called 'bottoming out' when the tube is fully compacted and usually is not considered to calculate the absorbed energy. The progressive folding modes of metallic tubes, having circular and square cross-sections, have been studied extensively. Several analytical models have been presented to predict the average crushing force and absorbed energy with sufficient accuracy; such as Alexander (Alexander 1960), Abramowicz (Abramowicz and Jones 1984), Wierzbicki (Wierzbicki et al. 1992) models.

Figure 2.3 - The characteristic feature of progressive folding; (a) Folds generation and propagation along the tube wall; (b) Typical force-displacement curve of a tube made of ductile materials



(a)

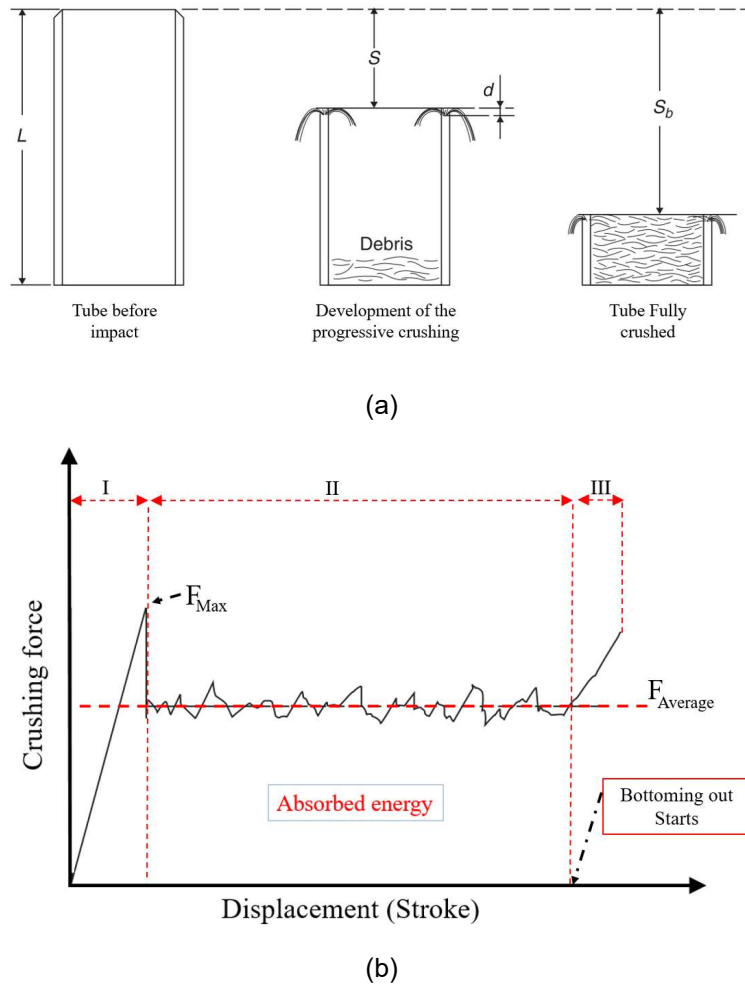


Source: (Hull 1991).

## 2.2.2 Progressive crushing of composite tubes

With a proper design, avoiding catastrophic failure modes, tubes made of brittle composite materials will collapse in several 'progressive crushing modes' under axial impact. In progressive crushing modes, a stable zone of micro-fractures forms after the peak load, and then further progresses along the tube length (Hull 1991). Figure 2.4 illustrates the characteristics of progressive crushing modes for a tube having an external chamfer as a crush initiator. Here also, the force-displacement curve could be divided into three different phases. Phase I of the force-displacement curve is related to crushing of the chamfered end (as a trigger) then a stable crush zone will be generated, which develops progressively further during compression (phase II). Further progression, more crushed debris will be trapped inside the tube. These will be compacted and eventually, the crushing force starts to increase, phase III 'bottoming out'.

Figure 2.4 - The progressive crushing mode; (a) Typical tube deformation; (b) Typical force-displacement curve of composite tubes under compressive load.



Source: (Hull 1991)

### 2.3 Material and crashworthiness

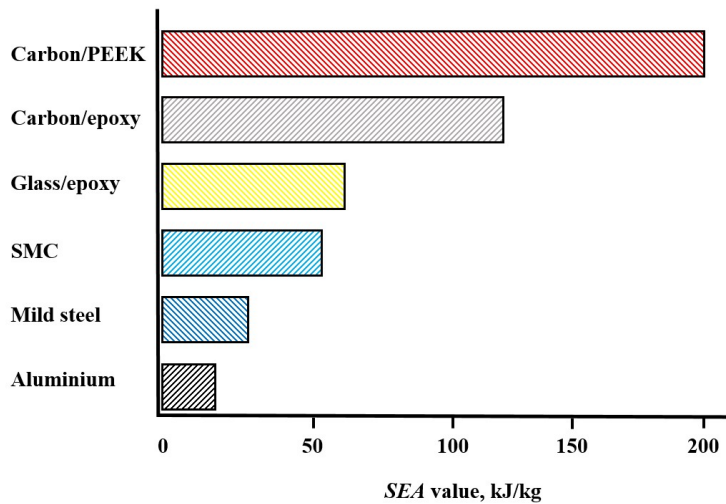
The ability of a vehicle to protect its passengers during an accident is called crashworthiness. In order to investigate the crashworthiness of structures, several evaluation criteria have been utilized and developed. The Specific Energy Absorption, SEA has become the underlying criterion for lightweight designs since the SEA relates the absorbed energy to the mass of the absorber, Eq. 2.1.

$$SEA = \frac{1}{m_{lc}} \int_0^{l_c} F dx = \frac{AE}{m_{lc}} \quad (2.1)$$

where  $AE$ , is the total energy absorbed by the absorber, the area under the force-displacement curve, and  $m_{lc}$  is the mass of the damaged part.

Figure 2.5 presents the typical SEA value for some materials (Lu and Yu 2003) revealing the lightweight superiority of composite materials in crashworthy design.

Figure 2.5 - Typical values of SEA for some materials.



Source: (Lu and Yu 2003)

Table 2.1 lists and compares metal and composite materials in crashworthy design.

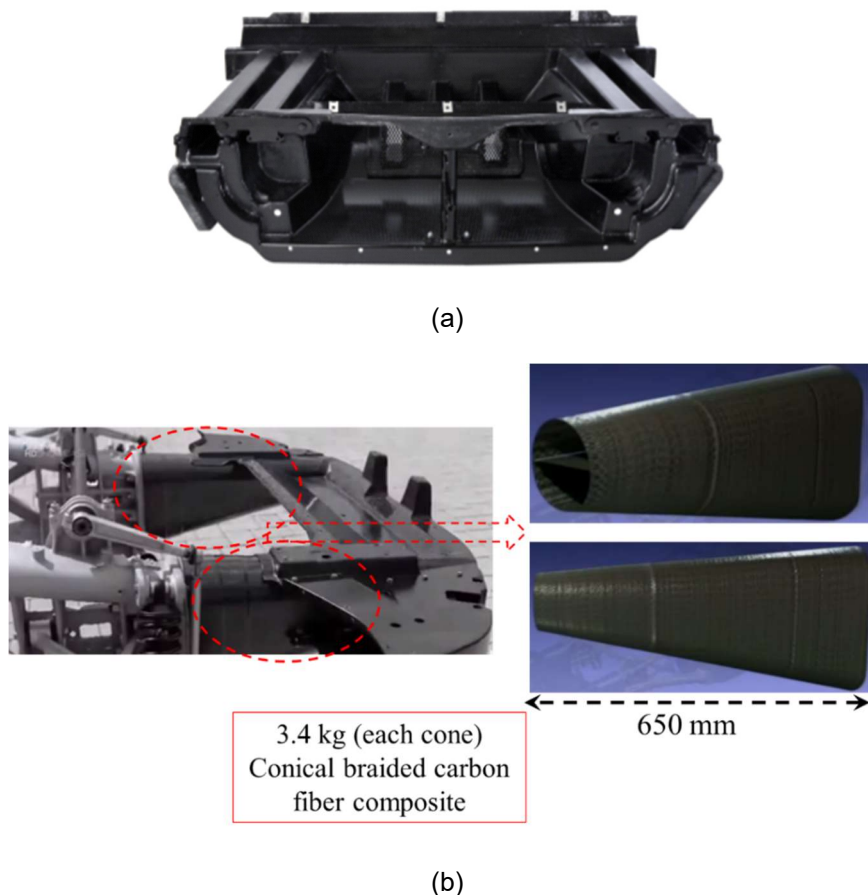
Table 2.1. Comparison between metallic and composite materials

Item	Metals	Composite (CFRP and GFRP)
<b>Crashworthiness</b>		
Specific energy absorption, $SEA$		✓✓
Similar deceleration profile respect to an ideal absorber		✓
Price and manufacturing time	✓✓	
<b>Extra features</b>		
Corrosion resistance		✓✓
Fatigue life		✓✓

Although composite materials could be advantageous to the automotive industry, due to the higher price and time-consuming manufacturing process their application is limited to the expensive luxury sports car with few products per year. CFRP usage into more accessible vehicles is increasing; such as BMW i3 (30k units per year) and Toyota Prius Prime (45k units per year). This transition is due to emerging electric cars, environmental issues, fossil fuel price increase and improvement in the driving experience.

Besides incorporation of composite materials (especially CFRPs and GFRPs) in the roof, hood and passenger cell of mid-volume vehicles, specially designed composite frontal energy absorbers were used in some automobiles like crash-box of Lotus Elise and conical carbon-reinforced composite in the bumper system of McLaren SLR, see Figure 2.6.

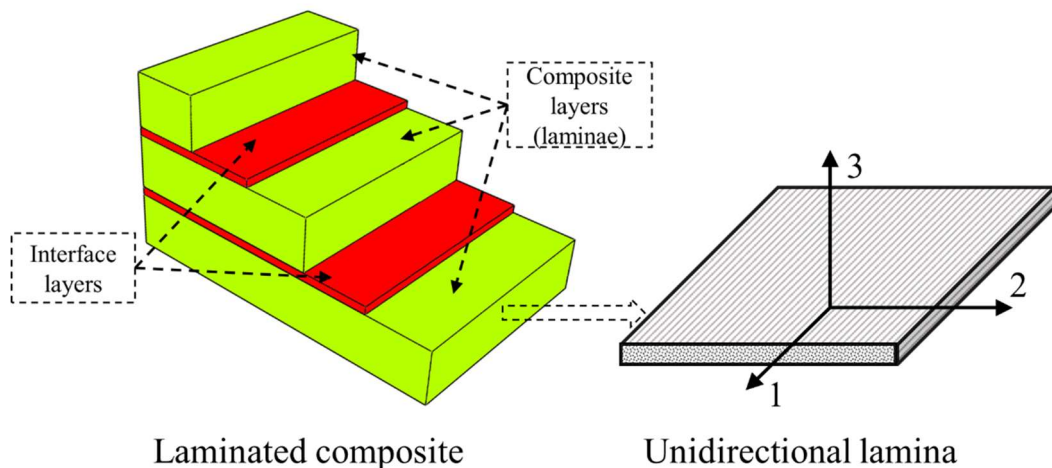
Figure 2.6 - Two examples of carbon-reinforced composite frontal energy-absorber; (a) The 7.5 kg energy absorber of Lotus Elis; (b) Conical frontal energy absorbers of McLaren SLR.



## 2.4 Progressive crushing modes of laminated composite tubes

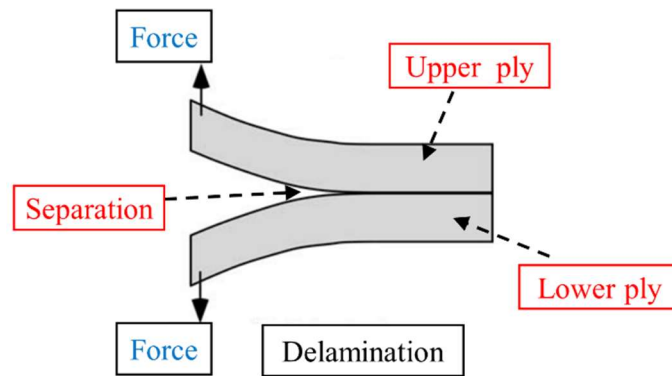
At least two laminae (plies or layers) with different mechanical properties are stacked and bonded together to build a more useful material called laminate (Figure 2.7). Thus mechanical properties of a laminate component will be controlled by intra-laminar (inter-ply) properties of each lamina and also interface (inter-laminar) properties between adjacent layers. The failure modes of a laminate could be categorized as; (I) intra-laminar and (I) inter-laminar failure modes. Figure 2.8 presents some macroscopic failure modes in laminated components. Usually, the failed area in a laminated composite consists of a combination of several intra- and inter-laminar failure modes.

Figure 2.7 - Lay-up definition of laminated composite made of unidirectional laminae.

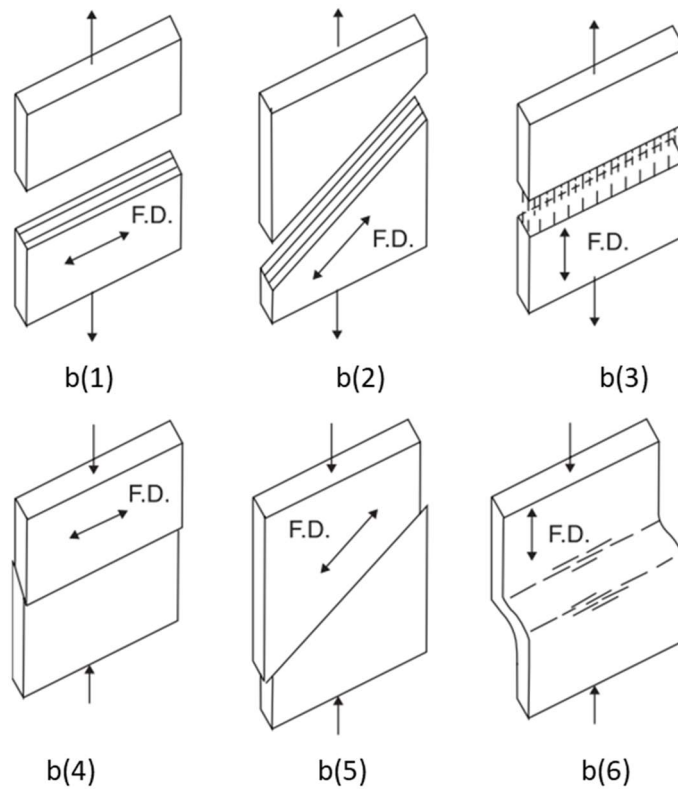


Source: The author.

Figure 2.8 - Some failure modes in laminated components; (a) Inter-laminar (delamination); (b) Intra-laminar failure modes of unidirectional lamina under uniaxial tension and compression.



(a)



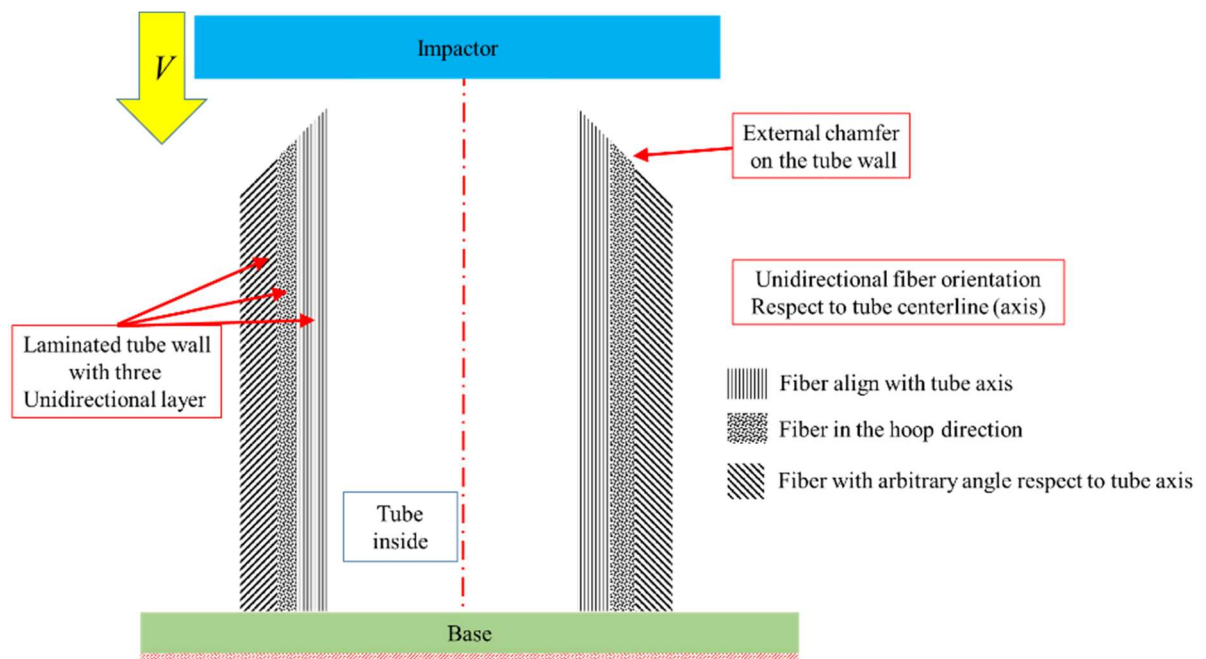
(b)

Source: (a): (Anderson, L 2004); (b): (Lu and Yu 2003)

Figure 2.9 shows the cut-view of a laminated tube placed on a stationary base to be impacted (or compressed) by an impactor (platen). The fiber orientation of each unidirectional lamina (UD) is measured with respect to the tube axis (which is parallel

to loading direction). In this figure the innermost UD lamina has fiber parallel to tube's axis (0-direction), the middle UD has fiber in the hoop direction (90° respect to tube's axis) and the outermost layer has fiber with an arbitrary direction with respect to tube's axis. This definition is very important since the failure mode of each unidirectional lamina is highly dependent on its direction respect to the loading direction.

Figure 2.9 - Cut-view of a tube with external chamfer being impacted by an impactor.



Source: The author.

In a laminated tube made of brittle materials subjected to compressive load, each lamina after being destabilized can fail in different manner, mainly controlled by its fiber orientation and stacking sequence of the laminated. The failure modes in the crushed zone of a tubular composite absorber can be classified as (I) fragmentation or transverse shearing, (II) splaying or lamina bending and (III) brittle fracturing<sup>1</sup> (Hull 1991; Mamalis et al. 1998).

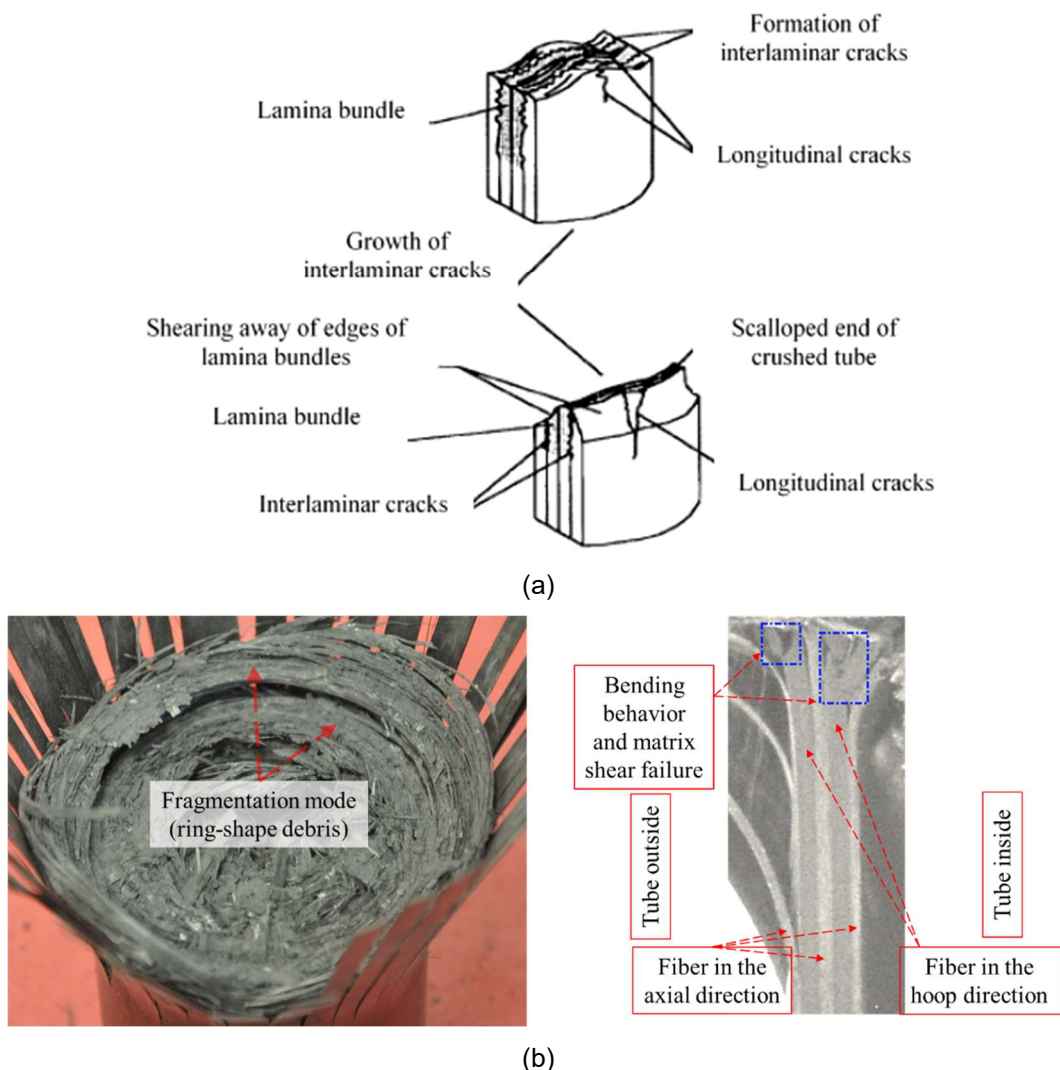
<sup>1</sup> Brittle fracturing sometimes is not considered as a main failure mode because it is a combination of the fragmentation and splaying modes.

These three main failure modes in tubular composite components under quasi-static and axial impact is comprehensively explained by Hull (Hull 1991), Jacob et al. (Jacob et al. 2002) and textbook by Mamalis et al. (Mamalis et al. 1998) and Lu and Yu (Lu and Yu 2003). These references are extensively used to describe failure modes and effective parameters that control the crushing behavior of composite laminated tubes.

#### **2.4.1 Fragmentation mode**

The fragmentation mode is characterized by a wedge-shaped laminate cross-section with one or multiple short inter-laminar and longitudinal cracks that form partial lamina bundles, see Figure 2.10. The main energy absorption mechanisms are fracturing of lamina (Chiu, Falzon, Ruan, et al. 2015; Jacob et al. 2002) and layers experience several short-length matrix fractures due to transverse shearing or sharp bending (Chiu, Falzon, Ruan, et al. 2015; Jackson et al. 2011). This failure mode is likely to occur while fibers are oriented in the hoop direction of the tube, perpendicular to loading direction (Figure 2.8(b4)) since such a lamina has poor bending performance under compressive load. The behavior of laminae, having fiber in the hoop direction, highly depends on their fiber orientation and not on stacking sequence of the adjacent layers. A laminate tube having high percent of fibers oriented in the hoop direction is not suitable for axial energy absorber (Hull 1991) since the fragmentation model would be controlled by resin properties.

Figure 2.10 - Fragmentation failure mode; (a) Schematic features of fragmentation failure mode in tube wall;(b) Some features of fragmentation failure mode in the wall of a cross-ply, $[0/90]_n$ , tube under compression.



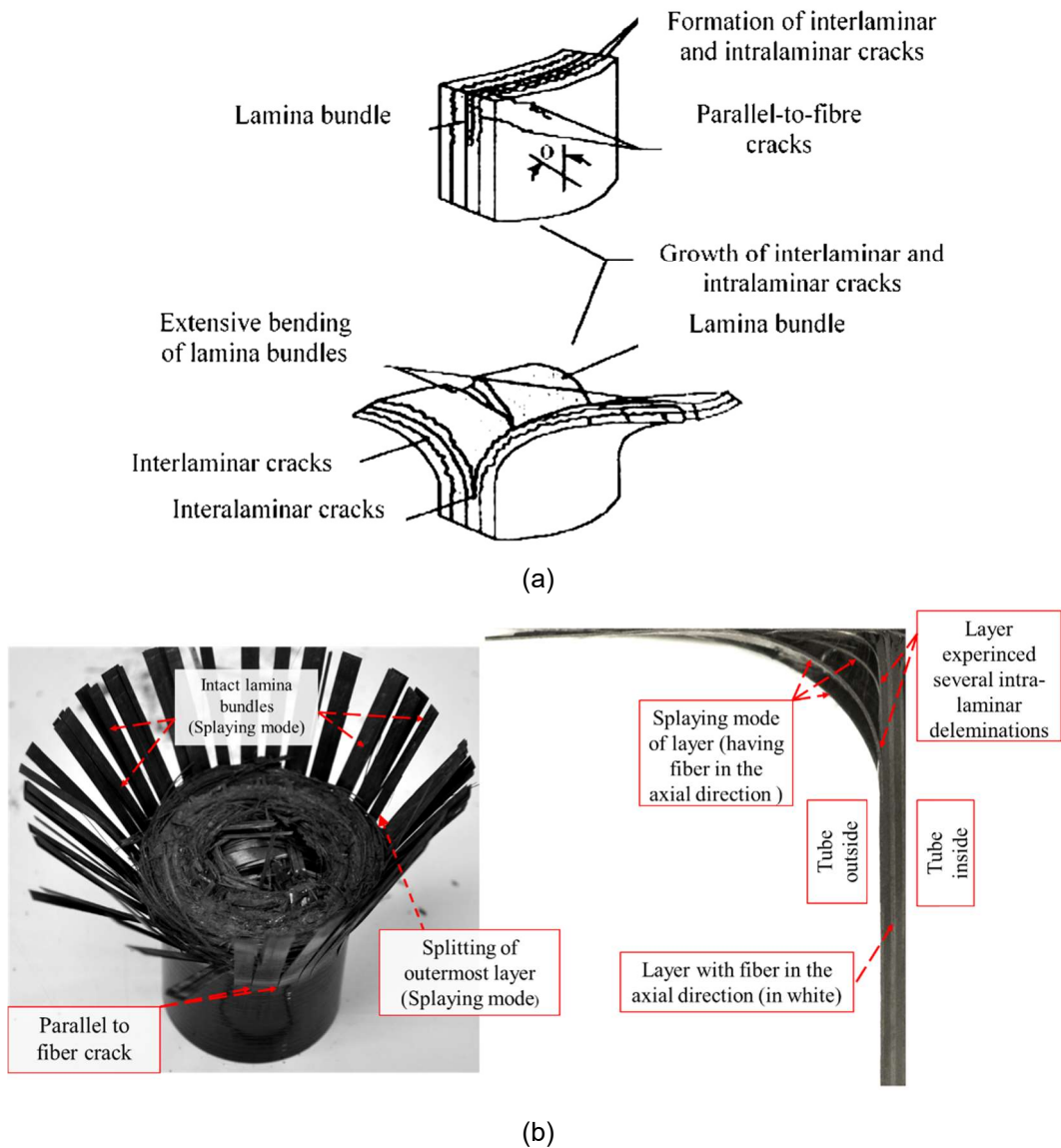
Source: (a): (Jacob et al. 2002); (b): The author.

#### 2.4.2 Splaying mode and brittle fracturing

For a laminae with fiber in the tube axis direction ( $0^\circ$  laminae), the boundary condition (orientation of adjacent layers) can play an important role in damaging behavior of these laminae. In general longitudinal crack in the resin-rich area of  $0^\circ$  laminae initiate and develop along the tube length. Thus this layers splayed and formed the lamina bundles which undergoes bending under compressive load (Splaying mode). The boundary condition of these layers, provided by surrounding layers, control the lamina bundles length. The main difference between 'Splaying mode' and 'Brittle

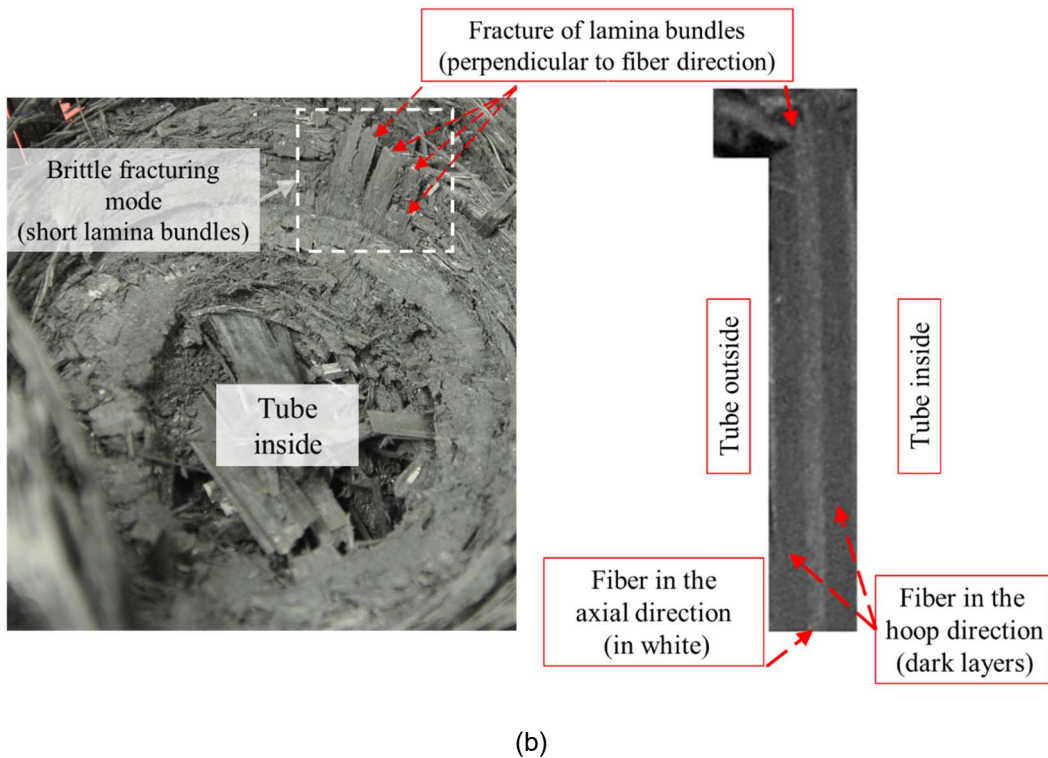
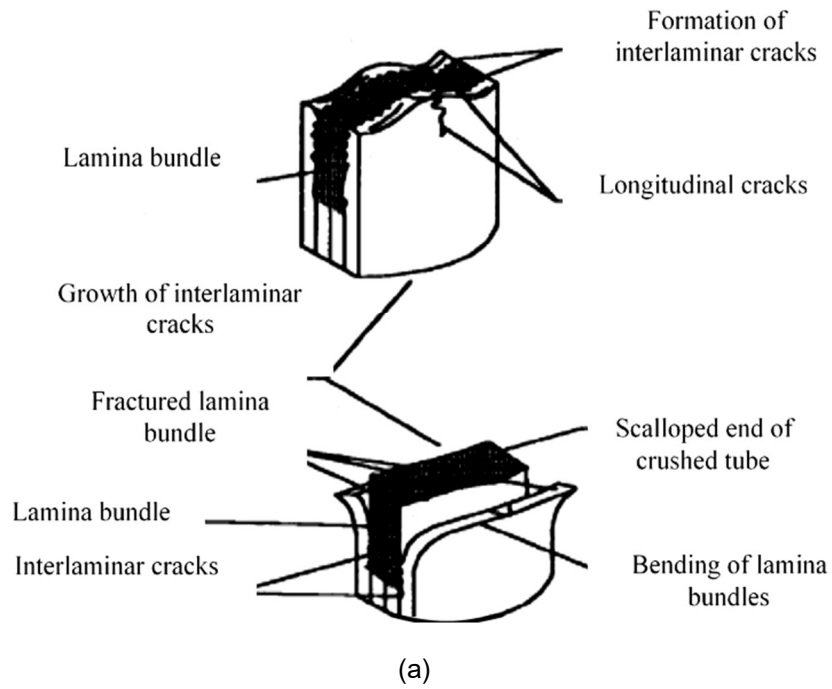
fracturing mode' is related to the length of splayed lamina bundles the latter has shorter lamina bundles. Figure 2.11 and Figure 2.12 present the splaying mode (characterized by long and intact lamina bundles) and brittle fracturing (characterized by short broken lamina bundles), respectively.

Figure 2.11 - Splaying mode; (a) Schematic features of splaying mode: (b) Some features of splaying failure mode in the wall of a cross-ply,  $[0/90]_n$ , tube under compression.



Source: (a): (Jacob et al. 2002); (b): The author.

Figure 2.12 - Brittle fracturing modes; (a) Schematic features of brittle fracturing mode in the tube's wall; (b) Some features of brittle fracturing mode in the wall of a cross-ply,  $[0/90]_n$ , tube under compression.



Source: (a): (Jacob et al. 2002); (b): The author.

Table 2.2 summarizes the failure modes in the composite tubular absorber under axial loading. It is important to differentiate between possible failure modes since it has been identified (Chiu, Falzon, Ruan, et al. 2015; Jacob et al. 2002) that an increase in the amount of fiber fracture leads to an increase of the absorbed energy (fiber-dominated damage mechanism). The splaying and brittle fracturing modes comprise fiber-dominated damage mechanism. Then knowledge about effective parameters would allow engineers to control failure modes (shifting from poor crashworthy design to suitable one).

Table 2.2 - Summary of failure modes of composite materials Hull (Hull 1991).

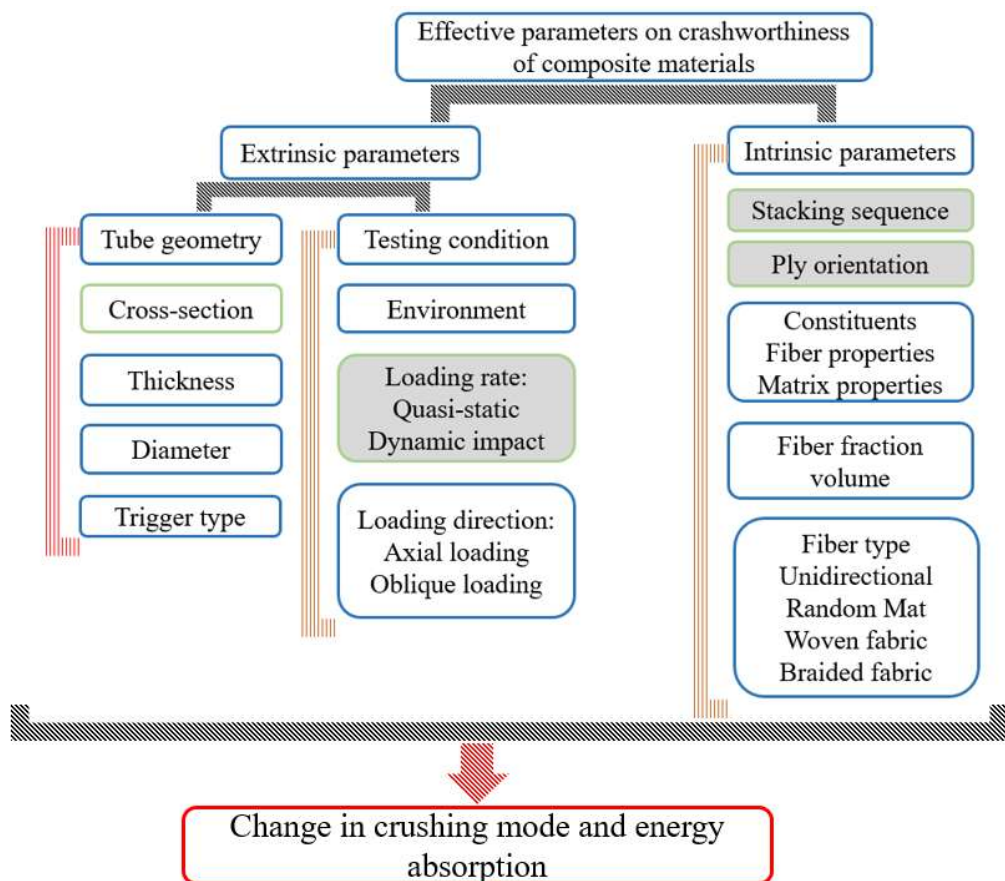
	Mode of fracture		
	Splaying	Fragmentation	Brittle fracturing
Visual Appearance	Long axial cracks (along tube length). Fronds are developed but do not fracture (Splitting).	Short axial cracks (along tube length) Sheared off sections of the tube	Short-Intermediate axial crack (along tube length)
Dissipating mechanism	Crack initiation and propagation along the tube Friction between striker and tubes debris Lamina bundles bending	Fracture of constituents	Cracks initiation and propagation Fracture of matrix and fibers Friction

## 2-5 Effective parameters on crushing mode and energy absorption of tubular composite absorbers

The textbook by Mamalis et al. (Mamalis et al. 1998) and paper by Hull (Hull 1991) describe in detail the energy-absorbing behavior of thin-walled structural components under different loading conditions. Jacob et al. (Jacob et al. 2002) provided a comprehensive review of the energy absorption of polymeric composites in the automotive industry. They classified the effective parameters on the energy

absorption behavior of composite tubes under axial compression. These parameters can affect the crushing mode (change from fragmentation to splaying or combination of these two main crushing modes, and vice-versa) and eventually can affect the energy absorption performance of thin-walled laminated tubes. These effective parameters presented in Figure 2.13 can be classified into two groups; (i) intrinsic parameters and (ii) extrinsic parameters (Hamada and Ramakrishna 1997). The effects of these parameters, the major ones being ply orientation, stacking sequence and loading rate, on energy absorption of composite absorbers have been studied by several researchers.

Figure 2.13 - Effective parameters on the energy absorption of composite tubes.



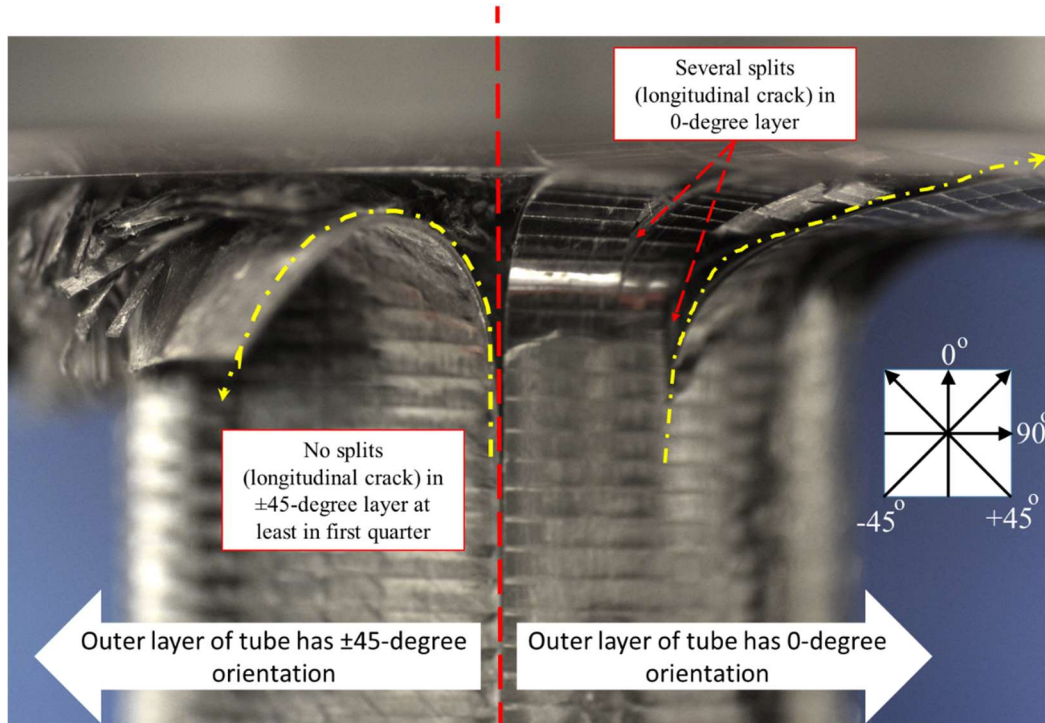
Source: The author.

### 2.5.1 Effects of stacking sequence and ply orientation on crush performance of laminated tubes

Unidirectional materials (like CFRPs) have highly orthotropic mechanical behavior; thus, their fibers orientation regarding the loading direction would be very effective in the manner they fail and bear the load. The Hoop to Axial ratio (H:A) of fiber arrangement in a laminate tube would affect the load-bearing and crushing behavior significantly. A unidirectional lamina has very high strength (stiffness) along the fiber and very low strength (stiffness) transverse to the fiber direction. In a tubular laminate absorber, a unidirectional lamina oriented in hoop direction (circumferential) has very low axial strength (stiffness) and very high hoop strength (stiffness), H:A is very high. Such a lamina fails by fragmentation mode. Contrary, a unidirectional lamina having fiber in the direction of the tube axis has very low H:A ratio and could fail by splaying mode. Longitudinal cracks are likely to happen in this layer due to very low hoop strength.

Figure 2.14 shows the effect of ply orientation on the bending performance of the outermost layers of tubes under axial compression. The ply orientation makes a significant difference in bending (and indeed damaging) of outermost layers in two different tubes. The boundary conditions of the outermost layers in two different tubes are the same (one side restricted and one side free). Therefore, their behaviors only depend on H:A ratio of their fiber contents. The radius of curvature of  $\pm 45^\circ$  layer is smaller than the curvature of the  $0^\circ$  layer because of higher restriction in hoop direction provided by  $\pm 45^\circ$  layer by itself, see the yellow lines in Figure 2.14.

Figure 2.14 - Effect of ply orientation on lamina bending (outer layers); Left: tube has an outermost layer with  $\pm 45^\circ$  orientation respect to loading direction; Right: tube has an outermost layer with  $0^\circ$  orientation respect to the loading direction.

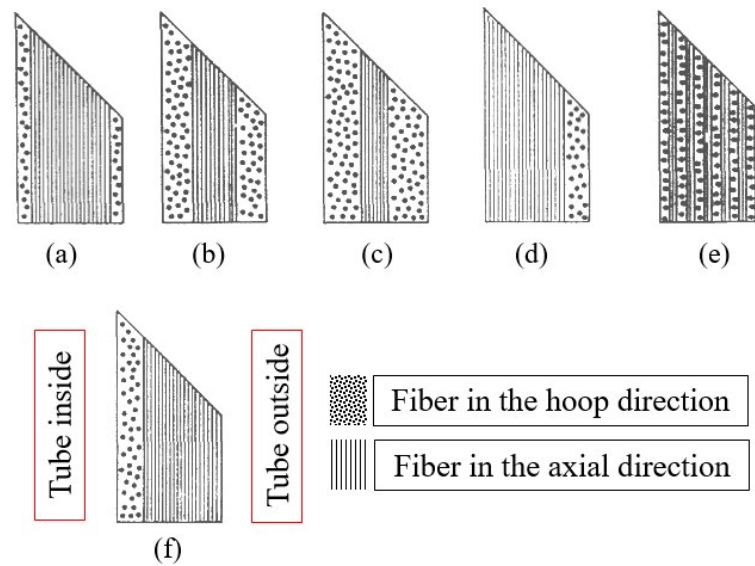


Source: The author.

The effect of ply orientation on the crushing performance of tubes under axial impact has been investigated extensively (Farley 1983, 1991; Hu et al. 2016; Mahdi, Hamouda, and Sebaey 2014; Wang et al. 2016). Based on similar studies by 1991, Hull (Hull 1991) predicted the general features of crushing modes in a tube under axial compression while considering the H:A.

In a laminate, the behavior of unidirectional laminae will be affected by the adjacent layers. Some experimental results showed that besides the percentage of plies orientation (H:A), their distribution (stacking sequence) has significant effects on crushing modes of the laminate tube and the absorbed energy. Therefore, several researchers investigated the stacking sequence role in the crushing performance of composite absorbers (Quaresimin et al. 2013; Scueser and L.E 1987; Wang et al. 2016). Table 2.3 lists the Specific Crushing Stress for carbon fiber-epoxy tubes with different ply orientations and different stacking sequences, types (a) to (f), illustrated in Figure 2.15.

Figure 2.15 - Carbon fiber orientation and distribution in the tube's wall.



Source: (Hull 1991)

Table 2.3 - Effect of fiber orientation and fiber distribution through the tube's wall on the crushing behavior of carbon fiber-epoxy tubes under different loading rate (Hull 1991).

Effect examined	H:A	Position of plies	Specific crushing stress ( $\text{kN/m}^2$ )/( $\text{kg/m}^3$ )		
			4 mm/s	2000 mm/s	
Different distribution	(a)	1:3	Symmetrical	71	109
	(d)	1:3	All hoop inside	88	64
	(f)	1:3	All hoop outside	6	16
Symmetrical distribution	(a)	1:3	Symmetrical	71	109
	(b)	3:2		74	65
	(c)	3:1		60	54
Symmetrical and interleaved distribution	(b)	3:2	Symmetrical	74	65
	(e)	3:2	Interleaved	43	37

Results presented in Table 2.3 shows that besides the H:A ratio, the distribution of fiber through the tube's wall has a significant effect on crushing performance of laminated absorbers.

This table also shows that the loading rate can affect the energy absorption of tubular composite energy-absorbers significantly.

### 2.5.2 Loading rate effects on crashworthiness of composite tubes

Since an energy-absorber is likely to experience a wide range of loading rates, a design based on only quasi-static analysis may not be valid under dynamic impact conditions. The matrices used in composite materials are usually viscoelastic, which means their response to loading will be rate dependent. On the other hand, the fibers (e.g., carbon fibers) are linear elastic so they will be less susceptible to a change in properties with loading rate.

It is reported that the effect of the testing rate on Specific Energy Absorption, SEA is related to the failure mode, i.e., the mechanism that controls the crushing process is rate-dependent, Farley (Farley 1991). For instance, where the fibers play the dominant role in the failure mechanisms, the energy absorption should not be a function of the test rate. However, due to anisotropic behavior for laminated composites, effects of ply orientation, stacking sequence and constituents' type (different types of fiber and matrix), contradictory reports have been observed in the literature (Jacob et al. 2002).

Table 1. Some publications that studied the crushing speed effects on the value of Specific Energy Absorption, SEA.

Reference	Method	Loading rate (m/s)	Section	Fiber type/ layup	Effect on SEA
Palanivelu [9]	DH	9.3 to 14	Circular tube	Glass fiber	No change
			Square tube		Increased
David [13]	HM	1e-3 to 10	C-section	Carbon fiber [(0/90) <sub>2</sub> /0/(90/0) <sub>2</sub> ]	Decreased
Jackson [12]	HM	3.3 e-4 to 8.5	C-section	Carbon	Decreased
Brighton [25]	HM	1.67e-4 to 4	Tube	Carbon-epoxy [0/90] <sub>4</sub>	Decreased
				Glass-polypropylene fabric	No change
Thornton [7]	HM	2.1e-4 to 15	Pultruded tubes	Glass fiber-polyester resin	Increased
				Glass fiber-vinyl ester resin	Increase or decrease depending on

Table 1. Some publications that studied the crushing speed effects on the value of Specific Energy Absorption, SEA.

Reference	Method	Loading rate (m/s)	Section	Fiber type/ layup	Effect on SEA
					the tube's geometry
Farley [8]	HM	1e-4 to 12	Tube	Graphite-epoxy ([0/±θ] <sub>2</sub> )	No change
				Kevlar-epoxy Graphite-epoxy ([±θ] <sub>3</sub> )	Increased
Chiu [14]	HM	1.7e-5 to 8	Tube	Carbon-epoxy prepreg [0/90/0/90] <sub>s</sub>	No change
Wang [5]	HM-DH	1.6e-4 to 10.2	Tube	Carbon fiber	Decreased

HM: Hydraulic machine

DH: Drop hammer

Several researchers have found that the SEA of samples decreases with increased test speed. Results by Schmueser and Wickliffe (Scueser and L.E 1987) also show that the SEA decreased by 30% with a test speed increase, and suggested that studies based entirely on quasi-static test data can overestimate the energy absorption levels under dynamic conditions. Brighton (Brighton et al. 2009), Jackson (Jackson et al. 2011), David (David, Johnson, and Voggenreiter 2013), and Wang (Wang et al. 2016) also reported a decrease in SEA value of composite tubes under axial compression.

Thornton (Thornton 1990) investigated the energy absorption behavior of pultruded glass/polyester and glass/vinyl ester tubes in the crushing speed range from 2.1E-4 m/s to 15 m/s. A ten percent decrease with increasing test speed in the case of glass/vinyl ester tubes and a 20% increase in energy absorption in the case of glass/polyester tubes were reported (Thornton 1990). This issue can be related to the higher tensile strength and modulus of the vinyl ester. Thornton et al. (Thornton, Tao, and Robertson 1991) later investigated glass fiber/vinyl ester rods. The specific energy was seen to increase linearly with log (testing rate).

Palanivelu (Palanivelu, Van Paepegem, Degrieck, Van Ackeren, Kakogiannis, Van Hemelrijck, et al. 2010) reported an increase in SEA of glass fiber tube with square cross-section; however, the SEA value of tube with circular cross-section

remained unchanged. Farley (Farley 1991) observed the same finding for graphite-epoxy tubes with different ply-orientation. He reported an increase in the SEA value of tube with  $[\pm\theta]_3$  stacking sequence, the contrary, the crushing performance of tube with  $[0/\pm\theta]_2$  was not rate-sensitive. Chiu (Chiu, Falzon, Ruan, et al. 2015) studied cross-ply carbon fiber tube with circular cross-section and reported no change in the crashworthy criteria.

The following points on the loading effect on energy absorption of composite tubes can be thus summarized.

- The mode of failure is dependent on the loading rate. Ply delamination can affect the failure modes of composite tubes; therefore, the difference between the static and dynamic results could be related to the sensitivity of interlaminar fracture toughness (matrix) to loading rate (Schmueser and Wickliffe 1987).
- The findings related to the dynamic loading of composite tubes are in contrast to the dependences observed in metallic tubes where SEA usually increases with the increase of the loading rate. The latter behavior is also related to the change of the material properties when the material strengthen due to the strain rate effects (Karagiozova, Alves, and Jones 2000; Karagiozova and Jones 2001).
- The strain rate sensitivity remains of primary concern in crashworthy design (Chiu, Falzon, Ruan, et al. 2015; David et al. 2013; Jackson et al. 2011; Wang et al. 2016).

### **2.5.3 Effect of tube geometry**

Effect of diameter to thickness ratio ( $D/t$ ) has been investigated extensively (Ramakrishna et al. 1995; Wang et al. 2016). There is a definite trend between wall thickness to diameter ( $t/D$ ) ratio and SEA value. Thin tubes and tubes with low  $t/D$  ratio fail by unstable buckling (very low absorbed energy). The optimal wall thickness and  $t/D$  ratio were reported to be 2-3mm and approximately 0.6, respectively (Ramakrishna et al. 1995). Although these values will vary for the different materials, they provide a reasonable basis for tube geometry design. It is important to note that square tubes may require a greater wall thickness to ensure stable crush.

The damage initiation by introducing various triggers was discussed in the literature where it is pointed out that, without a trigger mechanism, composites can

fail by catastrophic failure modes like unstable axial collapse or compressive shear (Jacob et al. 2002). Trigger effects on the crashworthiness of composite tubes have been investigated extensively (Czaplicki, Robertson, and Thornton 1991; Gui, Zhang, and Fan 2009; Huang and Wang 2010; Okano, Nakai, and Hamada 2005; Thuis and Metz 1994; Tong and Xu 2018; Yang, Nakai, and Hamada 2009). External chamfer, tulip trigger, and plug initiators are the most popular crush initiator for tubular composite absorbers under axial compression. Farley (Farley 1983) found that by introducing a chamfer the peak load can be significantly reduced (which is desired) without affecting the sustained crushing load. Czaplicki et al. (Czaplicki et al. 1991) reported that one-end tulip trigger in square tubes increased the SEA value in comparison with the chamfer trigger by roughly 100%.

## **2.6 Methods to predict the crushing performance of tubular composite components**

As mentioned earlier, numerous parameters control the crushing performance of composite materials. Thus experimentally finding the optimum composite product from coupon level to real scale model is costly due to several required prototypes testing. Several analytical models have been presented (Ching Quek et al. 2001; Mamalis, Yuan, and Viegelaahn 1992) predicting the energy absorption of laminated tubular absorbers. However, these analytical models have not gained wide attention to predict the crushing behavior of composite tubes. Knowing crushing modes of each layer in the laminated tube, e.g., the number of separation between layers, is the primary assumption that means the tube should experimentally be crushed so these analytical models can 'predict' the absorbed energy. Therefore, alternative methods are required where the crushing performance of tubular composite parts under dynamic loading can be foreseen.

### **2.6.1 Finite element simulation of axial impact on tubes**

Finite element analysis has been accepted as a powerful and advantageous modeling tool in many engineering applications. The importance of this virtual modeling tool for the composite material is highlighted due to above-mentioned intrinsic and extrinsic parameters that affect composite behavior. Using a valid FE

model, optimum composite components could be developed faster, in comparison with the experimental procedure. Several commercial FE packages; such as Abaqus, LS-Dyna, and PAM-CRASH, offer composite modulus allowing engineers capable of modeling of different loading conditions and scenarios on composite structures.

Force-displacement curve and failure modes have been considered as two underlying criteria to verify the accuracy of the FE model of composite components under impact loading. However, the latter criterion is more difficult to be achieved due to some limitations in commercial FE packages. A brief review of publications dealing with finite element simulation of axial loading on tubular laminated components is presented in the sequel.

### **2.6.2 Approaches to model axial tubular laminated absorber**

Since delamination plays a very important role in damaging behavior of a laminate composite part (Barbero 2013), the simulation approaches were categorized into two groups; (I) Single-layer model and (II) Multi-layered, the former not considering delamination effects.

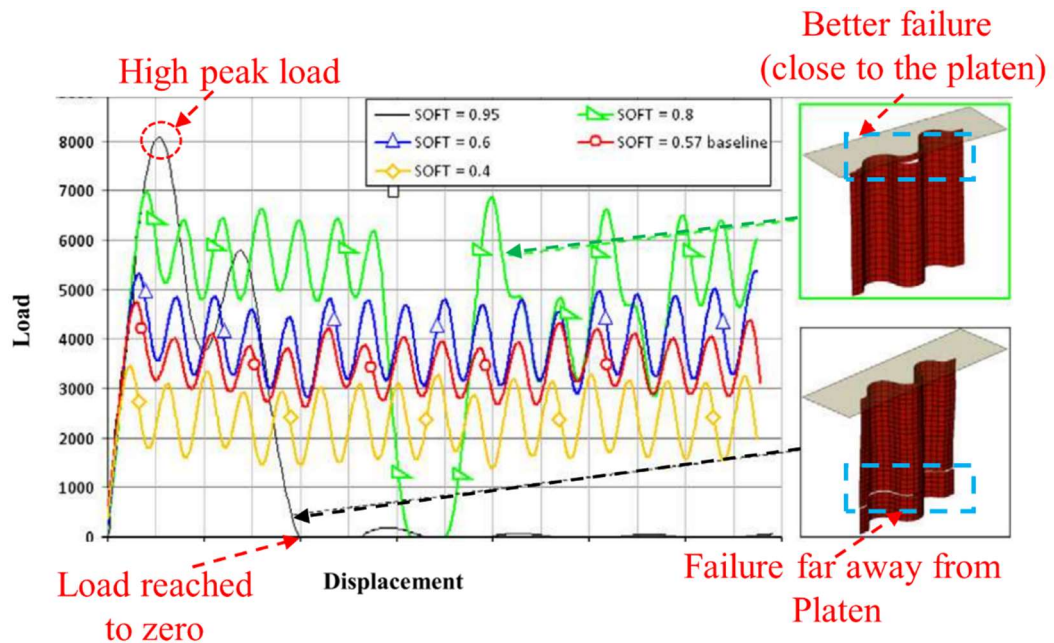
#### **➤ Equivalent single layer approach**

By using a single-layer approach, the analysis of a heterogeneous laminated component is reduced to the analysis of a homogeneous anisotropic component. The stacking sequence of lamination will be replaced by mechanical properties of an equivalent section (the integration points through the thickness represent the composite plies). The single-layer approach is advantageous to commercial FE software since the required element number and, eventually, CPU time will be reduced. However, the single-layer approach may be more appropriate to analyze the global behavior of laminated composite.

The single-layer approach could predict the 'progressive folding' performance of ductile materials, such as metal and less brittle composites tubes (Morthorst and Horst 2004) with acceptable accuracy. However, modeling 'progressive crushing modes' in tubes made of the brittle composite layer is more complicated and usually required massive calibrations (Cherniaev, Butcher, and Montesano 2018; Feraboli et al. 2011), see Figure 2.16. A simplified single-layer model of a laminated tube cannot

model delamination. Therefore, without massive material and impact calibrations, the force-displacement of such that model characterized by dramatically high peak load followed by dramatically load drop.

Figure 2.16 - Effect of material calibration on the crushing behavior of carbon-reinforced components under the axial impact.



Source: (Feraboli et al. 2011)

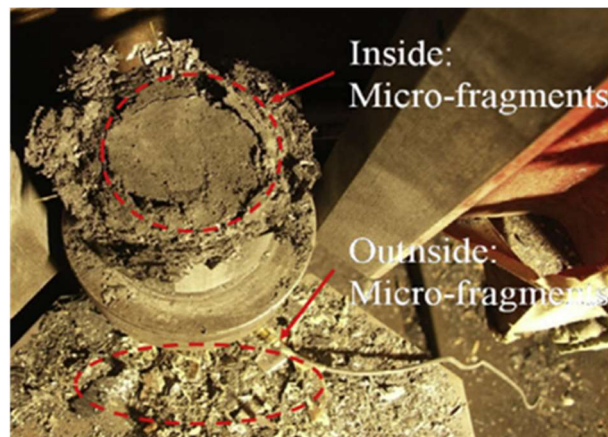
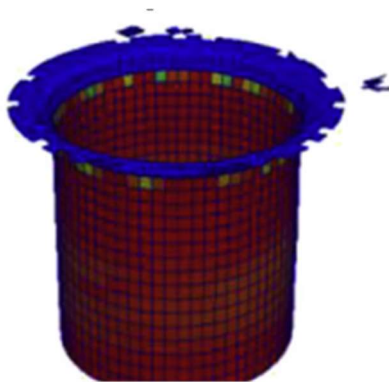
Some researchers tried to perform axial impact on tubular laminated composite absorbers by using single-layer approach, as listed in Table 2.4. An example of force-displacement and failure mode in a laminated tube modeled by single-layer approach is depicted in Figure 2.17. An acceptable similarity between force-displacement curves (experimental and numerical) has been reported, also simulated tubes underwent progressive damaging is mainly concentrated on the region where the hammer and the tube extrusion come into contact with each other (Luo et al. 2016).

Table 2.4 - Examples of single-layer laminated specimens under axial compression.

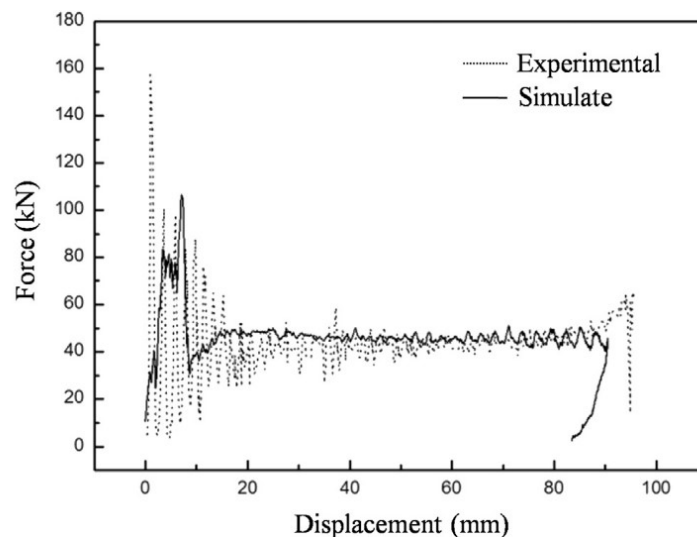
Research	Intra-layer modeling	Software	Cross-section material
----------	----------------------	----------	------------------------

(Feraboli et al. 2011)	Shell element	LS-Dyna	CFRP Prepreg tape Corrugated specimen
(Ghasemnejad et al. 2009)	Shell element	ANSYS/Dyna	Square tube GFRP
(Luo et al. 2016)	Shell element	MSC-DYTRAN Subroutine	CFRP Circular tube
(Zhu et al. 2018)	Shell element (S4R)	Abaqus	Square tube CFRP
(Cherniaev et al. 2018)	Shell element	LS-Dyna	Square tube CFRP

Figure 2.17 - An example of force-displacement and failure mode predicted by a single-layer approach of axial crushing on CFRP tube specimen.



(a)



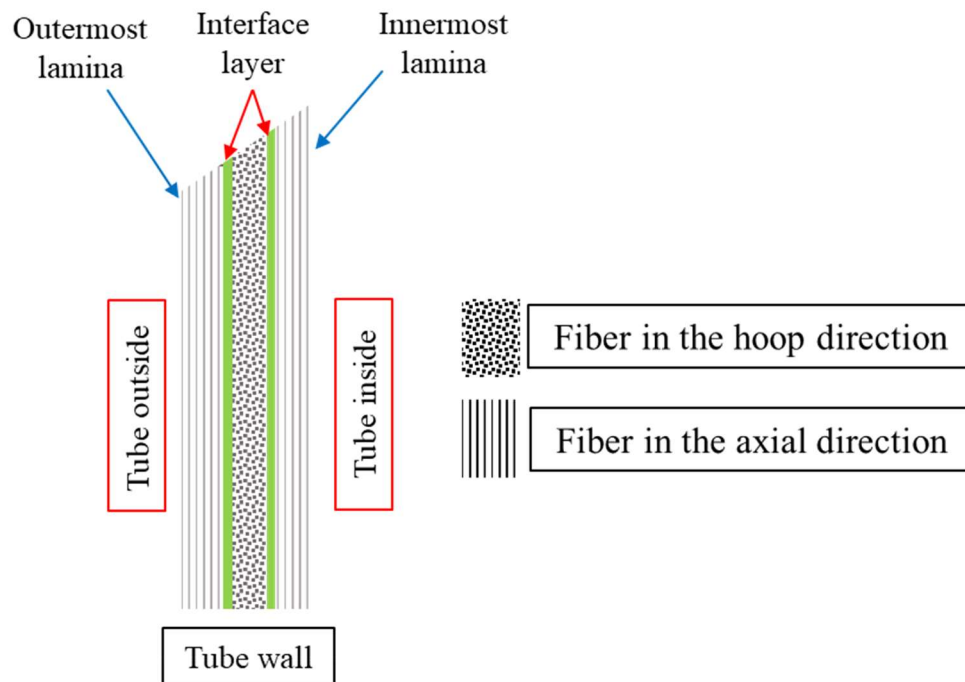
(b)

Source: (Luo et al. 2016).

### ➤ **Multi-layer approach**

This approach is gaining more and more attention since the layer-wise model is capable of modeling both intra- and inter-laminar behavior of laminated composites. Each layer in the model represents a ply (or more than one ply) with a specific orientation, material properties, and thickness. Thus one layer of shell (Morthorst and Horst 2004; Siromani, Awerbuch, and Tan 2014; Zhao et al. 2019) or solid (Chiu, Falzon, Boman, et al. 2015a; Tan et al. 2016; Tan, Falzon, and Price 2015) elements will be used to model each lamina in the thickness direction of laminate, and adjacent laminae should be tied with any possible inter-laminar modeling techniques like Cohesive Zone Model. The main feature of the multi-layer approach of a laminated tube is depicted in Figure 2.18.

Figure 2.18 - Multi-layer model of the laminated component, including intra- and inter-layer modeling.



Source: The author.

The multi-layer modeling approach is more complicated and computationally more expensive rather than the equivalent single-layer approach. However, it allows more realistic results, both the force-displacement curve and fracture morphology. Table 2.5 lists recent work that used a multi-layer approach to simulate axial impact loading on tubular absorbers. The emphasis is on; (I) discretization of the composite lamina (i.e., element type), (II) interface modeling technique, (III) utilized software and (IV) geometry of the specimen and material type.

Table 2.5. Example of recent multi-layer modeling approach of tubular absorbers under axial impact.

Reference	Intra-layer modeling	Inter-layer modeling	Software	Cross-section / material
(Morthorst and Horst 2004)	Shell element	Solid isotropic resin	LS-Dyna	Conical tube Glass fabric – epoxy
(Mamalis et al. 2006)	Shell element	Tie-break	LS-Dyna	Square tube CFRP
(Siromani et al. 2014)	Shell element	Tie-break	LS-Dyna	Circular tube graphite/epoxy
(Reuter, Sauerland, and Tröster 2017)	Shell element	Tie-break	LS-Dyna	Circular tubes CFRP
(Huang and Wang 2009)	Shell element	Tie-break	LS-Dyna	Circular tubes CFRP
(McGregor et al. 2017; McGregor, Vaziri, and Xiao 2010)	Shell element	Tie-break	LS-Dyna User-material	braided composite Square tubes
(Palanivelu, Van Paepegem, Degrieck, Van Ackeren, Kakogiannis, Wastiels, et al. 2010)	Continuum shell (SC8R)	CZE	Abaqus	Square Circular pultruded glass-polyester
(Sokolinsky, Indermuehle, and Hurtado 2011)	Continuum shell (SC8R)	CZS	Abaqus User-material	Corrugated plate Fabric carbon fiber
(Zhu Yigang, Wang Jin, and Zhang Zilong 2012)	Continuum shell (SC8R)	CZS	Abaqus	Square tube CFRP

(Patel, Vusa, and Guedes Soares 2019)	Continuum shell (SC8R)	CZS	Abaqus User-material	Circular tube CFRP GFRP
(Chiu et al. 2016; Chiu, Falzon, Boman, et al. 2015b)	Solid element	CZS	Abaqus User-material	Carbon fiber Hat shaped, Semi-circular, corrugated and web specimens
(Tan et al. 2016)	Solid element	CZS	Abaqus User-material	CFRP (AS4/PEK) Corrugated specimens
(Tan et al. 2015)	Solid element	CZS	Abaqus User-material	CFRPs Small wedge
(Zhu et al. 2018)	Shell element (S4R)	CZE	Abaqus	Circular tube Hybrid CFRP /Al
(Zhao et al. 2019)	Shell element (S4R)	CZE	Abaqus	Tapered tubes woven Fabric CFRP

CZE: Cohesive Zone Model- Element-based in Abaqus.

CZS: Cohesive Zone Model- Surface-based in Abaqus.

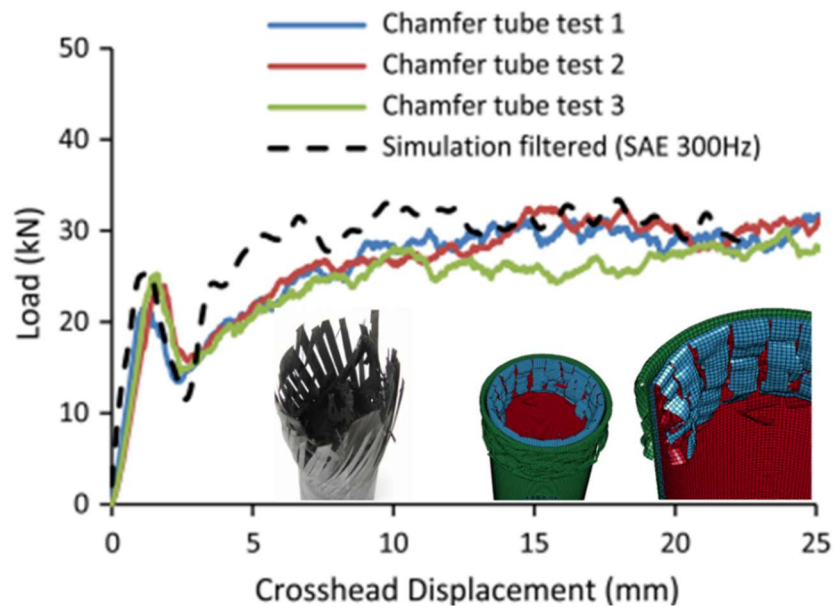
CFRP: Carbon fiber-reinforced plastic.

GFRP: Glass fiber-reinforced plastic.

Force-displacement and fracture morphology of some the simulation work presented in Table 2.5 are presented as two main criteria in Figures 2.19 to 2.22. Regardless methods and techniques to model intra- and inter-laminar behaviors, tube geometry and trigger mechanism have a very strong role to achieve failure modes similar to experimental tests. For instance, failure modes of simulation of the tubes having a square cross-section and circular tubes with plug damage initiator have been more successful (McGregor et al. 2010; Siromani et al. 2014). On the contrary, failure modes in tubes with (or without=flat end) external chamfer, impacted by flat platen,

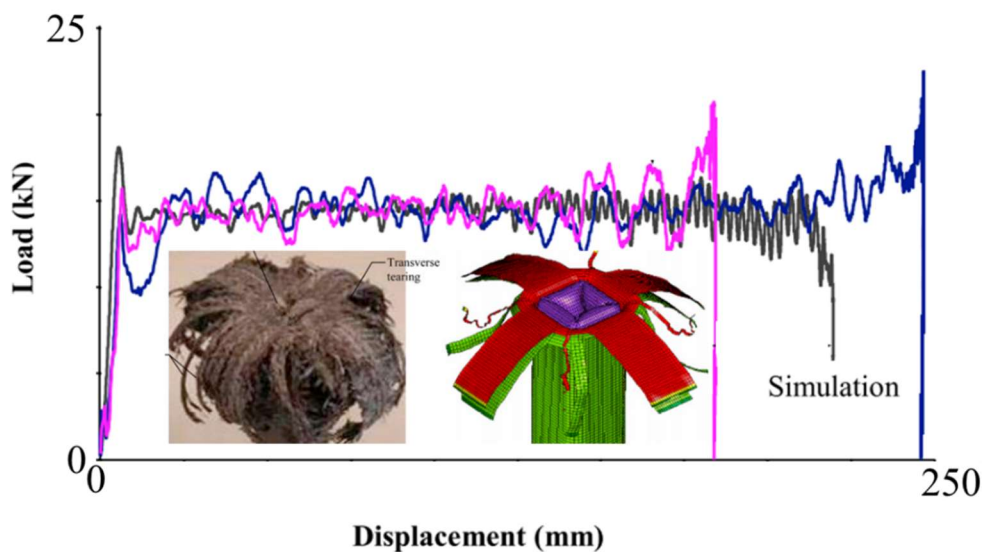
has been reported less successful especially to capture ‘axial splitting’ of the outermost layer (made of UD lamina) in splaying model, see Figure 2.11.

Figure 2.19 - Force-displacement and failure mode of tubes using multi-layer (shell element) in LS-Dyna.



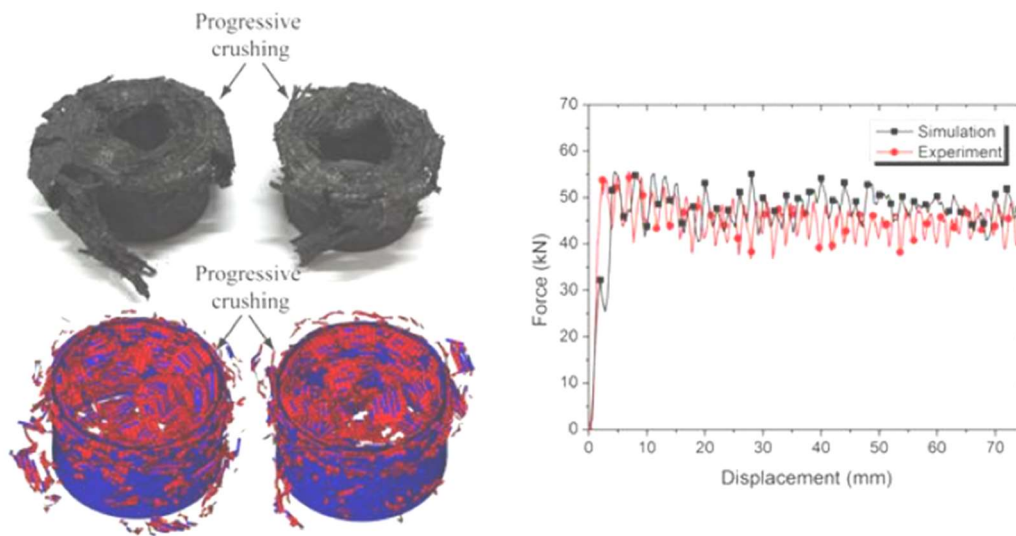
Source: (Siromani et al. 2014).

Figure 2.20 - Force-displacement and failure mode of square tubes using multi-layer (shell element) in LS-Dyna.



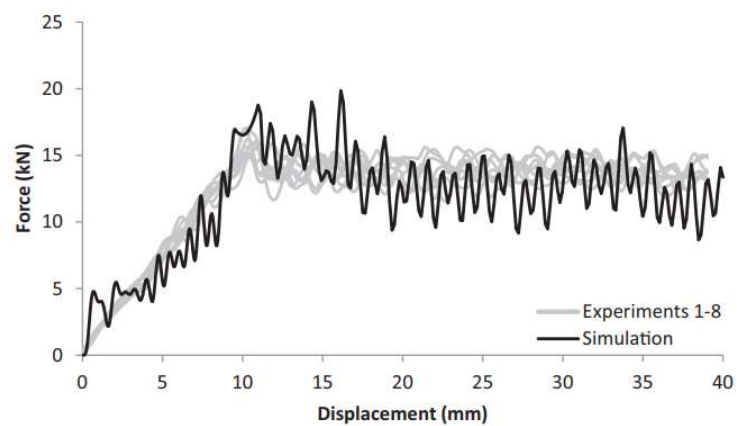
Source: (McGregor et al. 2010)

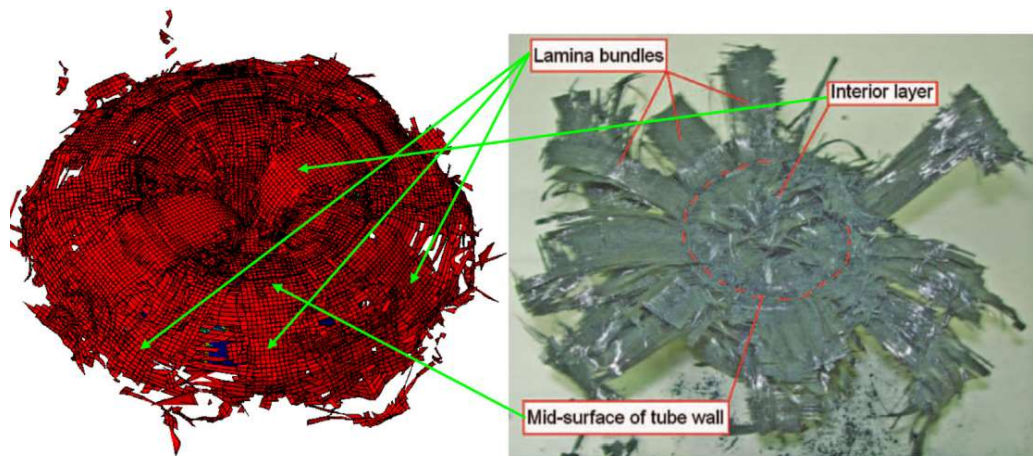
Figure 2.21 - Force-displacement and failure mode of circular tubes with using multi-layer (shell element for CFRP) in Abaqus.



Source: (Zhu et al. 2018).

Figure 2.22 - Force-displacement and failure mode of circular tubes with using multi-layer (the solid element for CFRP) in Abaqus (implemented a material subroutine).

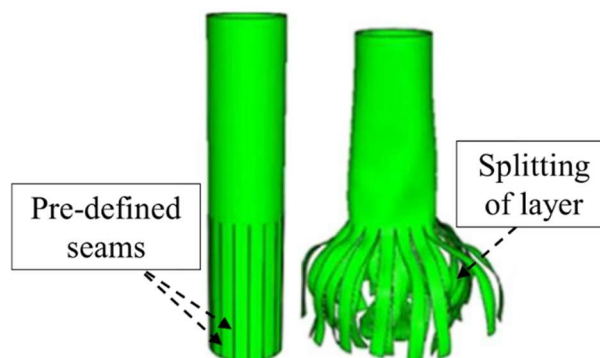




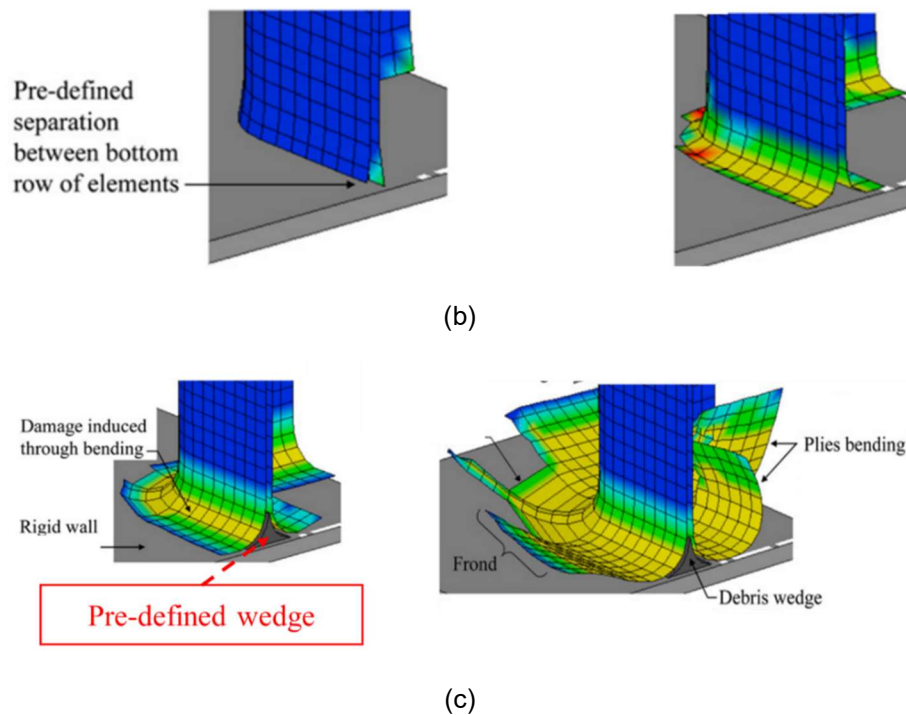
Source: (Chiu, Falzon, Boman, et al. 2015a).

Few special modeling technique have been utilized to achieve the axial splitting of the outermost layer in tubes under axial impact. For instance, pre-defined axial seams in the outermost layer (Palanivelu, Van Paepegem, Degrieck, Kakogiannis, et al. 2010) (Figure 2.23(a)), short pre-defined separation area between different layers at the end of the tube (Figure 2.23(b)) and pre-defined wedge in the tube center-wall (Figure 2.23(c)) to facilitate 'splaying mode'.

Figure 2.23 - Some special modeling technique in order to have a better splaying mode and axial splitting of the outermost layer in circular tubes under axial impact.



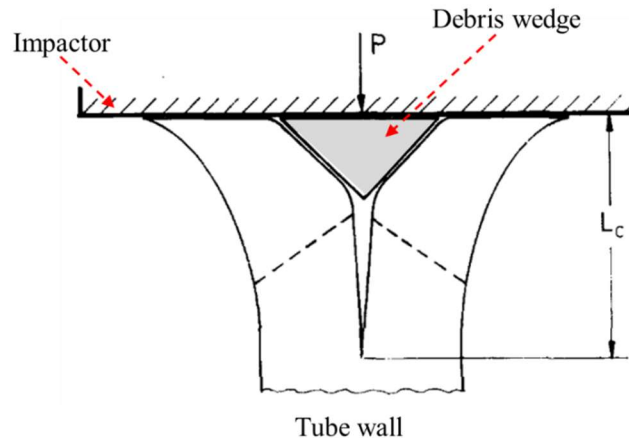
(a)



Source: (a): (Palanivelu, Van Paepegem, Degrieck, Kakogiannis, et al. 2010); (b,c): (McGregor et al. 2010).

Incorporation of solid debris wedge into the FE model (McGregor et al. 2010) is based on the experimental investigations, see Figure 2.24. Trapped debris between the impactor and crush front form a wedge-shaped region that facilitates the propagation of the center-wall crack along the tube's wall (Mamalis et al. 1996). The pre-defined wedge in the FE model is very similar to plug damage initiator. Thus, its shape and dimension may affect the crushing performance of composite tubes, similar to plug damage initiator effect.

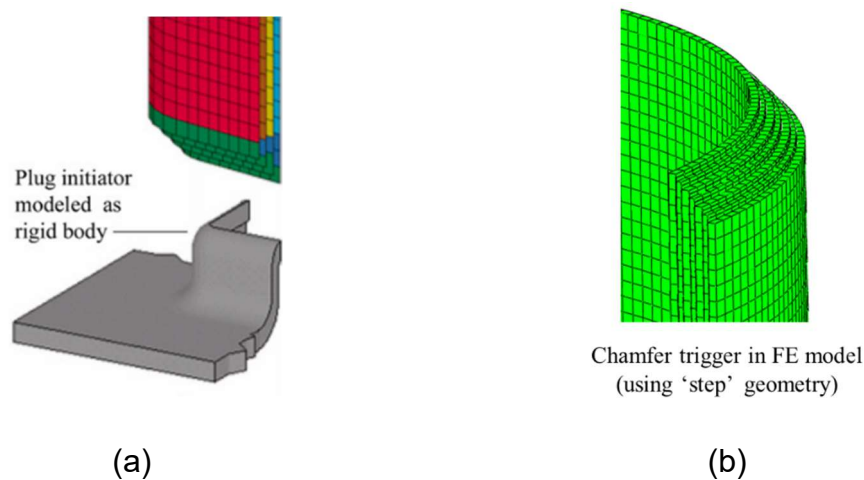
Figure 2.24 - Debris wedge in the crush front.



Source: (Mamalis et al. 1996).

In several finite element simulations, chamfer trigger has been modeled by using 'stepped wall' geometry (Chiu et al. 2016; Palanivelu, Van Paepegem, Degrieck, Kakogiannis, et al. 2010). Reproducing the progressive crushing by 'stepped wall' geometry is more complicated than FE models with plug initiator. The plug initiates and controls the progressive crushing during simulation, while chamfer will vanish at the beginning of the simulation. Figure 2.25 shows chamfer and plug initiator in FE simulation.

Figure 2.25 - Two types of crush initiator in FE simulation; (a) Plug initiator; (b) External chamfer.



Source: (a): (McGregor et al. 2010); (b): The author.

Table 2.5 shows that element with mid-surface formulation (2D shell element) has been extensively used to model crushing performance of tubes in LS-Dyna. This issue can be related to a richer material model library in LS-Dyna for composite materials, MAT58, MAT54, and MAT262, and relatively more straightforward interface modeling technique like tie-break.

Plane stress shell element (S4R) in Abaqus has been used in a few publications (Zhao et al. 2019; Zhu et al. 2018) to model multi-layer tubes under axial impact. One reason can be related to complicated interface modeling with this element. The continuum shell element (SC8 and SC8R) received more attention rather than S4R element in Abaqus. Besides the continuum shell element, the solid element has been used to model multi-layer composite absorber under axial impact in Abaqus. In Abaqus continuum elements (shell and solid) have better contact behavior rather than the conventional shell (S4R) (Dassault Systèmes Simulia 2014). Thus interface modeling of continuum element is more straightforward and perhaps due to this issue, S4R shell element has been less considered to model laminated absorbers under axial impact.

Several researchers used 2D built-in models available in commercial software (modeling composite plies); however, few researchers implemented their own constitutive models to represent intra-laminar behavior of composite plies, e.g., CODAM model by McGregor et al. (McGregor et al. 2017, 2010) in LS-Dyna and 3D constitutive models proposed by Chiu et al. (Chiu et al. 2016; Chiu, Falzon, Boman, et al. 2015b) and Tan et al. (Tan et al. 2016) in Abaqus.

Interface modeling techniques based on contact formulation have been extensively used to bond the laminae in multi-layer composite absorbers, e.g., 'Tiebreak' feature in LS-Dyna and surface-based cohesive zone model (CZS) in Abaqus. These two techniques do not require an extra set of elements to represent interface layers. Therefore, the FE simulation will be faster with these techniques. The element-based cohesive zone model (CZE) has been used to bond the S4R shell element in Abaqus to model laminated absorber under axial compression (Zhao et al. 2019; Zhu et al. 2018), It seems the authors could not use the more straightforward

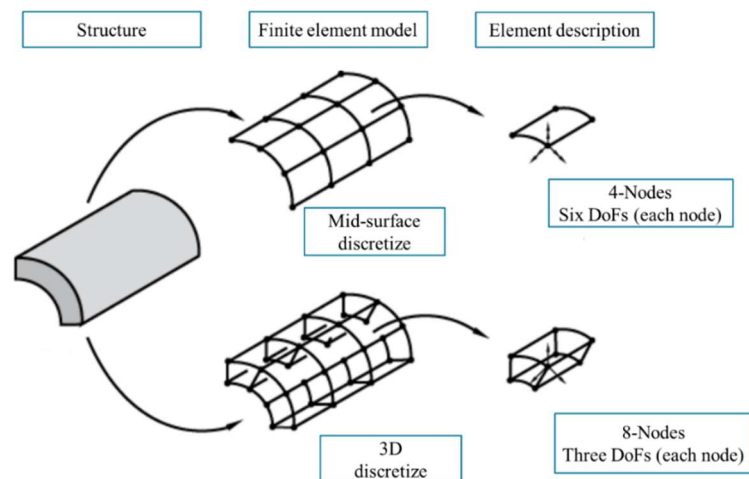
surface-based cohesive model (CZS) due to poor contact behavior of S4R shell element in Abaqus.

### 2.6.3 Conventional shell and continuum shell elements in Abaqus

Shell elements are used to discretize parts in which one dimension, in the out-of-plane direction, is effectively smaller than the in-plane dimensions. Laminate structures are made of very thin lamina; thus, the laminae could be treated as shell-like components. Conventional shell elements (S4 or S4R) use this condition to discretize a body by reducing a thin 3D geometry at a mid-surface. These elements are applicable for both thick and thin shell-like structures. Conventional shell elements have six DoFs at each node, three translational and three rotational (Dassault Systèmes Simulia 2014).

Kinematic and constitutive behavior of continuum shell elements is similar to conventional shell elements; however, continuum shell elements discretize an entire 3D body similar to three-dimensional continuum solids. Continuum shell elements have only three translational degrees of freedom at each node. Continuum shell elements are useful for the very thick body (Dassault Systèmes Simulia 2014). Figure 2.26 compares conventional and continuum shell elements in Abaqus.

Figure 2.26 - Conventional versus continuum shell element.



Source: (Dassault Systèmes Simulia 2014).

## 2.7 Intra-laminar modeling of composite plies: Overview of the progressive failure analysis of fiber-reinforced composites

In general, there are two basic approaches to predict the failure of the composite lamina, micro-phenomenological<sup>1</sup>, and macro-phenomenological approaches (Vasiliev and Morozov 2013). In the micro-approach, failure is predicted through checking failure criteria proposed for homogeneous materials regarding stresses in the fibers and the matrix as separate constituents of the composite lamina. Although only the strengths of fibers and matrix are required, micro-approach is not suitable for practical analysis of composite components. This approach is more suitable for qualitative analysis, providing a better insight into the effects of quantitative data, mechanical properties of constituents and fraction volumes in composite, on mechanical properties of the composite (Daniel et al. 2006; Vasiliev and Morozov 2013).

In the macro-approach, a composite ply is treated as homogeneous but anisotropic material and ply micro-structures, constituents, would be ignored. Macro-mechanical failure criteria of composites ply are modified failure theories of isotropic materials, such as maximum shear stress, maximum normal stress, and von Mises, accounting strength and stiffness anisotropy of the lamina (Daniel et al. 2006).

In this thesis, UD lamina would be considered as homogeneous transversely isotropic material. Thus the smallest material unit is the lamina-level.

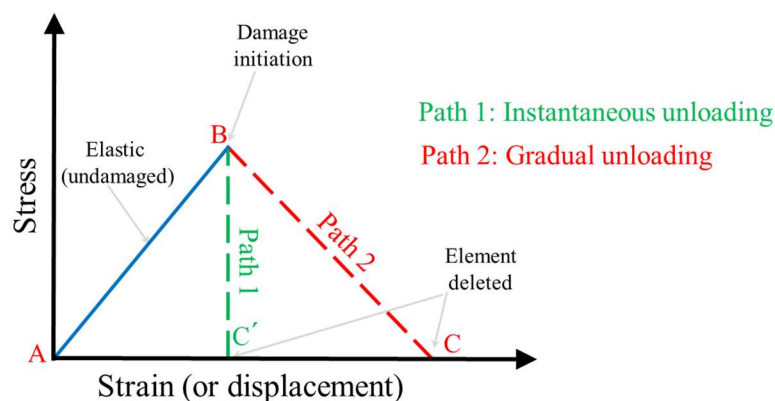
Even though brittle composite laminae have very small failure strain values, the load-bearing capacity of a laminated structure does not vanish suddenly after first failure initiation at a material point (Anderson, L 2004; Lopresto, Langella, and Abrate 2017) due to stress redistribution mechanism. Damaging process in composite structures has a progressive nature; thus, progressive failure analysis is advantageous to study the structural response of laminated composites under dynamic loading conditions.

---

<sup>1</sup> The term ‘phenomenological’ means that the actual physical mechanisms of failure at the microscopic material level are not considered and that we deal with stresses and strains (Vasiliev and Morozov 2013).

A material model in the Progressive Failure Analysis (PFA) should be able to represent the material response before and after the damage(s) onset. Therefore, this material model is a combination of a failure criterion and post-failure material property degradation scheme (Lopresto et al. 2017). The 'ABC' curve in Figure 2.27 illustrates the schematic presentation of a material response that has been considered widely to model in-plane progressive damaging of composite materials. The 'ABC' path also represents another possible material response, that the post-damaging behavior is less complicated rather post-damaging behavior of 'ABC' curve.

Figure 2.27 - The bilinear response of an element based on PFA.



Source: The author.

The material model (Figure 2.27) has an undamaged linear response between points 'A' and 'B'. This model is suitable for unidirectional lamina like carbon fiber – epoxy, that present a linear behavior under uniaxial in-plane loading.

Failure criteria will be used to predict the damage(s) onset (point 'B' in Figure 2.27). Some popular criteria for anisotropic material systems are described and compared in many textbooks (Christensen 2013; Daniel et al. 2006). It is possible to categorize the lamina-level failure theories in three groups, as follows (Daniel et al. 2006).

I. Non-interactive failure theories; such as maximum stress and maximum strain theories, while there is no interaction between different stress components on failure. The failure prediction will be check through comparing individual lamina stresses (strains) with corresponding ultimate strengths (ultimate strains).

II. Interactive failure theories; such as Tsai-Hill and Tsai-Wu failure criteria, these criteria are expressed as only one expression of stress components. In this case failure prediction does not refer to any failure modes, like different fiber/matrix failures modes.

III. Mode-based failure criteria; such as Hashin-Rotem and Puck failure criteria. In this case, for each actual failure modes, fiber/matrix in compression/tension, individual failure criterion is presented.

Table 2.6 compares widely used failure criteria considering stress interactions, ease of usage and required material input data

Table 2.6 - Comparison between some popular failure theories for composite materials (Daniel et al. 2006).

<b>Category</b>	<b>Theory</b>	<b>Required experimental characterization</b>	<b>Operational convenience</b>
Limit or non-interactive	Max Stress	Few parameters with simple testing	Inconvenient
	Max Strain		
Interactive	Strain-energy-based (Tsai-hill)	Both biaxial and uniaxial testing are required	Different functions for both tensile and compressive strengths are required
	Interactive tensor polynomial (Tsai-Wu)	Numerous parameters and comprehensive experimental tests	Operationally simple
Mixed	Failure mode separation (Hashin-Rotem)	Few parameters with simple testing	Somewhat inconvenient

In general, after damage initiation (point 'B' in Figure 2.27), the material properties of damaged finite elements will be degraded by two main degradation strategies (Lopresto et al. 2017). (I) Mechanical properties of the material at damaged

finite element(s) would be reduced to a negligible value very close to zero (path 1 in Figure 2.27); (II) a more sophisticated degradation scheme based on continuum damage mechanics (CDM) would be implemented to reduce material property gradually at the damaged area. For instance, MAT54 in LS-Dyna uses the first mentioned degradation law (so-called 'ply discount') with Chang-Chang damage criterion. In contrast, MLT model presented by Matzenmiller et al. (Matzenmiller, Lubliner, and Taylor 1995) is based on continuum damage mechanics (CDM) while after damage initiation, a gradual material softening will occur.

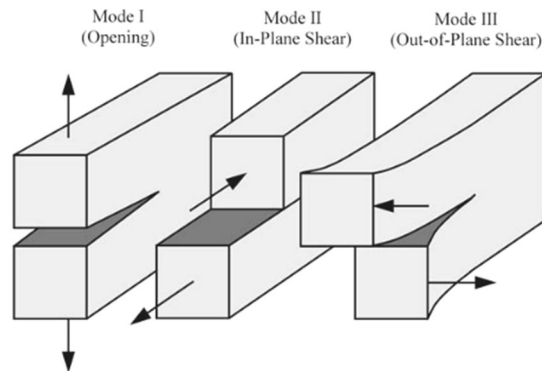
## **2.8 Interface modeling**

Inter-laminar failure or delamination has been widely investigated as one of the most critical failure modes in laminated composites. Debonding of two adjacent laminae, usually with different fiber orientation, occurs in their weak resin-rich interface area. Initial crack due to the manufacturing process, low-velocity impact and fatigue may cause and facilitate delamination even in very low loading (Barbero 2013).

Finite element analysis offers few techniques to predict delamination mode due to individual or combination of fracture modes presented in Figure 2.28. Virtual Crack Closure Technique (VCCT) and Cohesive Zone Models (CZMs) have been widely used to model interface. Similar to the intra-laminar progressive damaging, desired interface modeling techniques should comprise three features; (I) undamaged response, (II) damage initiation, and (III) properties degradation law. However, in contrast to CZMs, VCCT requires predefined initial crack and it is not able to predict damage initiation by itself (Bogenfeld, Kreikemeier, and Wille 2018). Thus, CZMs are more preferred for impact analysis and VCCT usually is utilized to calculate the energy release rate, ERR (Bogenfeld et al. 2018; Hallett and Harper 2015). CZM is a fracture-mechanical method which describes the initiation and the propagation of a crack in a predefined interface. Dugdale (Dugdale 1960) and Barenblatt (Barenblatt 1962) pioneered the cohesive zone model. However, the interface delamination captured by Allix and Ladeveze (Allix and Ladevèze 1992) used the CZM for the first time. CZM is well suited to model the delamination mode in laminated structures,

where crack paths are likely to occur in weak resin-rich interface of the laminae (Hallett and Harper 2015).

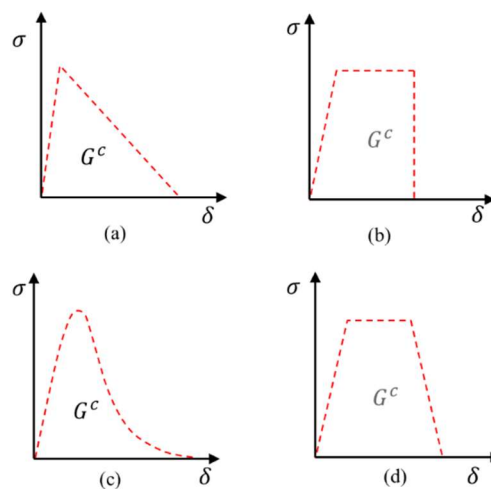
Figure 2.28 - Fracture modes.



Source: (Anderson, L 2004)

The constitutive relations for the cohesive method is expressed by using traction-separation law, as depicted in Figure 2.29. In the most straightforward and widely used traction-separation form, the material behaves elastically up to its maximum traction then it degrades linearly to zero at final displacement, Figure 2.29(a). However, few other shapes have been used to represent the traction-separation behavior of interface layer (Hallett and Harper 2015).

Figure 2.29 - Few cohesive traction-separation curves in the literature; (a) Bilinear, (b) Perfectly plastic, (c) Exponential, (d) Trapezoidal.



Source: (Hallett et al. 2008).

One of the essential features of the cohesive zone model based on traction–displacement curve is the absorbed energy, as calculated by the area under the curve.

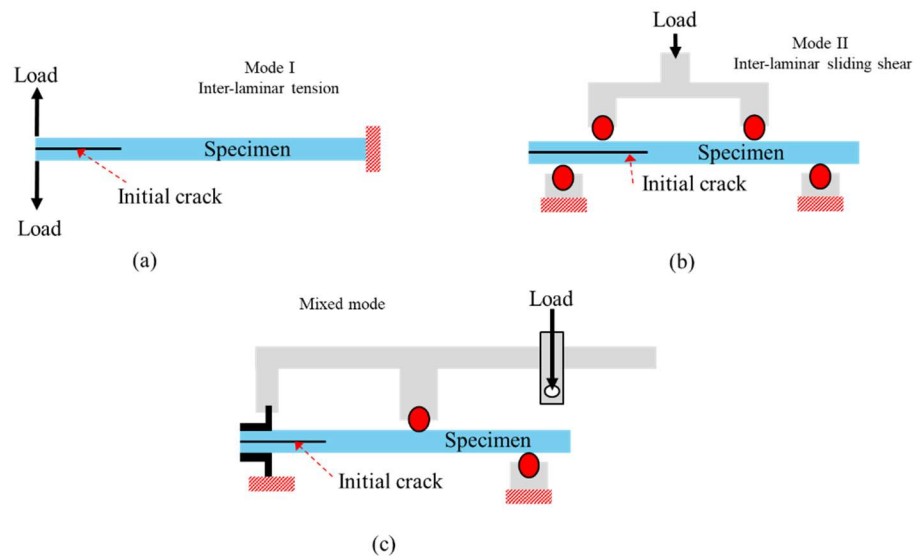
$$G^c = \int_0^{\delta_f} \sigma \cdot du \quad (2.2)$$

where  $\sigma$  is the interfacial stress,  $u$  is the crack opening displacement and  $\delta_f$  is the displacement at fully failure point.

In Abaqus, there are two methods in order to model the cohesive zone model between adjacent laminae; (I) surface-based cohesive model (CZS) and (II) element-based cohesive model (CZE). In contrast to the surface-based method, besides traction-separation law, any progressive material model based on CDM can be used as a constitutive relation for the element-based cohesive model. However, the main difference between these two models is that the cohesive behavior in the surface-based method is an interaction (contact) behavior, while in element-based method interface will be modeled as material properties. The surface-based cohesive model does not require element; thus, computationally is more efficient than the element-based cohesive mode.

Modeling of the individual loading modes (in Figure 2.28) provides many useful applications. However, the interaction between modes should be considered, since in the real application mixed-mode loading is more likely to occur (Hallett and Harper 2015). Besides difficulties related to the implementation of the cohesive zone model, a rigorous testing scheme is required to characterize the mixed-mode behavior, as presented in Figure 2.30. These tests required unique specimens and equipment. Although delamination has been extensively investigated, the delamination mechanism of composite panels is far from being fully understood (Lopresto et al. 2017).

Figure 2.30 - Inter-laminar fracture toughness characterization tests (a) double Cantilever Beam (DCB) (b) Four points bend end-notched flexure test (4ENF) and (c) Mixed-mode bending (MMB) tests.



Source: The author.

Delamination and its simulation in the laminated structures under compressive load are very complicated. Under compression loading, the delaminated layers may buckle and propagate due to the interaction between delamination growth and buckling. The presence of delamination may reduce the buckling load of the composite laminates drastically (Barbero 2013). This issue can decrease the load-bearing capacity (eventually energy dissipation capacity) of tubular energy absorber dramatically.

## 2.9 Summary

The content of this chapter is summarized in the following sentences.

- Crushing performance of laminated absorbers under axial impact has been considered extensively
  - Numerous intrinsic and extrinsic parameters affecting the crushing behavior of composites have been recognized

- Few contradictory findings have been reported, especially about rate sensitivity of crushing performance of tubes.
- Due to this contradiction, it is true to say that there is no universal method to characterize the crushing performance of composite absorber experimentally.
  - Reliable FE models are required to investigate the crushing performance of energy absorber faster and less expensively.
  - In Abaqus, conventional shell element (S4R), regardless of its computational benefits, has been less considered to model multi-layer laminate under axial compression (e.g. axial impact on laminated tubes).
  - Due to poor contact behavior of 2D shell element (S4R) in Abaqus, implementation of surface-based cohesive zone model is not straightforward. Successful results have been reported to simulate multilayer absorbers with S4R shell element while adjacent layers were tied with element-based cohesive zone model. In this model, 2D shell elements are tied with 3D cohesive elements. Therefore, studying the other possible techniques to bond S4R elements may be useful to simulate axial compression on laminated absorbers.

### **3 In-plane material characterization of UD lamina<sup>1</sup>**

The chapter aims to derive the mechanical properties of the unidirectional (UD) lamina from experimentally measured properties of non-flat tubular multidirectional laminated specimens. The specimens were cut from carbon fiber-epoxy tubes under investigation.

#### **3.1 Deriving lamina in-plane properties from testing on the laminated samples**

The mechanical properties of a lamina, such as elastic moduli, Poisson's ratio, in-plane shear modulus and failure strengths, are essential requirements to model the behavior of composite materials and analyze laminated structures, numerically and/or theoretically. Standard flat unidirectional (UD) specimens are used to measure mechanical properties and failure strength, i.e., tensile testing on  $[0_n]$  flat coupons. Using multidirectional specimens instead of unidirectional specimens has become a more attractive procedure in order to find the failure strengths of UD lamina by using 'back-out factor' (Measurement 2002). Indeed, the unidirectional laminated specimens are good enough to measure the elastic moduli, but not to measure the failure strength.

The lower failure strength of the multidirectional, angle-ply or cross-ply, composite specimens in comparison with the unidirectional laminated specimens, brings several advantages leading to a more reliable measurement of the failure strength. The higher failure strength of the material requires a higher gripping force to prevent slippage of the specimen in the jaws of the tensile machine. This issue causes higher stress concentration and eventually a premature failure in the gripping area. Thus, by means of cross-plyed or angle-plyed specimens, it is possible to avoid premature failure and use un-tabbed specimens for the tensile test, which decreases the preparation costs. Moreover, using multidirectional specimens with back-out factor leads to the measurement of higher strength values for UD lamina, yet preventing premature failure (Ghaemi and Fawaz 2002). Since multidirectional laminate fails at lower strengths, the results are less sensitive to specimen preparation and testing skills and eventually lower data scatter as it has been reported for strength measurement

---

<sup>1</sup> The contents of this chapter has been submitted to Composite Structures Journal.

(Measurement 2002; Yeow-Cheong 2005; Ghaemi and Fawaz 2002). The benefits and reasons for using a cross-ply laminated specimen to derive lamina failure strengths by applying Back-out Factor, BF, or Cross-Ply Factor, CPF are well documented in 'composite materials handbook - polymer matrix composites guidelines for characterization' (MIL-HDBK-17-1F).

In general, the classical laminate theory, CLT, has been utilized to find the extensional and bending stiffness constants of laminate structures from UD lamina's mechanical properties. The reverse procedure of CLT in conjunction with experimental tests on laminated composite has become attractive in order to back-out the lamina strength from laminate strength (J. Welsh and Adams 1996; J. S. Welsh and Adams 1997), which is difficult to measure directly from testing of unidirectional specimens with high accuracy (Ghaemi and Fawaz 2002). Usually, like in the pioneer studies of Refs. (J. Welsh and Adams 1996; J. S. Welsh and Adams 1997), it is necessary to know in advance the elastic lamina constants ( $E_1$ ,  $E_2$ ,  $\nu_{12}$  and  $G_{12}$ ) in order to calculate the 'back-out factor'. Therefore, besides testing on multidirectional laminated specimens (finding strength), extra tests on UD lamina or using Rule of Mixtures (ROM) are required to find UD lamina elastic moduli and calculate the back-out factor. Only then it is possible to calculate the lamina failure strength from tensile/compressive measured strengths of the multidirectional laminate specimens. This prerequisite was mentioned as a disadvantage and difficulty of using a back-out procedure (J. Welsh and Adams 1996; J. S. Welsh and Adams 1997).

Yeow-Cheong (Yeow-Cheong 2005) tried to remove this disadvantage and difficulty by incorporating a reverse of classical laminate theory (CLT) and experimental testing on angle-ply specimens. This work aimed to remove the extra tests on lamina specimens and back-out both lamina elastic moduli and strength from testing on the laminated specimens. However, no explicit lamina-laminate relations between elastic constants were presented (Yeow-Cheong 2005). Ghaemi et al. (Ghaemi and Fawaz 2002) questioned the reliability and accuracy of predicting the failure of multidirectional laminates based on the obtained lamina properties from UD specimens and emphasized on the need to obtain effective properties of laminae as derived from testing on the multidirectional laminated specimens.

Lasn et al. (Lasn, Klauson, and Echtermeyer 2015) presented explicit relationships between the UD lamina elastic moduli,  $E_1$ ,  $E_2$ , and mechanical properties

of symmetric cross-ply laminates subjected to simple axial and flexural tests on flat specimens and suggested some strategies to derive the UD lamina elastic moduli from laminate stiffnesses including optimization. The explicit lamina-laminate relationships between the elastic properties were presented as functions of both effective tensile and flexural laminate stiffnesses, volume fractions of the  $0^\circ$  and  $90^\circ$  plies in the laminate and two more parameters that represent the contributions of the  $0^\circ$  and  $90^\circ$  plies to the laminate bending stiffness.

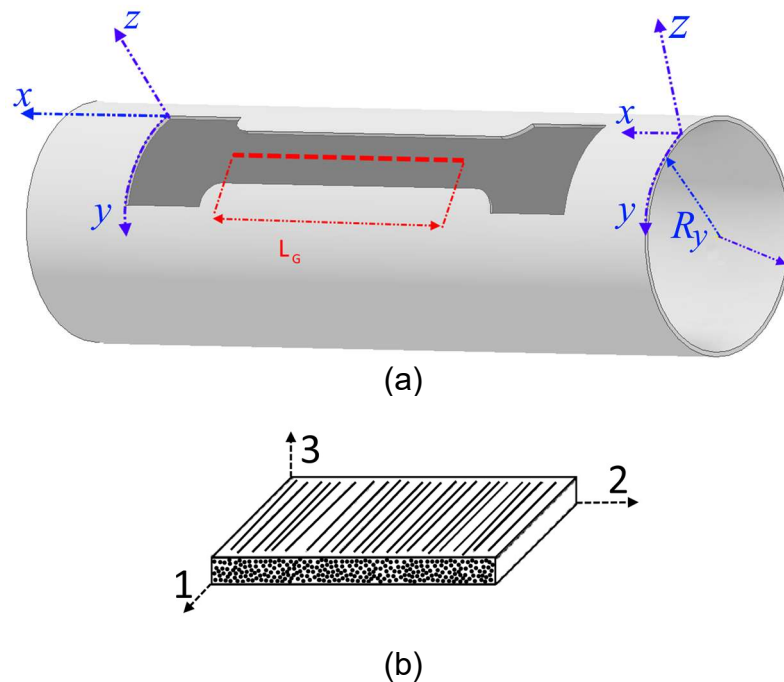
The majority of the studies on this subject deal with flat or straight-sided specimens to find the mechanical properties of the laminate composite. However, in some cases, flat coupons are not available as in the case of tubular filament-wound components. Cutting the required specimens from the real composite component is inevitable. Using non-flat and non-standard laminate specimens requires particular tests and makes the back-out procedure more complicated. On the other hand, testing specimens cut from the real structure would assure better quality consistency between the test coupons and final laminated structure.

## **3.2 Laminate to lamina relations**

### **3.2.1 Geometry and coordinate systems**

Figure 3.1(a) shows a tubular component and global curvilinear coordinate system  $(x,y,z)$  where axes  $x$  and  $y$  define the middle surface and  $z$ -direction is perpendicular to the middle surface at any point. In the present work, the radius of curvature,  $R_x$  is infinite and  $R_y$  is a constant equal to a finite value, thus defining a closed circular cylindrical shell. The  $x$ -direction is aligned with the tube axis and  $y$ -direction is aligned with the circumferential direction, as shown in Figure 3.1(a). The local material coordinate system for each unidirectional lamina is shown in Figure 3.1(b) where 1-direction shows the fiber orientation, 2-direction is the transverse planar direction and 3-direction is thickness direction.

Figure 3.1 - Geometry and coordinate system definitions; (a) Global curvilinear coordinate system  $(x,y,z)$  of the laminated tube and the tensile test sample cut from the circular tube; (b) Local lamina coordinate system.



Source: The author.

### 3.2.2 Constitutive relations of a laminate shell

Since considering the whole circular cylindrical tube is relatively difficult, using smaller parts of the tube would make both experimental and theoretical formulation less complicated. For instance, the dark gray dog-bone tensile specimen in Figure 3.1(a) could be cut from a tube in such a way that it satisfies the shallow shell conditions while still being representative of the mechanical properties of the composite material under tensile test. Then the theory of shallow shells can be utilized to analyze shells that become locally shallow when the original tube is divided into finite segments (Ventsel and Krauthammer 2001).

By analogy with a single lamina, the strain-force relations for a laminate component, which relate the in-plane normal and shear strains of a shell middle surface ( $\varepsilon_x^0$ ,  $\varepsilon_y^0$  and  $\gamma_s^0$ ) to the in-plane forces resultants ( $N_x$ ,  $N_y$  and  $N_s$ ), can be expressed by (Daniel et al. 2006)

$$\begin{bmatrix} \varepsilon_x^0 \\ \varepsilon_y^0 \\ \gamma_s^0 \end{bmatrix} = \frac{1}{h} \begin{bmatrix} \frac{1}{\bar{E}_x} & \frac{\bar{\nu}_{yx}}{\bar{E}_y} & \frac{\bar{\eta}_{sx}}{\bar{G}_{xy}} \\ \frac{\bar{\nu}_{xy}}{\bar{E}_x} & \frac{1}{\bar{E}_y} & \frac{\bar{\eta}_{sy}}{\bar{G}_{xy}} \\ \frac{\bar{\eta}_{sx}}{\bar{E}_x} & \frac{\bar{\eta}_{sy}}{\bar{E}_y} & \frac{1}{\bar{G}_{xy}} \end{bmatrix} \begin{bmatrix} N_x \\ N_y \\ N_s \end{bmatrix} \quad (3.1)$$

where  $\bar{E}_x$ ,  $\bar{E}_y$  are the effective laminate Young's moduli in the  $x$ - and  $y$ -directions respectively,  $\bar{G}_{xy}$  is the effective laminate shear modulus,  $\bar{\nu}_{yx}$  and  $\bar{\nu}_{xy}$  are laminate Poisson's ratios and  $\bar{\eta}$  with different subscripts are laminate shear coupling coefficients;  $h$  is the total thickness of the laminate.

For a general laminate component, it is more convenient to use force-strain relations in the form of compliance instead of stiffness by using CLT, see Appendix A. The effective engineering constants of a general laminated composite can be expressed from equality of Eq. (3.1) and Eq. (A4) as follows (Daniel et al. 2006)

$$\bar{E}_x = \frac{1}{ha_{xx}} \quad (3.2a)$$

$$\bar{E}_y = \frac{1}{ha_{yy}} \quad (3.2b)$$

$$\bar{\nu}_{yx} = -\frac{a_{yx}}{a_{xx}} \quad (3.2c)$$

$$\bar{G}_{xy} = \frac{1}{ha_{ss}} \quad (3.2d)$$

where  $a_{ij}$ ,  $i, j = x, y, s$ , are components of the compliance matrix of the laminated shell by using CLT. In the rest of this work the effective laminate properties notations will be presented in the form of  $E_x$ ,  $E_y$ ,  $\nu_{xy}$ , and  $G_{xy}$  instead of the overbar notations in Eqs. (3.1) and (3.2).

From Eqs. (3.2a) – (3.2d) it is possible to calculate the effective laminate mechanical properties as functions of lamina mechanical properties. The reverse procedure can be utilized to derive back the lamina mechanical properties from experimentally measured laminate properties in desired orthogonal directions. For general laminate composites like multidirectional laminates, it is more convenient to

use a ‘trial and error’ procedure in order to back-out the lamina properties from laminate ones when using Eq. (3.2). However, for the special balanced and symmetric laminates, it is possible to express the lamina-laminate mechanical properties relations explicitly, e.g. for the cross-ply tube in the present study. The explicit lamina-laminate mechanical properties relations are presented by Eq. (3.3), see Appendix B for detailed derivation.

$$G_{12} = G_{xy} \quad (3.3a)$$

$$Q_{11} = \frac{mQ_{xx} - (1 - m)Q_{yy}}{2m - 1} \quad (3.3b)$$

$$Q_{22} = \frac{Q_{xx} - mQ_{11}}{1 - m} \quad (3.3c)$$

$$\nu_{12} = \frac{\nu_{xy} Q_{yy}}{Q_{22}} \quad (3.3d)$$

$$\nu_{21} = \frac{\nu_{yx} Q_{xx}}{Q_{11}} \quad (3.3e)$$

$$E_1 = Q_{11}(1 - \nu_{12}\nu_{21}) \quad (3.3f)$$

$$E_2 = \frac{\nu_{21}E_1}{\nu_{12}} \quad (3.3g)$$

Here all four independent elastic constants of the UD lamina,  $E_1$ ,  $E_2$ ,  $\nu_{12}$  and  $G_{12}$ , were expressed explicitly as functions of the mechanical properties of a cross-ply laminate structure and  $m$ , the fraction of UD layers in the x-direction, of the laminate ( $Q_{ii} = \frac{E_i}{1 - \nu_{ij}\nu_{ji}}$ ,  $i, j = x, y$ ).

In the following sections, the mechanical responses of cross-ply and angle-ply tubular and curved specimens were measured first. Then the lamina mechanical properties and failure strength were calculated in order to validate the reverse procedure indicated by Eqs. (3.2) and (3.3).

### 3.3 Finding the mechanical properties of tubular non-standard laminate specimens cut from tubes

Unidirectional carbon fiber-epoxy prepregs were wrapped around a mandrel, having an outer diameter of 50 mm, with cross-ply and angle-ply layup configurations

in order to make tubes. The tubing and curing procedures were specified by the manufacturer (CFT in the UK). Tables 3.1 and 3.2 list the tubes geometry and the mechanical properties of UD lamina, provided by the manufacturer.

Table 3.1 - Description of laminated tubes.

Item	Tube configuration (a)	Tube configuration (b)
Stacking sequence <sup>1,2</sup>	[±45/0/±45/0/±45/0/±45]	[ <b>0</b> /( <b>90</b> ) <sub>2</sub> /0] <sub>s</sub>
Inner diameter (mm)	50.00	50.00
Outer diameter (mm)	54.70	54.38
Wall thickness (mm)	2.35	2.19
Short reference name	angle-ply	cross-ply

<sup>1</sup> 0°, ±45°, and 90° are measured from the tube axis, x-direction.

<sup>2</sup> **Bold layers** are 300 gsm Unidirectional (0.3 mm thick) and the others are 200 gsm Unidirectional (0.2 mm thick).

Table 3.2 - Nominal mechanical properties of UD carbon fiber/epoxy prepregs, provided by the manufacturer.

Property	Symbol	Units	UD lamina
Elastic modulus 0°	$E_1$	GPa	135
Elastic modulus 90°	$E_2$	GPa	10
In-plane shear modulus	$G_{12}$	GPa	5
Major Poisson's ratio	$\nu_{12}$	-	0.3
Ultimate tensile strength 0°	$S_{1t}$	MPa	1500
Ultimate tensile strength 90°	$S_{2t}$	MPa	50
Ultimate compressive strength 0°	$S_{1c}$	MPa	1200
Ultimate compressive strength 90°	$S_{2c}$	MPa	250
Ultimate shear strength	$F_6$	MPa	70

### 3.3.1 In-plane shear test on ring-shaped specimens and proposed shear test fixture

The shear properties characterization of composite materials is very important since the shear deformations are more critical in their analysis than that of the conventional homogeneous materials due to the relatively low shear to elastic moduli ratios (Bert 2001). There are few available tests when flat coupons are not available to measure the in-plane shear modulus and shear strength (Chamis 1981), as in the case

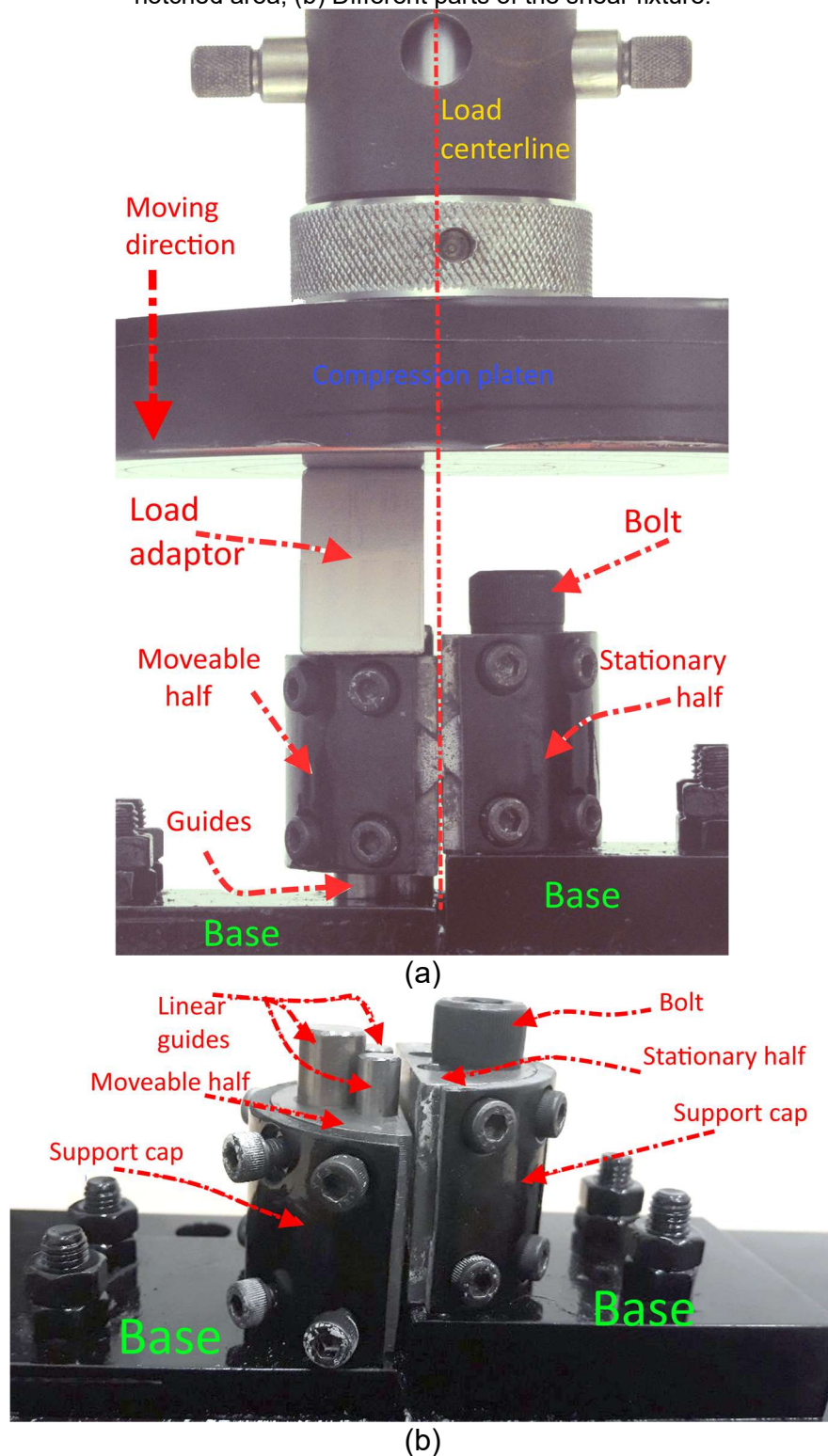
of the filament-wound components. Applying torsional load on a tube is one test method on tubular specimens. This test procedure, however, has some limitations and needs special ends preparation of the tubular specimen. Moreover, a relatively long tube specimen is needed. The four-point ring-twist test is an alternative test that is an accurate and economical way to determine the shear modulus of tubular components of isotropic and composite materials (Greszczuk 1981). The accuracy of the measured in-plane shear modulus by using Four-point ring-twist method depends on the dimensions of the rings (especially on the selection of the width of the ring) and hoop elastic modulus to shear modulus ratio (Greszczuk 1981). Moreover, the shear strength is out of the scope of this testing method. Furthermore, the elastic modulus of the specimen in the hoop direction must be known in advance in order to calculate the shear modulus.

A new fixture is proposed in the present work for measuring the in-plane shear modulus,  $G_{xy}$ , and shear strength,  $F_s$ , from testing on ring-shaped laminated composite specimens. The main idea is to apply shear load on V-notch sections of the ring-shaped specimens similar to standard shear test on flat specimens. This testing fixture would be helpful when standard flat shear coupons specimens according to Standard D 5379/D 5379M (ASTM 1998) are not available for tubular structures and components.

Figure 3.2 shows the proposed fixture for shear testing on circular specimens. The fixture has two halves, which were cut from a metallic bulk cylinder, with an outer diameter equal to the inner diameter of the composite rings. Each half has three holes in it which are introduced to restrict the motion of the halves. One of the halves is fixed entirely on the base and the other half can only move along its three linear guides, in the vertical direction. Two semi-circular caps were designed with grooves, equal to the width of the ring specimen in them in order to set-up and fix the ring-shaped specimen on the halves of the fixture. The grooves' depth is roughly equal to the wall thickness of the specimens. The base was designed in such a way that it has a step on itself in order to fix the stationary half from moving in the vertical direction and allows the vertical displacement of the moveable half. A U-shape metallic piece is used to serve as a load adaptor in order to transfer load from the compression platen of the universal testing machine to the moveable half in order to apply the shear load at notch area of the specimens. Detailed drawings are presented in Figure 3.3, and this geometry data

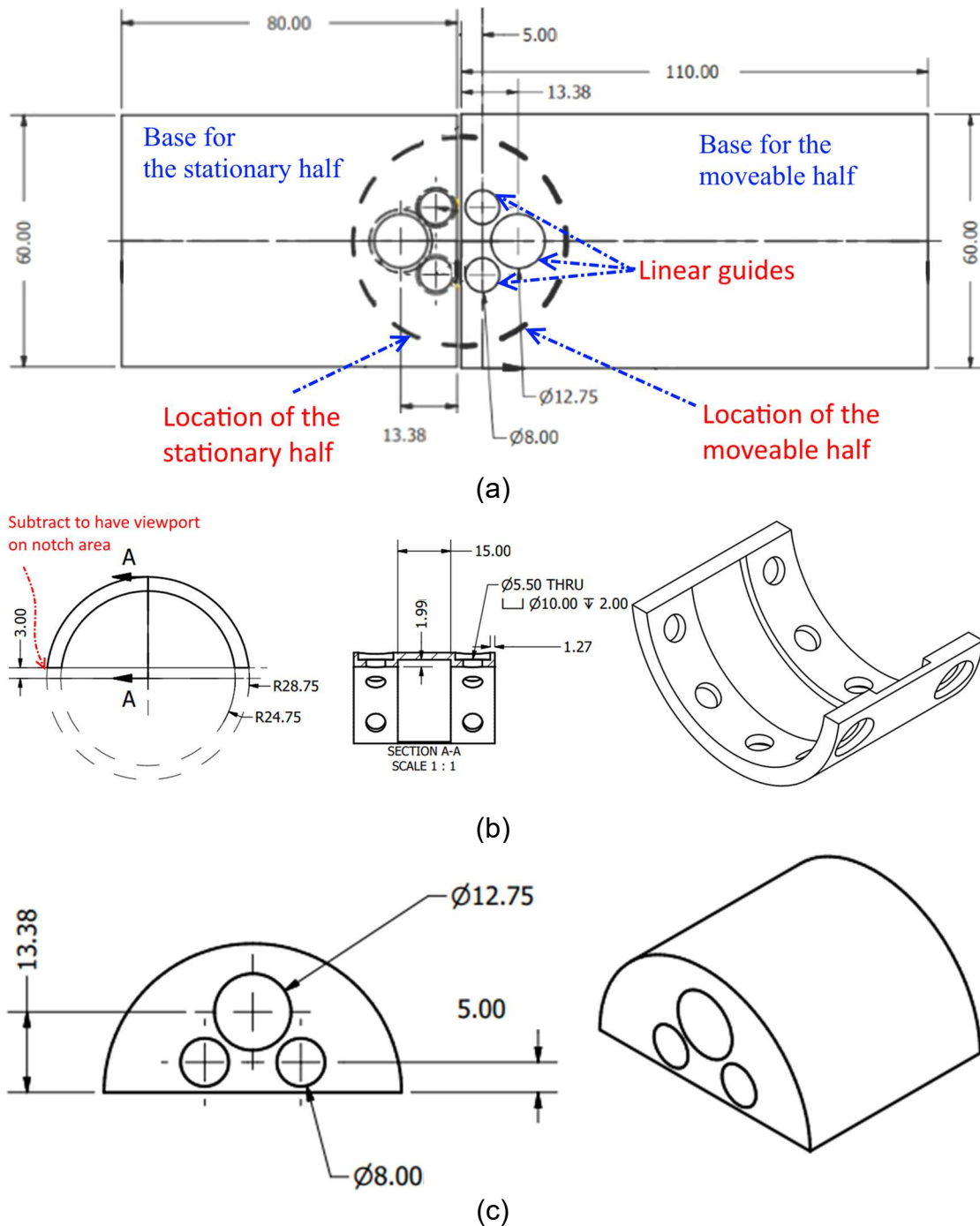
were used for tubes with dimensions, lay-up configurations and material presented in Tables 3.1 and 3.2.

Figure 3.2 - Shear test fixture; (a) Double V-notch ring specimens undergoing shear loading at notched area; (b) Different parts of the shear fixture.



Source: The author.

Figure 3.3 - Technical drawing of the shear fixture; (a) Top-view and general arrangement; (b) Semi-circular cap; (c) Half cylinder and its holes (dimensions in mm).

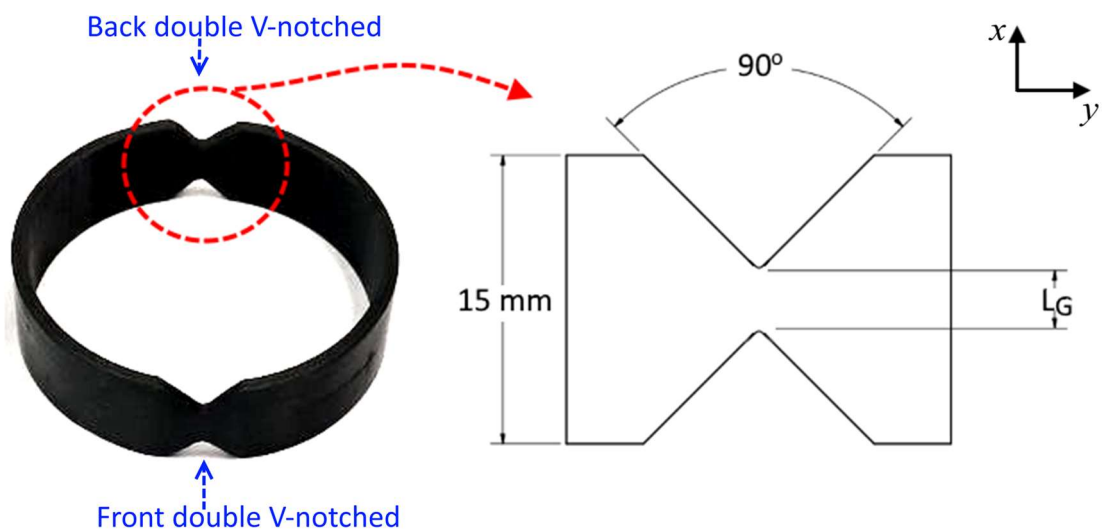


Source: The author.

The ring-shaped specimens were cut from the laminate tubes; then, two symmetric double V-notch areas are subtracted in order to introduce uniform distribution of shear stress at notch areas, as depicted in Figure 3.4.

Here, specimens having different gauge width,  $L_G$ , underwent shear deformation at the loading rate of 0.1 mm/min to verify the behavior of the designed shear fixture. Two-dimensional digital image correlation, 2D DIC, was used to measure the shear strain, as the gauge area is too small for mounting  $\pm 45^\circ$  extensometers. The average surface shear strain is considered within the narrow area of interest, roughly 1mm width at V-notch area.

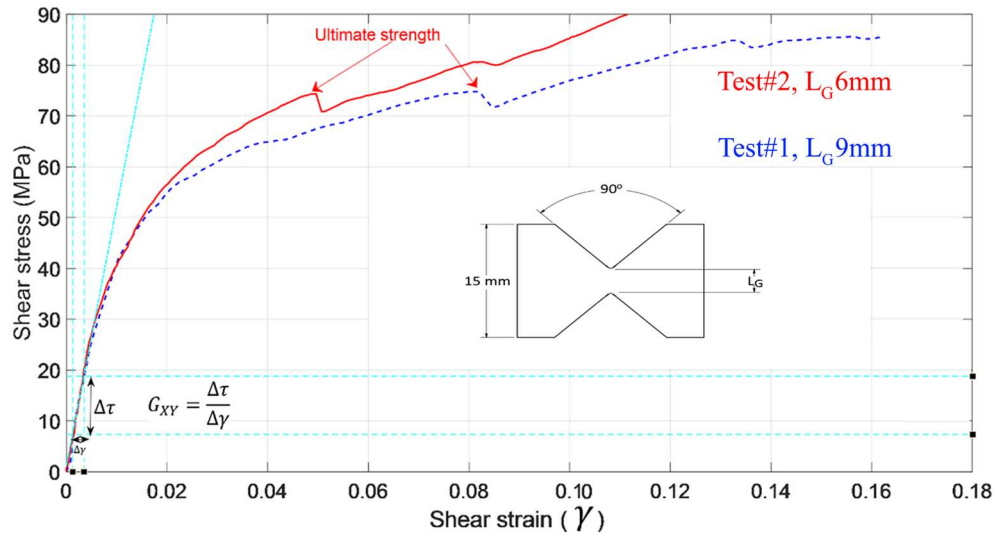
Figure 3.4 - Double V-notched specimens and projected sketch view of the notched area.



Source: The author.

Figure 3.5 shows the measured shear stress-strain curve for the cross-ply ring-shaped specimen. The maximum shear load-bearing capacity of the V-notched area of the present balanced and symmetric cross-ply specimens,  $[0/(90)_2/0]_s$  in Figure 3.5, was higher than the shear failure load. A similar phenomenon is mentioned in ASTM D5379 (ASTM 1998) for  $[0/90]_{ns}$ , SMC as the fibers may reorient following the shear failure, subsequently allowing the fibers to carry a major part of the load. Thus, the shear stress-strain curves in Figure 3.5 do not show the maximum shear stress-bearing capability of the cross-ply specimens. The ultimate shear strength, in this case, can usually be detected by visual observation of failure in the test section which is characterized by a significant drop in shear stress (load) (ASTM 1998), as illustrated in Figure 3.5.

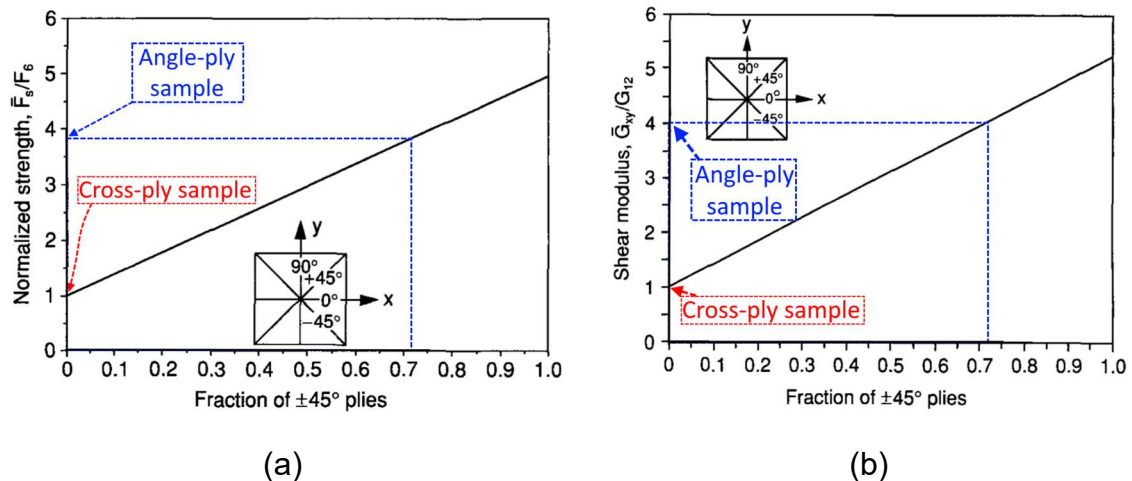
Figure 3.5 - Shear stress-deformation curves for double V-notched ring specimens.



Source: The author.

In order to validate the accuracy of the obtained shear properties, the measured shear properties of cross-ply and angle-ply ring-shaped specimens are compared with the values obtained from the 'carpet plot' in Figure 3.6 (Daniel et al. 2006). The detailed comparison is presented in Table 3.3. The nominal lamina in-plane shear strength and modulus,  $F_6$  and  $G_{12}$ , presented in Table 3.2 were used to utilize the carpet plots.

Figure 3.6 - Carpet plot for in-plane shear modulus and strength of  $[0_m/90_n/(\pm 45)_p]_s$  carbon/epoxy laminates (AS4/3501-6); (a) Normalized shear strength of laminate; (b) Normalized shear modulus of the laminate.



Source: (Daniel et al. 2006)

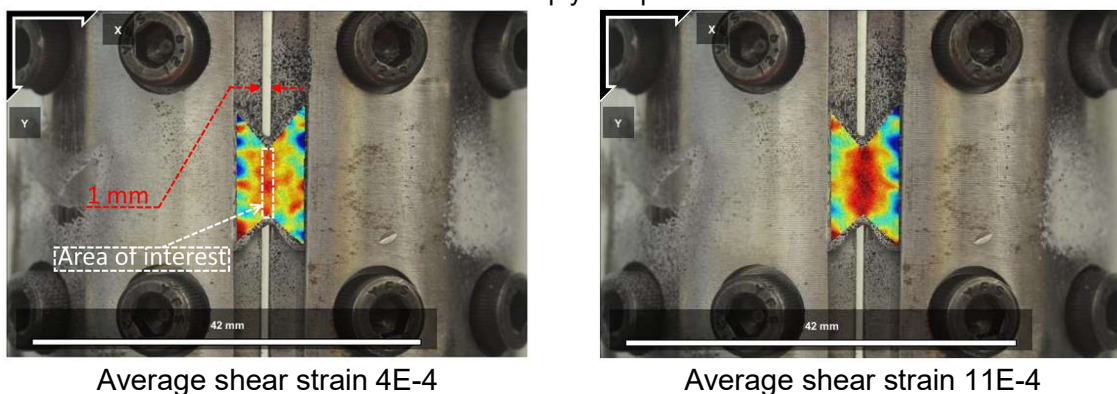
Table 3.3 - Comparison between measured shear properties by using the proposed fixture and calculated shear properties using carpet plot in Figure 3.6.

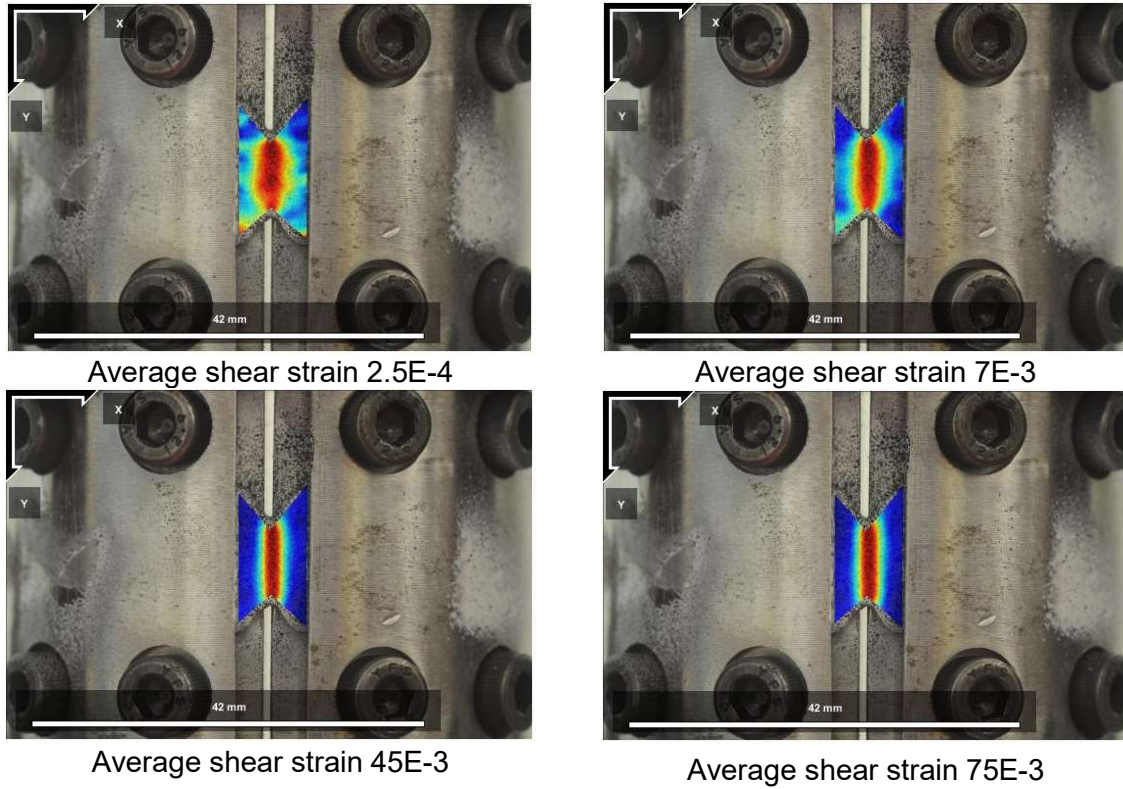
Method	Test number	Cross-ply sample	
		$G_{xy}$ (GPa)	$F_s$ (MPa)
Present shear testing	Test #1	5.18	74.79
	Test #2	4.76	74.25
	<b>Average</b>	<b>5.12</b>	<b>74.52</b>
Carpet plot Figures. 3.6 (a)-(b)*		5.00	70.00
Difference (%)		2.40%	6.45%

\*  $G_{12}$  and  $F_6$  are taken from Table 3.2.

Figures 3.7 shows the uniform shear strain distribution over the gauge area of the ring-shaped cross-ply specimen under shear testing with the proposed fixture. The uniformity of shear strain distribution is remarkable during the application of the shear force.

Figure 3.7 - Shear strain distribution and development within the notched gauge area, Test#1, cross-ply sample.

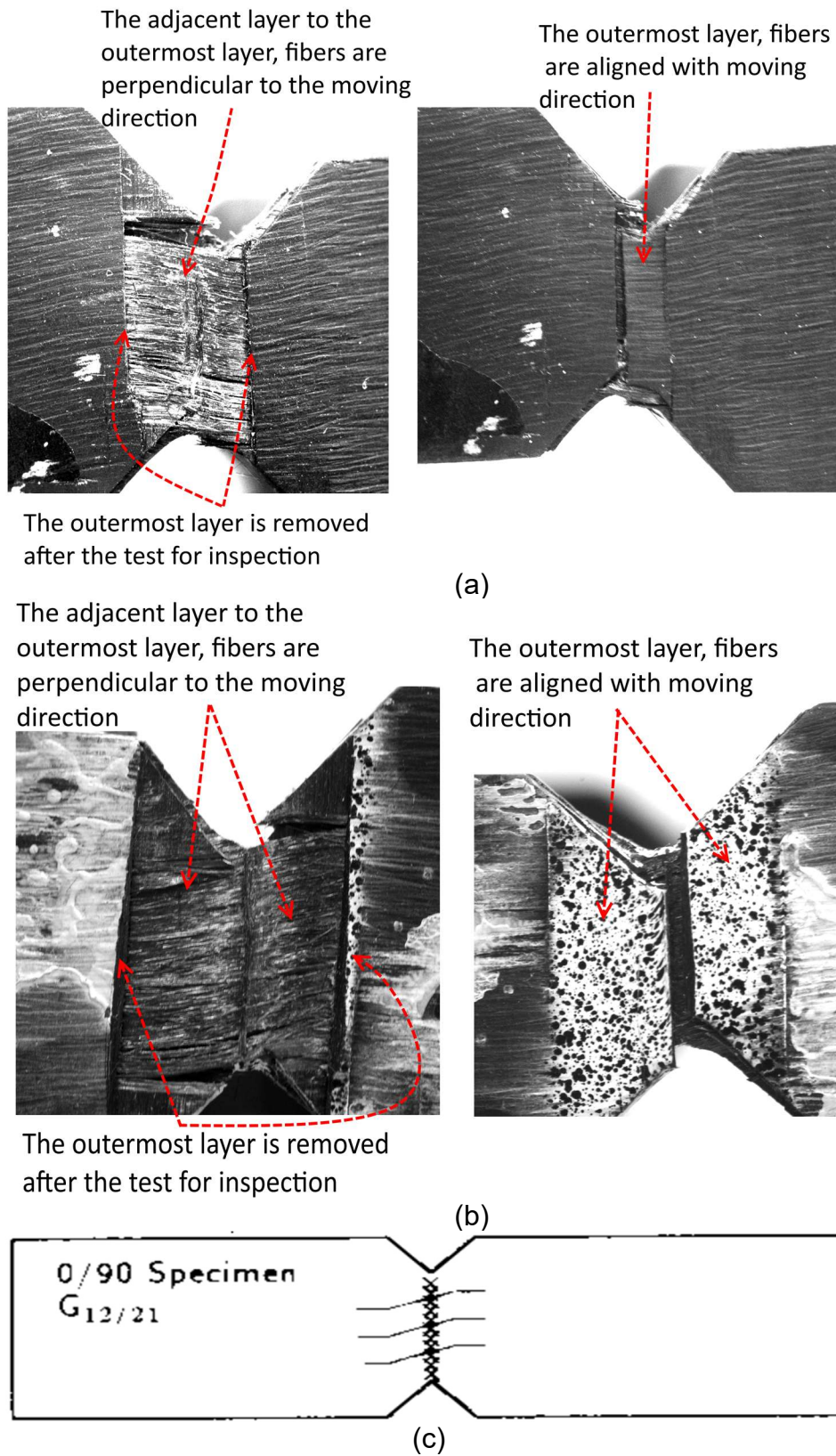




Source: The author.

Front and back views of the failure mode of cross-piled specimens after the shear test are presented in Figures 3.8. The acceptable shear failure mode of  $[0/90]_{ns}$  laminate family is presented as a reference in Figure 3.8(c) that shares several similarities with the failure mode of cross-piled ring specimen.

Figure 3.8 - Failure mode inspection of the cross-plyed specimen; (a) Back double V-notch failure mode; (b) Front double V-notched failure mode; (c) Typical acceptable failure mode for  $[0/90]_{ns}$  laminate composites.

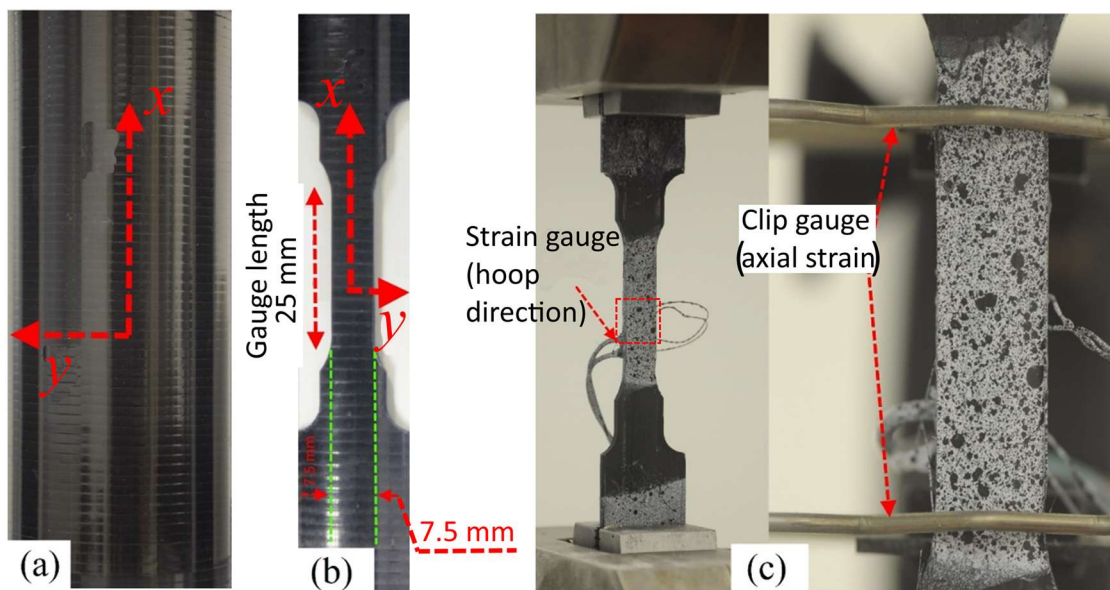


Source: (a,b): The author; (c): (ASTM 1998).

### 3.3.2 Axial tensile test on the non-flat laminate specimen

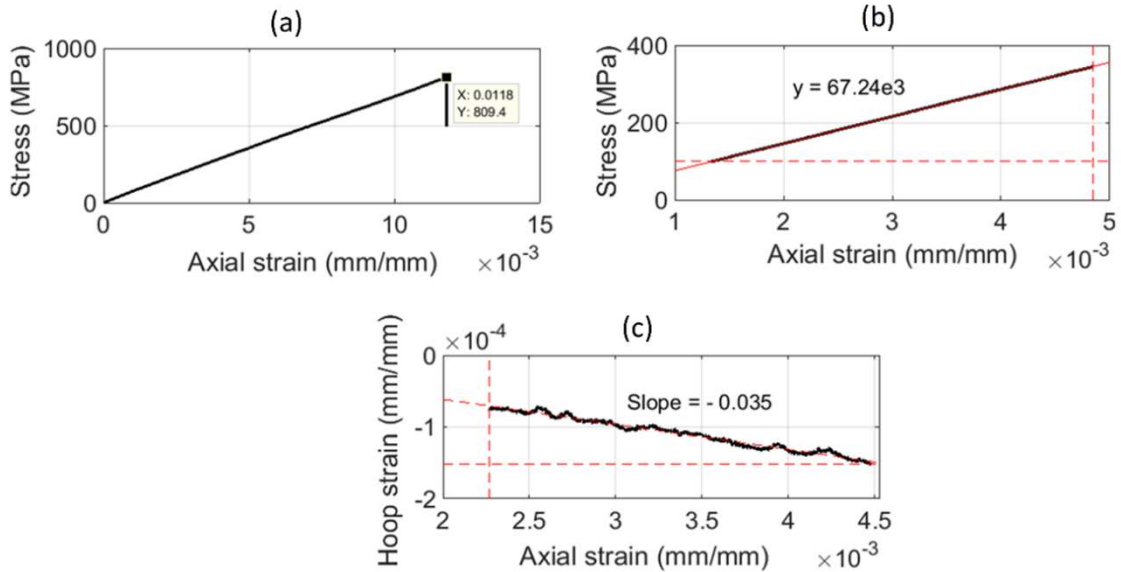
Figure 3.9(a) shows the laminate tube where the principal axes of the equivalent orthotropic material,  $x$  and  $y$ , are aligned with the axial and circumferential directions of the tube, respectively. Some dog-bone non-standard samples were cut from cross-plyed and angle-ply tubes and were tested under a uniaxial monotonic quasi-static tension, Figure 3.9(b) and Figure 3.9(c). The surface strains were measured in  $x$ - and  $y$ -directions using clip gauge and strain gauges, respectively. The elastic modulus in the  $x$ -direction,  $E_x$  and Poisson's ratio,  $\nu_{xy}$ , of the laminate specimens were found, as presented in Figure 3.10 and Table 3.4 for the cross-plyed test. Table 3.5 presents the predictions of the axial elastic modulus and failure strength of both cross-ply and angle-ply laminate specimens by using nominal mechanical properties of UD lamina and applying CLT and Hart Smith 10% rule.

Figure 3.9- Axial tensile test description; (a) Principal axes of equivalent orthotropic material on the cross-plyed laminate tube; (b) Axial tensile test specimen; (c) Test setup.



Source: The author.

Figure 3.10 - Axial tensile test results for the cross-piled specimen; (a) Stress-strain curve; (b) Partial stress-strain curve to measure the elastic modulus; (c) Hoop strain-axial strain curve to measure the Poisson's ratio.



Source: The author.

Table 3.4 - Measured tensile properties of laminate specimens, x-direction tensile test.

Specimens	Elastic modulus $E_x$ (GPa)	Poisson's ratio ( $\nu_{xy}$ )	Failure strain (mm/mm)	Failure stress $f_x$ (MPa)
Cross-ply #1	67.24	0.0357	0.01179	809.4
Cross-ply #2	67.67	0.0356	0.01102	791.1
Cross-ply #3	68.00	0.0355	0.0106 (@ 745.9 MPa) *	818.3
<b>Average</b>	<b>67.63</b>	<b>0.0356</b>	<b>0.011405</b>	<b>806.3</b>
Angle-ply #1	50.12	0.735	-	552.97
Angle-ply #2	48.53	-	0.01203	543.38
<b>Average</b>	<b>49.33</b>	<b>0.735</b>	<b>0.01203</b>	<b>548.175</b>

\* Clip-gauge slid after this point.

Table 3.5 - Prediction of laminate mechanical properties to check the test results.

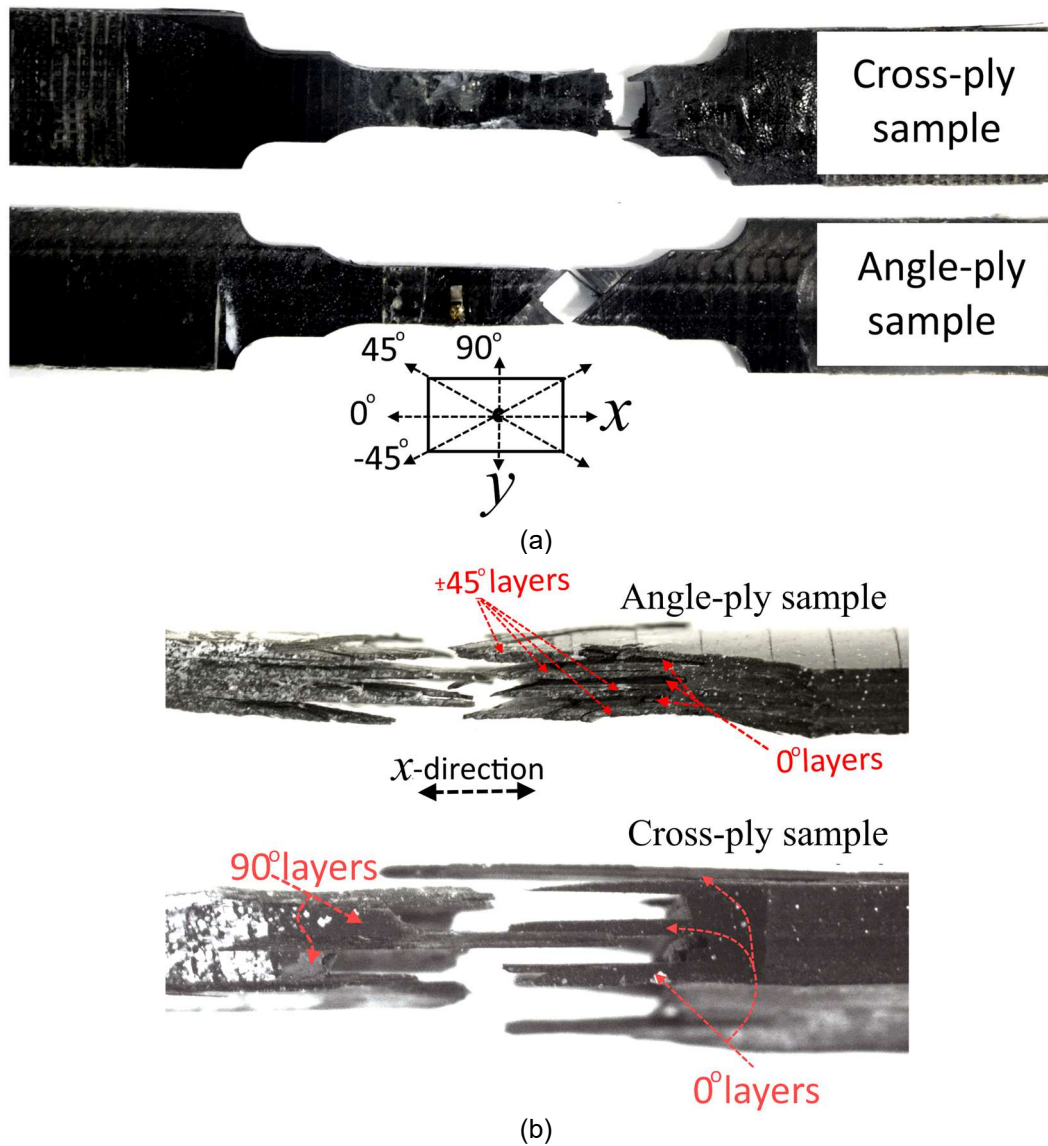
Method	Cross-plyed material [0/(90) <sub>2</sub> /0] <sub>s</sub>			Angle-ply material [±45/0/±45/0] <sub>s</sub>		
	$E_x$ (GPa)	( $\nu_{xy}$ )	$f_x$ (MPa)	$E_x$ (GPa)	( $\nu_{xy}$ )	$f_x$ (MPa)
10% rule	68.72*	-	762.18**	46.63*	-	514.5**
CLT (Eq.(3.2))	67.15	0.0384	-	50.19	0.726	-

\*  $E_x = E_1 \times (0.1 + 0.9 \times [\text{fraction of UD plies in x-direction}])$

\*\*  $f_x = 0.1 \times m_0 \times f_1 + 0.01 \times (m_{+45} + m_{90}) \times f_1$

Figure 3.11 shows different failure modes for angle-ply and cross-ply specimens. It is obvious from Figures 3.11(a) and 3.11(b) that the laminae failed parallel to their fiber orientations. The cross-plyed tensile specimens failed very close to their transition area. However, failure of the angle-ply specimens occurred far away from their transition area.

Figure 3.11 - The failure modes of carbon fiber samples under tensile tests; (a) Front view of failed samples; (b) Side-view of failed samples.



Source: The author.

### 3.3.3 Measuring the elastic modulus in hoop direction, $E_y$ , by using a tubular specimen

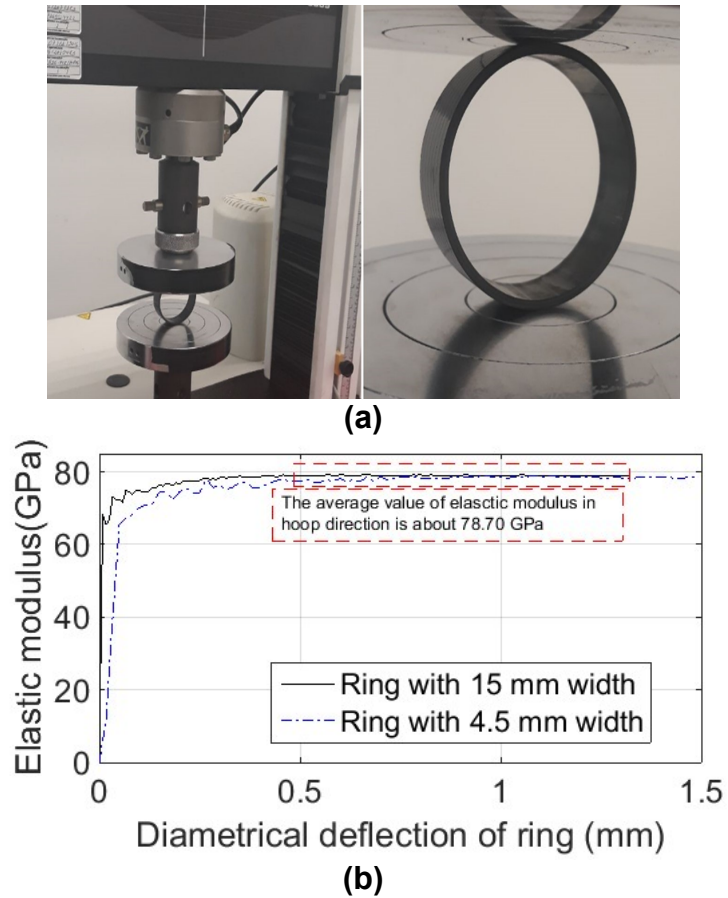
The internal pressure burst test on a tube can be used to obtain the mechanical properties of the material of tubular components, e.g., as in (Rasheed, Akbar, and Mirza 2013). However, pressurized tube test needs relatively long tube specimens (to avoid edges boundary condition effects), special sealing and equipment. The Split-disk test, ASTM D 2290 (ASTM Standards 2000), is among the simple experimental tests which has been used to find the elastic modulus in the hoop direction (Kaynak et al. 2005), although, there is no explicit procedure in ASTM D 2290 (ASTM Standards 2000) to calculate the elastic modulus in the hoop direction. Applying diametrical load on thin-walled rings (Young and Budynas 2002) is the most straightforward test to find elastic modulus in hoop direction which does not require special equipment and has been used for filamentary tubes by some researchers (Greszczuk 1981; Bert 2001).

Figure 3.12(a) shows a cross-plyed ring between the platens of the universal test machine applying a diametrical compressive load on the ring. The elastic modulus in the hoop direction is calculated by the following equation (Young and Budynas 2002)

$$E_y = \frac{PR_e^3}{I\Delta V} \left( \frac{\pi}{4} - \frac{2}{\pi} \right) \quad (3.4)$$

where  $P$  is the applied diametrical load,  $R_e$  is the ring's mean radius,  $I$  is area moment of inertia of ring cross-section about the principal axis perpendicular to the plane of the ring,  $\Delta V$  is the net vertical deflection of the ring at the application point of the load. A reliable value of  $E_y$  can be obtained for sufficiently large values of  $\Delta V$ , as shown in Figure 3.12(b). The average value of the measured hoop elastic modulus of angle-ply and cross-ply specimens, by using diametrical load and Eq. (3.4), is presented in Table 3.6. The results in Table 3.7 show that the measured elastic modulus in the circumferential direction for the cross-plyed ring-shaped specimens is very close to the predicted values by using 10% rule and CLT. On the contrary, the measured elastic modulus for the angle-ply specimens is considerably higher than those calculated by CLT and 10% rule.

Figure 3.12 - Lateral compression of the ring to calculate elastic modulus in hoop direction; (a) Cross-piled ring between platens of the machine; (b) The variation of calculated hoop elastic modulus versus the deflection of machine's cross-head.



Source: The author.

Table 3.6 - Elastic modulus in the tube's circumferential direction by applying a diametrical load on a ring.

<b>Specimens</b>	<b>Elastic modulus, <math>E_y</math> (GPa)</b>	<b>Ring's width (mm)</b>
Cross-ply #1	78.86	15.00
Cross-ply #2	78.54	4.50
<b>Average</b>	<b>78.70</b>	-
Angle-ply #1	35.50	15.00
Angle-ply #2	34.39	7.50
<b>Average</b>	<b>34.94</b>	-

Table 3.7 - Prediction of laminate elastic modulus in hoop direction by using classical laminate theory and Hart Smith 10% rule.

Method	Cross-plyed configuration [0/(90) <sub>2</sub> /0] <sub>s</sub>	Angle-ply configuration [±45/0/±45/0] <sub>s</sub>
	$E_y$ (GPa)	$E_y$ (GPa)
10% rule*	79.77	13.50
CLT (Eq. (3.2))	78.57	24.82

\*  $E_y = E_1 \times (0.1 + 0.9 \times [\text{fraction of UD plies in } y\text{-direction}])$

### 3.4 Calculating the UD lamina properties from measured mechanical properties of the multidirectional laminated tubes

Eqs. (3.3a)-(3.3g) and measured mechanical properties,  $E_x$ ,  $E_y$ ,  $\nu_{12}$  and  $G_{xy}$ , of cross-plyed carbon fiber specimens, were used to back-out the in-plane elastic constants,  $E_1$ ,  $E_2$ ,  $\nu_{12}$  and  $G_{12}$ , of the UD lamina. Then the backed-out elastic properties of the UD lamina are used to find the effective mechanical properties of the angle-ply tube and compared with the results from testing on angle-ply laminate specimens as mentioned earlier. Table 3.8 presents the calculated lamina properties from laminate testing and compares them with the UD carbon/epoxy elastic properties provided by the manufacturer. The effective mechanical properties of angle-ply specimens were calculated when using the predicted properties of UD lamina from cross-plyed specimens and Eqs. (3.2a)-(3.2d) and compared to the mechanical response of angle-ply specimens cut out from the tube in Table 3.9. The lateral compression test on rings led to accurate results for the elastic modulus of the cross-plyed laminate tube; however, the predicted elastic modulus in the circumferential direction for angle-ply rings shows a significant difference with calculated elastic modulus in hoop direction by using CLT.

Table 3.8 - Comparison between reverse calculated UD lamina mechanical properties and nominal properties provided by the tube manufacturer.

Nominal UD lamina properties from Table 3.2 for carbon/epoxy material				Predicted UD lamina properties Using Eqs. 3.3(a)-3.3(g) and testing on cross-plyed specimens			
Elastic moduli		Poisson's ratio	Shear modulus	Elastic moduli		Poisson's ratio	Shear modulus
$E_1$ (GPa)	$E_2$ (GPa)	$(\nu_{12})$	(GPa)	$E_1$ (GPa)	$E_2$ (GPa)	$(\nu_{12})$	(GPa)
135	10	0.3	5	136.32	9.32	0.294	5.12
				6%	-6.80%	-2.00%	2.40%
Difference (%)							

Table 3.9 - Prediction of the angle-ply laminate mechanical properties.

Method	Angle-ply material		
	$E_x$ (GPa)	$E_y$ (GPa)	$(\nu_{12})$
Test on specimens cut out from the tube	49.98	34.94	0.735
CLT (Eq.(2))	50.19	25.24	0.726
Difference (%)	0.4%	38.43%	1.24%

The derivation of the UD lamina tensile/compressive strength from experimental tests on multidirectional laminates, cross-ply or angle-ply, by using reverse CLT inherently has some assumptions such as (i) linear elastic behavior of both laminate and lamina up to failure point, (ii) both laminate and lamina fail at the same strain with the same mechanism (Measurement 2002). Carbon/epoxy material from  $[0_m/90_n]_s$  stacking sequence family satisfies well these two assumptions.

There are several 'back-out factors', BF, or 'cross-ply factor', CPF, to derive lamina strength,  $f_1$ , from cross-ply (Measurement 2002) or angle-ply (J. S. Welsh and Adams 1997) laminates failure strength,  $f_x$ . Here, three methods were used to calculate the lamina strength of carbon fiber material from cross-ply and angle-ply specimens' strength; (1) assuming linear elastic behavior of lamina and laminate up to failure, using Hook's law, (2) using cross-ply factor, CPF and BF factors in the literature and (3) using available rule of thumb relations such as Hart-Smith 10% rule, Eq. (3.5),

$$f_x = 0.1 \times m_0 \times f_1 + 0.01 \times (m_{\pm 45} + m_{90}) \times f_1 \quad (3.5)$$

where  $m_0$ ,  $m_{\pm 45}$  and  $m_{90}$  are fractions of UD plies oriented at  $0^\circ$ ,  $\pm 45^\circ$  and  $90^\circ$  with respect to the loading direction, respectively and  $f_x$  is taken from experimental tests on the laminate specimens, Table 3.4.

The cross-ply factor and back-out factor in Eq. (3.6) and Eq. (3.7) were used to find the lamina tensile failure from the laminate failure strength of cross-ply and angle-ply specimens, respectively.

$$f_x = \text{CPF} \times f_1$$

$$\text{CPF} = \frac{E_1[m_0 E_2 + (1 - m_0)E_1] - (\nu_{12} E_2)^2}{[m_0 E_1 + (1 - m_0)E_2][m_0 E_2 + (1 - m_0)E_1] - (\nu_{12} E_2)^2} \quad (3.6)$$

where  $m_0$  is the fraction of  $0^\circ$  plies in the loading direction,  $f_x$  is failure strength of the cross-ply laminate specimen under axial tensile test and  $E_1$ ,  $E_2$ ,  $\nu_{12}$  are elastic constants of UD lamina derived from Eqs. (3.3a)-(3.3g).

$$f_x = \text{BF} \times f_1$$

$$\text{BF} = h \frac{(\overline{Q}_{11}^0 A_{22} - \overline{Q}_{12}^0 A_{12})}{A_{22} A_{11} - A_{12}^2} \quad (3.7)$$

where  $h$  is the total laminate thickness,  $\overline{Q}_{ij}^0$  (Eqs (A8)) is  $ij$ -th element in transformed plane stress stiffness matrix of a UD lamina and  $A_{ij}$  (Eq. (A5)) is  $ij$ -th element in the laminate extensional  $[A]$  matrix.

The predicted axial tensile failure strength of UD lamina,  $f_1$ , is presented in Table 3.10 when using the tensile test results for laminated cross-ply and angle-ply dog-bone specimens.

Table 3.10 - Predicted failure tensile strength of UD carbon/epoxy material.

Method	Calculated failure of UD lamina, $f_1$ (MPa)	The difference from failure strength of the used UD carbon/epoxy material (%)
Linear elastic behavior (Hook's law) from the tensile test on cross-ply specimen*	1553	3.5
Using CP factor Eq. (3.6) from tensile test cross-ply specimen	1614	7.6
10% rule from tensile test on cross-ply specimen, Eq. (3.5)	1578	5.2
Linear elastic behavior (Hook's law) from the tensile test on angle-ply specimen*	1442	-4.0
Using BF factor Eq. (3.7) from tensile test angle-ply specimen testing	1454	-3.1
10% rule from the tensile test on an angle-ply specimen, Eq. (3.5)	1587	5.8

\* Failure strain of UD lamina and laminate are assumed to be equal.

$$f_1 = \frac{f_x E_1}{E_x}$$

### 3.5 Summary

In this chapter, explicit relations are presented to back-out four elastic constants of the unidirectional lamina from testing on cross-ply laminate specimens which are applicable to any balanced and symmetric cross-ply specimens, flat coupons or cylindrical specimens, subjected to compressive or tensile experimental tests. A good agreement has been observed between lamina back-calculated properties (including failure and elastic moduli) and available reported data of the used unidirectional carbon/epoxy material. The presented relationships could reduce the required number of tests, as most of the previously reported studies on back-out procedure need to find elastic properties of the lamina in advance with testing on unidirectional specimens. Therefore, the present work removes this disadvantage of the backing-out method. The obtained relationships are rather simple since only the volume fraction of UD plies in loading direction and monotonic tensile/compression results on cross-ply specimens are required.

A shear test fixture was proposed for applying shear force on ring-shaped specimens having double V-notched gauge area. The experimental tests on the new fixture yielded accurate results for the shear modulus and strength of the analyzed

cross-ply specimens. The designed shearing test fixture would be useful for tubular composites components for which standard flat shear test coupons are not available.

Several experimental test procedures were applied in order to find laminate mechanical properties of non-flat, non-standard specimens cut from a laminated tube. These testing procedures can be useful in the quality control process of laminated composite parts having a cylindrical geometry.

## 4 Experimental axial impact on CFRP tubes<sup>1</sup>

The primary objective of the present chapter is to analyze the possible effects of the loading conditions and layup configurations on the crushing behavior of circular CFRP tubes made of unidirectional prepreg material. For this purpose, several specimens with cross-ply and angle-ply layups were crushed quasi-statically and dynamically in a wide range of loading conditions including different combinations of mass and velocity of the striker. In particular, the effect of the layup configurations on deceleration (or crushing force) behavior of CFRP tubes was explored which has received limited attention in the reported studies. C-section specimens, having the same radii and layups as the full tube specimens, were quasi-statically crushed to study the cross-sectional effects on the SEA and crushing force. Furthermore, the tests on open cross-section helped to establish the crushing mechanism of each layer during compression, step-by-step, so bring better insight into the crushing mechanisms of each layer adjacent to different layers (or boundary conditions). The effects and importance of the axial splitting (lamina bending) of 0° outermost layers of cross-ply specimens on the average crushing force and SEA value under quasi-static compression are investigated. The experimental results and findings in this chapter are thought to be useful in the crashworthy design of composite kinematic energy absorbers.

The primary evaluation criteria in the crashworthy design were used in order to compare the crushing behavior of specimens. These criteria are defined by Eq. (4.1) to Eq. (4.3). The total energy absorbed by the absorber,  $AE$ , is equal to the area under force-displacement curve

$$AE = \int_0^{l_c} F dx \quad (4.1)$$

---

<sup>1</sup> The content of this chapter is published in the International Journal of Impact Engineering (<https://doi.org/10.1016/j.ijimpeng.2019.03.006>).

where  $F$  is the crushing force and  $l_c$  is the length of the damaged part of the absorber. The average crushing force,  $F_{ave}$ , is given by

$$F_{ave} = \frac{AE}{l_c}. \quad (4.2)$$

The specific energy absorption is the total absorbed energy divided by the mass of the damaged part of the absorber,  $m_{lc}$ ,

$$SEA = \frac{1}{m_{lc}} \int_0^{l_c} F dx = \frac{AE}{m_{lc}}. \quad (4.3)$$

#### 4.1 Experimental procedure

Unidirectional carbon fiber-epoxy prepregs were wrapped around a mandrel having an outer diameter of 50 mm with two different layups. The curing process was done into an autoclave by the manufacturer (CFT in the UK) and the received tubes were cut to make specimens with desired lengths. Two types of tubular specimens with different layups were designed to have the same cross-section area in order to minimize the geometry effects on the crushing performance of specimens. Nevertheless, approximately 8% difference between the cross-sections of the cross-ply and angle-ply specimens was measured. The properties of unidirectional CF material, provided by the manufacturer and experimentally measured values, and specimens' descriptions are presented in chapter 3.

The external chamfer is a trigger mechanism used to control the peak force without affecting the other crushing characteristics of tubes. Therefore, the specimens were chamfered externally with different angles at only one end. Tubes with square ends (without any damage initiator) were also impacted for comparison studies. The schematic illustration and some specimens are presented in Figure 4.1.

Figure 4.1 - The specimens; (a) Schematic presentation of specimens; (b) Some full tube specimens; (c) C-section specimens glued to the base.



Source: The author.

A coding system to name the specimens under different quasi-static and dynamic test conditions was conceived. For example, QA45 is referring to Quasi-static test on Angle-ply [ $\pm 45/0\dots$ ] specimen chamfered with  $45^\circ$ , DC60#3 refers to Dynamic impact test on Cross-ply [0/90...] tube with  $60^\circ$  external chamfer under dynamic condition number #3. For C-section specimens under quasi-static compression CS\_A60 (60 refers to external chamfer) and CS\_C45 (45 refers to external chamfer) refer to C-section specimens with angle-ply and cross-ply layup configurations, respectively.

Several quasi-static and dynamic experimental tests were performed as indicated in Table 4.1. Instron 3369 (50kN) and MTS (250kN) universal test machines were used to carry out the axial quasi-static compression tests. Figure 4.2(a) presents the test setup and specimens under quasi-static compression. The cross-head was set into motion with 0.5 mm/min velocity and the force and cross-head displacement were directly recorded for each test. The raw data was used to find the crashworthy assessment parameters. Photos of the crush mode of each specimen were taken during and after the test. Two tests were performed for each configuration. All tests were carried out in the room temperature.

Table 4.1. A general overview of specimens under investigation.

Tests	Loading rate (m/s)	Mass of the striker (kg)	Number of samples	Trigger type		
				Without chamfer	45° chamfer	60° chamfer
Quasi-static test	8.3E-6	-	12 circular tubes	X	X	X
			8 C-section	-	X	X
Dynamic set#1	6.72	102	16 circular tubes	X	X	X
Dynamic set#2	5.08	102	16 circular tubes	X	X	X
Dynamic set#3	5.01	205	15 circular tubes	X	X	X
Dynamic set#4	9.62	48.60	12 circular tubes	-	X	X

The drop tower facility at GMSIE (Group of Solid Mechanics and Structural Impact) at the University of Sao Paulo, shown in Figure 4.2(b), was used to carry out the dynamic axial impact tests. The specimen was freely placed on the base of the drop tower (without using any glue) and the striker was raised to a suitable height to give the desired impact velocity. Both laser velocimeter (Polytec OFV 3020) and high-speed camera (FASTCAM SA5 model 775K-M1) were used to acquire data for further calculation. For dynamic sets 1 to 3, laser velocimeter with 500 kHz sampling rate and high-speed camera with 20 kfps were used to measure the striker's velocity and displacement during the impact event. Two high-speed cameras were used for dynamic set#4 – one with 124 kfps to record the movement of the motion target to extract velocity and displacement of the striker for further calculations and the other camera to record the general view of the impact test with 6 kfps.

The force equilibrium of the striker can be expressed as follows

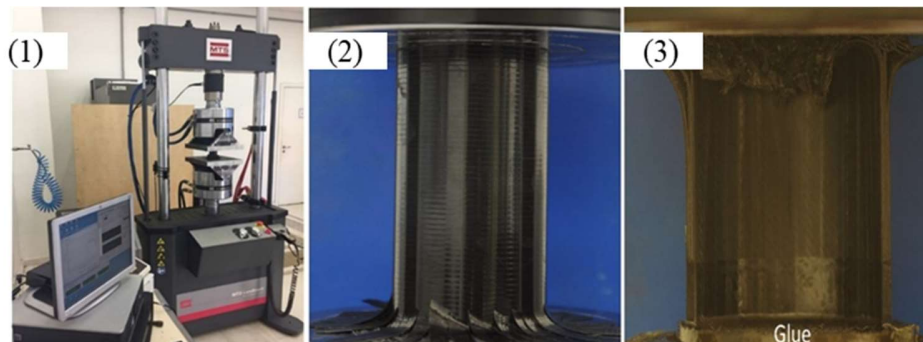
$$F_{Tube} = M(a + g) = M\left(\frac{dv}{dt} + g\right) \quad (4.4)$$

when friction and drag forces were disregarded;  $F_{Tube}$  is the crushing force on a tube,  $M$  is striker's mass,  $g$  and  $a$  are gravity and striker acceleration, respectively.

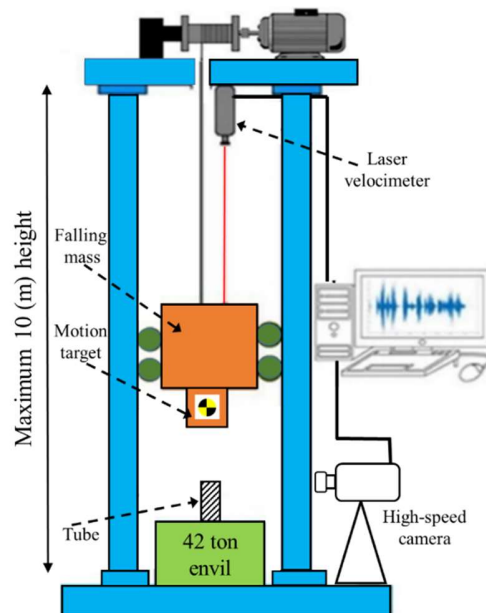
The absorbed energy,  $AE$ , in the dynamic tests can be calculated by using Eq. (4.1) or by writing the energy conservation law for the striker between start-end points of the impact (Eq. (4.5)), including the variation of kinetic and potential energies of the striker.

$$AE = \frac{1}{2}MV_0^2 + M\bar{g}l_c. \quad (4.5)$$

Figure 4.2 - Experimental test procedure; (a) Quasi-static test, (1) Quasi-static setup, (2) Full tube under compression and (3) C-shape specimen under compression; (b) Dynamic test, Schematic of the drop hammer test setup.



(a)



(b)

## 4.2 Results

All tested specimens experienced progressive crushing, even those without a chamfer. The crushing initiated from the top of tubes regardless of the loading speed. The assessment parameters of the crashworthiness for all tests are presented in Tables 4.2 to 4.6.

Table 4.2 - Test results at quasi-static compression (0.5 mm/min).

Sample	$AE$ (kJ)	$F_{ave}$ (kN)	$\sigma_{ave}$ (MPa)	$F_{max}$ (kN)	$\sigma_{max}$ (MPa)	$SEA$ (J/g)	$l_c$ (mm)
QA60	1.884	32.29	83.61	58.96	152.68	54.53	58.35
QA60	2.483	33.10	85.71	53.17	137.60	55.91	75.01
<b>Mean</b>	<b>2.183</b>	<b>32.69</b>	<b>84.66</b>	<b>56.06</b>	<b>145.14</b>	<b>55.22</b>	<b>66.68</b>
CS_A60	1.069	17.79	92.13	25.63	132.73	57.75	62.43
CS_A60	1.082	17.46	90.36	24.45	126.62	58.95	62.01
<b>Mean</b>	<b>1.076</b>	<b>17.62</b>	<b>91.25</b>	<b>25.04</b>	<b>129.67</b>	<b>58.35</b>	<b>62.22</b>
CS_C60	0.765	12.35	70.00	22.43	138.59	45.57	61.97
CS_C60	0.844	13.70	77.65	24.05	136.32	50.56	61.57
<b>Mean</b>	<b>0.804</b>	<b>13.02</b>	<b>73.83</b>	<b>23.24</b>	<b>137.46</b>	<b>48.06</b>	<b>61.77</b>
QC60	1.994	30.49	86.41	44.88	127.20	56.29	65.40
QC60	2.083	31.57	89.47	43.30	122.72	58.28	66.01
<b>Mean</b>	<b>2.038</b>	<b>31.03</b>	<b>87.94</b>	<b>44.09</b>	<b>124.96</b>	<b>57.28</b>	<b>65.71</b>
QA45	2.483	36.52	94.56	43.67	113.08	61.67	68.00
QA45	2.469	37.64	97.46	47.79	123.75	63.56	65.60
<b>Mean</b>	<b>2.476</b>	<b>37.08</b>	<b>96.01</b>	<b>45.73</b>	<b>118.41</b>	<b>62.61</b>	<b>66.80</b>
CS_A45	0.902	18.04	93.42	25.36	131.33	60.95	50.00
CS_A45	0.851	17.01	88.09	21.42	110.92	57.48	50.07
<b>Mean</b>	<b>0.876</b>	<b>17.52</b>	<b>90.75</b>	<b>23.39</b>	<b>121.13</b>	<b>59.22</b>	<b>50.03</b>
CS_C45	0.607	12.14	68.81	17.24	97.72	44.80	50.00
CS_C45	0.602	12.04	68.24	18.46	104.64	44.44	50.01
<b>Mean</b>	<b>0.604</b>	<b>12.09</b>	<b>68.53</b>	<b>17.85</b>	<b>101.18</b>	<b>44.62</b>	<b>50.00</b>
QC45	1.825	30.35	86.02	39.18	111.05	56.03	60.13
QC45	2.400	31.01	87.90	39.31	111.41	57.25	77.42
<b>Mean</b>	<b>2.113</b>	<b>30.68</b>	<b>86.96</b>	<b>39.24</b>	<b>111.23</b>	<b>56.64</b>	<b>68.77</b>
QA00	2.046	41.13	106.55	78.26	202.64	69.48	50.76
QA00	3.034	40.47	104.79	90.70	234.85	68.34	74.98
<b>Mean</b>	<b>2.540</b>	<b>40.80</b>	<b>105.67</b>	<b>84.48</b>	<b>218.74</b>	<b>68.91</b>	<b>62.87</b>
QC00	2.265	32.37	91.75	68.23	193.38	59.76	69.99
QC00	2.159	30.85	87.44	66.31	187.94	56.95	70.01
<b>Mean</b>	<b>2.212</b>	<b>31.61</b>	<b>89.60</b>	<b>67.27</b>	<b>190.66</b>	<b>58.35</b>	<b>70.00</b>

QA60 = Quasi-static test on Angle-ply, [ $\pm 45/0\dots$ ], specimen with 60° external chamfer.

QC00 = Quasi-static test on Cross-ply, [0/90...], specimen without chamfer.

Table 4.2 - Test results at quasi-static compression (0.5 mm/min).

Sample	AE (kJ)	$F_{ave}$ (kN)	$\sigma_{ave}$ (MPa)	$F_{max}$ (kN)	$\sigma_{max}$ (MPa)	SEA (J/g)	$l_c$ (mm)
CS_A45 = C-shape specimen with angle-ply layup externally chamfered with 45°.							
CS_C60= C-shape specimen with cross-ply layup externally chamfered with 60°.							

Table 4.3 - Test results for dynamic set#1, striker mass equals to 102 kg.

Sample	AE (kJ)	$F_{ave}$ (kN)	$\sigma_{ave}$ (MPa)	$F_{max}$ (kN)	$\sigma_{max}$ (MPa)	SEA (J/g)	$l_c$ (mm)	V (m/s)
DA60#1	2.463	35.10	90.86	64.30	166.49	59.25	70.20	6.84
DA60#1	2.251	35.76	92.61	71.23	184.44	60.39	63.03	6.73
DA60#1	2.388	37.19	96.31	-	-	62.81	64.20	6.55
<b>Mean</b>	<b>2.367</b>	<b>36.01</b>	<b>93.26</b>	<b>67.76</b>	<b>175.47</b>	<b>60.81</b>	<b>65.81</b>	<b>6.70</b>
DC60#1	2.545	31.19	88.40	-	-	57.58	81.60	6.92
DC60#1	2.260	31.17	88.36	63.12	178.89	57.56	72.50	6.54
DC60#1	2.045*	32.94	92.68	65.91	186.80	60.37	73.54	6.76
<b>Mean</b>	<b>2.403</b>	<b>31.76</b>	<b>89.81</b>	<b>64.51</b>	<b>182.85</b>	<b>58.50</b>	<b>75.88</b>	<b>6.74</b>
DA45#1	2.465	34.24	88.61	54.90	142.15	57.82	72.00	6.86
DA45#1	2.504	32.61	84.45	-	-	55.08	76.80	6.90
DA45#1	2.391	35.30	91.40	66.66	172.60	59.61	67.74	6.75
<b>Mean</b>	<b>2.453</b>	<b>34.05</b>	<b>88.15</b>	<b>60.78</b>	<b>157.38</b>	<b>57.50</b>	<b>72.18</b>	<b>6.84</b>
DC45#1	2.398	32.30	91.54	50.51	143.15	59.62	74.25	6.75
DC45#1	2.687	30.65	86.86	63.03	178.64	56.58	87.70	7.14
DC45#1	2.263	30.06	85.20	-	-	55.50	75.30	6.55
<b>Mean</b>	<b>2.449</b>	<b>31.00</b>	<b>87.87</b>	<b>56.77</b>	<b>160.90</b>	<b>57.23</b>	<b>79.08</b>	<b>6.81</b>
DA00#1	2.366	34.74	89.96	185.40	480.1	58.67	68.10	6.71
DA00#1	2.106	33.48	86.70	-	-	56.54	62.91	6.32
<b>Mean</b>	<b>2.236</b>	<b>34.11</b>	<b>88.33</b>	<b>185.40</b>	<b>480.1</b>	<b>57.60</b>	<b>65.50</b>	<b>6.51</b>
DC00#1	2.050	30.87	87.51	134.00	379.78	57.00	66.40	6.85
DC00#1	2.334	29.53	83.19	122.00	345.77	54.20	79.54	6.66
<b>Mean</b>	<b>2.192</b>	<b>30.20</b>	<b>85.35</b>	<b>128.00</b>	<b>362.78</b>	<b>55.60</b>	<b>72.97</b>	<b>6.75</b>

\* Laser signal lost in the final part of crushing event.

Table 4.4 - Test results for dynamic set#2, striker mass equals to 102 kg.

Sample	AE (kJ)	$F_{ave}$ (kN)	$\sigma_{ave}$ (MPa)	$F_{max}$ (kN)	$\sigma_{max}$ (MPa)	SEA (J/g)	$l_c$ (mm)	V (m/s)
DA60#2	1.349	34.90	90.36	66.80	172.97	58.93	38.66	5.07
DA60#2	1.372	35.34	92.06	69.50	179.96	60.05	38.60	5.11
DA60#2	1.318	35.17	91.06	-	-	59.40	37.50	5.01
<b>Mean</b>	<b>1.346</b>	<b>35.14</b>	<b>91.16</b>	<b>68.15</b>	<b>176.46</b>	<b>59.46</b>	<b>38.25</b>	<b>5.06</b>
DC60#2	1.203	31.80	90.86	68.73	194.79	58.72	37.82	4.96
DC60#2	1.325	31.11	88.17	64.48	182.75	57.43	42.60	5.01
DC60#2	1.393	31.67	89.77	71.59	202.90	58.44	43.98	5.14
<b>Mean</b>	<b>1.307</b>	<b>31.53</b>	<b>89.60</b>	<b>68.11</b>	<b>193.48</b>	<b>58.20</b>	<b>41.47</b>	<b>5.04</b>
DA45#2	1.321	35.17	91.07	60.01	155.38	59.40	37.57	5.02
DA45#2	1.322	35.46	91.84	66.78	172.91	59.90	37.27	5.02
DA45#2	1.411	37.57	97.30	58.27	150.88	63.45	37.55	5.19
<b>Mean</b>	<b>1.351</b>	<b>36.07</b>	<b>93.41</b>	<b>61.68</b>	<b>159.73</b>	<b>60.92</b>	<b>37.46</b>	<b>5.08</b>
DC45#2	1.335	30.81	87.31	46.23	131.02	56.87	43.32	5.03
DC45#2	1.353	30.27	85.78	52.34	148.34	55.88	44.69	5.06
DC45#2	1.333	31.29	88.70	54.20	153.61	57.76	44.24	5.02
<b>Mean</b>	<b>1.340</b>	<b>30.79</b>	<b>87.26</b>	<b>50.92</b>	<b>144.32</b>	<b>56.84</b>	<b>44.08</b>	<b>5.04</b>
DA00#2	1.362	31.60	81.84	149.41	386.87	53.37	43.30	5.085
DA00#2	1.333	33.30	86.23	121.00	313.31	56.23	40.00	5.034
<b>Mean</b>	<b>1.347</b>	<b>32.45</b>	<b>84.03</b>	<b>135.20</b>	<b>350.10</b>	<b>54.80</b>	<b>41.65</b>	<b>5.059</b>
DC00#2	1.339	30.39	86.14	114.30	323.95	56.11	44.06	5.039
DC00#2	1.364	30.66	86.90	-	-	56.60	44.48	5.065
<b>Mean</b>	<b>1.351</b>	<b>30.53</b>	<b>86.52</b>	<b>114.30</b>	<b>323.95</b>	<b>56.35</b>	<b>44.27</b>	<b>5.062</b>

Table 4.5 - Test results for dynamic set#3, striker mass equals to 205 kg.

Sample	AE (kJ)	$F_{ave}$ (kN)	$\sigma_{ave}$ (MPa)	$F_{max}$ (kN)	$\sigma_{max}$ (MPa)	SEA (J/g)	$l_c$ (mm)	V (m/s)
DA60#3	2.973	32.68	84.62	120.20	311.32	55.18	90.98	5.21
DA60#3	2.938	35.39	91.63	115.30	298.55	59.76	83.03	5.20
DA60#3	2.925	37.11	96.10	105.10	272.14	62.67	78.82	5.191
<b>Mean</b>	<b>2.945</b>	<b>35.06</b>	<b>90.78</b>	<b>113.54</b>	<b>294.00</b>	<b>59.20</b>	<b>84.28</b>	<b>5.20</b>
DC60#3	2.953	32.04	90.81	98.02	277.81	59.15	92.18	5.12
DC60#3	2.931	31.07	88.07	74.14	210.13	57.37	94.31	5.17
DC60#3	3.210	32.10	90.97	-	-	59.26	100.00	5.41
<b>Mean</b>	<b>3.031</b>	<b>31.74</b>	<b>89.95</b>	<b>86.08</b>	<b>243.97</b>	<b>58.59</b>	<b>95.50</b>	<b>5.23</b>
DA45#3	2.929	35.03	90.69	90.21	233.58	59.14	83.65	5.18
DA45#3	2.959	31.00	80.27	-	-	52.35	95.45	5.19
DA45#3	2.979	32.73	84.76	69.90	180.99	55.28	91.10	5.21
<b>Mean</b>	<b>2.956</b>	<b>32.92</b>	<b>85.24</b>	<b>80.05</b>	<b>207.29</b>	<b>55.59</b>	<b>90.07</b>	<b>5.19</b>
DC45#3	2.947	29.96	84.92	85.00	240.91	55.31	98.36	5.17

Table 4.5 - Test results for dynamic set#3, striker mass equals to 205 kg.

Sample	AE (kJ)	$F_{ave}$ (kN)	$\sigma_{ave}$ (MPa)	$F_{max}$ (kN)	$\sigma_{max}$ (MPa)	SEA (J/g)	$l_c$ (mm)	V (m/s)
DC45#3	3.002	32.09	90.97	89.86	254.68	59.25	93.52	5.24
<b>Mean</b>	<b>2.974</b>	<b>31.03</b>	<b>87.94</b>	<b>87.43</b>	<b>247.79</b>	<b>57.28</b>	<b>95.94</b>	<b>5.21</b>
DA00#3	3.099	33.83	87.51	215.20	557.20	57.12	91.25	5.32
DA00#3	2.993	32.22	83.43	-	-	54.43	92.30	5.22
<b>Mean</b>	<b>3.046</b>	<b>33.03</b>	<b>85.47</b>	<b>215.20</b>	<b>557.20</b>	<b>55.77</b>	<b>91.77</b>	<b>5.27</b>
DC00#3	2.974	31.90	90.43	198.80	563.60	58.90	93.21	5.21
DC00#3	2.932	32.50	92.10	188.21	533.40	59.98	90.24	5.18
<b>Mean</b>	<b>2.953</b>	<b>32.20</b>	<b>91.26</b>	<b>193.50</b>	<b>548.50</b>	<b>59.44</b>	<b>91.72</b>	<b>5.19</b>

Table 4.6 - Test results for dynamic set#4, striker mass equals to 48.60 kg.

Sample	AE (kJ)	$F_{ave}$ (kN)	$\sigma_{ave}$ (MPa)	$F_{max}$ (kN)	$\sigma_{max}$ (MPa)	SEA (J/g)	$l_c$ (mm)	V (m/s)
DA60#4	2.280	35.62	92.25	92.89	240.5	60.16	64.00	9.62
DA60#4	2.217	35.09	90.85	89.20	230.9	59.25	63.20	9.49
DA60#4	2.288	34.16	88.46	77.06	199.5	57.69	67.20	9.63
<b>Mean</b>	<b>2.262</b>	<b>34.95</b>	<b>90.52</b>	<b>86.38</b>	<b>223.6</b>	<b>59.03</b>	<b>64.80</b>	<b>9.58</b>
DC60#4	2.233	30.18	85.54	71.20	201.70	55.72	74.00	9.51
DC60#4	2.294	31.65	89.71	63.50	179.88	58.43	72.50	9.64
DC60#4	2.302	32.39	91.34	88.20	249.92	59.80	73.70	9.65
<b>Mean</b>	<b>2.276</b>	<b>31.41</b>	<b>88.86</b>	<b>74.30</b>	<b>210.51</b>	<b>57.98</b>	<b>73.40</b>	<b>9.60</b>
DA45#4	2.283	36.63	94.51	68.21	176.60	61.33	62.60	9.63
DA45#4	2.317	35.28	91.35	77.23	199.93	59.58	65.70	9.70
DA45#4	2.407	33.86	87.69	70.20	181.67	57.20	71.10	9.88
<b>Mean</b>	<b>2.335</b>	<b>35.24</b>	<b>91.18</b>	<b>71.88</b>	<b>186.12</b>	<b>59.37</b>	<b>66.46</b>	<b>9.73</b>
DC45#4	2.319	31.33	88.79	62.23	176.37	57.84	74.10	9.69
DC45#4	2.329	31.64	89.70	68.20	193.32	58.43	73.60	9.71
DC45#4	2.126	29.82	84.52	54.44	154.19	55.05	71.30	9.28
<b>Mean</b>	<b>2.258</b>	<b>30.93</b>	<b>87.67</b>	<b>61.62</b>	<b>174.60</b>	<b>57.11</b>	<b>73.00</b>	<b>9.56</b>

### 4.3 Discussion

#### 4.3.1 Damage modes of angle-ply tube specimens, [ $\pm 45/0...$ ]

Figure 4.3(a) shows photo sequences of the layer's deformation of a C-section angle-ply specimen under quasi-static compression. The white layers are  $0^\circ$  and black

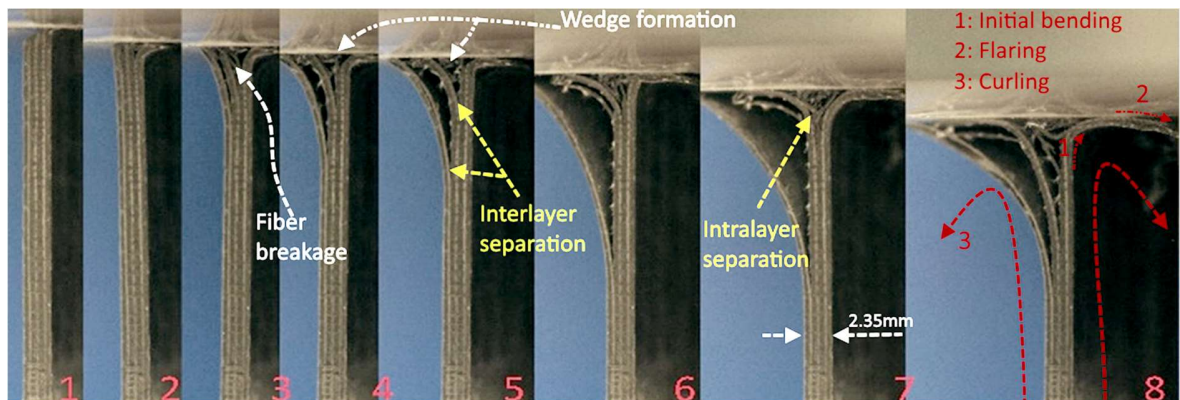
layers are  $\pm 45^\circ$  laminae. Figures 4.3(b)-(c) present the cut-views of full tube specimens after quasi-static and dynamic compression, respectively. Both  $0^\circ$  and  $\pm 45^\circ$  laminae showed a tendency for bending, flaring and curling processes similar to a tube inversion mechanism under conical die (Sun and Yang 2006), as shown in the last frame of Figure 4.3(a). After initial bending, the laminate starts to separate and the separated part loses its load-bearing capacity. Meanwhile, the layers splayed parallel to their corresponding fiber orientation angle, which is more obvious for the dynamic test in Figure 4.4(b). The damage failure mode of the angle-ply tube in Figure 4.4 is called a 'tearing damage mode' in some references (Schultz and Hyer 2001; Jackson et al. 2011; David, Johnson, and Voggenreiter 2013). Mamalis et al. (Mamalis et al. 1996) observed a similar fracture mechanism as in Figure 4.3(d) and theoretically showed that friction could be responsible for more than 50% of energy dissipated. The other effective parameters were listed as fronds bending, crack propagation and axial splitting between fronds (Mamalis et al. 1996). Later Mamalis et al. (Mamalis et al. 2004) proposed the same energy dissipating mechanism for carbon fiber rectangular tubes.

The delamination propagates further away from the compression platen in the open C-section specimen in comparison with the same process in closed tube specimens. The C-section specimens are more prone to become destabilized and develop larger lamina bending under compression load. In general, the flaring/curling radii of the internal/external fronds of the specimens under impact are much smaller than those of the specimens under quasi-static compression, for both full and C-sections, according to Figure 4.3. The bending of plies with a smaller radius caused a larger number of inter/intra layer separations during the dynamic test (Figure 4.3(c)), which is notable when comparing it with the number of separations in the quasi-static tests. This behavior is clearly observed in Figures 4.4(a), (b) and Figure 4.3. Nevertheless, there is no significant difference between the damaged zones of the angle-ply specimens under different dynamic loading conditions. Due to the large number of inter/intra layer separations, the fronds lost their flexural and compressive stiffness and became softer than the less separated fronds under quasi-static compression. The post-crash inspection of the angle-ply tubes after compression (Figures 4.3(b), 4.3(c)) shows that the center-wall crack under

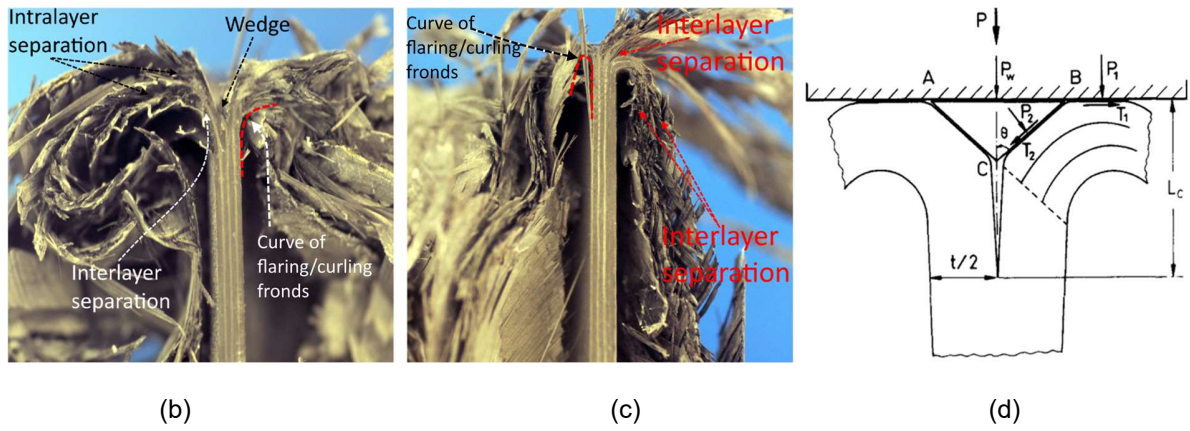
quasi-static compression has developed a ‘little’ further than the center-wall crack of the tubes under dynamic tests. The difference between the center-wall crack development (or V-shape wedge depth) is possibly caused by the lateral inertia effects which can explain the different flaring radii of inward/outward fronds in the quasi-static and dynamic test. In addition, the damaged parts split into more pieces under dynamic test which leads to a lower compressive and flexure stiffness in comparison with the fronds in the quasi-static test. The larger bending stiffness of the fronds can possibly lead to larger delamination, longer center-crack length and deeper V-shape wedge in the quasi-static test. It was previously reported in the literature that the debris wedge disappeared in the dynamic crushing zone (Mamalis, Yuan, and Viegelaahn 1992).

Moreover, the debris color of the impacted angle-ply tube is not as dark as the debris in the quasi-static test (Figure 4.4). This difference in color can be related to damages in the matrix (intralayer or interlayer separations) or damages in fiber which the former leads to more white debris, indicating inter/intra layer separations with minimum fiber breakage.

Figure 4.3 - Damage mechanism of different layers in angle-ply specimens; (a) Time-lapse of deformation of each layer of C-shape specimen; (b) Cut-view of full tube specimen after quasi-static compression; (c) Cut-view of full tube specimen after dynamic impact; (d) Schematic of fracture mechanism.

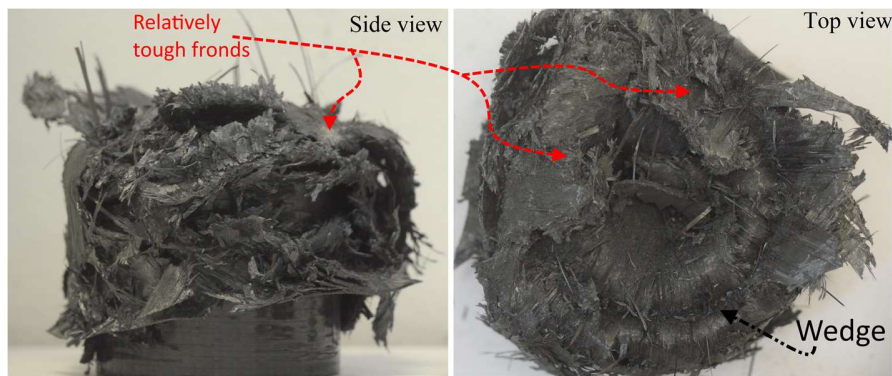


(a)

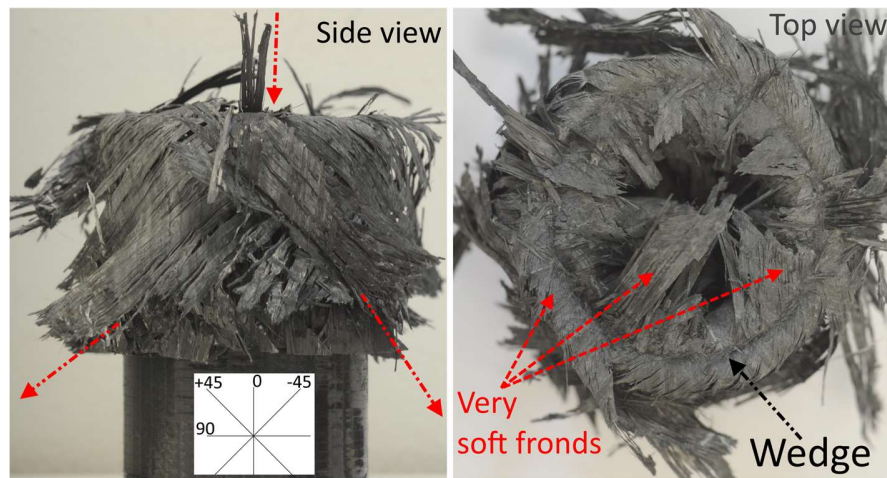


Source: (a,b,c): The author; (d): (Mamalis et al. 2004).

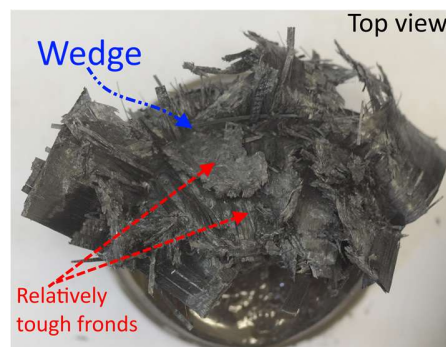
Figure 4.4 - Crushed zone views of angle-ply specimens; (a) Full tube specimen after quasi-static compression; (b) Full tube specimen after dynamic compression, dynamic set#2; (c) C-shape specimen after quasi-static compression.



(a)



(b)



(c)

Source: The author.

#### 4.3.2 The damage mode of cross-plyed specimens, [0/90...]

Figure 4.5(a) shows the crushing mechanism of the  $0^\circ$  and  $90^\circ$  layers in a cross-ply C-section specimen at certain time intervals during a quasi-static test. The white layers are  $0^\circ$  and black layers are  $90^\circ$  laminae. The axial to hoop strength ratio of each layer mainly defines its mode of failure. The  $0^\circ$  laminae, where the fibers are aligned with tube axis, have the highest axial to hoop strength ratio while the layers with  $90^\circ$  fibers orientation in circumferential direction possess the lowest axial to hoop strength ratio (Hull 1991). However, the different boundary conditions may change significantly the failure

mode of a layer. The compressive load destabilized the  $90^\circ$  layers and they failed by fragmentation mode, marked with 'I' in Figure 4.5(a) (frames 2→3, 4→5) in which the layers experience several short-length matrix fractures due to transverse shearing or sharp bending [12].

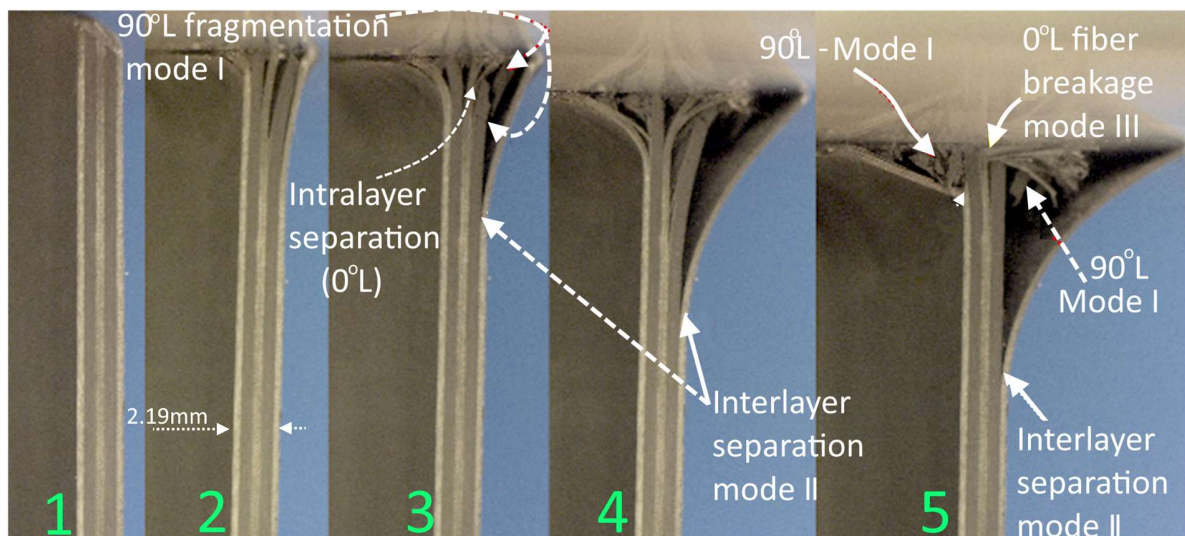
The boundary condition affects the failure mode of  $0^\circ$  layers. The innermost and outermost  $0^\circ$  layers, being constrained only at one side, tend to bend and fail as long intact strips by a 'splaying mode' marked as 'II' in Figure 4.5(a) (frames 2→5) displaying lamina bundle bending. The  $0^\circ$  layers in the middle of the tube wall are tightly constrained by the  $90^\circ$  layers from both sides. Therefore, the  $0^\circ$  layer splayed (and formed lamina bundle) and the lamina bundles break into short length stripes because of fiber breakage ('brittle fracturing mode'), as marked by 'III' in Figure 4.5(a) (frames 4→5). In fact, the crushing mechanism of  $0^\circ$  layer placed between  $90^\circ$  layers is a function of the behavior of  $90^\circ$  layers.

Based on the captured photos during quasi-static test on C-section samples, the failure sequence mechanisms of cross-ply specimens is as follow: (1) separation and delamination (frames 1→5), (2) splaying at outer/inner  $0^\circ$  layers and lamina bundles bending, (3) destabilizing and transverse shearing of  $90^\circ$  layers and (4) lamina bundle bending followed by brittle fracturing of  $0^\circ$  layer in the middle of wall thickness. These mechanisms randomly repeated during the crushing process. Figures 4.5(b) and 4.5(c) illustrate the cut-view of full tube specimens after quasi-static and dynamic tests, respectively. One can see that damage propagated faster in the innermost/outermost  $0^\circ$  layers than in layers  $[90_2/0]_s$ . Figure 4.5(d) is showing a schematic presentation of three modes of failure in brittle composites, sharing several similarities with Figures 4.5(b), 4.5(c).

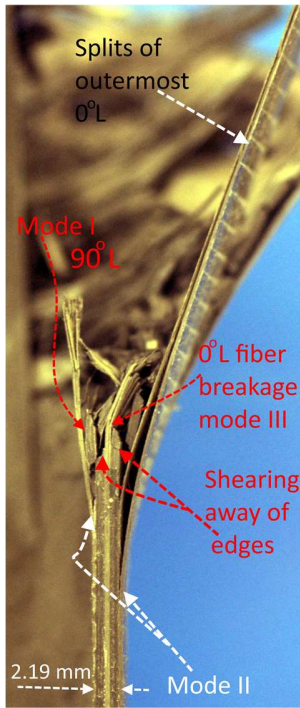
The top view of the damage appearance in cross-ply specimens is presented in Figure 4.6. The final damaged shape of each layer is identified based on its damage mechanism and explained by Figure 4.5(a). In general, there is no difference between tube crushed zone views under different dynamic sets (set#1 to set#4), however, some differences between the crushed zone of specimens under quasi-static and dynamic

loading have been observed, although their failure mechanisms are the same. For both quasi-static and dynamic tests, the  $90^\circ$  and  $0^\circ$  layers in the middle of the tube's wall were damaged by transverse shearing (Mode I) and brittle fracturing (Mode III), respectively. However, the shape, size and arrangement of the deformed internal  $0^\circ$  and  $90^\circ$  layers changed when increasing the loading rate as it is depicted in Figures 4.6(a), 4.6(b). The  $90^\circ$  layers failed due to matrix-dominant failure modes and formed ring-shaped parts when most of these ring-shaped parts were broken under likely high tensile forces in fiber that are arranged in the circumferential direction (Chiu et al. 2015).

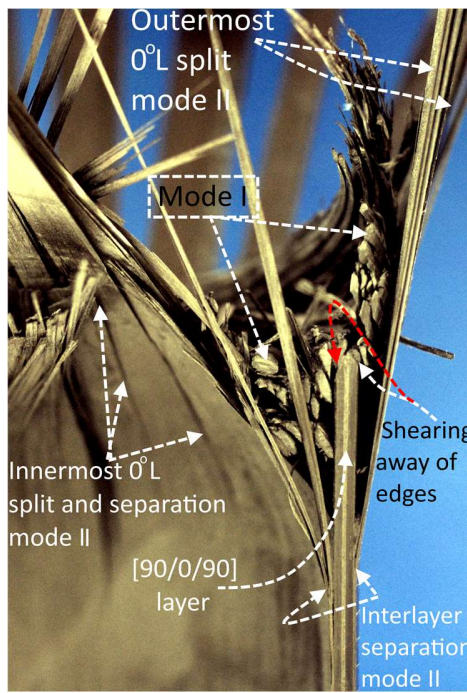
Figure 4.5 - Damage mechanism of different layers in cross-ply specimens; (a) Sequential deformation of each layer of the C-shape specimen, (I: fragmentation mode, II: splaying mode and III: brittle fracturing); (b) Cut-view of full tube specimen after quasi-static test; (c) Cut-view of full tube specimen after impact; (d) Schematic presentation of failure modes.



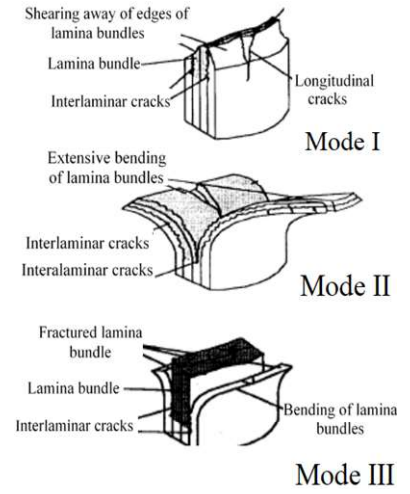
(a)



(b)



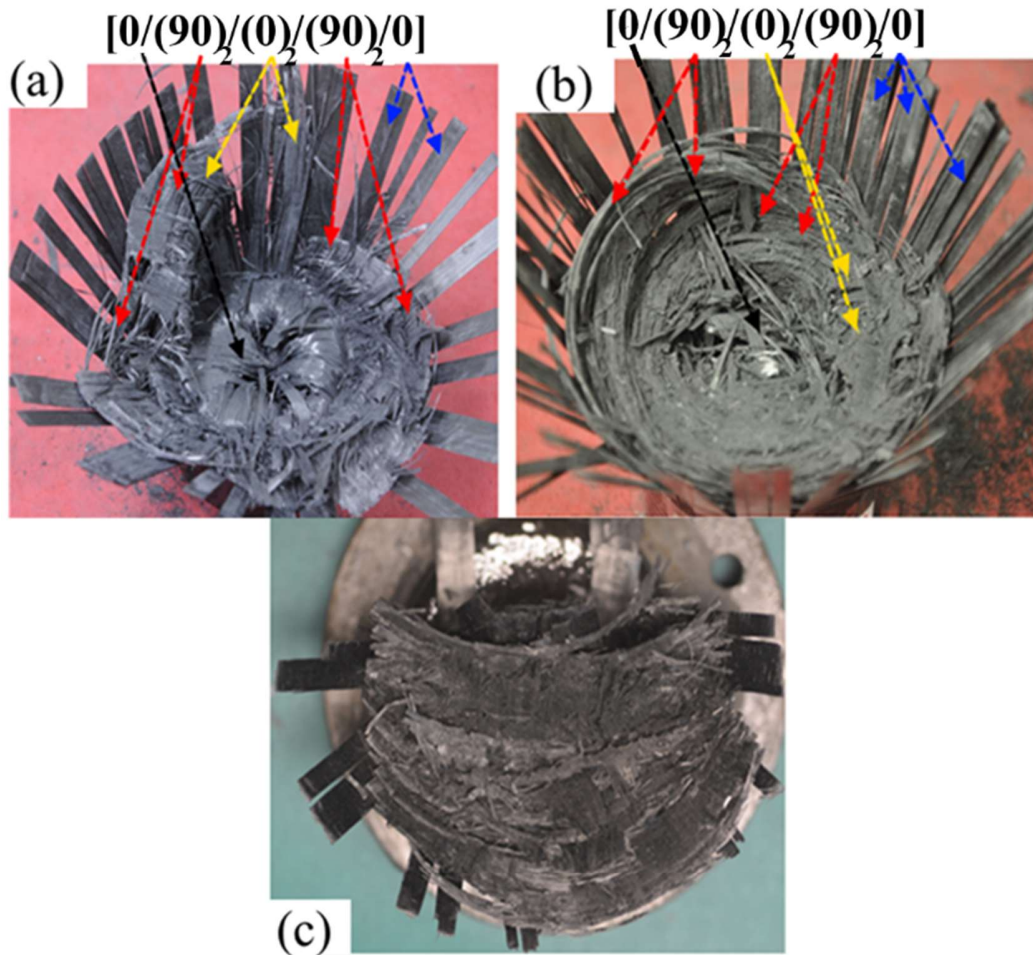
(c)



(d)

Source: (a,b,c): The author; (d): (Jacob et al. 2002)

Figure 4.6 - Top view of crushed zones of cross-ply specimens; (a) Full tube after quasi-static compression; (b) Full tube specimen after impact, dynamic set#2; (c) C-shape specimen after quasi-static compression.



Test	Damage at each layer (symmetric)		
	[0	$(90)_2$	0]
Quasi-static	Long strips bent inward (Mode II)	Ring-shape parts (Mode I)	Short longitudinal strips (Mode III)
Dynamic	Long strips bent inward (Mode II)	Ring-shape parts (Mode I)	Tiny particles (Mode III)

Source: The author.

### 4.3.3 Effect of the axial splitting of outermost 0° layer on crushing behavior of cross-ply specimens

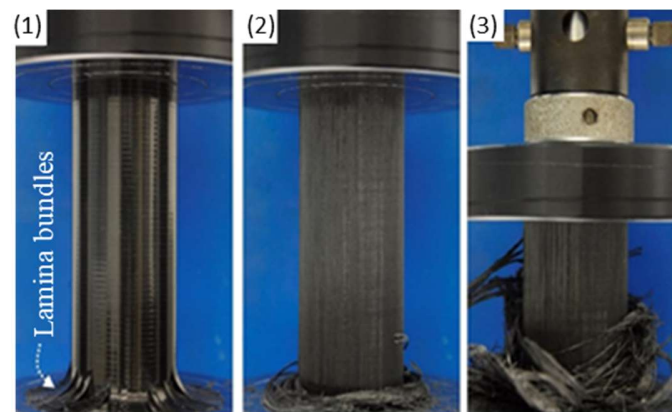
The outermost 0° layer splayed while damage occurred in the matrix due to the low circumferential strength of this layer. Interlayer separation (delamination) propagated far from the contact plane as shown by the crush front in Figure 4.5(a)-(c). The split 0° lamina bundles undergo 'lamina bundle bending', a phenomenon which is analyzed in this section in order to examine the role of the outermost 0° layer on the energy absorption performance of cross-ply specimens.

Figure 4.7(a) shows a quasi-static test on a cross-ply specimen. After 25 mm displacement, the cross-head of the universal machine has been stopped for 5 minutes and the lamina bundles of outer 0° layer were removed by hand. After that, the cross-head was set in motion to crush the remaining part of the specimen. A comparison between the force-displacement curves of two cross-ply specimens with and without outer 0° layer are shown in Figure 4.7(b). No significant effect on the crushing force of the specimen is observed after removing the split bundles of the outer 0° layer. The SEA is increased by 17 % when removing the outer 0° layer as the overall weight of the specimen decreased. Therefore, the inclusion of one-side constrained unidirectional 0° layers in axially loaded energy absorbers is not an optimal design solution. The low strength of the epoxy resin of the unidirectional CF material, used in this study, determines a very low transverse-to-axial (fiber direction) strength ratio which contributes to the development of multiple intra cracks in the delaminated outermost layer in the axial direction. Finally, this layer splits into numerous bundles (Figure 4.6(a), 4.6(b)) having no strength to bear the load. This example illustrates that an arrangement of the fibers only in the load-bearing direction does not increase the load-bearing capacity of specimens as this layer does not have any mechanism to confine crack (damage) propagation (Thornton 1979).

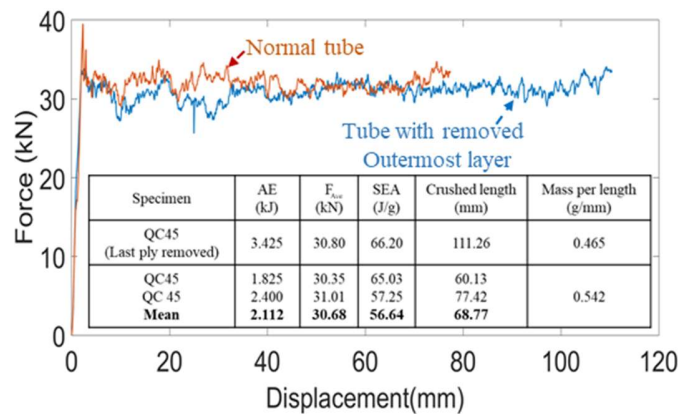
Splitting the outermost 0° layer and bending of lamina bundles, after the peak load is reached, has no significant effect on the average crushing force. The same conclusion is valid regarding the crushing behavior of the innermost 0° layer as it is also one-side constrained. Thus the  $[(90)_2/0]_s$  layers, Figures. 4.5(b), 4.5(c), are responsible for a large proportion of the load-bearing capacity of cross-ply specimens. An estimate of the energy

absorption capacity of the middle  $0^\circ$  layers placed between  $90^\circ$  layers is obtained in Appendix C.

Figure 4.7 - Effect of axial splitting of outermost  $0^\circ$  layer on the energy absorption capacity of cross-ply specimen; (a) Test description, (1) Before removing the outermost layer strips, (2) After removing the outermost layer's strips and (3) Further specimen's compression with removed outermost layer; (b) Force-displacement curve and results.



(a)



(b)

Source: The author.

The above-described test (Figure 4.7(b)) can be also used to interpret the contribution of friction. A decrease of 4.6 kN of the average crushing force (dropped from 30.8 kN to 26.2 kN) was recorded during the 5-minutes interval when the upper platen of the machine was stopped to remove the splits of the outermost  $0^\circ$  layer (Figure 4.7(a)). It

was revealed that this force decrease was not due to the removal of the outermost  $0^\circ$  layer as the average load reached and sustained around 30.8 kN force after setting the machine to motion until the test terminated. The force reduction of 4.6 kN is related to the motion; thus, it can arise from friction and further development of existing damages as well as new damages initiation, which resist against the motion of platen.

#### **4.3.4 Force-displacement characteristics**

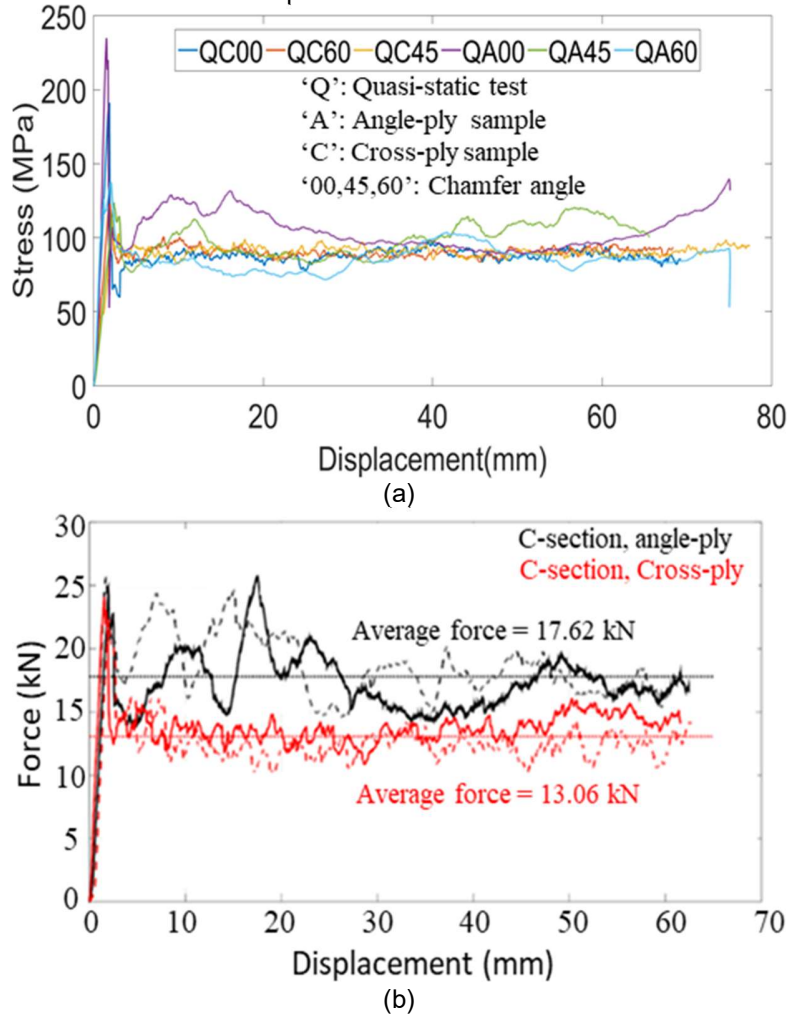
The stress values and some stress-displacement curves are presented in addition to the force values and force-displacement curves to minimize the effect of the small difference in the wall thicknesses of the two types of specimens on their energy absorption capacity. The stress and force values for all specimens under different loading conditions are presented in details in Tables 4.2 to 4.6.

##### **4.3.4.1 Typical force-displacement response, quasi-static tests**

Figure 4.8(a) shows the variation of steady-state crushing stress, SSCS, for some selected specimens that represent the typical behavior of the cross-ply and angle-ply layup configurations under quasi-static compression. Although there is a very clear consistency between stress (force) responses of the specimens with the same layup, it is obvious that the ply orientation has a significant effect on the general shape of crushing stress-displacement curves so indicating a distinct crushing behavior. Small fluctuations of the crushing stress of the specimens with cross-ply, [0/90...] stacking sequence, around its average stress value of 10 MPa are observed, while fluctuations with a larger magnitude of 35 MPa characterize the crushing stress of specimens with [ $\pm 45/0$ ...] stacking sequence. This distinct difference between tube absorbers with the same material only due to the change in layup configuration has not been discussed in details in the literature. In general, cross-ply specimens showed a more predictable crushing stress (force) response than angle-ply specimens under static tests. Table 4.2 lists force and stress results for all specimens under quasi-static test.

Figure 4.8(b) shows the force-displacement curves for C-section specimens under quasi-static compression. The average crushing force and average stress of C-section specimens are presented in Table 4.2 in details. For cross-ply layup specimens, the sum of the average crushing forces of two C-section halves is 16% and 21% lower than the average crushing force of the full tube specimens with 45° and 60° external chamfers, respectively. However, the sum of the average forces of two C-section halves of angle-ply specimens showed a  $\pm 5\%$  difference with the average crushing force of full tube specimens with 45° and 60° external chamfers. The test results show that the division of the full tube into two halves decreased the structural integrity which affected more significantly the load bearing capacity of cross-ply tubes than angle-ply specimens. Therefore, the sensitivity of cross-ply layup was higher than the sensitivity of angle-ply specimens. The fibers of 90° layers in the full cross-ply tube specimen underwent a large tensile stress in the circumferential direction that damaged and formed ring-shape parts due to tensile hoop stress (Figure 4.6), a phenomenon which has been reported in other publications (Chiu et al. 2015). By dividing the cross-ply tube into two halves, the hoop stiffness of the laminate tube is decreased while affecting the crushing behavior of the middle 0° layers that are responsible for the significant part of the load-bearing capacity of the cross-ply specimens (see Appendix).

Figure 4.8 - Typical crushing behavior of angle-ply and cross-ply specimens under quasi-static compression; (a) Stress-displacement curves of full tube specimens; (b) Force-displacement curves of C-shape tubes with 60° external chamfer.



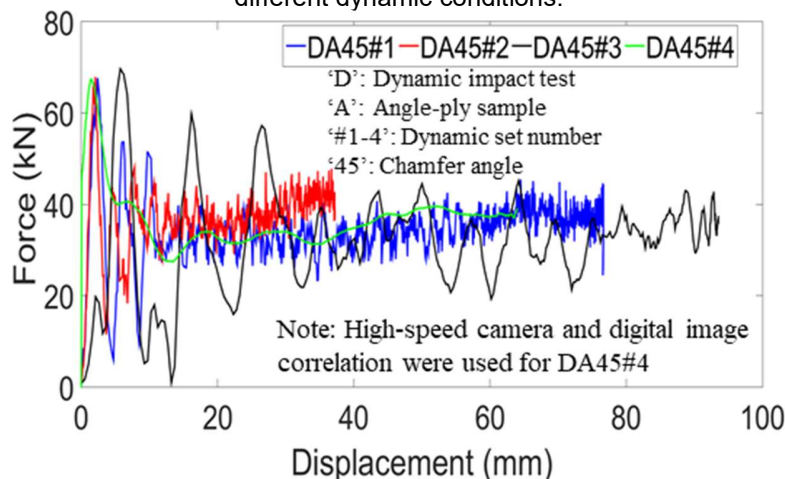
Source: The author.

As it was expected, the external chamfer controlled the peak load value since specimens without trigger experienced the highest peak load (peak stress) and those with 45° external chamfer experienced the lowest values of the peak load (peak stress) for both layups, see Figure 4.8(a) and Table 4.2. The quasi-static tests revealed some sensitivity of the crushing behavior to the chamfer angle for the angle-ply specimens, [ $\pm 45/0\dots$ ]. It should be also noted that the tubes without chamfer responded by the highest average crushing force while the specimens with 60° external chamfer are characterized by the lowest average force.

#### 4.3.4.2 Typical force-displacement response, impact tests

Dynamic crushing force, because of the nature of high-speed impacting, contains higher frequency noise comparing to the crushing force of specimens under quasi-static compression so that the impact tests led to a high-frequency content in the load readings. Table 4.3 to 4.6 present the values of maximum and average crushing forces (stresses) of all specimens under dynamic loading. Figure 4.9 shows the force-displacement curves of angle-ply specimens with 45° chamfer under four different loading conditions. Good agreement between extracted results from laser velocimeter (sets 1 to 3) and high-speed camera (124 kfps, set# 4) is observed. For dynamic sets 1 to 3, Butterworth filter (B = 1 and A = 0.005) and for set#4 moving average filter (smooth function) in MATLAB are used for signal conditioning.

Figure 4.9 - Typical force-displacement curve of angle-ply specimens with 45° chamfer under different dynamic conditions.

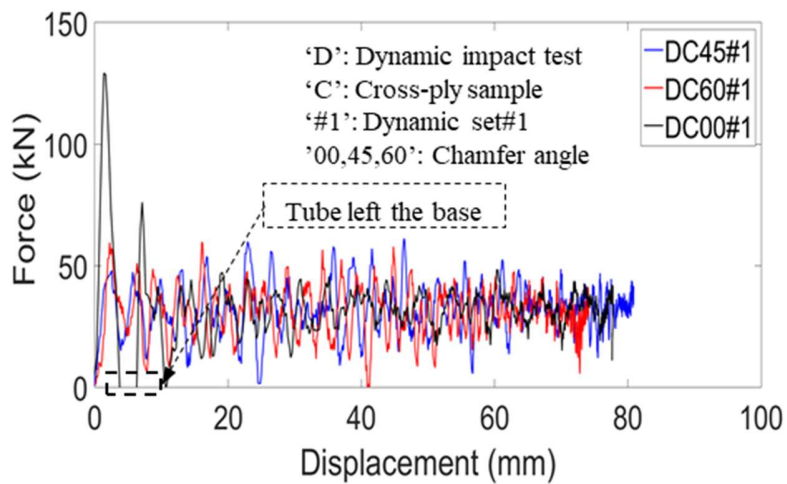


Source: The author.

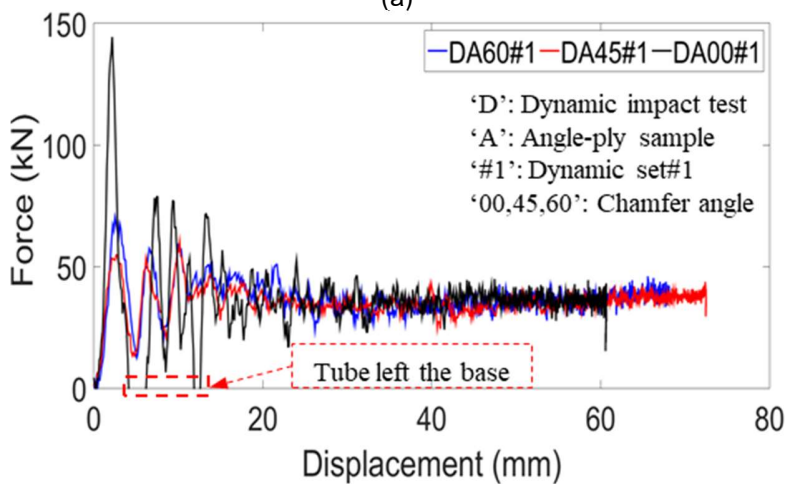
In general, for all dynamic tests, the specimens with a trigger experienced a smoother damage initiation stage than specimens without trigger, moreover, specimens without trigger took off the base for a fraction of milli-second after the peak load. Typical force-displacement curves for dynamic tests set#1 and set#2, as representative for dynamic sets, are presented in Figures 4.10 and 4.11 for two different layup configurations. Figure 4.12 shows that the fluctuations of the crushing stresses of the

angle-ply specimens under dynamic compression are smaller than those of stress fluctuations of cross-ply specimens. In general, the angle-ply specimens responded by a smoother steady-state crushing stress (force) after damage initiation than the cross-ply specimens as it is obvious when comparing Figure 4.10(a) with Figure 4.10(b) and Figure 4.11(a) with Figure 4.11(b) and Figure 4.12.

Figure 4.10 - Force-displacement curves for dynamic set#1; (a) Cross-ply [0/90...] specimens; (b) Angle-ply [ $\pm 45/0$ ] specimens.



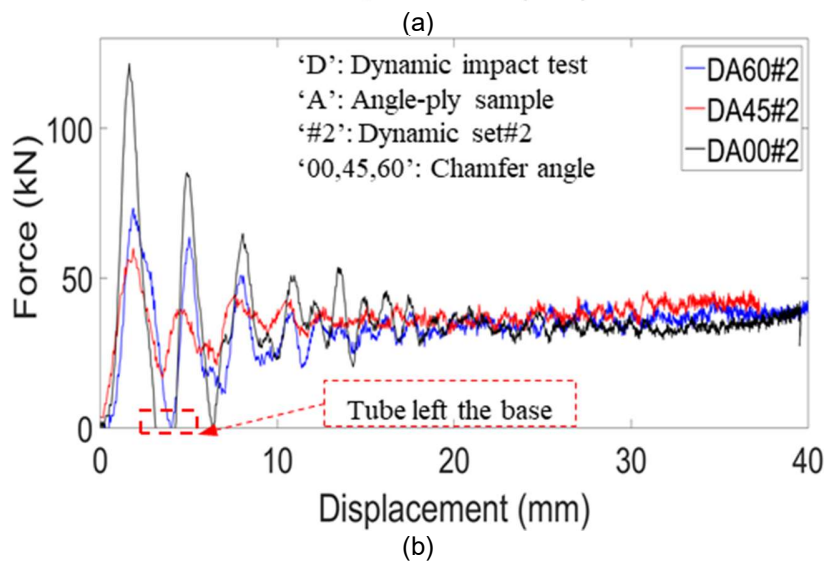
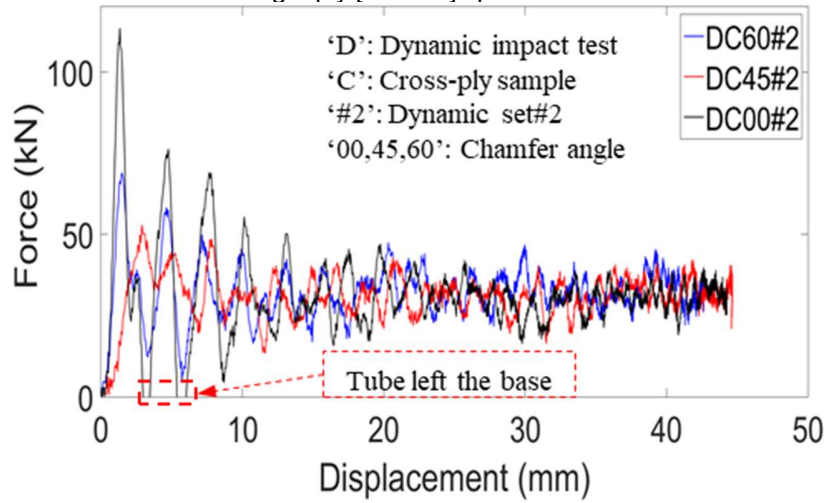
(a)



(b)

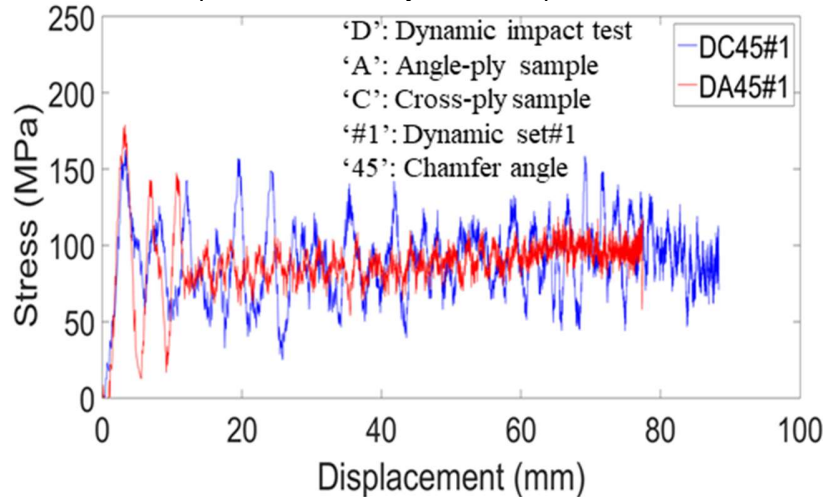
Source: The author.

Figure 4.11 - Force-displacement curves for dynamic set#2; (a) Cross-ply [0/90...] specimens; (b) Angle-ply [ $\pm 45/0$ ...] specimens.



Source: The author.

Figure 4.12 - Typical stress variation curves of angle-ply [ $\pm 45/0\dots$ ] and cross-ply [0/90...] specimens under dynamic compression.



Source: The author.

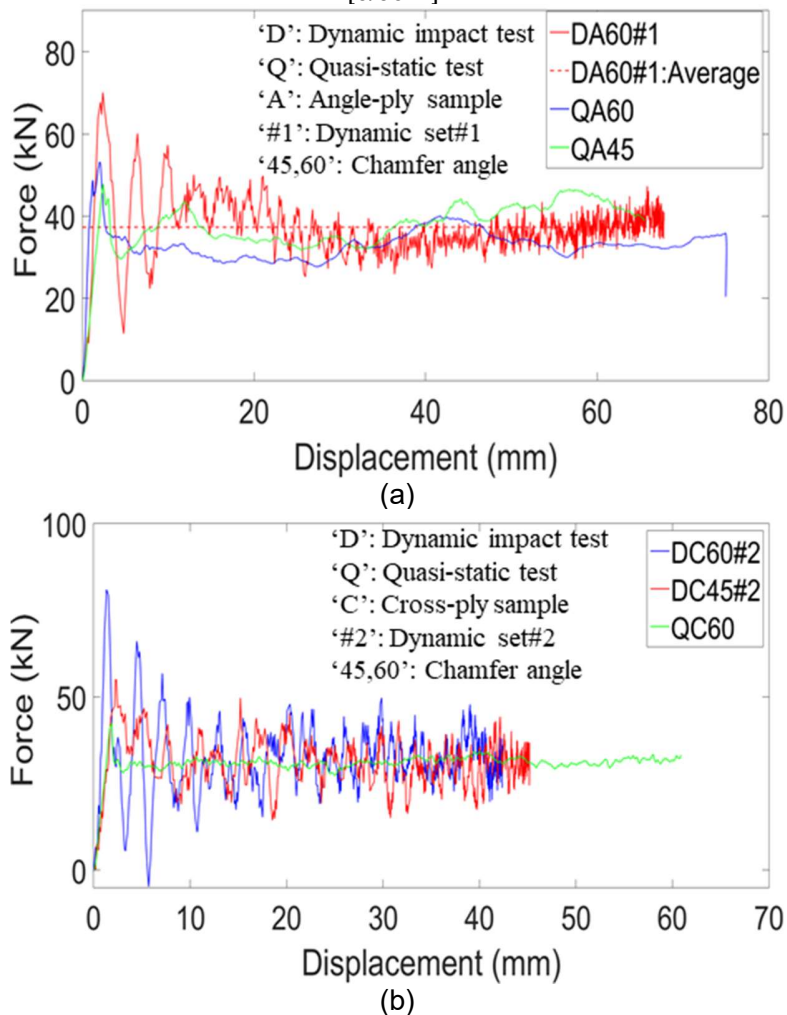
#### 4.3.4.3 Dynamic effects on the force-displacement curves

The force-displacement curves due to impact loading are compared with those due to quasi-static compression of angle-ply and cross-ply specimens in Figures 4.13(a) and 4.13(b), respectively. Due to inertia effects, the peak load of specimens under dynamic loading is some 1.5 times the peak load of specimens under quasi-static compression. However, no dynamic effect on the average force of the cross-ply specimens was observed while the dynamic average force characterizing the angle-ply specimen with  $60^\circ$  chamfer is somewhat higher than the quasi-static one.

Figure 4.14 compares the average crushing stress values of all full tube specimens under quasi-static and dynamic compression tests. In general, average crushing stresses of cross-ply specimens are very consistent and different loading conditions (increase in impact velocity and increase/decrease in the mass of the striker) have no significant effects on the value of crushing stresses of these specimens. However, the variation of the average crushing stresses of angle-ply specimens is less consistent. For instance, the average stress values of QA00 and QA45 are about 16% higher than

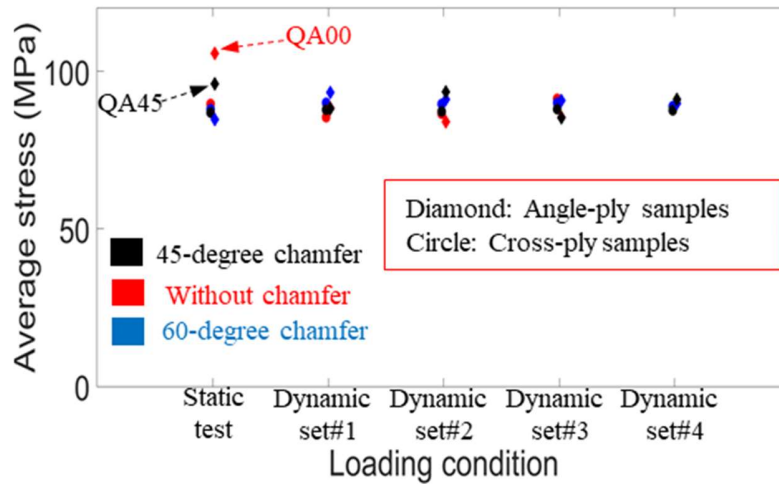
angle-ply specimens with the same chamfer under dynamic tests. On the other hand, the average stress of QA60 is lower than average stress values of angle-ply specimens with 60° chamfer under dynamic compression. The load-bearing before damage initiation was at least two times the load-bearing after damage initiation, see Table 4.2. The load-bearing capacity of the specimens arises from their resistance against moving platen of the test machine, including in-plane and out-of-plane stiffnesses.

Figure 4.13 - Comparison between force-displacement curves of specimens under quasi-static compression and axial impact; (a) Angle-ply specimens, [ $\pm 45/0\dots$ ]; (b) Cross-ply specimens, [ $0/90\dots$ ].



Source: The author.

Figure 4.14 - Comparison between the average stresses of specimens under quasi-static compression and axial impact.



Source: The author.

#### 4.3.5 SEA Value

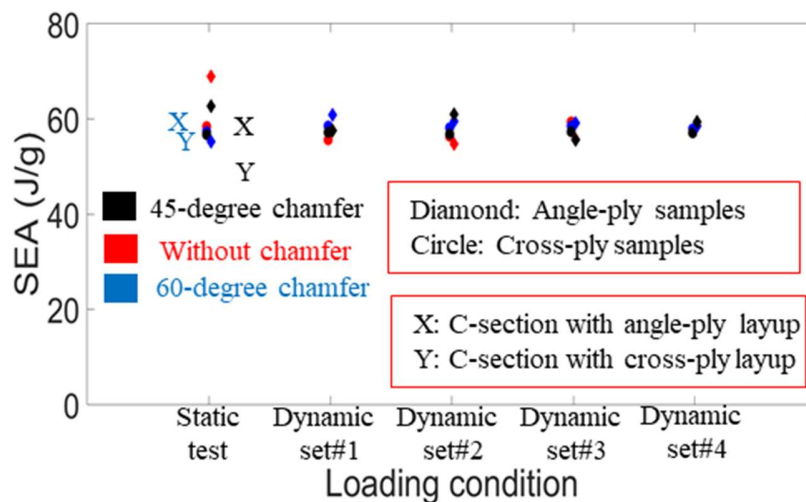
The specific energy absorption, SEA, is the most important crashworthy criterion which ties the energy absorption capacity to the weight of an absorber. Figure 4.15 compares the SEA presented in Tables 4.2 to 4.6. SEA values of the full cross-ply tube specimens are neither sensitive to the impact velocity nor to the increase or decrease of the striker mass (different kinetic energies).

A consistent conclusion regarding the angle-ply tubular specimens cannot be made as the SEA values of QA00 and QA45 are higher than SEA values of the same specimens under different dynamic condition sets. A dependency of the quasi-static SEA values on the external chamfer angle have been observed when the highest SAE value was obtained for the specimens without chamfer (QA00) while the lowest SEA values were found for specimens with 60° chamfer (QA60).

Table 4.2 and Figure 4.15 show that the division of the full tube specimens into two C-shape halves leads to different effects on the SEA values for cross-ply and angle-ply specimens. The SEA value of angle-ply C-section specimens are 5% higher than SEA

values for full tube angle-ply specimens with 60° while it is 5% lower for specimens with 45° chamfers. However, The SEA values of C-section cross-ply specimens are 21% and 16% lower than the SEA values of full tube cross-ply with 45° and 60° external chamfers, respectively. The SEA values of C-section cross-ply specimens are obviously lower than the SEA values of the C-section angle-ply specimens. It is clear that the open section angle-play specimens are more effective in terms of energy absorption in comparison with the open section cross-play specimens.

Figure 4.15 - The comparison between SEA values under different loading rates and conditions.



Source: The author.

#### 4.3.6 Effects of the loading rate

Based on the presented results, it can be concluded that the crashworthy assessment parameters SEA and average crushing force of the examined cross-play and angle-play tubes are not sensitive to the loading rate (Figure 4.15). 'The fiber-dominated nature of the material response' was quoted in the previous publications to justify the strain rate independency of the crushing behavior of carbon fiber material. For instance, Chiu et al. (Chiu et al. 2015) reached this conclusion for unidirectional Hexcel HexPly T700/M21

carbon–epoxy prepreg with a  $[0/90/0/90]_s$  layup. However, it was observed in the present study that the inner and outer  $0^\circ$  layers in cross-ply layup  $[0/(90)_2/0]_s$  specimens failed and split due to matrix failure, which did not have a significant effect on crushing performance, Figure 4.7(b). Thus, it is possible to consider  $[(90)_2/0]_s$  as an effective equivalent instead of the whole  $[0/(90)_2/0]_s$  unit, in which, the majority of its fibers (75%) are oriented at  $90^\circ$ . As it is shown in Figure 4.7(a), the matrix failure contributes significantly to the overall damage response of the cross-ply specimens. It is interesting also to note that the middle layer of this specimen type experienced more fiber breakage under impact than under a quasi-static compression as shown in Figures 4.6(a) and 4.6(b).

The crushed zones of the angle-ply specimens due to quasi-static compression and impact presented in Figure 4.4(a) and 4.4(b) depict different fiber breakage pattern caused by the different loading conditions but nevertheless, the overall response of the angle-ply specimens does not exhibit sensitivity to the loading rate. Obviously, a further study is necessary to carry out in order to understand the cause of the seemingly inertia insensitivity of the analyzed tubes.

#### 4.4 Summary

In this chapter, full circular and C-shape cylindrical sections were tested under quasi-static compression and impact loading to investigate the effects of open/closed cross-sections, layup configuration and loading condition on the energy absorption performance of carbon fiber-epoxy tubes. Four different combinations of striker's mass and velocity were considered to impact tubes with different loading rates or kinetic energies.

It was observed that the effect of different layup configurations on the SEA value is more significant for open C-shape sections than for full circular cylinders, as the difference between SEA values were more distinct between cross-ply and angle-ply C-shape specimens. Considerably lower SEA values of the C-shape sections were obtained in comparison with the corresponding value of the full cross-ply tubes.

The different combinations of mass and velocity of the striker used in the impact tests had no significant effect on crushing behavior of both layups. Moreover, the cross-

ply and angle-ply specimens showed a clear strain rate independency for moderate impact velocities.

The UD laminae strength in transverse to fiber direction as well as the resistance of the laminated structure to delamination are highly dictated by the resin strength. The load-bearing contribution of the one-side constrained axially-loaded UD layers, for instance, the outermost  $0^\circ$  layer in the cross-ply tube, was found to be negligible, as the delamination of this layer develops faster in the analyzed carbon fiber – epoxy system thus leading to an extreme reduction of the layer load-carrying capacity. Therefore, adding this one-side constrained layer to a laminated axial energy absorber would only increase its overall weight and eventually decrease the SEA value. By contrary, the load-bearing of the  $[(90)_2/0]_s$  configuration was very significant and somewhat predictable with using Euler buckling formula for clamped-free lamina bundle. This finding emphasizes the importance of optimal layup configuration in the absorbers design. It was obtained that the energy absorbed by  $0^\circ$  layer in the middle of  $[(90)_2/0]_s$  layers of cross-ply specimens, due to buckling and kinking of this layer, is about 35% of the total absorbed energy during quasi-static compression. The remaining energy is absorbed by the damage mechanisms in other layers and matrix as well as friction, but these parts have not been calculated in the present study.

## 5 Description of the multi-layer FE model

This chapter aims to investigate the performance of the conventional shell element (S4R) to model intra-ply (lamina) behavior of laminated tubular absorber undergoing axial compressive load. In-built progressive failure analysis (PFA) based on Hashin's criteria will be used to model intra-laminar behavior of composite laminae. Instead of using the mainstream bonding techniques, element-based cohesive zone (CZE) and surface-based cohesive zone (CZS) available in Abaqus, here each two adjacent shell layers are tied together. Instead of tying the adjacent laminae directly, a thin layer of conventional shell elements with isotropic mechanical behavior was inserted between two laminae and laminae were tied to this thin isotropic layer. A suitable built-in progressive failure model, available in Abaqus material library, will be assigned to the resin layers to represent the interface behavior in the laminated tube.

### 5.1 Intra- and inter-laminar modeling in the literature

Since the laminae are likely to undergo significant bending deformation under impact loading, the candidate element for modeling these laminae should be capable of capturing bending correctly. Thus, mid-surface shell elements with 6 DOFs (three rotational and three translational DoFs at each node) are promising candidates to model the intra-ply behavior. However, based on the review presented in Chapter 2, it has been observed that shell element with the mid-surface formulation (S4R) in Abaqus has been rarely considered (Zhao et al. 2019; Zhu et al. 2018) to establish multi-layer FE mode of laminated absorbers under impact loading. Notably, the mid-surface shell element in LS-Dyna has been widely used to simulate the multi-layer composite parts under axial impact (Morthorst and Horst 2004; Mamalis et al. 2006; Siromani, Awerbuch, and Tan 2014; Reuter, Sauerland, and Tröster 2017; Huang and Wang 2009; McGregor, Vaziri, and Xiao 2010; McGregor et al. 2017).

The interface thickness in laminated composites is negligible, so tiebreak in LS-Dyna and surface-based cohesive model (CZS) in Abaqus are the ideal techniques to bond the adjacent laminae together. No extra elements are required to represent the interface layer; thus, the finite element model would be computationally more efficient. Tiebreak interaction has been predominantly utilized to bond the mid-surface shell

elements in LS-Dyna to model multi-layer composite absorbers under axial impact. However, very few successful multi-layer models with using CZS and conventional shell element (S4R ) have been simulated in Abaqus (Dlugosch et al. 2017). The CZS technique is based on a master-slave contact algorithm; thus, results depend on the contact behavior of the bonded elements. For laminate composite under compressive loading, a contact problem arises which leads to large and physically unrealistic delamination causing eventually a premature structural instability predicted by the model (Bogenfeld, Kreikemeier, and Wille 2018). This phenomenon is well observed for conventional shell element (S4R or S4) under compressive load due to a poor contact response of these elements. Therefore simulations that used the S4R element together with the CZS in Abaqus has been seldom reported for structures undergoing axial compressive loading. Few researchers (Zhu et al. 2018; Zhao et al. 2019) tied the S4R elements with using element-based cohesive zone model (CZE) in Abaqus to model laminated tubes under axial impact. However, the CZE requires extra continuum elements to represent the interface between laminae and its implementation is less straightforward rather than CZS model. The limited application of the S4R element in Abaqus to model multi-layer structure under dynamic impact can be related to the issues mentioned above.

Continuum shell element (SC8R) and conventional shell element (S4R) have a similar formulation (Dassault Systèmes Simulia 2014); however, the continuum shell element discretizes the whole continuum body and has better contact behavior. Therefore, models comprise of continuum shell and the CZS bonding technique have shown a more stable response under axial compression rather than S4R element (Bogenfeld, Kreikemeier, and Wille 2018). This issue can be related to the better contact behavior of the continuum element rather than the mid-surface element. Thus continuum shell has been used to model multi-layer laminated absorbers under the axial impact (Palanivelu et al. 2010; Sokolinsky, Indermuehle, and Hurtado 2011; Zhu Yigang, Wang Jin, and Zhang Zilong 2012; Patel, Vusa, and Guedes Soares 2019). Although the continuum shell elements can be used for any thickness, thin continuum shell elements may result in a small stable time increment in Abaqus/Explicit since the stable time increment can be controlled by the continuum shell element thickness, particularly for thin shell applications (Dassault Systèmes Simulia 2014) (like

composite laminae). This issue may increase significantly the number of increments taken to complete the analysis when compared to the same problem modeled with conventional shell elements (Dassault Systèmes Simulia 2014).

It is also possible to incorporate three-dimensional brick solid elements with one layer of bricks representing a ply of composite material. However, it would be costly to run such a model if the lay-up had more than a few plies. Moreover, to improve the bending behavior of a single lamina of solid element should have more than one element through the thickness direction (Matthews et al. 2000). For example, Chiu et al. (Chiu et al. 2015, 2016) and Tan et al. (Tan, Falzon, and Price 2015; Tan et al. 2016) have used solid element to represent composite ply. Each layer has three solid elements through the thickness, to improve the bending behavior of solid element. Such a model for a relatively large energy absorber with an approximate thickness equals to 2 mm is computationally inefficient. In theory, the technique of layering brick elements through the thickness of the relatively thin plate or shell leads to very ill-conditioned sets of equations (Matthews et al. 2000). Three-dimensional solid element is more suitable where the composite lay-up is thick, and the geometry is more solid than shell-like or when a 3D stress field analysis in the material is required. It is important to note that in the most publications relevant to the axial impact of composite absorbers, the global response, in terms of force-displacement characteristic without going to detailed stress analysis, gives sufficient information about the structural performance. Therefore, elements with mid-surface formulation are more suitable than using the three-dimensional element for this kind of simulation.

## **5.2 General description of the proposed multi-layer model of laminated specimens**

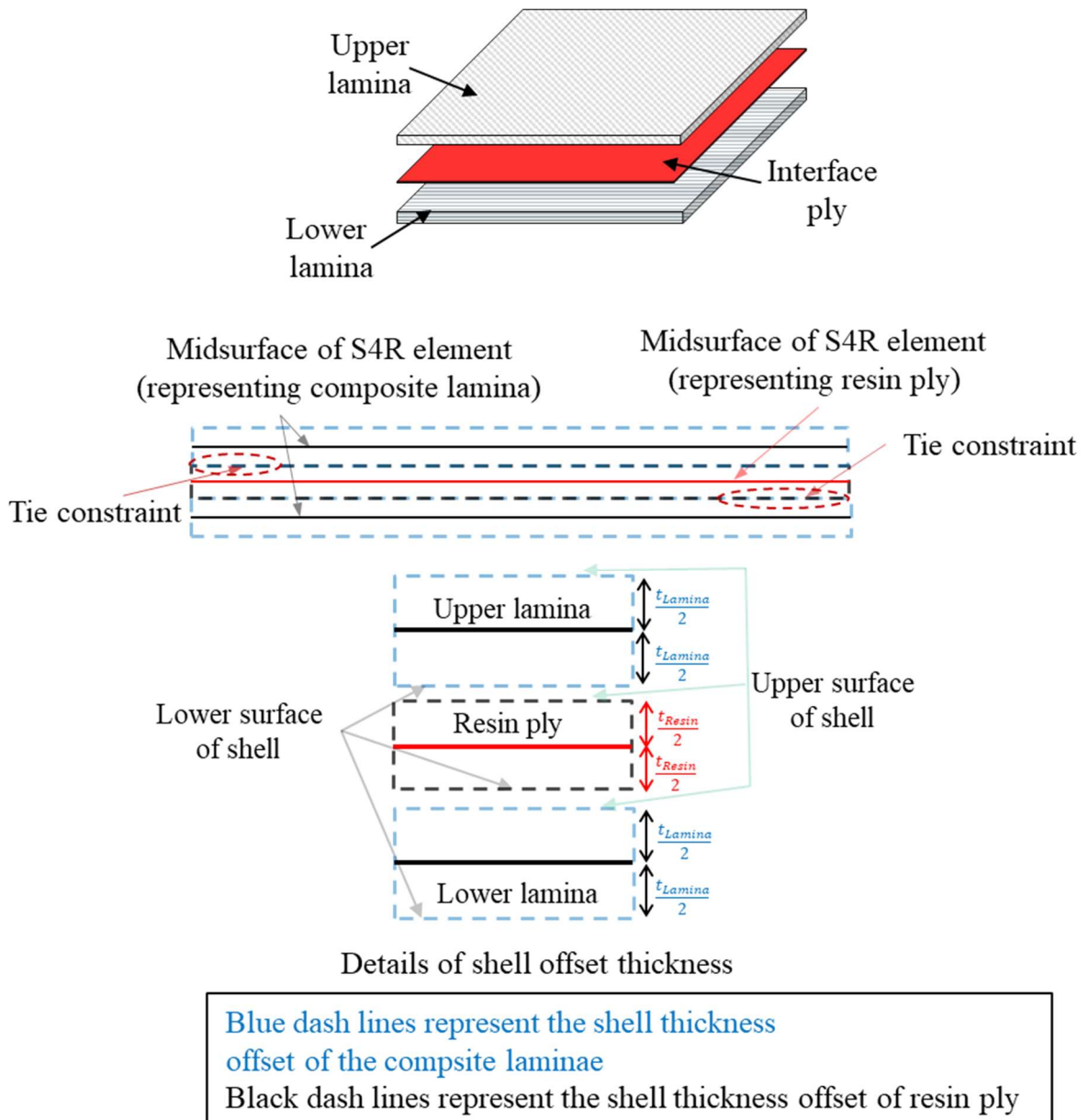
Figure 5.1 shows a general overview of stacking and layers connectivity for the multi-layer specimens in the present study. Between two adjacent composite laminae, a ply with resin mechanical properties was inserted. Surface to surface discretization method is used to tie resin plies to composite laminae. The composite laminae and resin plies are considered as master-surface and slave-surfaces, respectively. In Abaqus/Explicit, by default, shell offset thicknesses are considered for in contact constraints of the conventional shell (S4 element). Therefore, the resin's upper/ lower

surfaces were tied to the corresponding upper/lower surfaces of the adjacent laminae shell offset. To control the quality of the tie interaction between composite laminae and resin plies, besides mechanical properties of resin material, it is possible to adjust 'tie rotational DoFs' in constraint edit module.

Reduced integrated conventional shell element (S4R) is utilized to discretize both composite laminae and resin plies. Reduced integration facilitates material degradation through a CDM model, while a fully integrated element is more likely to experience severe distortion and eventually causes instability in explicit simulation (Bogenfeld, Kreikemeier, and Wille 2018). Hour-glassing is possible to occur in reduced integrated elements (Dassault Systèmes Simulia 2014), so enhanced hourglass control will be used.

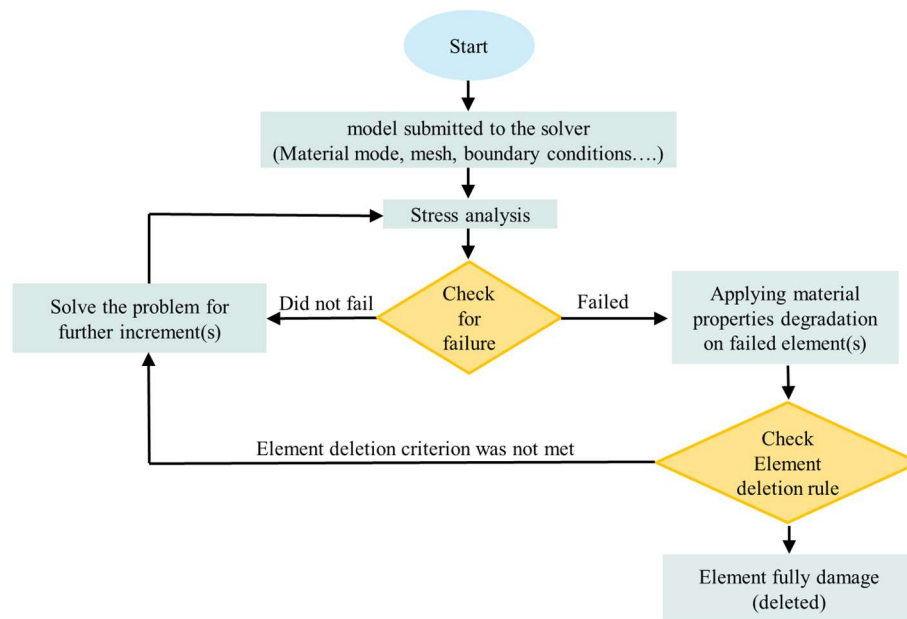
Plane stress Progressive Failure Analysis (PFA) in Abaqus/Explicit was utilized to model successive damaging mechanisms in UD composite laminae and also isotropic resin plies. Progressive failure analysis for fiber-reinforced materials is utilized to model the intra-laminar behavior of composite laminae. Progressive failure analysis for isotropic materials in Abaqus library is used to model interface behavior. Figure 5.2 shows a general flowchart of progressive failure analysis.

Figure 5.1 - A general overview of the multi-layer approach in the present study.



Source: The author.

Figure 5.2 - Progressive failure analysis flowchart.



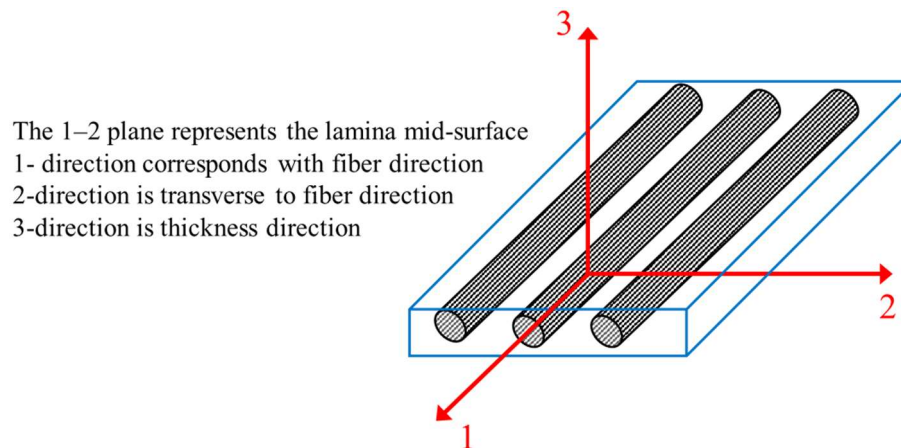
Source: The author.

### 5.3 In-plane Progressive failure analysis of fiber-reinforced composites in Abaqus

Although several three-dimensional constitutive models (Donadon et al. 2008; Chiu et al. 2015; Tan et al. 2016; Tan, Falzon, and Price 2015) have been introduced for composite material yet, here the progressive damage failure analysis base on plane stress state in Abaqus will be used to model intra-laminar behavior of composite material.

Abaqus contains several damage models to simulate progressive failure crushing in different materials. For anisotropic composite material with elastic-brittle nature also a damage model is provided to predict the damage initiation and damage evolution based on MLT continuum damage model presented by Matzenmiller et al. (Matzenmiller, Lubliner, and Taylor 1995). The model is suitable for fiber-reinforced materials like unidirectional (UD) lamina, as depicted in Figure 5.3.

Figure 5.3 - A unidirectional lamina and its local coordinate system.



Source: The author.

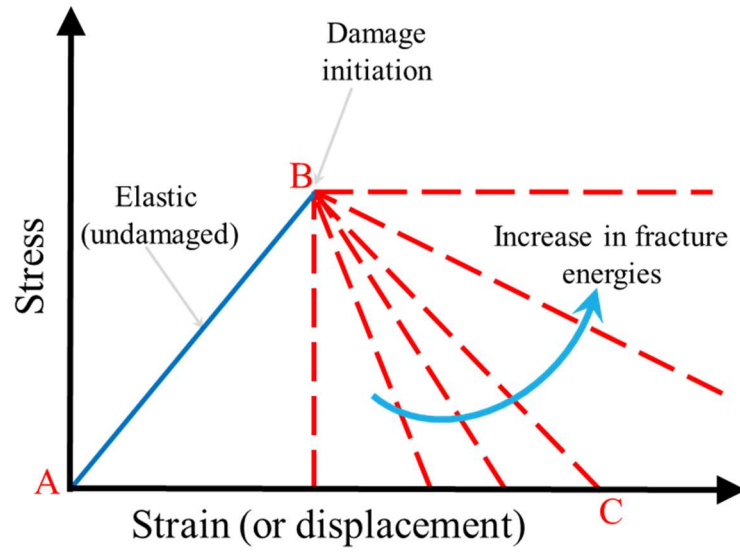
Here a bilinear stress-strain curve represents the material behavior, Figure 5.4. This model has three main features:

- Linear elastic response of material up to damage(s) initiation, ('AB')
- Mode-based damage initiation criteria, ('B')
- Gradual energy-based damage evolution scheme based on CDM, ('BC')

The progressive failure mode for fiber-reinforced composite materials considers four distinct failure modes (uses mode-based failure criteria). For each mode, a bilinear stress-strain curve (Figure 5.4) should be considered. These four failure modes are as follows.

- I. Fiber rupture under tension,
- II. Fiber buckling and kinking under compression,
- III. Matrix cracking under transverse to the fiber tension and shearing, and
- IV. Matrix crushing under transverse compression and shearing

Figure 5.4 - The typical bilinear response of composite material.



Source: The author.

The response of a UD lamina in plane stress condition can be expressed by Eq. 5.1, which represents undamaged-damaged behavior of orthotropic material (Dassault Systèmes Simulia 2014).

$$\sigma = C_d \varepsilon \quad (5.1)$$

where  $\varepsilon$  denotes the strain,  $\sigma$  is true stress, and  $C_d$  is the elasticity matrix of an orthotropic material in a 2D plane stress state. The elasticity matrix ( $C_d$ ) and its parameters can be written in the following forms (Dassault Systèmes Simulia 2014).

$$C_d = \frac{1}{D} \begin{bmatrix} (1-d_1)E_1 & (1-d_2)(1-d_1)E_1\nu_{21} & 0 \\ (1-d_2)(1-d_1)E_2\nu_{12} & (1-d_2)E_2 & 0 \\ 0 & 0 & (1-d_s)G_{12}D \end{bmatrix} \quad (5.2)$$

$$D = 1 - (1-d_1)(1-d_2)\nu_{21}\nu_{12} \quad (5.2(b))$$

$$d_s = 1 - (1 - d_1^c)(1 - d_1^t)(1 - d_2^c)(1 - d_2^t) \quad 5.2(c)$$

where  $d_s$ ,  $d_1$ ,  $d_2$  represent the current state of damage in shear mode, 1-direction and 2-direction, respectively. These three state variables should be calculated from four damage variables  $d_i^j$  in the 1- and 2-directions ( $i = 1, 2$ ) under compression or tension ( $j = c, t$ )<sup>1</sup>.

Before damage(s) initiation ( $D = 1 - \nu_{21}\nu_{12}$  and  $ds = d_1 = d_2 = 0$ ) Eq. 1 represents the linear elastic behavior of an orthotropic material having elastic moduli,  $E_i$ , shear modulus  $G_{ij}$  and Poisson's ratios,  $\nu_{ij}$  ( $i = 1, 2$  and  $j = 1, 2$ ).

Matzenmiller et al. (Matzenmiller, Lubliner, and Taylor 1995) considered Hashin's criteria to predict the damage initiation since assumed the four failure modes above mentioned. Thus, damage initiation(s) in the progressive failure analysis of fiber-reinforced material in Abaqus is based on criteria proposed by Hashin-Rotem (Hashin and Rotem 1973) and Hashin (Hashin 1980). In Abaqus, this damage model must be assigned to elements having plane stress formulation, including conventional shell, continuum shell, and membrane elements. Hashin's criterion for four failure modes in-plane stress condition given by

$$\begin{aligned} &\text{Tensile fiber} \\ &(\sigma_{11} > 0) \end{aligned} \quad \left( \frac{\hat{\sigma}_{11}}{X^T} \right)^2 + \left( \frac{\hat{\sigma}_{12}}{S^L} \right)^2 = 1 \quad (5.3)$$

$$\begin{aligned} &\text{Compressive fiber} \\ &(\sigma_{11} < 0) \end{aligned} \quad \left( \frac{\hat{\sigma}_{11}}{X^C} \right)^2 = 1 \quad (5.4)$$

---

<sup>1</sup> Subscripts 1 and 2 in Abaqus Analysis User's manual are presented by  $f$  (fiber direction) and  $m$  (matrix direction), respectively.

$$\begin{array}{l} \text{Tensile matrix} \\ (\sigma_{22} > 0) \end{array} \quad \left( \frac{\hat{\sigma}_{22}}{Y^T} \right)^2 + \left( \frac{\hat{\sigma}_{12}}{S^L} \right)^2 = 1 \quad (5.5)$$

$$\begin{array}{l} \text{Compressive} \\ \text{matrix } (\sigma_{22} < 0) \end{array} \quad \left( \frac{\hat{\sigma}_{22}}{2S^T} \right)^2 + \left[ \left( \frac{Y^C}{2S^T} \right)^2 - 1 \right] \left( \frac{\hat{\sigma}_{22}}{Y^C} \right) + \left( \frac{\hat{\sigma}_{12}}{S^L} \right)^2 = 1 \quad (5.6)$$

where stress components ( $\hat{\sigma}$ ) are effective stresses. A damage operator ( $M$ ) relates the effective stress tensor ( $\hat{\sigma}$ ) to true the stress tensor ( $\sigma$ ), as expressed by Eq. 5.7.

$$\hat{\sigma} = M\sigma \quad 5.7(a)$$

$$M = \begin{bmatrix} \frac{1}{(1-d_1)} & 0 & 0 \\ 0 & \frac{1}{(1-d_2)} & 0 \\ 0 & 0 & \frac{1}{(1-d_3)} \end{bmatrix} \quad 5.7(b) \quad (5.7)$$

The damage operator ( $M$ ) is an identity matrix before damage(s) initiation. Thus, effective and true stresses are equal,  $\hat{\sigma} = \sigma$ . Once at least on damage mode has occurred, the damage operator ( $M$ ) will change, and eventually, the effective stress and true stress are not equal anymore.

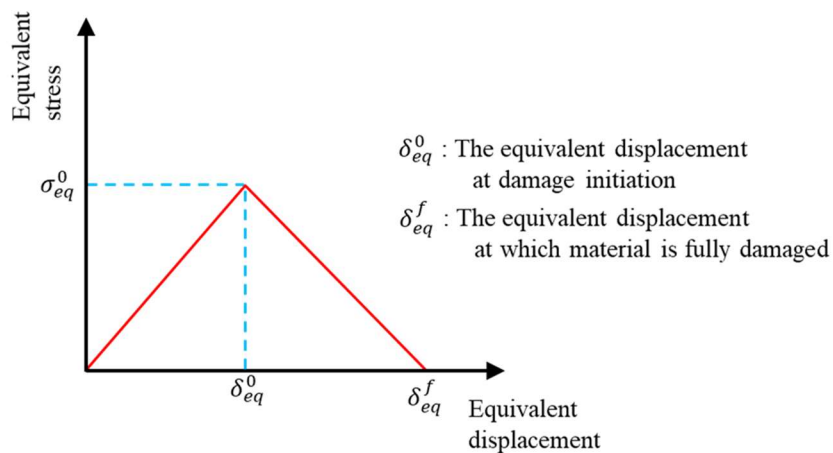
Besides four independent elastic parameters including elastic moduli and major Poisson's ratio, six strength parameters should be provided in order to define the threshold of the undamaged elastic region (from point 'A' to point 'B'). These required strength parameters for a UD lamina are introduced in Table 5.1.

Table 5.1 - Required in-plane material properties to represent the undamaged response of the model for fiber-reinforced materials in Abaqus.

Parameter	direction	Symbol
Tensile strength	Fiber direction	$X^T$
	Transverse to the fiber direction	$Y^T$
Compressive strength	Fiber direction	$X^C$
	Transverse to the fiber direction	$Y^C$
Shear strength	Longitudinal	$S^L$
	Transverse	$S^T$

The 'BC' path (Figure 5.4) represents the post-damage behavior of the material. Once a failure criterion is satisfied, the corresponding damage variables will gradually change from zero to one ( $d = 0 \rightarrow 1$ ) during material softening. Since the material softening is mesh sensitive, a characteristic length ( $L^c$ ) is introduced by Abaqus to alleviate the mesh dependency during material evolution (Dassault Systèmes Simulia 2014). For shell elements, this characteristic length is computed as the square root of the element area. By using this characteristic length, the constitutive law is expressed as an equivalent stress-displacement relation instead of stress-strain one, as depicted by Figure 5.5.

Figure 5.5 - Equivalent stress-displacement curve for a fiber-reinforced material in Abaqus progressive failure analysis.



Source: The author.

The elastic parameters, elastic moduli, and failure stress parameters control the value of equivalent displacement ( $\delta_{eq}^0$ ) at damage initiation for each damage mode. For each of the damage mode mentioned above, equivalent stress and displacement are defined as below.

$$\begin{aligned} \delta_{eq}^{ft} &= L^c \sqrt{\langle \varepsilon_{11} \rangle^2 + \varepsilon_{12}^2} \\ \text{Fiber tension} & \\ (\hat{\sigma}_{11} \geq 0) & \quad \sigma_{eq}^{ft} = \frac{\langle \sigma_{11} \rangle \langle \varepsilon_{11} \rangle + \tau_{12} \varepsilon_{12}}{\delta_{eq}^{ft} / L^c} \end{aligned} \quad 5.8(a)$$

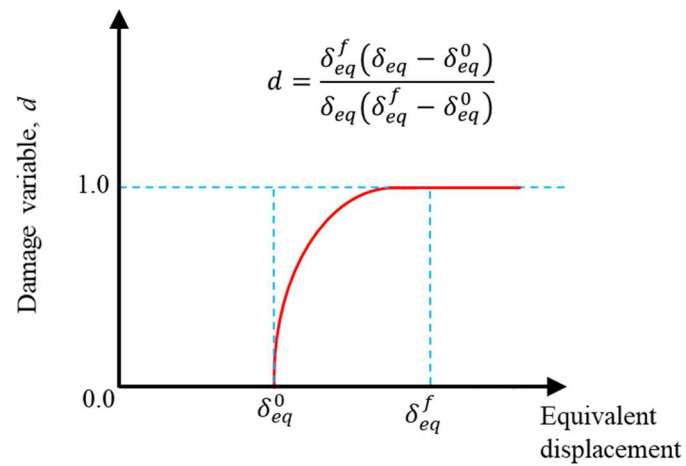
$$\begin{aligned} \delta_{eq}^{fc} &= L^c \langle -\varepsilon_{11} \rangle \\ \text{Fiber} & \\ \text{compression} & \\ (\hat{\sigma}_{11} < 0) & \quad \sigma_{eq}^{fc} = \frac{\langle -\sigma_{11} \rangle \langle -\varepsilon_{11} \rangle}{\delta_{eq}^{fc} / L^c} \end{aligned} \quad 5.8(b)$$

$$\begin{aligned} \delta_{eq}^{mt} &= L^c \sqrt{\langle \varepsilon_{22} \rangle^2 + \varepsilon_{12}^2} \\ \text{Matrix tension} & \\ (\hat{\sigma}_{22} \geq 0) & \quad \sigma_{eq}^{mt} = \frac{\langle \sigma_{22} \rangle \langle \varepsilon_{22} \rangle + \tau_{12} \varepsilon_{12}}{\delta_{eq}^{mt} / L^c} \end{aligned} \quad 5.8(c)$$

$$\begin{aligned} \delta_{eq}^{mc} &= L^c \sqrt{\langle -\varepsilon_{22} \rangle^2 + \varepsilon_{12}^2} \\ \text{Matrix} & \\ \text{compression} & \\ (\hat{\sigma}_{11} < 0) & \quad \sigma_{eq}^{mc} = \frac{\langle -\sigma_{22} \rangle \langle \varepsilon_{22} \rangle + \tau_{12} \varepsilon_{12}}{\delta_{eq}^{mc} / L^c} \end{aligned} \quad 5.8(d)$$

For a specific failure mode, the damage variable will evolve like that presented in Figure 5.6. All four failure modes have the same damage evolution with different input parameters.

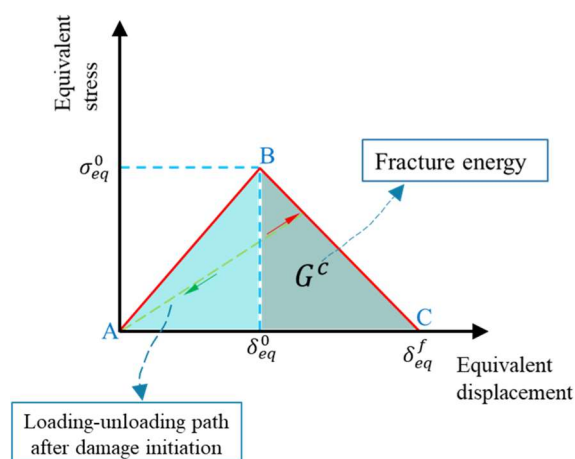
Figure 5.6 - Evolution of damage variable for a specific failure mode.



Source: The author.

In contrast to equivalent displacement corresponding to damage initiation point ( $\delta_{eq}^0$ ), the value of equivalent displacement corresponding to the total failure ( $\delta_{eq}^f$ ) for each specific failure mode depends on corresponding fracture energy ( $G^C$ ). The fracture energy (for each mode) should be calculated from area under 'ABC' triangle of the equivalent stress-displacement curve for the corresponding failure mode, see Figure 5.7.

Figure 5.7 - Equivalent stress-displacement curve and fracture energy.



Source: The author.

The area under triangle 'ABC' can be divided into the areas of two triangles with different color as depicted in Figure 5.7. The area under triangle in light green depends only on elastic properties and strengths of material in the corresponding failure mode, since the value of the  $\delta_{eq}^0$  depends only on the elastic properties and strengths of the material. However, the value of  $\delta_{eq}^f$  depends on the input value of fracture energy  $G^c$  ( $G^c$  is equal to total area under ABC triangle).

Four fracture energies must be provided into the progressive failure analysis of fiber-reinforced material in Abaqus,  $G_{ft}^c$ ,  $G_{fc}^c$ ,  $G_{mt}^c$  and  $G_{mc}^c$ . These fracture energies are dissipated energies during fracture at four failure modes mentioned previously. Table 5.2 lists these fracture energies.

Table 5.2 - Required fracture energies in the progressive failure analysis of fiber-reinforced composite in Abaqus.

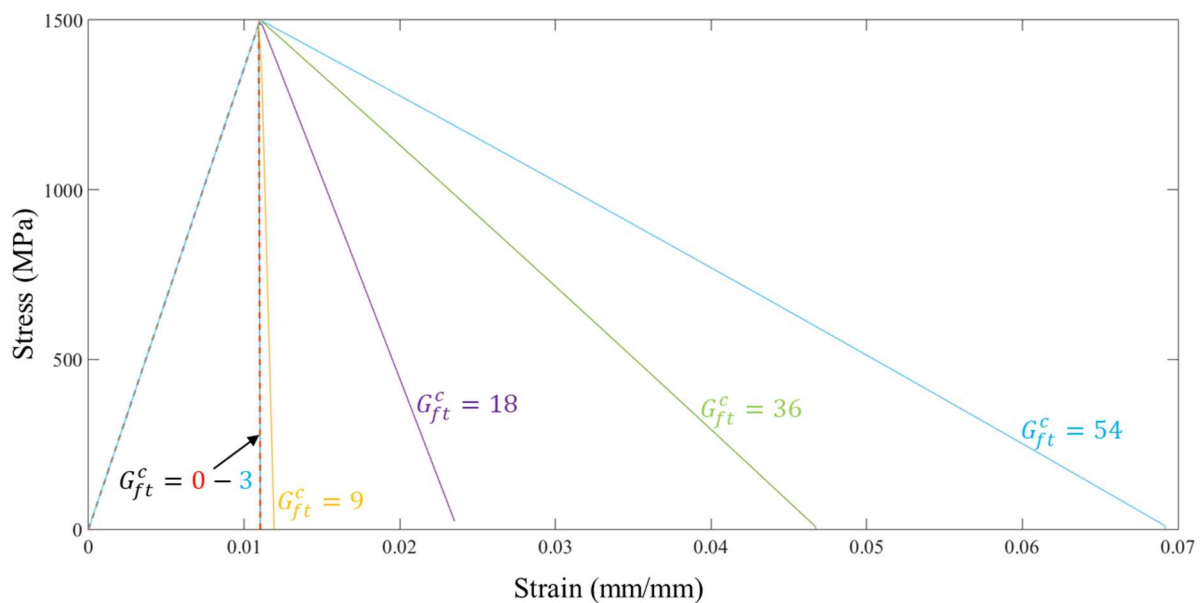
Fracture energy	loading	Symbol	Calculation
1-direction*	Tension	$G_{ft}^c$	The area under the equivalent stress-displacement curve for tension parallel to the fiber direction
	Compression	$G_{fc}^c$	The area under the equivalent stress-displacement curve for compression parallel to the fiber direction
2-direction*	Tension	$G_{mt}^c$	The area under the equivalent stress-displacement curve for tension transverse to the fiber direction
	Compression	$G_{mc}^c$	The area under the equivalent stress-displacement curve for compression transverse to the fiber direction

\* 1- and 2-directions are parallel and transverse to the fiber direction, respectively.

Figure 5.8 shows the stress-strain curves of a UD lamina under tensile load on a single conventional shell element (S4R) in Abaqus for different values of tensile fracture energy in the fiber direction ( $G_{ft}^c$ ). It is evident that the value of fracture energy

has no effect on the value of stress and strain up to the damage initiation point, on the contrary, the values of strain after damage initiation point depend on the value of fracture energy. Thus with an increase in the fracture energy, the maximum bearing load remains constant; however, the load-bearing capacity decreased with a less acute slope after damage initiation. In other word maximum load (stress) will be carried by the element for a longer time (higher strain).

Figure 5.8 - Effect of fracture energy in the fiber direction on the stress-strain curve of a single S4R element under axial tension, parallel to the fiber direction.



Source: The author.

Compact Tension (CT) and Compact Compression (CC) tests have been used to determine fiber-dominant fracture energies of the composite material by several researchers (Pinho, Robinson, and Iannucci 2006; Jose et al. 2001). These testing methods are originally proposed for metals as described in ASTM E399 and E1820, even though, several researchers used these methods to find intralaminar fracture energies as inputs data for simulating axial crushing of composite absorbers (Tan et al. 2016; McGregor et al. 2017). In Abaqus User's manual (Dassault Systèmes Simulia 2014), it is written that fracture energy values 'must be provided by the user by calculating the area under the equivalent stress-displacement curves of uniaxial

tension/compression tests, 'ABC' triangle in Figure 5.7. However, no definite limit for equivalent failure displacement ( $\delta_{eq}^f$ ) is mentioned in Abaqus manual.

In Appendix D, the value of fracture energies for investigation on the crushing behavior of composite absorbers under axial loading and lateral impact on laminated plates are presented. The values of fracture energies are reported by Chiu et al. (Chiu et al. 2016) and used as input parameters in a 3D material model to analyze the axial impact on the composite absorber. Here, the elastic energy (energy absorbed up to damage initiation point) is used as a benchmark to compare the fracture energies. The fracture energies in other references related to axial compression on composite absorbers are in the same range as those presented in Appendix D.

Matrix-dominated fracture energies (the transverse to fiber direction) are usually considered very low in the literature, even lower than expected energies up to damage initiation. Fracture energies, lower than elastic energy up to damage, will be ignored by Abaqus. Thus, once damage initiation occurred, the load will drop to zero instantaneously. Another point is about high fracture energies in the fiber direction. These high values (usually five times than the elastic energy) increase the load-bearing capacity of composite components. It means the final strain of FEs in the model is larger than the experimentally measured failure strain. Also, there is some contradiction about reported fracture energies; for instance, for the same composite material Shi et al. (Shi, Pinna, and Soutis 2016) used 91.60 (N/mm) and 79.9 (N/mm) while Zhang (Zhang, Duodu, and Gu 2017) used 10 (N/mm) and 10 (N/mm) for fracture energies in the fiber direction.

The last part of progressive failure analysis for fiber-reinforced materials, point 'C' in Figure 5.4, is the element deletion option. This feature controls the way Abaqus treats severely damaged elements. Section controls are provided to specify the value of the maximum stiffness degradation  $D_{max}$  (default equals one) and whether element deletion occurs when the degradation reaches this level. By default, an element will be deleted when it is fully damaged, i.e.,  $D = D_{max}$ ; however, it is possible to disable the element deletion control.

## 5.4 Inter-lamina modeling

### 5.4.1 Inter-lamina modeling: Cohesive Element

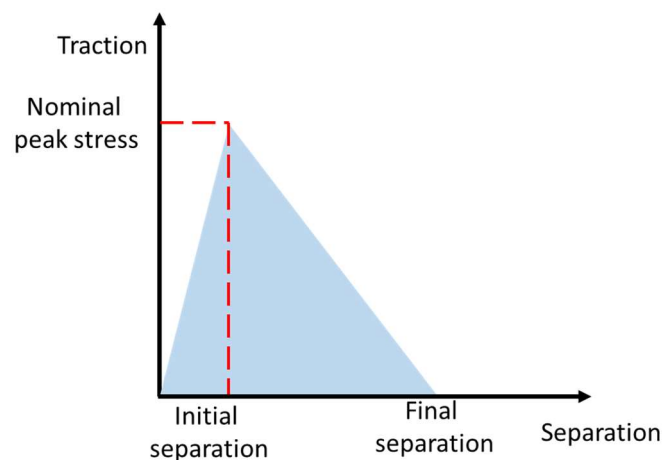
The cohesive element based upon the bilinear traction-separation law in terms of damage criteria and damage evolution will be used to bond adjacent composite laminae. Thus the cohesive model has a linear elastic response before delamination. Eq. 5.9 represents the uncoupled normal and shear traction components in the elastic region.

$$t = \begin{Bmatrix} t_n \\ t_s \\ t_t \end{Bmatrix} = \begin{bmatrix} k_n & 0 & 0 \\ 0 & k_t & 0 \\ 0 & 0 & k_s \end{bmatrix} \begin{Bmatrix} \epsilon_n \\ \epsilon_t \\ \epsilon_s \end{Bmatrix} \quad (5.9)$$

The nominal traction stress vector,  $t$ , consists of three components (two components  $t_n$ ,  $t_s$ , and  $t_t$ , which represent the normal and the two shear tractions, respectively).

Damage of the traction-separation response is defined within the same general framework used for conventional materials (progressive failure of material). This response includes; (I) a damage initiation criterion, (II) a damage evolution law, and (III) a choice of element removal (or deletion) upon reaching a completely damaged state. Once damage initiation criterion is reached, material damage can occur according to a damage evolution law, as Figure 5.9 presents a typical traction-separation response with failure mechanism.

Figure 5.9 – Typical traction-separation response including linear elastic, damage initiation and material degradation.



Source: (Dassault Systèmes Simulia 2014)

Several damage initiation criteria are available and are discussed below, e.g., quadratic nominal stress criterion as expressed by Eq. 5.10. Once the criterion reached value 1.0 the degradation properties will start.

$$\left\{ \frac{\langle t_n \rangle}{t_n^0} \right\}^2 + \left\{ \frac{t_t}{t_t^0} \right\}^2 + \left\{ \frac{t_s}{t_s^0} \right\}^2 = 1 \quad (5.10)$$

where  $t_n^0, t_t^0, t_s^0$  represent the peak values of the nominal stresses in pure normal and shear directions.

After damage initiation, the damage evolution law dictates the material stiffness degradation by introducing Scalar damage variable,  $D$ .

$$t_n = \begin{cases} (1 - D)\bar{t}_n, & \bar{t}_n \geq 0 \\ \bar{t}_n, & \text{otherwise (no damage to compressive stiffness)} \end{cases} \quad (5.11)$$

$$t_t = (1 - D)\bar{t}_t$$

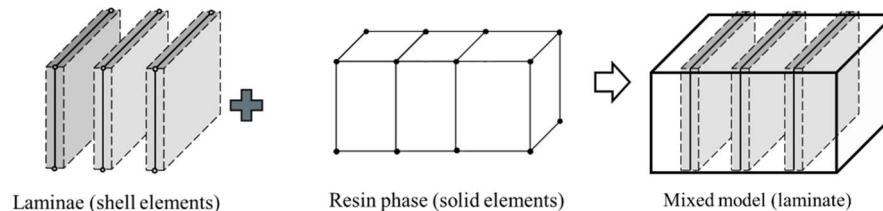
$$t_s = (1 - D)s$$

In the present work cohesive element with quadratic nominal stress criterion and linear energy material stiffness degradation will be used in the new section.

#### 5.4.2 Inter-lamina modeling: Isotropic resin plies

Morthorst and Horst (Morthorst and Horst 2004) used a model that consists of multi-shell layers of composite laminae embedded in solid elements having isotropic properties of the matrix material. Figure 5.10 shows the features of their FE model. Except for this model, using the progressive damaging model to represent the interface of the laminated composite under impact loading is very rare.

Figure 5.10 - Using solid resin with isotropic behavior to represent the interface between composite laminae.



Source: The author (Figure regenerated).

Dlugosch (Dlugosch et al. 2017) studied hybrid steel/CFRP absorber under axial compressive load. They used the conventional shell element (S4R) to discretize the CFRP and metal layers. Two approaches were utilized to bond the CFRP layer to steel layer; (I) surface-based cohesive model (CZS) and (II) simple rigid tie constraint between the CFRP and steel layers. However, the rigid tie between two layers never vanishes except when one of the substrates (the weaker one) is fully damaged.

In the present thesis, instead of directly tying two adjacent layers, one layer of conventional shell element (S4R) will be inserted between composite layers (they also are discretized with S4R shell elements), as explained in Figure 5.1. The conventional shell element does not allow the adjacent composite laminae to separate by mode I (opening mode), thus, the separation of layers will be controlled by the in-plane behavior of resin ply.

Available mechanical properties of epoxy resin in the literature will be used as mechanical properties of the interface layers. A progressive failure model (based on CDM) will be assigned to the resin layers that includes three parts; (I) linear elastic (undamaged), (II) damage initiation (i.e., yield criterion) and (III) post damage response and element deletion.

There are two approaches to model polymers yielding; the use of non-linear viscoelasticity and the direct application of metal plasticity (Ward and Sweeney 2012). In the present thesis, the in-built material model for metal plasticity in Abaqus will be

used for resin layers. In contrast to metals, hydrostatic stress can affect polymers yielding (Ward and Sweeney 2012). Therefore, modified criteria that take into account the hydrostatic stress effect on the epoxy resin flow should be considered.

The proposed modeling technique may have a few advantages when compared to the main-stream interface modeling in Abaqus, such as cohesive zone models.

- Mechanical properties of the bulk material, epoxy resin, can be used which makes modeling more straightforward
- Sophisticated testing scheme including DCB, 4ENF, and MMB tests, is required to use mixed-mode cohesive zone models. On the contrary, the proposed method does not require these complicated tests.
- Available data input for cohesive models in the literature should be adjusted for a new material system and laminate. However, the proposed method does not require massive material modification.

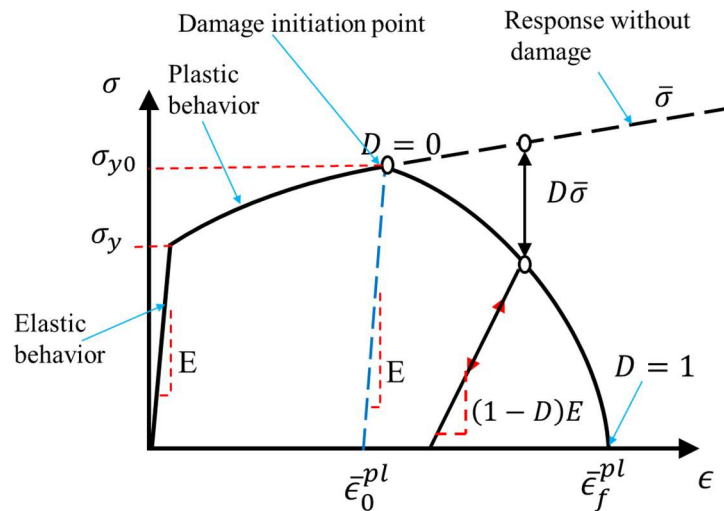
Table 5.3 lists the features of the selected material model (available in Abaqus material library) for the epoxy resin to the model interface layer between composite laminae.

Table 5.3 - A general overview of the material model for epoxy resin in the present thesis.

<b>Material model parts</b>	<b>Description</b>	<b>Input data</b>
Undamaged response	Elastic (isotropic behavior)	➤ Elastic modulus ➤ Poisson's ratio
Damage initiation criterion	Ductile damage criterion + Isotropic plastic hardening	➤ Tabular yield stress - plastic strain ➤ Triaxiality
Post-damage response	Damage evolution	➤ Linear fracture energy

Figure 5.11 illustrates the typical stress-strain response of a material undergoing damage. In the context of an elastic-plastic material with isotropic hardening, the damage manifests itself in two forms; (I) softening of the yield stress and (II) degradation of the elasticity.

Figure 5.11 - Typical stress-strain curve for elastic-plastic behavior.



Source: (Dassault Systèmes Simulia 2014).

In the figure  $\sigma_{y0}$  and  $\bar{\epsilon}_0^{pl}$  are the yield stress and equivalent plastic strain at the onset of damage, and  $\bar{\epsilon}_f^{pl}$  is the equivalent plastic strain at failure. However, to alleviate the mesh dependency of softening, plastic strains will be replaced by equivalent displacements ( $\bar{u}^{pl}$  and  $\bar{u}_f^{pl}$ ) using a characteristic length ( $L$ ).

Linear dissipation energy will be selected here to represent the damage evolution. Fracture energy per unit area ( $G_f$ ) will be calculated, and this fracture energy will be dissipated during the damage process directly. Instantaneous failure will occur if  $G_f$  is specified as 0. However, this choice is not recommended and should be used with care because it causes a sudden drop in the stress at the material point that can lead to dynamic instabilities.

Once the damage initiation criterion is met ( $\sigma_{y0}$ ), the damage variable increases according to

$$D = \frac{\bar{u}^{pl}}{\bar{u}_f^{pl}} \quad (5.12)$$

The equivalent plastic displacement at failure ( $\bar{u}_f^{pl}$ ) will be calculated via

$$\bar{u}_f^{pl} = \frac{2G_f}{\sigma_{y0}} \quad (5.13)$$

where the material parameter ( $\sigma_{y0}$ ) is the yield stress of resin material.

The fracture energy per unit area ( $G_f$ ) can be calculated by

$$G_f = \int_{\bar{\epsilon}_0^{pl}}^{\bar{\epsilon}_f^{pl}} L\sigma_y d\bar{\epsilon}^{pl} = \int_0^{\bar{u}_f^{pl}} \sigma_y d\bar{u}^{pl} \quad (5.14)$$

## 5.5 Summary

In this chapter intra- and inter-laminar modeling procedures were described to develop a multi-layer model of laminated structures. Two-dimensional progressive failure of fiber-reinforced composite in Abaqus was considered to model UD lamina behavior. The cohesive element was described to model interface behavior, besides a relatively simple tying method based on using isotropic shell layers. Since the latter interface modeling technique does not allow the opening fracture mode (mode I), its behavior will be compared to the cohesive element by comparing tubular models under axial impact.

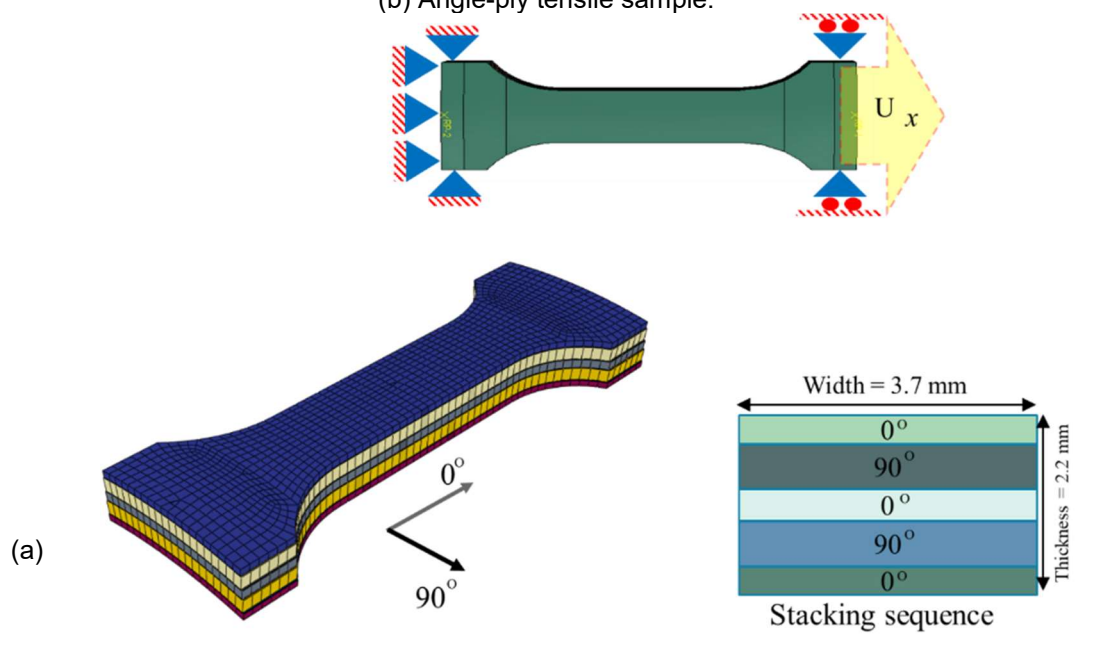
## 6 Finite element simulation and results

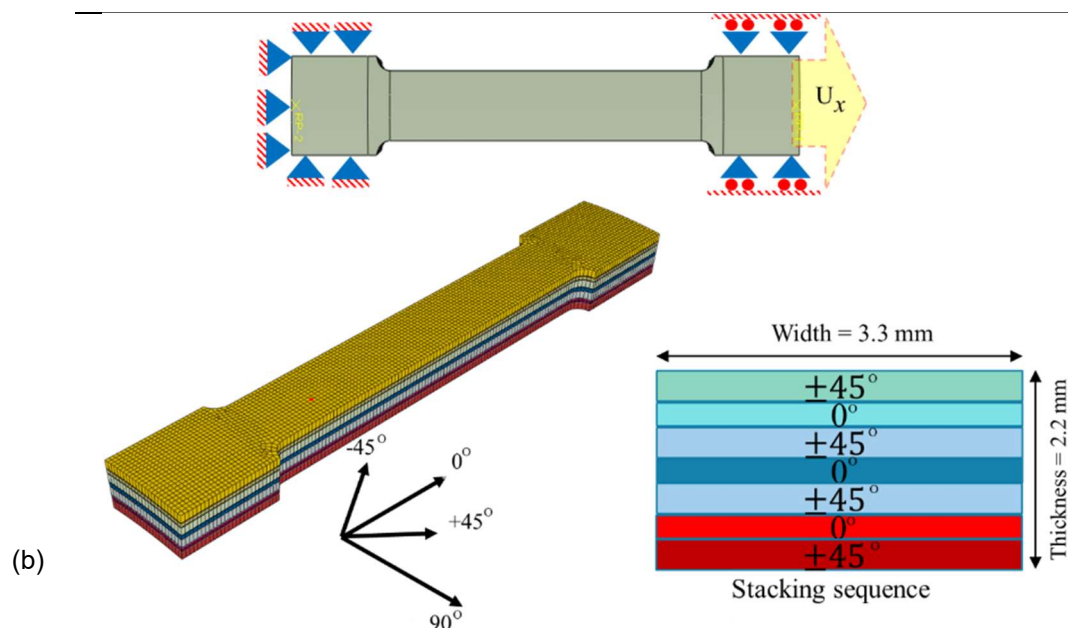
In this chapter tensile test, shear test and axial dynamic impact tests were simulated by using finite element multi-layer model described in the previous chapter. Tensile test results in chapter three were used to calibrate material properties.

### 6.1 Numerical simulations: Tensile and shear tests

Before performing axial impact simulation on tubes, FE model of tensile and shear tests, presented in chapter three, were simulated using the proposed multi-layer model. Abaqus/Explicit code was used to simulate both tensile and shear tests. Mass scaling was applied to the models in order to speed up the simulations. Figure 6.1 shows the virtual models of the tensile samples with the stacking sequence and dimensions of the angle-ply and cross-ply tubes.

Figure 6.1 - The 'dog-bone' sample for tensile test simulations; (a) Cross-plyed tensile sample; (b) Angle-ply tensile sample.





Source: The author

Table 6.1 lists the in-plane material properties of unidirectional CFRP lamina and epoxy resin. For UD composite material, the measured mechanical properties in chapter three were used in the material model. Fracture energies in the transverse direction of the fibers,  $G_{mc}^c$  and  $G_{mt}^c$ , were assumed and kept constant. These values are higher than those presented in the literature relevant to the axial and lateral impact on laminated parts. However, due to the highly anisotropic behavior of UD material in the present research ( $\frac{E_1}{E_2} \gg 1$  and  $\frac{S_1}{S_2} \gg 1$ ) the fracture energies in the transverse direction to the fibers have no significant effect on the laminate load-bearing.

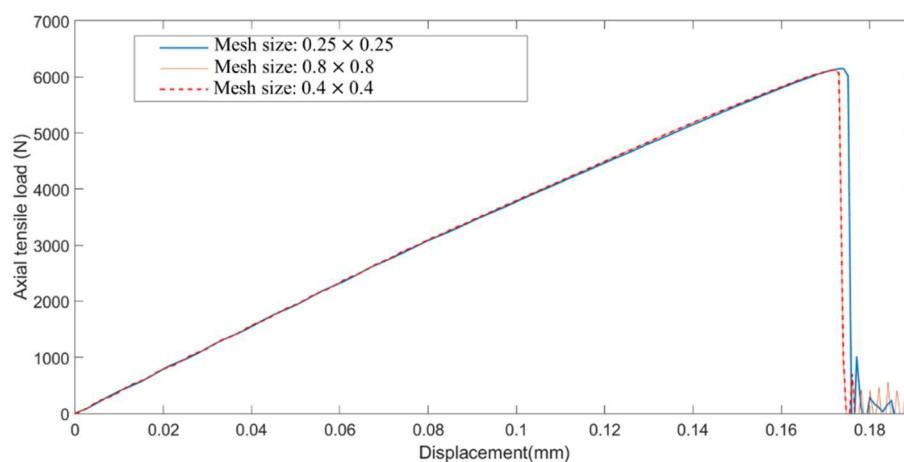
Table 6.1- Mechanical properties of the resin plies and UD carbon fiber/epoxy prepreps, from testing on non-standard specimens extracted from CFRP tubes.

Property	Symbol	Units	UD lamina
<b>CFRP laminae</b>			
Elastic modulus 0°	$E_1$	GPa	136.00
Elastic modulus 90°	$E_2$	GPa	9.30
In-plane shear modulus	$G_{12}$	GPa	5.10
Major Poisson's ratio	$\nu_{12}$	-	0.294
Ultimate tensile strength 0°	$X^T$	MPa	1550
Ultimate tensile strength 90°	$Y^T$	MPa	50*
Ultimate compressive strength 0°	$X^C$	MPa	1200*
Ultimate compressive strength 90°	$Y^C$	MPa	250*
Ultimate shear strength	$S^L$	MPa	74.00

Tensile fracture energy, fiber direction	$G_{ft}^c$	N/mm	19-133
Compressive fracture energy, fiber direction	$G_{fc}^c$	N/mm	11-44
Tensile fracture energy, transverse to fiber	$G_{mt}^c$	N/mm	0.15**
Compressive fracture energy, transverse to fiber	$G_{mc}^c$	N/mm	0.45**
<b>Cohesive element properties</b>			
Penalty stiffness			$k_n = 10e5$ $k_t = 10e5$ $k_s = 10e5$
Damage initiation (Chiu et al. 2016)			$t_n^0 = 64 \text{ MPa}$ $t_t^0 = 80 \text{ MPa}$ $t_s^0 = 80 \text{ MPa}$
Fracture energies (Chiu et al. 2016)			$G_I = 0.15 \left(\frac{N}{mm}\right)$ $G_{II} = 2.50 \left(\frac{N}{mm}\right)$
<b>Resin plies (Singh, Kumar, and Mohite 2017)</b>			
Elastic modulus	$E$	GPa	3.36
Poisson's ratio	$\nu$	-	0.35
Fracture energy	$G_f$	N/mm	0.05
<b>Plasticity</b>			
	Yield stress (MPa)	Plastic strain	
	18.24	0.00	
	42.33	0.0034	
* Provided by the tube's manufacturer.			
** From Ref. (Chiu et al. 2016)			

Figure 6.2 illustrates the effect of mesh size on the force-displacement curve of cross-plyed tensile sample under tension. There is no significant mesh dependency effect on the force-displacement curves.

Figure 6.2 - Axial tensile load versus displacement curve for cross-ply tensile specimen FE models with different global mesh size.



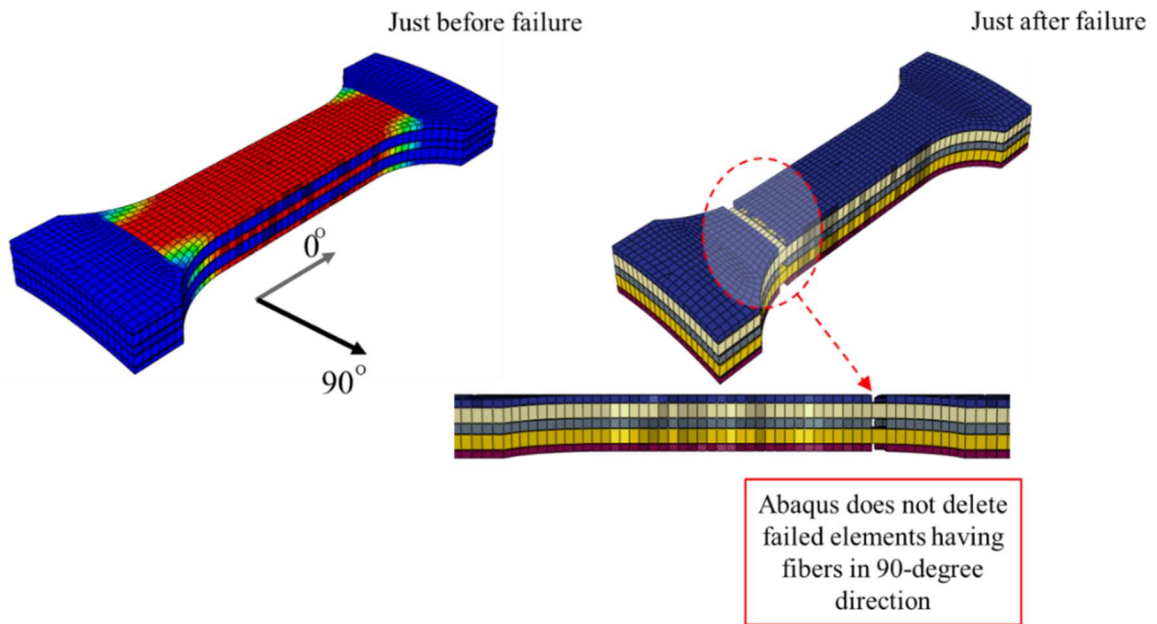
Source: The author

Figures 6.3 and 6.4 present the cross-ply and angle-ply specimens in the final stage of tensile simulation, respectively. Remarkably, Abaqus has some limitations to delete elements with different fiber orientations. The  $0^\circ$  layers, parallel to the loading direction were deleted in both specimens. Layers having fibers transverse to the loading direction and layers having  $\pm 45^\circ$  fibers orientation were not deleted, although these layers were unloaded.

Figures 6.5 and 6.6 illustrate the stress-strain curves for cross-ply and angle-ply tensile simulations, respectively, while the effects of different fracture energy values in the direction of the fibers ( $G_{ft}^c, G_{fc}^c$ )<sup>1</sup> were analyzed. From Figures 6.5 and 6.6, it is evident that an increase in the tensile fracture energy increased the failure stress slightly. The final strain had been increased significantly, as it was expected. Thus with higher fracture energies, the maximum stress (load) in the laminated sample will be carried for a longer time (a larger deformation), unloading occurs with a less acute slope.

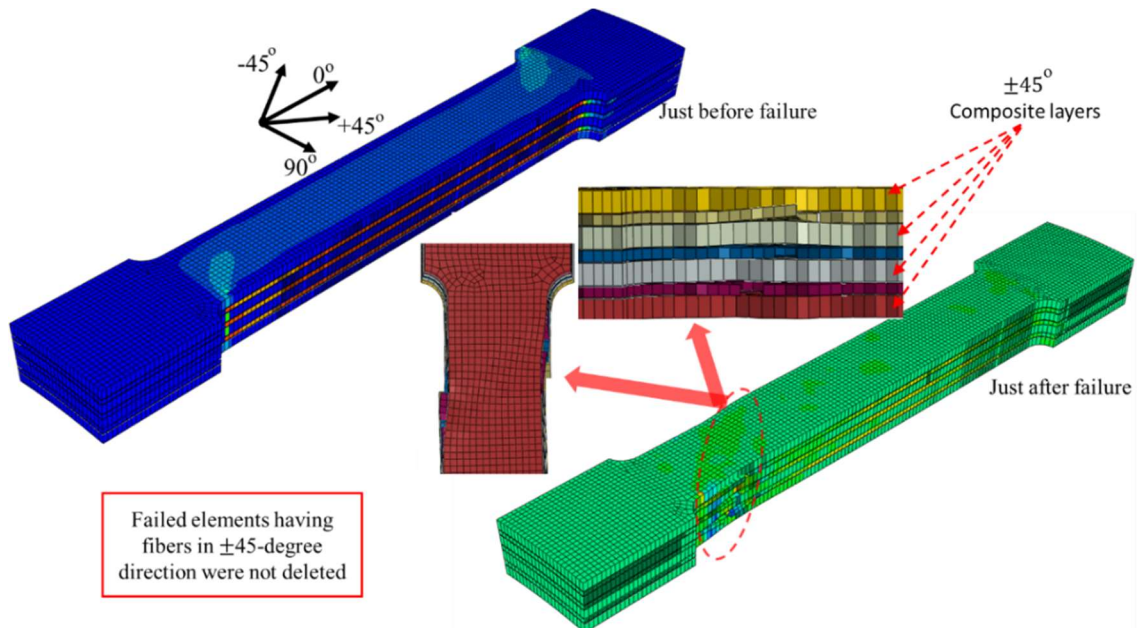
<sup>1</sup> The compressive fracture energy in the fiber direction ( $G_{fc}^c$ ) is less likely to affect the axial tensile result, however, different values are selected.

Figure 6.3 - Cross-ply specimens just before and after failure under tensile load.



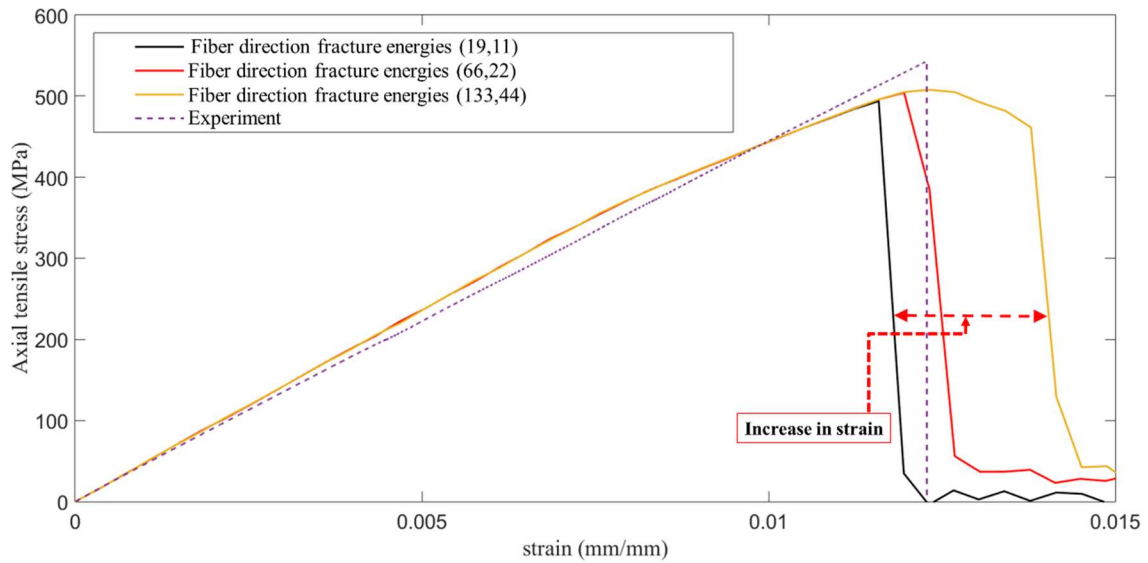
Source: The author

Figure 6.4 - Angle-ply specimens just before and after failure under tensile load.



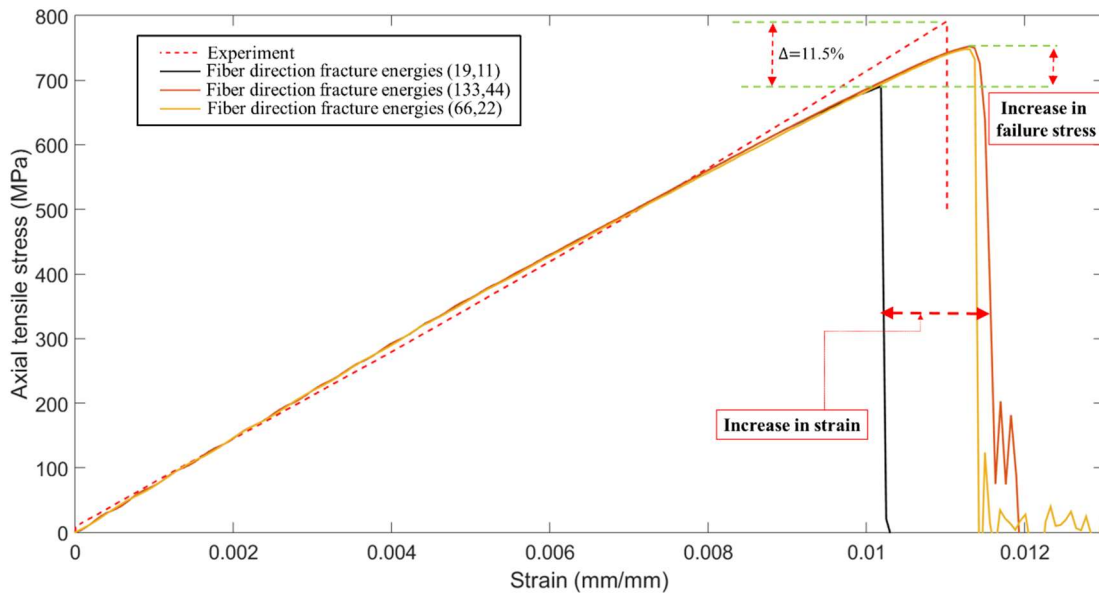
Source: The author

Figure 6.5 - Effect of fracture energies (fiber direction) on the load-bearing capacity of cross-ply laminate under uniaxial tension.



Source: The author

Figure 6.6 - Effect of fracture energies (fiber direction) on the load-bearing capacity of angle-ply laminate under uniaxial tension.



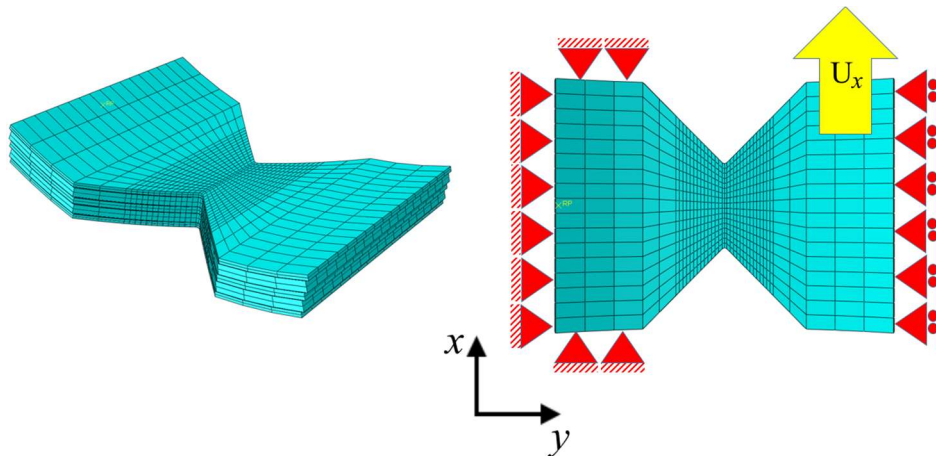
Source: The author

From Figures 6.5 and 6.6, it seems that a tensile fracture energy in the fiber direction around 90 (N/mm) is a choice leading to similar stress-strain curves for both cross-ply and angle-ply specimens under tensile test (this value is close to the fracture energy presented in Ref. (Chiu et al. 2016)). From the same reference, (Chiu et al.

2016), fracture energy in the direction transverse to the fibers was selected equal to 79 (N/mm)

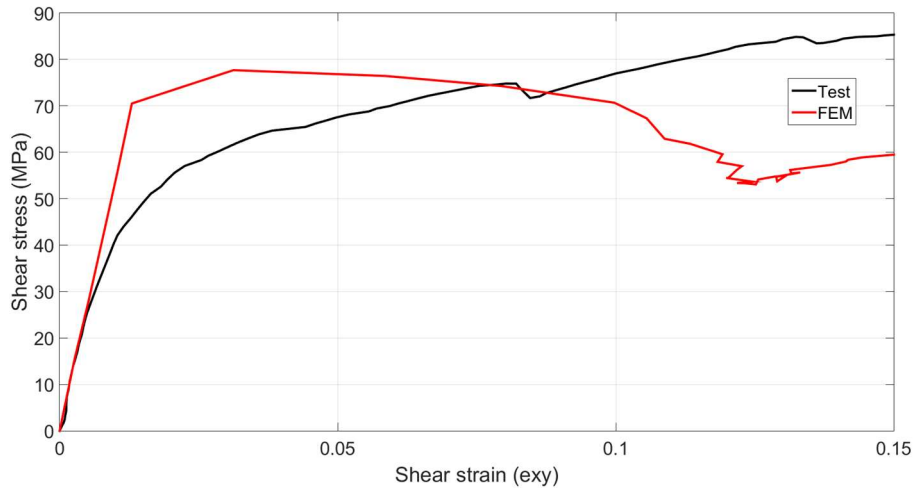
Furthermore, an FE model of a double V-notch shear specimen with multi-layer shell elements was constructed to reproduce the shear test on the ring-shaped sample with cross-ply stacking sequence. It is assumed that in the experimental test, the cap supports (described in chapter three) restrict all degrees of freedom of the ring's part in between the support caps and cylinder halves. Therefore, only a double V-notch section of whole ring-shaped specimen was modeled here, as depicted in Figure 6.7. The shear stress variation during the simulation is illustrated in Figure 6.8. The stress is calculated when dividing the shear force by shear cross-section area and the maximum shear stress obtained by the FE model is about 72.2 MPa (roughly 3% lower than the experimentally measured maximum shear stress). Figure 6.9 shows the shear stress just before and after the failure of the layers with fibers oriented in the  $y$ -direction and fibers oriented in the  $x$ -direction.

Figure 6.7 - The discretized model of the double V-notch shear sample.



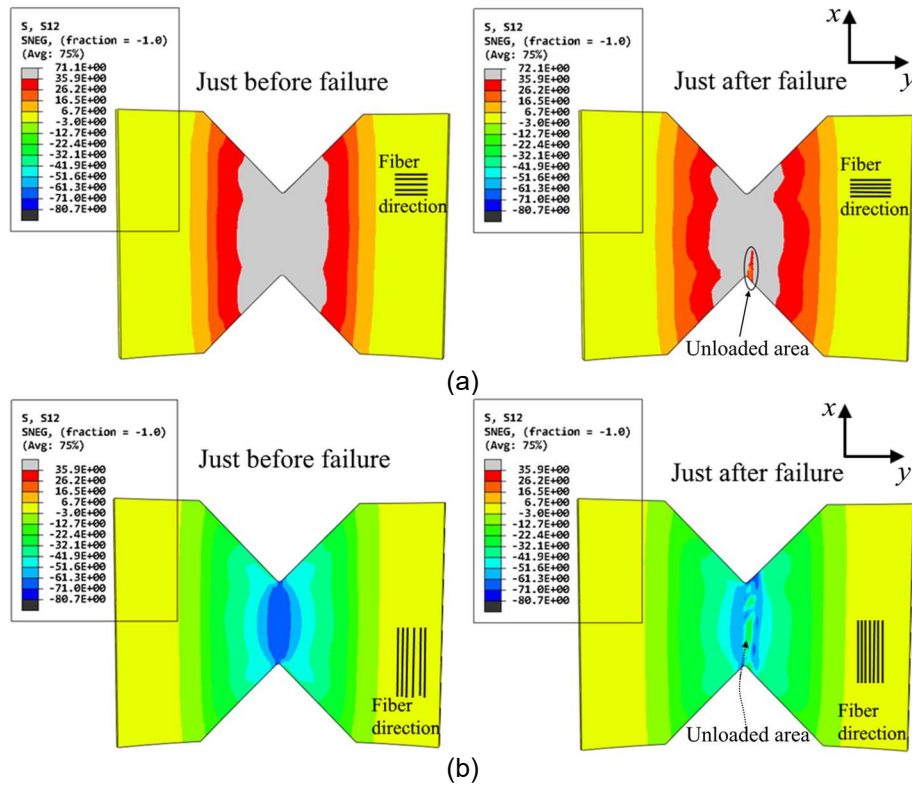
Source: The author

Figure 6.8 - Shear stress-displacement curve of a cross-plyed double V-notch shear specimen.



Source: The author

Figure 6.9 - Shear stress distribution in layers with different fiber orientation; (a) The layer having fibers in the y-direction; (b) The layer having fibers in the x-direction.

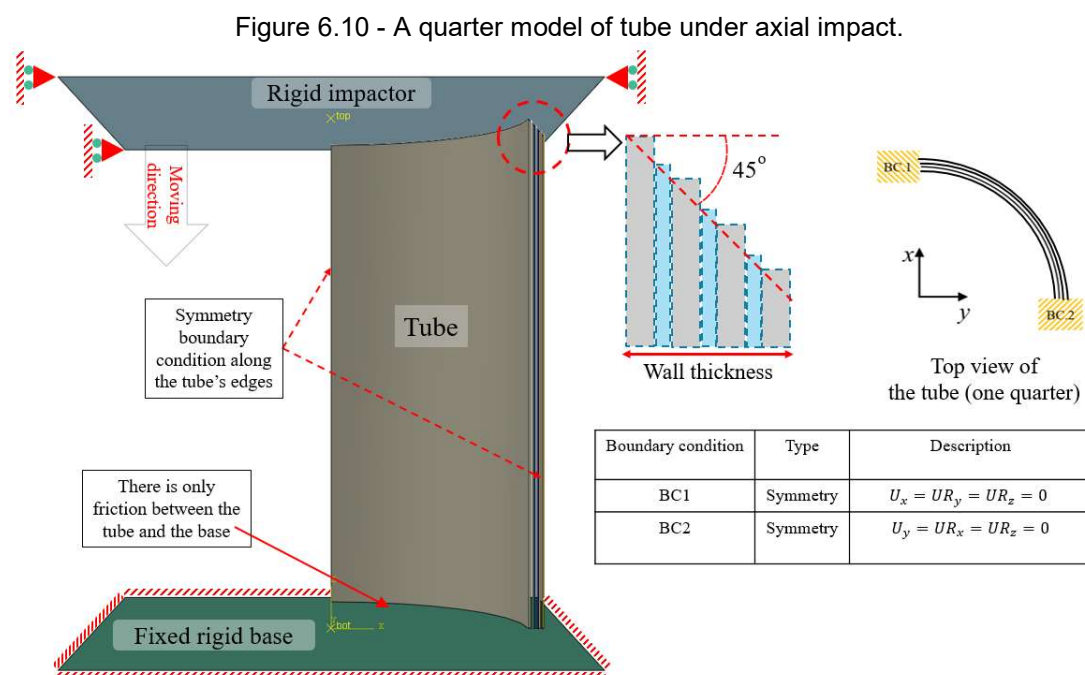


Source: The author.

## 6.2 Numerical simulations: Axial impact on CFRP tubes

### 6.2.1 General description of FE model of axial impact on CFRP tubes

It was found from the drop tests, presented in chapter four, that the chamfer angle has no significant effect on the average crushing force of the laminated tubes under different dynamic impact conditions. Moreover, the SEA value and average crushing force were not sensitive to the loading rate. Therefore, only tubes with 45-degree chamfer under dynamic impact condition #1 (impact velocity = 7 m/s and impactor mass = 102 kg) were model in this chapter. In order to reduce computational time, a quarter ( $1/4$ ) model of tubes with proper symmetry boundary conditions was considered for both angle-ply and cross-ply tubes. General features of the FE model of axial impact is presented in Figure 6.10, illustrating boundary conditions, interaction, and external 45° chamfer as crush initiator.



Source: The author.

In order to reduce the computational time, the quarter tubes with tube  $L = 50$  mm length was used, which is shorter than the tested specimens having a typical initial length between 100-150 mm. This length (50 mm) will ensure a stable progressive

crushing of the tubes and results in a realistic prediction of energy absorption performance of the tubes.

The external 45° chamfer was model using 'stepped length' geometry as illustrated in Figure 6.10. A fully fixed rigid plate is used to support the tube at the bottom. All degrees of freedom of the upper rigid impactor are fixed except for the displacement degree in the moving direction. A point mass with prescribed initial velocity is attached to the reference point of the rigid upper plate. The general contact formulation in Abaqus with a friction coefficient of 0.12 and a 'hard contact' interaction for normal behavior was used to model the contact between all parts of the models.

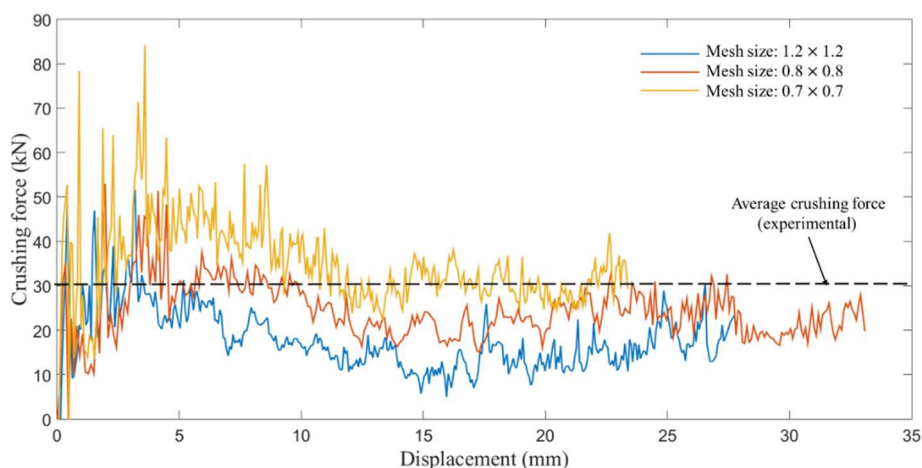
Two measures will be considered to compare the numerical and experimental outcomes; (I) force-displacement curves and (II) the damaged appearance of tubes and composite laminae (fracture morphology). The former measure comprises all crashworthy criteria such as SEA, average crushing force, peak load; thus, comparing the force-displacement curves will be enough to validate the numerical model with experimental results.

### **6.3 Simulation results for cross-ply specimen under axial impact**

#### **6.3.1 Effect of mesh size on average crushing force**

Figure 6.11 shows the force-displacement curves of three different simulation runs of the cross-ply tube. Mesh size has a significant effect on the crushing force of tubes. In contrast to the tensile test simulations, a small change in the mesh size leads to a significant effect on the crushing force of the tube under axial impact. It is worth to note that mesh size for resin layers always was considered as 0.6 mm × 0.6 mm in the tube models. From Figure 6.11, it seems that a mesh size of 0.7 mm × 0.7 mm leads to reasonable results. Therefore, for all cross-ply tubes, the global mesh size will be equal to 0.7 mm. The description of cross-ply tube specimen is presented in Table 6.2.

Figure 6.11 - Effect of mesh size on the crushing force of cross-ply tube specimen.



Source: The author.

Table 6.2 - Description of FE models of the cross-piled tube to check the resin response and different ply to represent the stacking sequence.

Finite element model description of cross-ply tube	
	Stacking sequence [0/90/0/90/0]
	Ply thickness (mm) [0.3/0.6/0.4/0.6/0.3]
Model	Lamina mesh size (mm) [0.7/0.7/0.7/0.7/0.7]
	Number of resin plies 4
	Resin plies mesh size (mm) 0.6

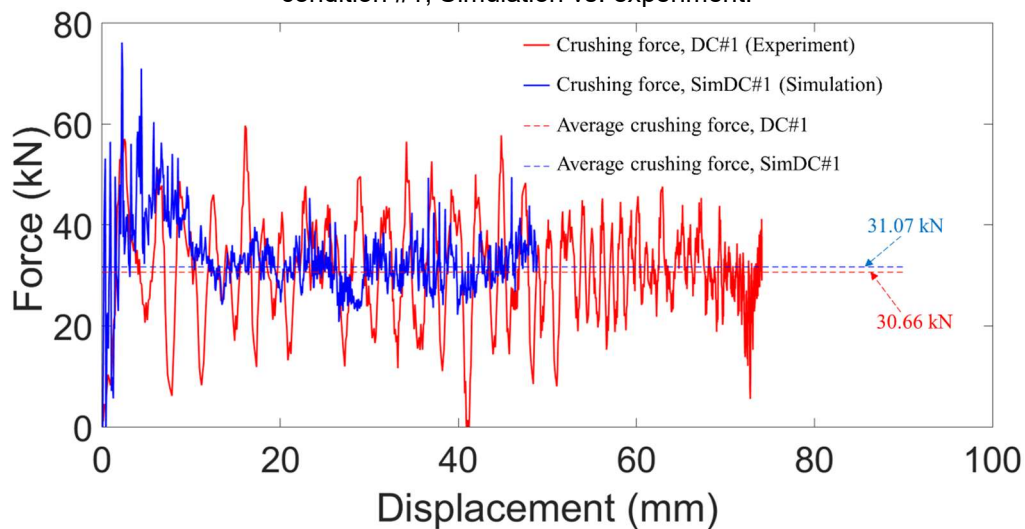
<sup>1</sup> 0° and 90° are measured from the tube axis.

## 6.4 Results

### 6.4.1 Force-displacement and fracture morphology for cross-ply tube under axial impact

Figure 6.12 illustrates the force-displacement curve for a cross-ply tube under dynamic condition #1 (mass impactor = 102 kg and impact velocity = 7 m/s). There is an acceptable similarity between force-displacement curves of simulation and experiment. However, the predicted peak load is higher than the experiment.

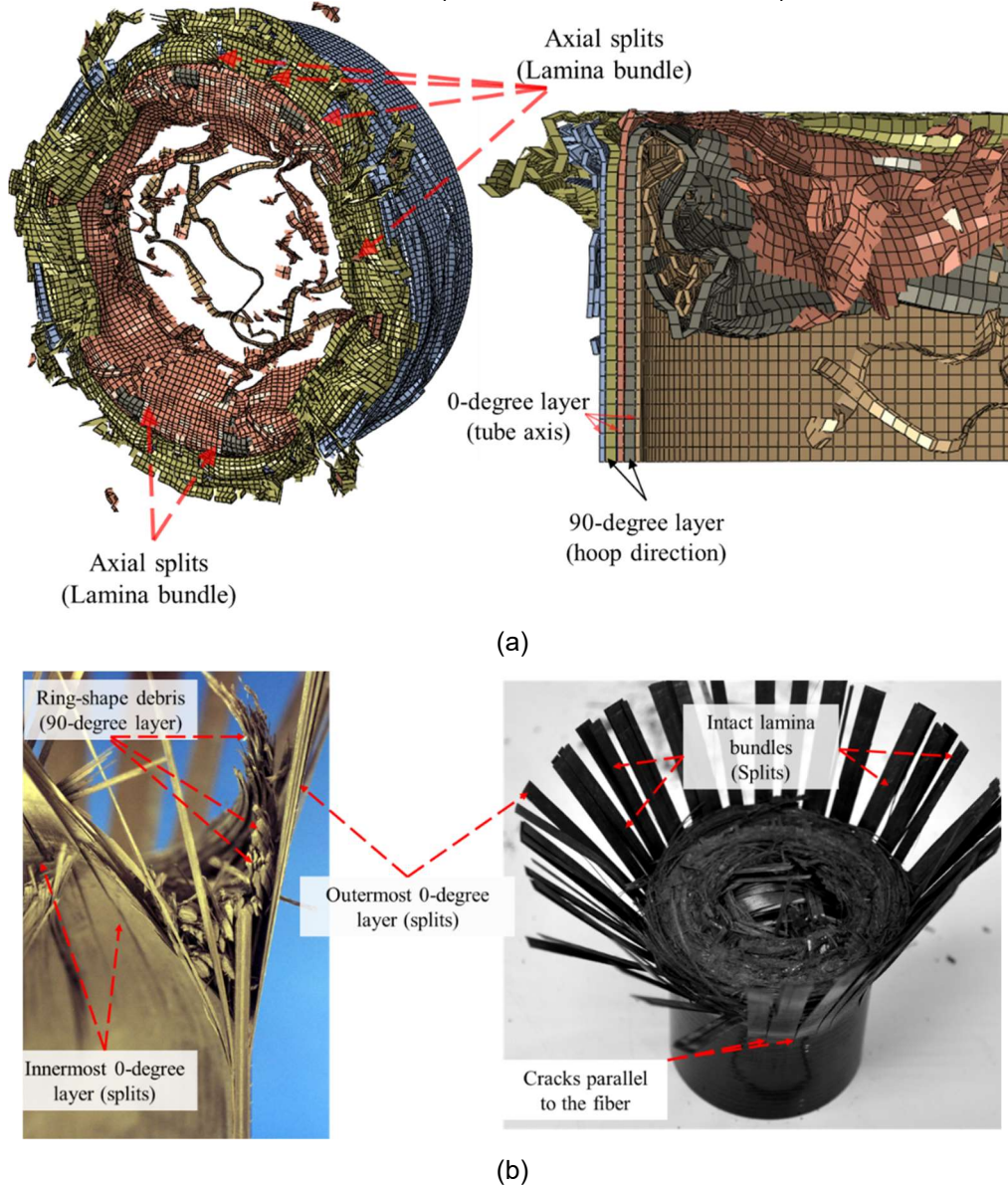
Figure 6.12 - Force-displacement curves of the cross-ply tube under dynamic impact condition #1; Simulation vs. experiment.



Source: The author.

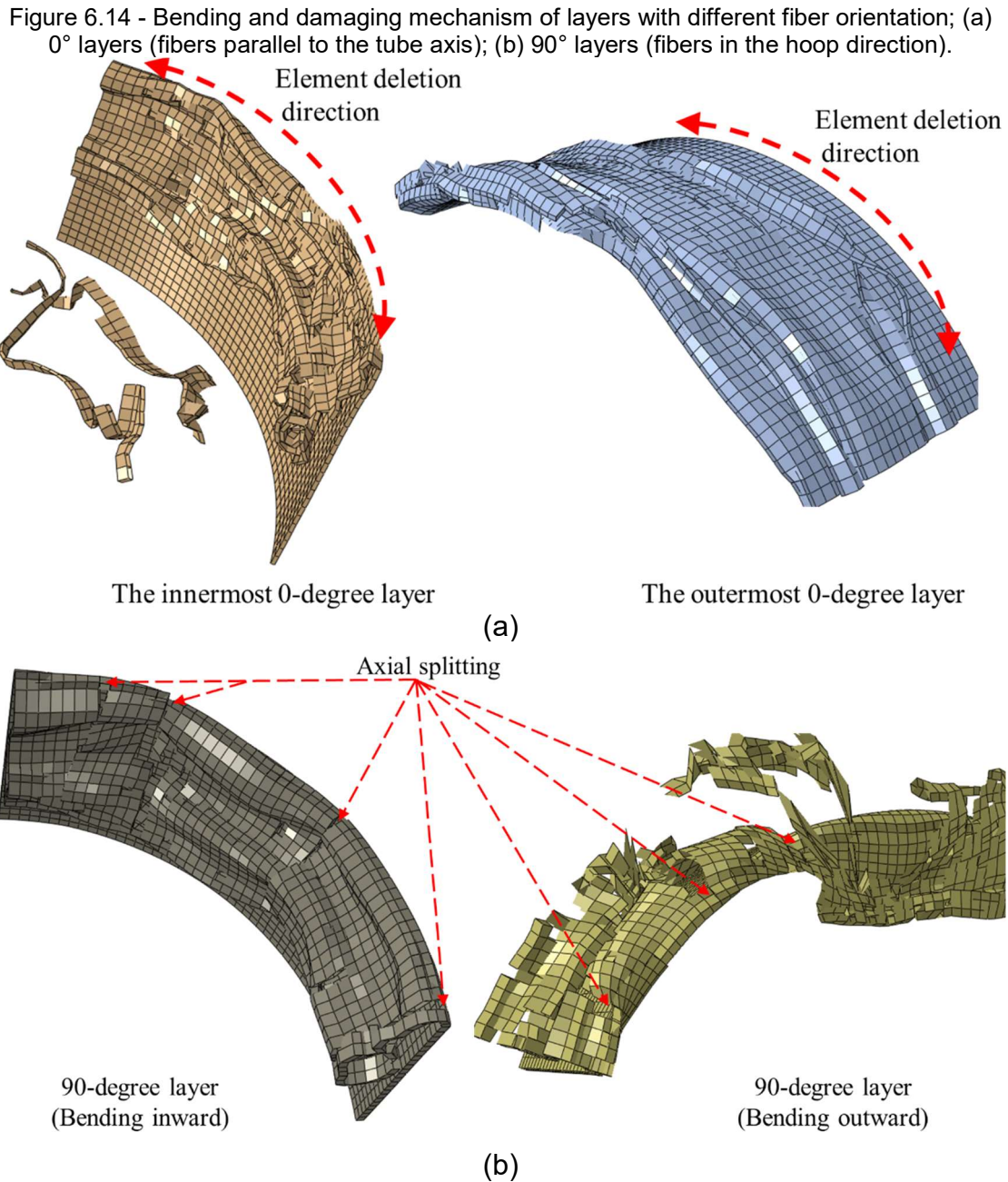
Although the tube progressively crushed from the contact area with the impactor and the layers separated reasonably, several dissimilarities are apparent in the comparison between post-impact photos of the cross-ply tube, and the numerical ones, see Figure 6.13. The main difference is about the axial splitting of the innermost and outermost  $0^\circ$  layers in the simulation and experiment.

Figure 6.13 - Fracture morphology of cross-ply specimen after axial dynamic impact (for numerical results (shell thickness render is ON).



Source: The author

Figure 6.14 shows that damages have developed in an unexpected direction in the different layers of the cross-ply specimen. From the experimental results (Figure 6.13(b)), it was expected that the outermost and innermost  $0^\circ$  layers split into long intact lamina bundles and splayed. Moreover, it was expected that  $90^\circ$  layers damaged and form small ring-shape debris. However, completely reverse damaging behaviors have been observed in the simulation for  $0^\circ$  and  $90^\circ$  layers, see Figure 6.14.



Source: The author.

It is worth to note that the FE model of the cross-ply specimen could predict the force-displacement with fewer efforts; however, the model failed to reproduce the reasonable damaging appearance of the laminae.

#### 6.4.2 Simulation results for the angle-ply specimen under axial impact

Table 6.3 lists the description of the FE model for the angle-ply specimen under the axial dynamic impact. The  $\pm 45^\circ$  layers are modeled with a single layer of shell

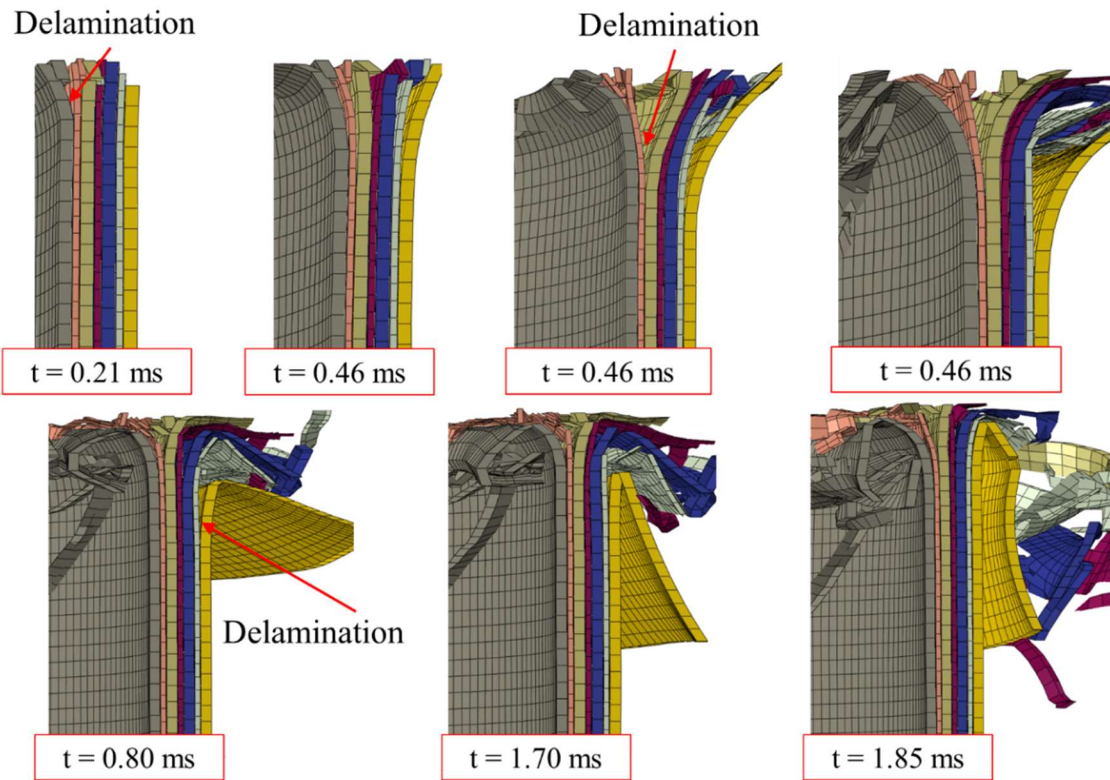
elements. Global mesh size for the  $\pm 45^\circ$  layers equals 0.7 mm ( $0.7 \times 0.7$ ), for  $0^\circ$  layers equals to 0.65 mm ( $0.65 \times 0.65$ ) and for resin plies mesh size is equal to 0.6 mm ( $0.6 \times 0.6$ ).

Table 6.3 - Description of FE models of the angle-ply specimen tube.

<b>Finite element model, description of angle-ply tube</b>		
Model	Stacking sequence	$[\pm 45/0/\pm 45/0/\pm 45/0/\pm 45]$
	Ply thickness (mm)	$[0.4/0.2/0.4/0.2/0.4/0.2/0.4]$
	Lamina mesh size (mm)	$[0.7/0.65/0.7/0.65/0.7/0.65/0.7]$
	Number of resin plies	6
	Resin plies mesh size (mm)	0.6

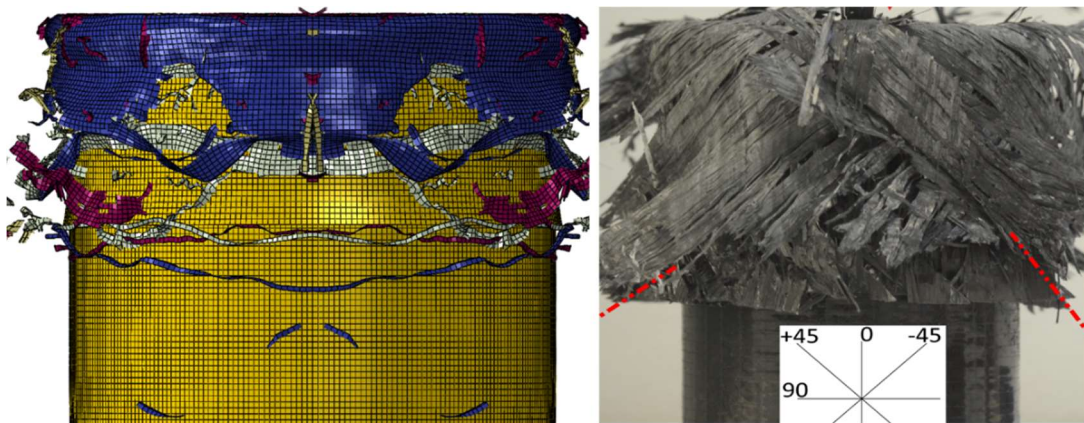
Figure 6.15 shows the time-lapse of deformation of each layer of the angle-ply tube under the dynamic impact. Bending behavior of plies (especially the innermost and outermost  $\pm 45^\circ$  layers) is very similar to experimental results. Figures 6.16 and 6.17 show the side-view and top-view of the angle-ply specimen, respectively, and compare them with experimental observation. The  $0^\circ$  layers in the angle-ply also underwent outward/inward bending. However, in contrast to the experiment tests, these layers broke and formed small flying debris in the FE model. In general, the similarity between experimental and numerical crush morphology for the angle-ply specimen is more apparent rather than the cross-ply specimen.

Figure 6.15 - Deformation of each layer of the angle-ply specimen under the dynamic impact (shell thickness render is ON).



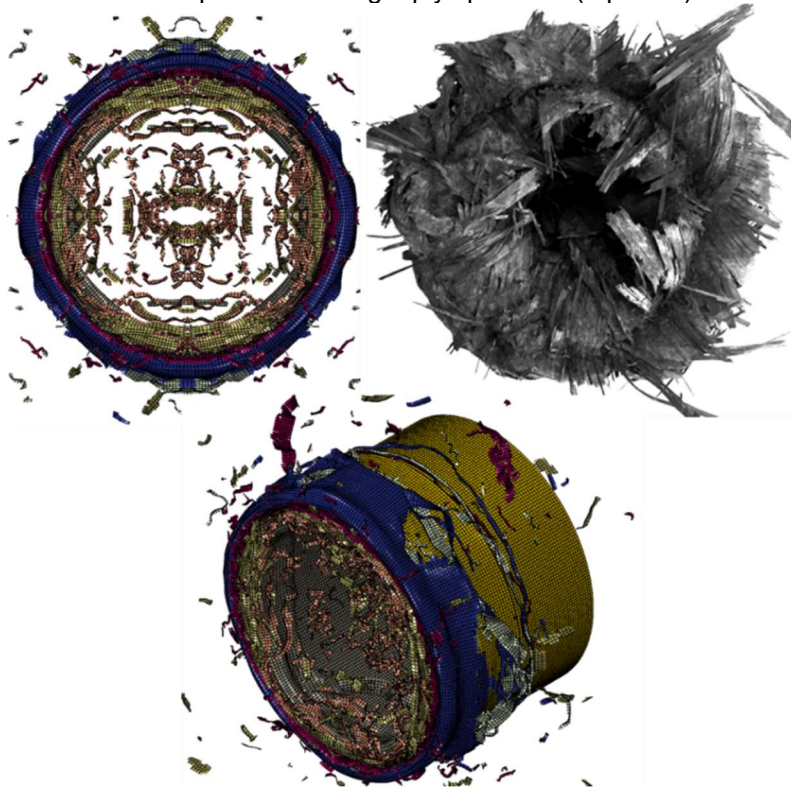
Source: The author.

Figure 6.16 - Compression between damage morphology for experimental and numerical axial impact on the angle-ply specimen (side-view).



Source: The author.

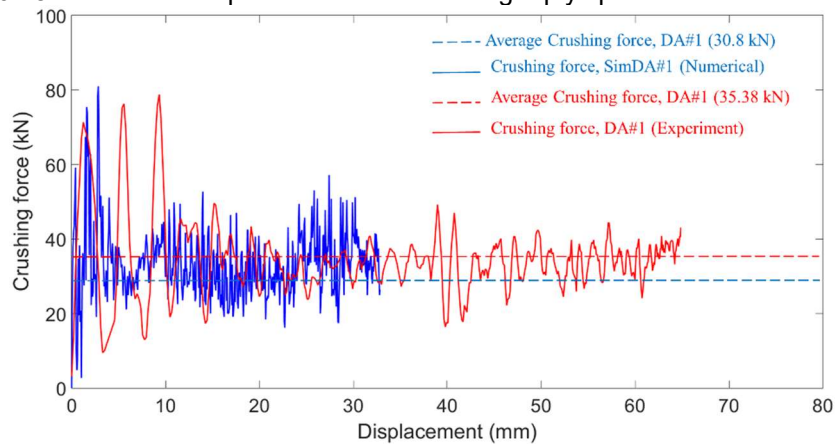
Figure 6.17 - Compression between damage morphology for experimental and numerical axial impact on the angle-ply specimen (top-view).



Source: The author.

The force-displacement curve for angle-ply specimen under axial impact is present in Figure 6.18. The average crushing force, predicted by the FE model, is lower than the experimental result.

Figure 6.18 - The force-displacement curve for angle-ply specimen under axial impact.

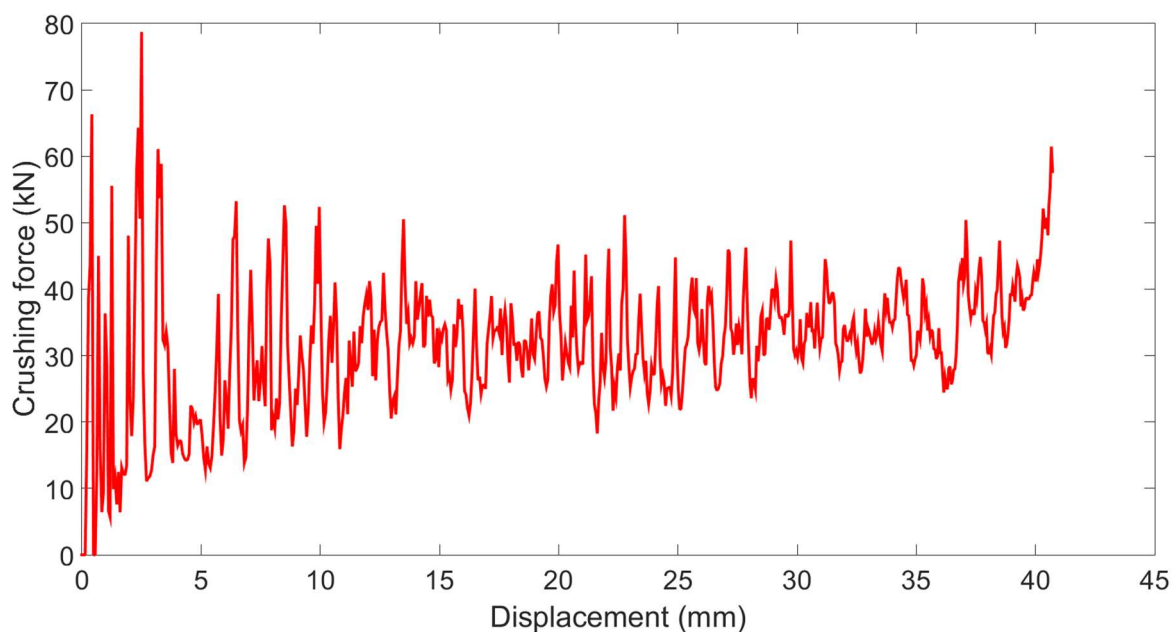


Source: The author.

### 6.4.3 Simulation results for models with cohesive element

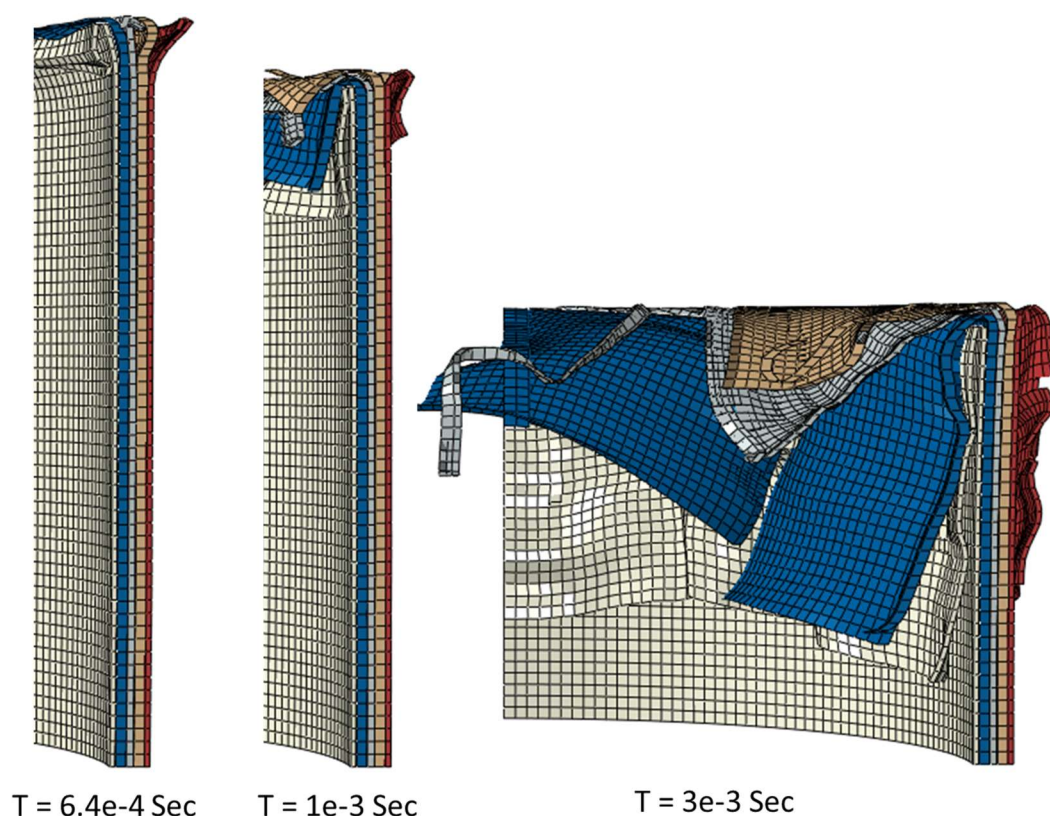
This model is similar to the previous model, however, resin plies are replaced by layers of cohesive element. Figure 6.19 and 6.20 present force-displacement curve and crush morphology for numerical simulation of the cross-ply specimens. The model reproduced the reasonable crushing force in comparison with experimental tests. The same observation for damage morphology of the previous FE model (model having resin plies) are obvious of this FE model with cohesive element. Here also FE model failed to reproduce the 'splitting' of UD lamina observed in the experimental tests.

Figure 6.19 - The force-displacement curve for cross-ply specimen under axial impact.



Source: The author.

Figure 6.20 - Damage morphology for cross-ply tube simulation with cohesive element.



Source: The author.

## 6.5 Summary

In this chapter, the axial impact on composite tubes was simulated by using the plane stress shell element in Abaqus. Both material calibration and impact calibration were utilized to reach reasonable results.

Axial tensile tests on the cross-ply and angle-ply specimens were simulated in order to find tensile fracture energy in the fiber direction (with comparing to experimental tests). However, due to limited material characterization, the other fracture energies and fracture energy of resin plies were selected from the data available in the literature.

The FE models in this chapter reproduced force-displacement curves with the selected combination of mechanical properties of resin and lamina with good accuracy, however, reproduced crushed debris were not similar to those observed in the experimental part.

A new model has been presented in Appendix E in order to reproduce similar debris by using shell elements besides reasonable crushing force. Although this model reproduces very similar crushed morphology and force, it requires more study to justify the procedure and its assumptions.

## 7 Conclusion

The energy absorption capacity of tubular CFRP components, fabricated of unidirectional carbon fiber-epoxy prepregs, was investigated experimentally and numerically. Two different layups were investigated, cross-ply ([0/90/0/90/0]) and angle-ply ( $[\pm 45/0/\pm 45/0/\pm 45/0/\pm 45]$ ). These tubular components can be considered as a simplified model of frontal crash-box in the automobile body.

In the experimental part, in-plane material properties characterization of UD lamina and energy absorption characterization of tubular composite parts under axial load have been performed.

In order to characterize the in-plane mechanical properties of UD lamina, several experimental tests were conducted on non-flat, non-standard specimens cut from the tubes. Using classical laminate theory (CLT) and experimental tests on the laminated coupons, in-plane mechanical properties of the unidirectional lamina were found (especially the properties in the fiber direction).

A shear test fixture was proposed in order to find in-plane shearing behavior of composite materials from testing on ring-shaped specimens. The proposed shearing fixture would be advantageous for tubular composites components for which standard flat shear test coupons are not available while very few methods are proposed to characterize shearing behavior of tubular specimens.

The main portion of the experimental work was related to the energy absorption characterization of full circular and C-section specimens subjected to axial loading (from quasi-static compression to dynamic impact loading). Effects of layup configuration, loading rate, different mass of the impactor (for dynamic impact tests), and cross-section shape (only quasi-static) were studied.

A general conclusion about the effect of cross-section shape was not possible while in contrast to angle-ply specimens, the C-section specimens having cross-ply layup showed a decrease in SEA value in comparison to full tube specimens.

Although the loading rate has changed the crushed appearance of the crash front in both layups, the SEA value was found to be insensitive to the loading rate. SEA values of both stacking sequences approximately were in the same range, although damaging behavior and crushed morphology of two specimens were different.

The findings agree with the general conclusion in the literature that it is difficult to reach an overall conclusion about crushing behavior of composite material solely by experimental tests since there are many intrinsic and extrinsic parameters affecting composite behavior. Thus much more efforts are needed to develop and improve alternative methods such as finite element analysis in order to investigate the crushing behavior of composite materials.

In the numerical part, a multi-layer model of the laminated tube was developed in Abaqus software using a stacked-shell combination. The conventional shell element in Abaqus (S4R) was used to model composite lamina (intra-ply). This element has been of little use in modeling laminate composite when comparing with continuum element in Abaqus and mid-surface shell element in LS-Dyna.

The direct application of cohesive surfaces to bond adjacent S4R shell elements is not straightforward, in comparison to continuum elements. Thus, element-based cohesive models (bonding S4R shell elements with COH3D8 cohesive elements) with traction-separation formulation have been used in not so many finite element simulations of the axial impact of laminate tubes. However, in the present research project, besides 3D cohesive element (COH3D8), S4R element was used to discretize the resin ply (interface layer) between two adjacent laminae. An available material model (in Abaqus library) with progressive damaging response was assigned to the isotropic resin piles. The objective was to investigate alternative methods to bond laminae in a relatively large structure with a complicated condition like dynamic impact. The adaptation of isotropic shell elements to represent interface behavior has some possible advantages rather than using COH3D8 element, as follows:

- Its implementation is more straightforward rather than COH3D8.
- Bulk material properties can be used for interface modeling; thus, several experimental tests, like DCB, 4ENF, and MMB, are not required.
- Three-dimensional cohesive element (COH3D8) is an 8-node with only three translational DOFs (at each node). In contrast, the S4R shell element has four nodes with six degrees of freedom per node (both translational and rotational). Therefore, the cohesive element cannot fully couple the deformation of the adjacent composite laminae. Tying two neighboring S4R elements (laminae) with an S4R layer (resin ply) may result in a fully coupled deformation between two composite shell layers.

Finite element model, based on modeling unidirectional lamina described in the Abaqus documentation, resulted in reasonable crushing force for the cross-ply tubes under axial impact. However, the average crushing force for angle-ply simulation was lower than the experimental tests. In contrast, the similarity between the crushed morphology of angle-ply specimen (between the FE model and experiment) was remarkable rather than the cross-ply specimen. In general bending behavior of  $\pm 45^\circ$  layers (respect to tube axis) in the angle-ply tube was much better than  $0^\circ$  and  $90^\circ$  layers.

Fracture energies and mesh size were found to be the most the significant parameters in the simulation of axial impact on tubular composite absorbers. However, in this research due to limited experimental tests (in material characterization part), only tensile fracture energy of UD lamina in the fiber direction was calibrated based on tensile tests and simulations on the tensile samples. The three other fracture energies and fracture energy of interface material were selected from the relevant work in the literature.

## References

- Abramowicz, Włodzimierz and Norman Jones. 1984. "Dynamic Axial Crushing of Circular Tubes." *International Journal of Impact Engineering* 2(3):263–81.
- Alexander, J. M. 1960. "An Approximate Analysis of the Collapse of Thin Cylindrical Shells under Axial Loading." *The Quarterly Journal of Mechanics and Applied Mathematics* 13(1):10–15.
- Allix, O. and P. Ladevèze. 1992. "Interlaminar Interface Modelling for the Prediction of Delamination." *Composite Structures* 22(4):235–42.
- Ambrasio, Jorge A. c., Manuel F. o. Seabra Pereira, and Fernando Pina da Silva. 1997. *Crashworthiness of Transportation Systems: Structural Impact and Occupant Protection*.
- Anderson, L. T. 2004. *Fracture Mechanics - Fundamentals and Applications*. 3rd Ed. CRC Press.
- ASTM. 1998. "ASTM D 5379, Standard Test Method for Shear Properties of Composite Materials by the v-Notched Beam Method." 13.
- ASTM Standards. 2000. "ASTM D2290-00 - Standard Test Method for Apparent Hoop Tensile Strength of Plastic or Reinforced Plastic Pipe by Split Disk Method." 1–5.
- Barbero, Ever J. 2013. *Finite Element Analysis of Composite Materials Using Abaqus*. 1st Ed. CRC Press.
- Barenblatt, G. I. 1962. "The Mathematical Theory of Equilibrium Cracks in Brittle Fracture." Pp. 55–129 in.
- Bert, C. W. 2001. "Improved Equation for Shear Modulus Using Four-Point Ring-Twist Test Data." *Journal of Thermoplastic Composite Materials* 14(6):489–97.
- Bogenfeld, Raffael, Janko Kreikemeier, and Tobias Wille. 2018. "Review and Benchmark Study on the Analysis of Low-Velocity Impact on Composite Laminates." *Engineering Failure Analysis* 86(August 2017):72–99.
- Brighton, Aaron, Mark Forrest, Mike Starbuck, Donald Erdman, and Bronwyn Fox. 2009. "Strain Rate Effects on the Energy Absorption of Rapidly Manufactured Composite Tubes." *Journal of Composite Materials* 43(20):2183–2200.
- Chamis, CC, ed. 1981. *Test Methods and Design Allowables for Fibrous Composites*. 100 Barr Harbor Drive, PO Box C700, West Conshohocken, PA 19428-2959: ASTM International.
- Cherniaev, Aleksandr, Clifford Butcher, and John Montesano. 2018. "Predicting the Axial Crush Response of CFRP Tubes Using Three Damage-Based Constitutive Models." *Thin-Walled Structures* 129(April):349–64.
- Ching Quek, Shu, Anthony M. Waas, Jennifer Hoffman, and Venkatesh Agaram. 2001. "The Crushing Response of Braided and CSM Glass Reinforced Composite Tubes." *Composite Structures* 52(1):103–12.
- Chiu, Louis N. S., Brian G. Falzon, Romain Boman, Bernard Chen, and Wenyi Yan. 2015a. "Finite Element Modelling of Composite Structures under Crushing Load." *Composite Structures* 131:215–28.
- Chiu, Louis N. S., Brian G. Falzon, Romain Boman, Bernard Chen, and Wenyi Yan. 2015b. "Finite Element Modelling of Composite Structures under Crushing Load." *Composite Structures* 131:215–28.
- Chiu, Louis N. S., Brian G. Falzon, Bernard Chen, and Wenyi Yan. 2016. "Validation of a 3D Damage Model for Predicting the Response of Composite Structures under Crushing Loads." *Composite Structures* 147:65–73.

- Chiu, Louis N. S., Brian G. Falzon, Dong Ruan, Shanqing Xu, Rodney S. Thomson, Bernard Chen, and Wenyi Yan. 2015. "Crush Responses of Composite Cylinder under Quasi-Static and Dynamic Loading." *Composite Structures* 131:90–98.
- Christensen, Richard M. 2013. *The Theory of Materials Failure*. Oxford University Press.
- Czaplicki, Michael J., Richard E. Robertson, and Peter H. Thornton. 1991. "Comparison of Bevel and Tulip Triggered Pultruded Tubes for Energy Absorption." *Composites Science and Technology* 40(1):31–46.
- Daniel, Isaac M., Ori Lshai, New York, and H. Oxford. 2006. *Engineering Mechanics of Composite Materials*. Second Edi.
- Dassault Systèmes Simulia. 2014. "Abaqus 6.14. Analysis User's Guide." IV.
- David, Matthew, Alastair F. Johnson, and H. Voggenreiter. 2013. "Analysis of Crushing Response of Composite Crashworthy Structures." *Applied Composite Materials* 20(5):773–87.
- Dlugosch, M., J. Fritsch, D. Lukaszewicz, and S. Hiermaier. 2017. "Experimental Investigation and Evaluation of Numerical Modeling Approaches for Hybrid-FRP-Steel Sections under Impact Loading for the Application in Automotive Crash-Structures." *Composite Structures* 174:338–47.
- Donadon, M. V., L. Iannucci, B. G. Falzon, J. M. Hodgkinson, and S. F. M. de Almeida. 2008. "A Progressive Failure Model for Composite Laminates Subjected to Low Velocity Impact Damage." *Computers and Structures* 86(11–12):1232–52.
- Dugdale, D. S. 1960. "Yielding of Steel Sheets Containing Slits." *Journal of the Mechanics and Physics of Solids* 8(2):100–104.
- Farley, Gary L. 1983. "Energy Absorption of Composite Materials." *Journal of Composite Materials* 17(3):267–79.
- Farley, Gary L. 1991. "The Effects of Crushing Speed on the Energy-Absorption Capability of Composite Tubes." *Journal of Composite Materials* 25(10):1314–29.
- Feraboli, Paolo, Bonnie Wade, Francesco Deleo, Mostafa Rassaian, Mark Higgins, and Alan Byar. 2011. "LS-DYNA MAT54 Modeling of the Axial Crushing of a Composite Tape Sinusoidal Specimen." *Composites Part A: Applied Science and Manufacturing* 42(11):1809–25.
- Ghaemi, Hamid and Zouheir Fawaz. 2002. "Experimental Evaluation of Effective Tensile Properties of Laminated Composites." *Advanced Composite Materials* 11(February 2013):223–37.
- Ghasemnejad, H., B. R. K. Blackman, H. Hadavinia, and B. Sudall. 2009. "Experimental Studies on Fracture Characterisation and Energy Absorption of GFRP Composite Box Structures." *Composite Structures* 88(2):253–61.
- Greszczuk, Lb. 1981. "Application of Four-Point Ring-Twist Test for Determining Shear Modulus of Filamentary Composites." Pp. 21–21–13 in *Test Methods and Design Allowables for Fibrous Composites*. 100 Barr Harbor Drive, PO Box C700, West Conshohocken, PA 19428-2959: ASTM International.
- Gui, L. J., P. Zhang, and Z. J. Fan. 2009. "Energy Absorption Properties of Braided Glass/Epoxy Tubes Subjected to Quasi-Static Axial Crushing." *International Journal of Crashworthiness* 14(1):17–23.
- Hallett, S. R. and P. W. Harper. 2015. "Modelling Delamination with Cohesive Interface Elements." Pp. 55–72 in *Numerical Modelling of Failure in Advanced Composite Materials*. Elsevier.
- Hallett, Stephen R., Wen-Guang Jiang, Bijoy Sri Khan, and Michael R. Wisnom. 2008.

- “Modelling the Interaction between Matrix Cracks and Delamination Damage in Scaled Quasi-Isotropic Specimens.” *Composites Science and Technology* 68(1):80–89.
- Hamada, H. and S. Ramakrishna. 1997. “A Fem Method for Prediction of Energy Absorption Capability of Crashworthy Polymer Composite Materials.” *Journal of Reinforced Plastics and Composites* 16(3):226–42.
- Hashin, Z. 1980. “Failure Criteria for Unidirectional Fiber Composites.” *Journal of Applied Mechanics* 47(2):329.
- Hashin, Z. and A. Rotem. 1973. “A Fatigue Failure Criterion for Fiber Reinforced Materials.” *Journal of Composite Materials* 7(4):448–64.
- Hu, Dayong, Chong Zhang, Xiaobing Ma, and Bin Song. 2016. “Effect of Fiber Orientation on Energy Absorption Characteristics of Glass Cloth/Epoxy Composite Tubes under Axial Quasi-Static and Impact Crushing Condition.” *Composites Part A: Applied Science and Manufacturing* 90:489–501.
- Huang, Jiancheng and Xinwei Wang. 2009. “Numerical and Experimental Investigations on the Axial Crushing Response of Composite Tubes.” *Composite Structures* 91(2):222–28.
- Huang, Jiancheng and Xinwei Wang. 2010. “On a New Crush Trigger for Energy Absorption of Composite Tubes.” *International Journal of Crashworthiness* 15(6):625–34.
- Hull, D. 1991. “A Unified Approach to Progressive Crushing of Fiber-Reinforced Composite Tubes.” *Composites Science and Technology* 40(4):377–421.
- Jackson, A., S. Dutton, A. J. Gunnion, and D. Kelly. 2011. “Investigation into Laminate Design of Open Carbon-Fibre/Epoxy Sections by Quasi-Static and Dynamic Crushing.” *Composite Structures* 93(10):2646–54.
- Jacob, George C., John F. Fellers, Srdan Simunovic, and J. Michael Starbuck. 2002. “Energy Absorption in Polymer Composites for Automotive Crashworthiness.” *Journal of Composite Materials* 36(7):813–50.
- Jose, S., R. Ramesh Kumar, M. K. Jana, and G. Venkateswara Rao. 2001. “Intralaminar Fracture Toughness of a Cross-Ply Laminate and Its Constituent Sub-Laminates.” *Composites Science and Technology* 61(8):1115–22.
- Karagiozova, D., M. Alves, and Norman Jones. 2000. “Inertia Effects in Axisymmetrically Deformed Cylindrical Shells under Axial Impact.” *International Journal of Impact Engineering* 24(10):1083–1115.
- Karagiozova, D. and Norman Jones. 2001. “Dynamic Effects on Buckling and Energy Absorption of Cylindrical Shells under Axial Impact.” *Thin-Walled Structures* 39(7):583–610.
- Kaynak, Cevdet, E. Salim Erdiller, Levend Parnas, and Fikret Senel. 2005. “Use of Split-Disk Tests for the Process Parameters of Filament Wound Epoxy Composite Tubes.” *Polymer Testing* 24(5):648–55.
- Lasn, K., A. Klauson, and A. T. Echtermeyer. 2015. “Back-Calculation of Elastic Moduli of a Ply from the Moduli of Cross-Ply Laminates.” *Mechanics of Composite Materials* 51(1):55–68.
- Long, Shuchang, Xiaohu Yao, and Xiaoqing Zhang. 2015. “Delamination Prediction in Composite Laminates under Low-Velocity Impact.” *Composite Structures* 132:290–98.
- Lopresto, Valentina, Antonio Langella, and Serge Abrate, eds. 2017. *Dynamic Response and Failure of Composite Materials and Structures*. First Edit.
- Lu, Guoxing and Tongxi Yu. 2003. *Energy Absorption of Structures and Materials*. Vol. 30. First Edit. Woodhead Publishing.

- Luo, Haibo, Ying Yan, Xiangji Meng, and Can Jin. 2016. "Progressive Failure Analysis and Energy-Absorbing Experiment of Composite Tubes under Axial Dynamic Impact." *Composites Part B: Engineering* 87:1–11.
- Mahdi, E., A. M. S. Hamouda, and T. A. Sebaey. 2014. "The Effect of Fiber Orientation on the Energy Absorption Capability of Axially Crushed Composite Tubes." *Materials and Design* 56:923–28.
- Mamalis, A. G., D. E. Manolakos, G. A. Demosthenous, and M. B. Ioannidis. 1996. "Analysis of Failure Mechanisms Observed in Axial Collapse of Thin-Walled Circular Fibreglass Composite Tubes." *Thin-Walled Structures* 24(4):335–52.
- Mamalis, A. G., D. E. Manolakos, G. A. Demosthenous, and M. B. Ioannidis. 1998. *Crashworthiness of Composite Thin-Walled Structural Components*. First edit. CRC Press.
- Mamalis, A. G., D. E. Manolakos, M. B. Ioannidis, and D. P. Papapostolou. 2004. "Crashworthy Characteristics of Axially Statically Compressed Thin-Walled Square CFRP Composite Tubes: Experimental." *Composite Structures* 63(3–4):347–60.
- Mamalis, A. G., D. E. Manolakos, M. B. Ioannidis, and D. P. Papapostolou. 2006. "The Static and Dynamic Axial Collapse of CFRP Square Tubes: Finite Element Modelling." *Composite Structures* 74(2):213–25.
- Mamalis, A. G., Y. B. Yuan, and G. L. Viegelahn. 1992. "Collapse of Thin-Wall Composite Sections Subjected to High Speed Axial Loading." *International Journal of Vehicle Design* 13(5–6):564–79.
- Marathe, Shrikant R. 2013. "Light Weighting in Automotive Industry." in *Automotive Manufacturing Solutions India Conference*.
- Matthews, F. L., G. A. O. Davies, D. Hitchings, and C. Soutis. 2000. "Composites and Finite Element Analysis." Pp. 71–93 in *Finite Element Modelling of Composite Materials and Structures*. Elsevier.
- Matzenmiller, A., J. Lubliner, and R. L. Taylor. 1995. "A Constitutive Model for Anisotropic Damage in Fiber-Composites." *Mechanics of Materials* 20(2):125–52.
- McGregor, Carla, Reza Vaziri, and Xinran Xiao. 2010. "Finite Element Modelling of the Progressive Crushing of Braided Composite Tubes under Axial Impact." *International Journal of Impact Engineering* 37(6):662–72.
- McGregor, Carla, Navid Zobeiry, Reza Vaziri, Anoush Poursartip, and Xinran Xiao. 2017. "Calibration and Validation of a Continuum Damage Mechanics Model in Aid of Axial Crush Simulation of Braided Composite Tubes." *Composites Part A: Applied Science and Manufacturing* 95:208–19.
- Measurement, N. O. T. 2002. "Handbook Composite Materials Handbook Volume 1 . Polymer Matrix Composites Guidelines for Characterization." *Measurement* 1(June).
- Morthorst, M. and P. Horst. 2004. "Failure Model for Composite Materials under Quasi-Static Crushing Conditions." *Journal of Strain Analysis for Engineering Design* 39(5):411–21.
- Okano, M., A. Nakai, and H. Hamada. 2005. "Axial Crushing Performance of Braided Composite Tubes." *International Journal of Crashworthiness* 10(3):287–94.
- Palanivelu, Sivakumar, Wim Van Paepegem, Joris Degrieck, Johan Van Ackeren, Dimitrios Kakogiannis, Danny Van Hemelrijck, Jan Wastiels, and John Vantomme. 2010. "Experimental Study on the Axial Crushing Behaviour of Pultruded Composite Tubes." *Polymer Testing* 29(2):224–34.
- Palanivelu, Sivakumar, Wim Van Paepegem, Joris Degrieck, Johan Van Ackeren, Dimitrios Kakogiannis, Jan Wastiels, Danny Van Hemelrijck, and John Vantomme. 2010.

- “Parametric Study of Crushing Parameters and Failure Patterns of Pultruded Composite Tubes Using Cohesive Elements and Seam: Part II - Multiple Delaminations and Initial Geometric Imperfections.” *Polymer Testing* 29(7):803–14.
- Palanivelu, Sivakumar, Wim Van Paepegem, Joris Degrieck, Dimitrios Kakogiannis, Johan Van Ackeren, Danny Van Hemelrijck, Jan Wastiels, and John Vantomme. 2010. “Parametric Study of Crushing Parameters and Failure Patterns of Pultruded Composite Tubes Using Cohesive Elements and Seam, Part I: Central Delamination and Triggering Modelling.” *Polymer Testing* 29(6):729–41.
- Patel, Shivdayal, Venkata Ravi Vusa, and C. Guedes Soares. 2019. “Crashworthiness Analysis of Polymer Composites under Axial and Oblique Impact Loading.” *International Journal of Mechanical Sciences* 156(December 2018):221–34.
- Pinho, S. T., P. Robinson, and L. Iannucci. 2006. “Fracture Toughness of the Tensile and Compressive Fibre Failure Modes in Laminated Composites.” *Composites Science and Technology* 66(13):2069–79.
- Quaresimin, Marino, Mauro Ricotta, Livio Martello, and Stefano Mian. 2013. “Energy Absorption in Composite Laminates under Impact Loading.” *Composites Part B: Engineering* 44(1):133–40.
- Raimondo, L., L. Iannucci, P. Robinson, and P. T. Curtis. 2012. “A Progressive Failure Model for Mesh-Size-Independent FE Analysis of Composite Laminates Subject to Low-Velocity Impact Damage.” *Composites Science and Technology* 72(5):624–32.
- Ramakrishna, S., H. Hamada, Z. Maekawa, and H. Sato. 1995. “Energy Absorption Behavior of Carbon-Fiber-Reinforced Thermoplastic Composite Tubes.” *Journal of Thermoplastic Composite Materials* 8(3):323–44.
- Rasheed, Touqeer, Sohaib Akbar, and Sajid Mirza. 2013. “Experimental Investigation of Filament-Wound Composite Tubes for Mechanical Characterization by Internal Pressure Testing.” *Proceedings of 2013 10th International Bhurban Conference on Applied Sciences and Technology, IBCAST 2013* 25–29.
- Reddy, J. N. 2003. *Mechanics of Laminated Composite Plates and Shells: Theory and Analysis*. Second Edi. CRC Press.
- Reuter, Corin, Kim Henning Sauerland, and Thomas Tröster. 2017. “Experimental and Numerical Crushing Analysis of Circular CFRP Tubes under Axial Impact Loading.” *Composite Structures* 174:33–44.
- Schmueser, D. W. and L. E. Wickliffe. 1987. “Impact Energy Absorption of Continuous Fiber Composite Tubes.” *Journal of Engineering Materials and Technology* 109(1):72.
- Schultz, M. R. and M. W. Hyer. 2001. “Static Energy Absorption Capacity of Graphite-Epoxy Tubes.” *Journal of Composite Materials* 35(19):1747–61.
- Scueser, D. W. and Wickliffe L.E. 1987. “Impact Energy Absorption of Continuous Fibre Composite Tubes.” *Journal of Engineering Materials and Technology* 72-77.
- Shi, Y., C. Pinna, and C. Soutis. 2016. “Low-Velocity Impact of Composite Laminates.” Pp. 117–46 in *Dynamic Deformation, Damage and Fracture in Composite Materials and Structures*. Elsevier.
- Sills, Pau. 2008. “A Novel Solution for Achieving Lightweight, Safe Vehicle Structures Through Composites.” in *ARB Symposium Greenhouse Gas Reduction Sacramento, California*.
- Singh, Gurmeet, David Kumar, and P. M. Mohite. 2017. “Damage Modelling of Epoxy Material under Uniaxial Tension Based on Micromechanics and Experimental Analysis.” *Archive of Applied Mechanics* 87(4):721–36.
- Siromani, Deepak, Jonathan Awerbuch, and Tein Min Tan. 2014. “Finite Element Modeling of

- the Crushing Behavior of Thin-Walled CFRP Tubes under Axial Compression." *Composites Part B: Engineering* 64:50–58.
- Sokolinsky, Vladimir S., Kyle C. Indermuehle, and Juan A. Hurtado. 2011. "Numerical Simulation of the Crushing Process of a Corrugated Composite Plate." *Composites Part A: Applied Science and Manufacturing* 42(9):1119–26.
- Soto, A., E. V. González, P. Maimí, F. Martín de la Escalera, J. R. Sainz de Aja, and E. Alvarez. 2018. "Low Velocity Impact and Compression after Impact Simulation of Thin Ply Laminates." *Composites Part A: Applied Science and Manufacturing* 109:413–27.
- Sun, Z. C. and H. Yang. 2006. "Free Deformation Mechanism and Change of Forming Mode in Tube Inversion under Conical Die." *Journal of Materials Processing Technology* 177(1–3):171–74.
- Tan, Wei, Brian G. Falzon, Louis N. S. Chiu, and Mark Price. 2015. "Predicting Low Velocity Impact Damage and Compression-After-Impact (CAI) Behaviour of Composite Laminates." *Composites Part A: Applied Science and Manufacturing* 71:212–26.
- Tan, Wei, Brian G. Falzon, and Mark Price. 2015. "Predicting the Crushing Behaviour of Composite Material Using High-Fidelity Finite Element Modelling." *International Journal of Crashworthiness* 20(1):60–77.
- Tan, Wei, Brian G. Falzon, Mark Price, and Haibao Liu. 2016. "The Role of Material Characterisation in the Crush Modelling of Thermoplastic Composite Structures." *Composite Structures* 153:914–27.
- Thornton, P. H. 1979. "Energy Absorption in Composite Structures." *Journal of Composite Materials* 13(3):247–62.
- Thornton, P. H. 1990. "The Crush Behavior of Pultruded Tubes at High Strain Rates." *Journal of Composite Materials* 24(6):594–615.
- Thornton, P. H., W. H. Tao, and R. E. Robertson. 1991. "Crash Energy Management: Axial Crush of Unidirectional Fiber Composite Rods." Pp. 489–96 in *New Development and Applications*.
- Thuis, H. G. S. J. and V. H. Metz. 1994. "The Influence of Trigger Configurations and Laminate Lay-up on the Failure Mode of Composite Crush Cylinders." *Composite Structures* 28(2):131–37.
- Tong, Yan and Yuanming Xu. 2018. "Improvement of Crash Energy Absorption of 2D Braided Composite Tubes through an Innovative Chamfer External Triggers." *International Journal of Impact Engineering* 111:11–20.
- Vasiliev, Valery and Evgeny Morozov. 2013. *Advanced Mechanics of Composite Materials and Structural Elements [Electronic Resource]*. 3rd Editio. Elsevier.
- Ventsel, Eduard and Theodor Krauthammer. 2001. *Thin Plates and Shells*. CRC Press.
- Wang, Yifan, Jiusheng Feng, Jianghao Wu, and Dayong Hu. 2016. "Effects of Fiber Orientation and Wall Thickness on Energy Absorption Characteristics of Carbon-Reinforced Composite Tubes under Different Loading Conditions." *Composite Structures* 153:356–68.
- Ward, Ian M. and John Sweeney. 2012. *Mechanical Properties of Solid Polymers*. edited by 3rd Edition. Chichester, UK: John Wiley & Sons, Ltd.
- Welsh, J. S. and Donald F. Adams. 1997. "Testing of Angle-Ply Laminates to Obtain Unidirectional Composite Compression Strengths." *Composites Part A: Applied Science and Manufacturing* 28(4):387–96.
- Welsh, Js and DF Adams. 1996. "Unidirectional Composite Compression Strengths Obtained by Testing Cross-Ply Laminates." *Journal of Composites Technology & Research*

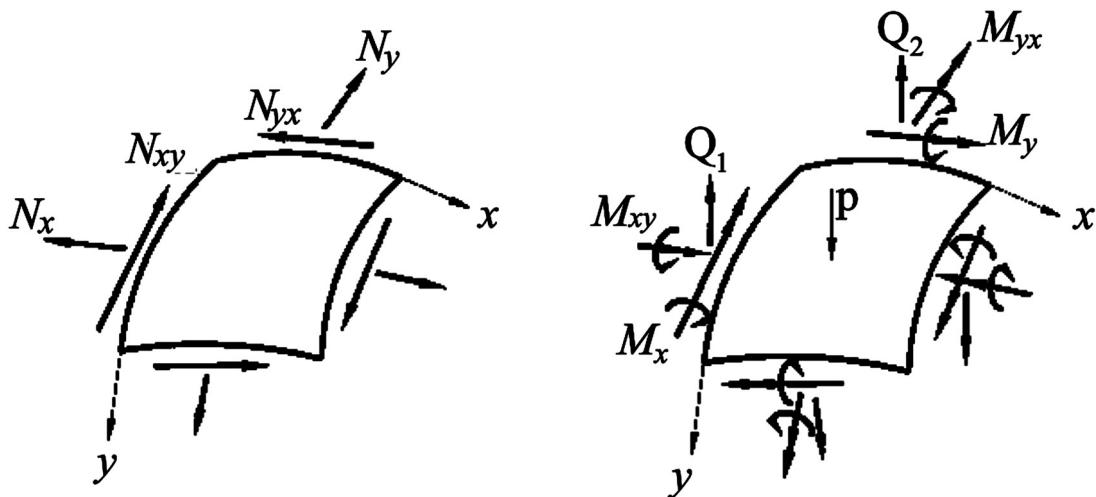
- 18(04):241–48.
- Wierzbicki, T., S. U. Bhat, W. Abramowicz, and D. Brodtkin. 1992. “Alexander Revisited—A Two Folding Elements Model of Progressive Crushing of Tubes.” *International Journal of Solids and Structures* 29(24):3269–88.
- World Health Organization. 2018. *Global Status Report on Road Safety*.
- Yang, Yuqiu, Asami Nakai, and Hiroyuki Hamada. 2009. “A Method to Improve the Energy Absorption Capability of Fibre-Reinforced Composite Tubes.” *International Journal of Crashworthiness* 14(4):315–22.
- Yeow-Cheong, N. G. 2005. “Deriving Composite Lamina Properties from Laminate Properties Using Classical Lamination Theory and Failure Criteria.” *Journal of Composite Materials* 39(14):1295–1306.
- Young, W. C. and R. G. Budynas. 2002. *Roark’s Formulas for Stress and Strain*. Seventh Ed. The McGraw-Hill Companies, Inc.
- Zhang, Chao, Enock A. Duodu, and Jinan Gu. 2017. “Finite Element Modeling of Damage Development in Cross-Ply Composite Laminates Subjected to Low Velocity Impact.” *Composite Structures* 173:219–27.
- Zhao, Xuan, Guohua Zhu, Chenyu Zhou, and Qiang Yu. 2019. “Crashworthiness Analysis and Design of Composite Tapered Tubes under Multiple Load Cases.” *Composite Structures* 222(April):110920.
- Zhu, Guohua, Guangyong Sun, Hang Yu, Shunfeng Li, and Qing Li. 2018. “Energy Absorption of Metal, Composite and Metal/Composite Hybrid Structures under Oblique Crushing Loading.” *International Journal of Mechanical Sciences* 135(November 2017):458–83.
- Zhu Yigang, Wang Jin, and Zhang Zilong. 2012. “Finite Element Simulation on Impact Energy Absorption of Carbon Fiber Laminated Plate.” *Computer Aided Engineering* 22(2).

## **Appendices**

## Appendix A: Strain-force relations of laminated component based on CLT

The constitutive relations for a thin shallow laminated shell can be expressed by Eq. (A1) which relates the in-plane force resultants,  $\{N\}$ , moment resultant,  $\{M\}$  and shear forces,  $\{Q\}$  to the deformations of the laminate middle surface (Reddy 2003). Figure A1 shows the force and moment resultant on a shell element. The matrices  $[A]$ ,  $[B]$  and  $[D]$  are  $3 \times 3$  matrices of extensional, bending-extensional and bending stiffnesses of the laminate, respectively (Reddy 2003; Daniel et al. 2006). The matrices  $[a]$ ,  $[b]$ ,  $[c]$  and  $[d]$  are the laminate compliance matrices (Daniel et al. 2006; Reddy 2003). The relations used to calculate the stiffness matrices,  $[A]$ ,  $[B]$  and  $[D]$ , by CLT are presented in many textbooks (Reddy 2003; Daniel et al. 2006).

Figure A1 - Stress resultants on a shell element.



Source: (Reddy 2003)

$$\begin{Bmatrix} \{N\} \\ \{M\} \end{Bmatrix} = \begin{bmatrix} [A] & [B] \\ [B] & [D] \end{bmatrix} \begin{Bmatrix} \{\varepsilon^0\} \\ \{\kappa\} \end{Bmatrix}, \quad \begin{Bmatrix} Q_1 \\ Q_2 \end{Bmatrix} = \begin{bmatrix} A_{44} & A_{45} \\ A_{54} & A_{55} \end{bmatrix} \begin{Bmatrix} \varepsilon_4^0 \\ \varepsilon_5^0 \end{Bmatrix}, \quad (\text{A1})$$

where  $\varepsilon_4^0$  and  $\varepsilon_5^0$  are out-of-plane shear strain of shell mid-surface ( $\sigma_{13}^0, \sigma_{23}^0$ )

$$\begin{Bmatrix} \{\varepsilon^0\} \\ \{\kappa\} \end{Bmatrix} = \begin{bmatrix} [a] & [b] \\ [c] & [d] \end{bmatrix} \begin{Bmatrix} \{N\} \\ \{M\} \end{Bmatrix} \quad (\text{A2})$$

$$\begin{bmatrix} [a] & [b] \\ [c] & [d] \end{bmatrix} = \begin{bmatrix} [A] & [B] \\ [B] & [D] \end{bmatrix}^{-1}$$

For a general laminate subjected to in-plane loading, Eqs. (A1) and (A2) can be reduced as follows (Daniel et al. 2006).

$$\begin{bmatrix} N_x \\ N_y \\ N_s \end{bmatrix} = \begin{bmatrix} A_{xx} & A_{xy} & A_{xs} \\ A_{yx} & A_{yy} & A_{ys} \\ A_{sx} & A_{sy} & A_{ss} \end{bmatrix} \begin{bmatrix} \varepsilon_x^0 \\ \varepsilon_y^0 \\ \gamma_s^0 \end{bmatrix} \quad (\text{A3})$$

$$\begin{bmatrix} \varepsilon_x^0 \\ \varepsilon_y^0 \\ \gamma_s^0 \end{bmatrix} = \begin{bmatrix} a_{xx} & a_{xy} & a_{xs} \\ a_{yx} & a_{yy} & a_{ys} \\ a_{sx} & a_{sy} & a_{ss} \end{bmatrix} \begin{bmatrix} N_x \\ N_y \\ N_s \end{bmatrix} = \begin{bmatrix} \varepsilon_x^0 \\ \varepsilon_y^0 \\ \gamma_s^0 \end{bmatrix} = [a] \begin{bmatrix} N_x \\ N_y \\ N_s \end{bmatrix} \quad (\text{A4})$$

The laminate stiffness matrices,  $[A]$ ,  $[B]$  and  $[D]$ , by CLT can be expressed as follows (Reddy 2003).

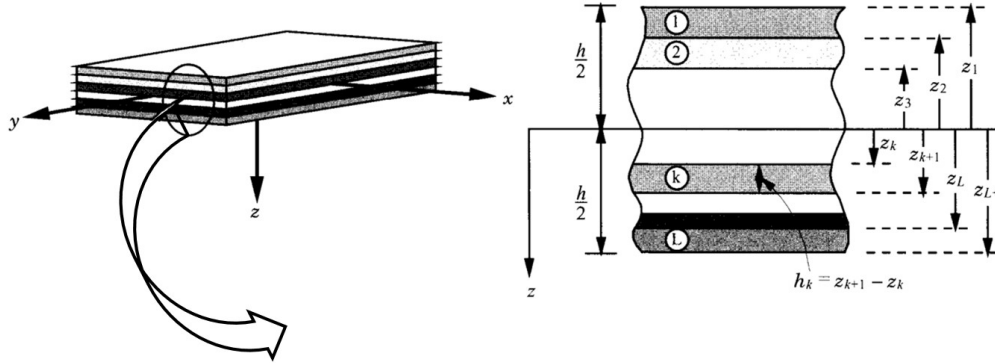
$$A_{ij} = \sum_{k=1}^n \bar{Q}_{ij}^{(k)} (z_{k+1} - z_k), i, j = 1, 2, 6 \quad (\text{A5})$$

$$B_{ij} = \frac{1}{2} \sum_{k=1}^n \bar{Q}_{ij}^{(k)} (z_{k+1}^2 - z_k^2), i, j = 1, 2, 6 \quad (\text{A6})$$

$$D_{ij} = \frac{1}{3} \sum_{k=1}^n \bar{Q}_{ij}^{(k)} (z_{k+1}^3 - z_k^3), i, j = 1, 2, 6 \quad (\text{A7})$$

where  $\bar{Q}_{ij}^{(k)}$  are the transformed stiffnesses of the  $k$ -th lamina and  $z_k$  is lamina distance from shell middle surface, see Figure A2. The transformed stiffnesses of a lamina can be expressed by Eq. (A8) while the angle between  $x$ -direction of the laminate and 1-direction of lamina equals to  $\theta$ -degree ( $\sin\theta = n$ ,  $\cos\theta = m$ ).

Figure A2 - Coordinate system and layer numbering.



Source: (Reddy 2003).

$$\bar{Q}_{11} = Q_{11}m^4 + 2(Q_{12} + 2Q_{66})m^2n^2 + Q_{22}n^4 \quad (\text{A8a})$$

$$\bar{Q}_{12} = (Q_{11} + Q_{22} - 4Q_{66})m^2n^2 + Q_{12}(n^4 + m^4) \quad (\text{A8b})$$

$$\bar{Q}_{22} = Q_{11}n^4 + 2(Q_{12} + 2Q_{66})m^2n^2 + Q_{22}m^4 \quad (\text{A8c})$$

$$\bar{Q}_{16} = (Q_{11} - Q_{12} - 2Q_{66})m^3n + (Q_{12} - Q_{22} + 2Q_{66})n^3m \quad (\text{A8d})$$

$$\bar{Q}_{26} = (Q_{11} - Q_{12} - 2Q_{66})n^3m + (Q_{12} - Q_{22} + 2Q_{66})m^3n \quad (\text{A8e})$$

$$\bar{Q}_{66} = (Q_{11} + Q_{22} - 2Q_{12} - 2Q_{66})m^2n^2 + Q_{66}((n^4 + m^4)) \quad (\text{A8f})$$

$$\bar{Q}_{44} = Q_{44}m^2 + Q_{55}n^2 \quad (\text{A8g})$$

$$\bar{Q}_{45} = (Q_{55} - Q_{44})mn \quad (\text{A8h})$$

$$\bar{Q}_{55} = Q_{44}n^2 + Q_{55}m^2 \quad (\text{A8i})$$

$$Q_{11} = \frac{E_1}{1 - \nu_{12}\nu_{21}} \quad (\text{A9a})$$

$$Q_{22} = \frac{E_2}{1 - \nu_{12}\nu_{21}} \quad (\text{A9b})$$

$$Q_{12} = \nu_{12} Q_{22} \quad (\text{A9c})$$

$$Q_{21} = \nu_{21} Q_{11} \quad (\text{A9d})$$

$$Q_{66} = G_{12} \quad (\text{A9e})$$

## Appendix B: Derivation of explicit lamina-laminate relations for the in-plane mechanical properties of cross-plyed specimens

The in-plane/flexure coupling laminate moduli,  $B_{ij}$  and in-plane normal/shear couplings  $A_{13}$ ,  $A_{23}$  for a balanced and symmetric cross-plyed tube are zeros, thus the force-deformation relation yields to Eq. (B1). The UD plies in a balanced and symmetric cross-plyed laminate are oriented parallel to, or balanced about two perpendicular axes, so-called principal laminate axes. At a macroscopic level, this laminate can be considered as a homogeneous orthotropic material in which the two above mentioned perpendicular axes are the principal axes of an equivalent material, known as an orthotropic laminate (Daniel et al. 2006). Thus, an equivalent orthotropic for balance-symmetric cross-plyed laminate is conceivable. The force-deformation relation of an orthotropic shell-like component is presented in Eq. (B2) as

$$\begin{Bmatrix} N_{xx} \\ N_{yy} \\ N_{xy} \end{Bmatrix} = \begin{bmatrix} A_{xx} & A_{xy} & 0 \\ A_{yx} & A_{yy} & 0 \\ 0 & 0 & A_{33} \end{bmatrix} \begin{Bmatrix} \varepsilon_{xx}^0 \\ \varepsilon_{yy}^0 \\ \gamma_{xy}^0 \end{Bmatrix} \quad (\text{B1})$$

$$\begin{Bmatrix} N_{xx} \\ N_{yy} \\ N_{xy} \end{Bmatrix} = \begin{bmatrix} C_{xx} & C_{xy} & 0 \\ C_{yx} & C_{yy} & 0 \\ 0 & 0 & C_{33} \end{bmatrix} \begin{Bmatrix} \varepsilon_{xx}^0 \\ \varepsilon_{yy}^0 \\ \gamma_{xy}^0 \end{Bmatrix}. \quad (\text{B2})$$

The components of in-plane stiffness matrices in Eqs. (B1) and (B2), when UD plies are arranged parallel/transverse to the  $x$ - and  $y$ -directions of the laminate, are defined by Eqs. (B3) and (B4) by using CLT and definition of orthotropic material, respectively. The general relationships to calculate  $A_{ij}$  components are defined by Eqs. (B8) and (B9).

$$A_{xx} = h_0 Q_{11} + h_{90} Q_{22} \quad (\text{B3a})$$

$$A_{xy} = A_{12} = Q_{12}(h_0 + h_{90}) = Q_{12}h = Q_{21}h \quad (\text{B3b})$$

$$A_{yy} = h_0 Q_{22} + h_{90} Q_{11} \quad (\text{B3c})$$

$$A_{33} = Q_{66}(h_0 + h_{90}) = G_{12}h \quad (\text{B3d})$$

$$C_{xx} = \frac{E_x h}{1 - \nu_{xy}\nu_{yx}} \quad (\text{B4a})$$

$$C_{yy} = \frac{E_y h}{1 - \nu_{xy}\nu_{yx}} \quad (\text{B4b})$$

$$C_{yx} = C_{xy} = \frac{\nu_{xy} E_y h}{1 - \nu_{xy}\nu_{yx}} = \frac{\nu_{yx} E_x h}{1 - \nu_{xy}\nu_{yx}} \quad (\text{B4c})$$

$$G_{33} = hG_{xy} \quad (\text{B4d})$$

where  $h$ ,  $h_0$ ,  $h_{90}$  are the total thickness of the laminate, the total thickness of UD layers in the  $x$ -direction and the total thickness of UD plies in the  $y$ -direction of the lamination, respectively.  $E_i$ ,  $\nu_{ij}$  and  $G_{ij}$  are mechanical properties of UD lamina ( $i = 1, j = 2$ ) and mechanical properties of the orthotropic laminate ( $i = x, j = y$ ).

Eqs. (B1) and (B2) are identical, therefore, the corresponding components of extensional matrix  $[A]$  (Eq. (B1)) and stretching matrix  $[C]$  (Eq. (B2)) must be equal i.e.  $A_{ij} = C_{ij}$ . These qualities are presented by Eq. (B5).

$$\frac{E_x h}{1 - \nu_{xy}\nu_{yx}} = h_0 Q_{11} + h_{90} Q_{22} \quad (\text{B5a})$$

$$\frac{E_y h}{1 - \nu_{xy}\nu_{yx}} = h_0 Q_{22} + h_{90} Q_{11} \quad (\text{B5b})$$

$$\frac{\nu_{xy} E_y h}{1 - \nu_{xy}\nu_{yx}} = Q_{12}(h_0 + h_{90}) = h\nu_{12} Q_{22} \quad (\text{B5c})$$

$$\frac{\nu_{yx} E_x h}{1 - \nu_{xy}\nu_{yx}} = Q_{21}(h_0 + h_{90}) = h\nu_{21} Q_{11} \quad (\text{B5d})$$

$$hG_{xy} = Q_{66}(h_0 + h_{90}) = G_{12}h \quad (\text{B5e})$$

By solving Eqs. (B5), the mechanical properties of UD lamina can be expressed explicitly as functions of the mechanical properties of the orthotropic laminate, or effective mechanical properties of cross-plyed specimens, as presented in chapter 3.

### Appendix C: Role of the $[(90)_2/0]_s$ inner layers of the cross-plyed specimen in the energy absorption capacity

The compressive behavior of the middle  $0^\circ$  layers placed between  $90^\circ$  layers includes splitting of  $0^\circ$  layers into lamina bundles which undergo buckling and kinking and finally break in short length pieces due to fiber breakage, transverse to fiber orientation. Figure C1 (a) shows schematically the  $[(90)_2/0]_s$  layers which the  $0^\circ$  layer split into  $N$  lamina bundles of  $a$  mm width,  $b$  mm thickness and  $\Delta l$  mm unsupported beam length. The buckling process can be modeled by a clamped-free buckling of a beam (Thornton 1979), with the critical buckling load,  $P_{cb}$ , lamina bundle being

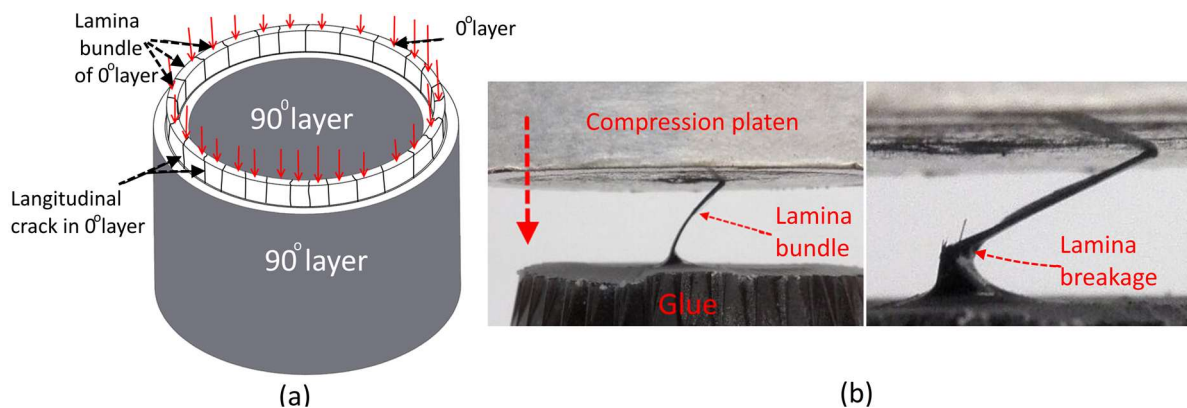
$$P_{cb} = \frac{\pi^2 EI}{4(\Delta l)^2} \quad (C1)$$

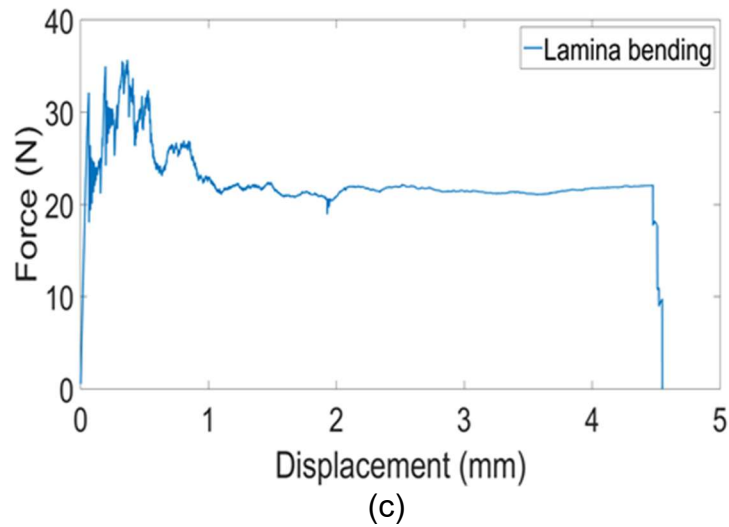
where  $I = b^3 a/12$ . Therefore, the critical buckling load of the whole  $0^\circ$  layer in the middle of  $[(90)_2/0]_s$  reads

$$P = P_{cb} \times N \quad (C2)$$

where the number of bundles  $N = 2\pi R(0^\circ)/a$  and  $R(0^\circ)$  is the radius of the  $0^\circ$  layer.

Figure C1 - Lamina bundle performance under compression; (a)  $0^\circ$  layer split in lamina bundles; (b) Experimental compression on a single lamina bundle; (c) Performance of a lamina bundle with 7.5 mm unsupported length, 6.3 mm width and 0.23 mm thickness.





Source: The author.

According to Figure 4.5(a) (frame 5),  $\Delta l$  is approximately equal to 3 mm and the total thickness of the two adjacent plies with  $0^\circ$  fiber orientation is 0.4 mm (Figure 4.5(b)) while the surrounding undamaged  $90^\circ$  layers provide clamped conditions at the distal end of the bundle. The process of damaging the surrounding  $90^\circ$  layers and buckling of the clamped-free middle  $0^\circ$  layers repeated several times during the crush event. The sustained average crushing force can be estimated as 32 kN approximately according to Eq. (C2) when using  $E = 135\text{GPa}$  (elastic modulus of UD lamina). The obtained force value is therefore comparable with the average crushing force of a cross-plyed tube under quasi-static compression (Table 4-3).

A simple compression test is shown in Figure C1 (b) was designed to estimate the energy absorbed by  $0^\circ$  layers in  $[(90)_2/0]_s$  aggregate due to buckling until lamina bundle breakage. An intact lamina bundle (taken from the outer  $0^\circ$  layer) is glued in epoxy resin modeling the clamped condition and subjected to axial compression. For convenience, a longer lamina bundle of  $l_{test} = 7.5$  mm unsupported length, width  $a = 6.3$  mm and thickness  $b_{test} = 0.23$  mm was glued and underwent quasi-static compression. The measured force-displacement history per unit bundle width,  $F_{test}$ , until breaking, is shown in Figure C1(c). Using this curve, the absorbed energy of the bundle is calculated as

$$AE_{Bundle,Test} = a \int_0^{\delta_{test}} F_{test} dx = 0.108J \quad (C3)$$

for a crushing distance  $\delta_{test} = 4.5$  mm. This energy is used to obtain the average load of the bundle

$$F_{Av,Test} = \frac{AE_{Bundle,Test}}{\delta_{test}}. \quad (C4)$$

The energy obtained in the compression test was scaled next to find the energy absorbed by the  $0^\circ$  layers in  $[(90)_2/0]_s$  aggregate with an unsupported length  $l_s = \Delta l = 3$  mm, thickness  $b_s = 0.4$  mm and  $a_s = 6.3$  mm. It is assumed that the force-displacement curve can be scaled by the buckling load and crushing distance can be scaled by the lengths of the two geometries so that the scaled average force of the above bundle is

$$F_{Av,s} = F_{Av,Test} \frac{l_{test}^2 b_s^3}{b_{test}^3 l_s^2} \quad (C5)$$

while the scaled crushing distance is

$$\delta_s = \delta_{test} \frac{l_s}{l_{test}}. \quad (C6)$$

Thus, the energy absorbed by the scaled bundle is

$$AE_{Bundle,s} = F_{Av,s} \times \delta_s = AE_{Bundle,Test} \frac{b_s^3 l_{test}}{b_{test}^3 l_s} = 1.34J \quad (C7)$$

The energy absorbed by the entire  $0^\circ$  lamina in  $[(90)_2/0]_s$  aggregate is then  $AE_s = N \times AE_{Bundle,s} = 34.84$  J. With a conservative assumption, the same crushing process will repeat 20 times for a tube with 60 mm crushed length ( $60/3 = 20$ ) to result in absorbed energy of 696 J. Therefore, the bending and fracture of lamina bundles (in effective  $[(90)_2/0]_s$  layers of cross-ply specimen) is responsible for about 35% of the total absorbed energy of approximately 2000 J (see Table 4.3 for cross-ply specimens under quasi-static compression). Considering that the damage of the  $90^\circ$  layers due to

fibers and matrix failure as well as friction dissipate a certain amount of the compression energy, it appears that the both-side constrained  $0^\circ$  lamina is responsible for the absorption of a significant proportion of the total energy being one of the major mechanisms of energy absorption of cross-ply tubes (Wang et al. 2016; Jacob et al. 2002).

## Appendix D: Values of fracture energies presented in the literature related to the axial impact on composite absorbers and lateral impact on laminated plates

Table D.1 lists the fracture energies used to model axial impact on composite absorbers and compares these values with the energies stored in element (1×1 mm size) up to damage initiation point. Table D.2 makes the same comparison between fracture energies presented in simulations of lateral impact on laminated composite by using Abaqus/Explicit code.

Table D.1 - Fracture energies presented in the literature related to the axial impact simulation on composite absorbers.									
(Chiu et al. 2016)	Mechanical properties								
	$E_1$	$E_2$	$G_{12}$	$\nu_{12}$	$X^T$	$X^C$	$Y^T$	$Y^C$	$S_{12}$
	135	9.12	5.67	0.31	2326	1236	51	209	87.9
	Fracture energies in the reference								
	$G_{ft}^c$	$G_{fc}^c$	$G_{mt}^c$	$G_{mc}^c$					
	108	58.4	0.425	1.1					
	Energy under equivalent stress- displacement curve up to damage initiation								
	$G_{ft}^c$	$G_{fc}^c$	$G_{mt}^c$	$G_{mc}^c$					
	20.72	5.65	0.82	3.07					
	Difference between energies in the references to the energies up to damage initiation points (%)								
	421%	933%	-48%	-64%					
	Mechanical properties								
	$E_1$	$E_2$	$G_{12}$	$\nu_{12}$	$X^T$	$X^C$	$Y^T$	$Y^C$	$S_{12}$
	142	8.4	4.6	0.32	2282	1465	65	290	105
	Fracture energies in the reference								
	$G_{ft}^c$	$G_{fc}^c$	$G_{mt}^c$	$G_{mc}^c$					
	108	58.4	0.331	1.1					
	Energy under equivalent stress- displacement curve up to damage initiation								
	$G_{ft}^c$	$G_{fc}^c$	$G_{mt}^c$	$G_{mc}^c$					
	19.53	7.55	1.45	6.20					
	Difference between energies in the references to the energies up to damage initiation points (%)								
	453%	620%	-77%	82%					
	Mechanical properties								
	$E_1$	$E_2$	$G_{12}$	$\nu_{12}$	$X^T$	$X^C$	$Y^T$	$Y^C$	$S_{12}$
138	8.42	3.93	0.257	1496	1026	90	211	77	
Fracture energies in the reference									
$G_{ft}^c$	$G_{fc}^c$	$G_{mt}^c$	$G_{mc}^c$						
91	79	0.15	0.45						

Table D.1 - Fracture energies presented in the literature related to the axial impact simulation on composite absorbers.								
Energy under equivalent stress- displacement curve up to damage initiation								
$G_{ft}^c$		$G_{fc}^c$		$G_{mt}^c$		$G_{mc}^c$		
8.86		3.81		1.23		3.39		
Difference between energies in the references to the energies up to damage initiation points (%)								
927%		1973%		-87%		-86%		
Mechanical properties								
$E_1$	$E_2$	$G_{12}$	$\nu_{12}$	$X^T$	$X^C$	$Y^T$	$Y^C$	$S_{12}$
127	8.41	4.21	0.309	2200	1470	48.9	199	154
Fracture energies in the reference								
$G_{ft}^c$		$G_{fc}^c$		$G_{mt}^c$		$G_{mc}^c$		
108		58.4		0.504		1.1		
Energy under equivalent stress- displacement curve up to damage initiation								
$G_{ft}^c$		$G_{fc}^c$		$G_{mt}^c$		$G_{mc}^c$		
21.87		8.50		2.95		5.17		
Difference between energies in the references to the energies up to damage initiation points (%)								
394%		587%		-83%		-78%		
Note: Unit for elastic moduli are GPa, for fracture energies is mJ/mm <sup>2</sup> and for strengths is MPa.								

Table D.2 - Fracture energies presented in the literature related to the lateral impact simulation on composite plates									
(Tan et al. 2015)	Mechanical properties								
	$E_1$	$E_2$	$G_{12}$	$\nu_{12}$	$X^T$	$X^C$	$Y^T$	$Y^C$	$S_{12}$
	130	7.7	4.8	0.3	2080	1250	60	290	110
	Fracture energies in the reference								
	$G_{ft}^c$		$G_{fc}^c$		$G_{mt}^c$		$G_{mc}^c$		
	133		10		0.5		1.6		
(Zhang, Duodu, and Gu 2017)	Mechanical properties								
	$E_1$	$E_2$	$G_{12}$	$\nu_{12}$	$X^T$	$X^C$	$Y^T$	$Y^C$	$S_{12}$
	153	10.3	6.0	0.3	2537	1580	82	236	90
	Fracture energies in the reference								
	$G_{ft}^c$		$G_{fc}^c$		$G_{mt}^c$		$G_{mc}^c$		
	10		10		1		1		
(Raimondo et al. 2012)	Mechanical properties								
	$E_1$	$E_2$	$G_{12}$	$\nu_{12}$	$X^T$	$X^C$	$Y^T$	$Y^C$	$S_{12}$
	114	8.6	4.45	0.3	1850	1200	35	170	75
	Fracture energies in the reference								
	$G_{ft}^c$		$G_{fc}^c$		$G_{mt}^c$		$G_{mc}^c$		
	40		40		0.170		1.2		
(Long, Yao, and Zhang 2015)	Mechanical properties								
	$E_1$	$E_2$	$G_{12}$	$\nu_{12}$	$X^T$	$X^C$	$Y^T$	$Y^C$	$S_{12}$
	110	7.8	40	0.32	2093	870	50	198	104
	Fracture energies in the reference								
	$G_{ft}^c$		$G_{fc}^c$		$G_{mt}^c$		$G_{mc}^c$		
	10		10		1		1		
(Soto et al. 2018)	Mechanical properties								
	$E_1$	$E_2$	$G_{12}$	$\nu_{12}$	$X^T$	$X^C$	$Y^T$	$Y^C$	$S_{12}$

Table D.2 - Fracture energies presented in the literature related to the lateral impact simulation on composite plates									
	61.4	61.4	3.78	0.042	975.4	975.4	550	550	85.9
	Fracture energies in the reference								
	$G_{ft}^c$		$G_{fc}^c$		$G_{mt}^c$		$G_{mc}^c$		
	65.4		65.4		$1 \times 10^{-5}$		$1 \times 10^{-5}$		
(Shi, Pinna, and Soutis 2016)	Mechanical properties								
	$E_1$	$E_2$	$G_{12}$	$\nu_{12}$	$X^T$	$X^C$	$Y^T$	$Y^C$	$S_{12}$
	153	10.3	6	0.3	2537	1580	82	236	90
	Fracture energies in the reference								
	$G_{ft}^c$		$G_{fc}^c$		$G_{mt}^c$		$G_{mc}^c$		
	91.6		79.9		0.22		2		
Note: Unit for elastic moduli are GPa, for fracture energies is mJ/mm <sup>2</sup> and for strengths is MPa.									

## **Appendix E: A new model to change input parameters in Abaqus progressive failure analysis**

In the previous section, it was observed that 2D progressive analysis for fiber-reinforced composites in Abaqus failed to reproduce correct behavior of UD lamina especially about crushed morphology in  $0^\circ$  (fibers are parallel to tube axis) and  $90^\circ$  (fibers in the hoop direction) layers in the cross-plyed tubular specimen under axial impact. This section aims to change the regular input method of the material properties of UD lamina in order to have an acceptable force-displacement curve and a better fracture appearance of the tubes.

### **E.1 Description of the new model**

Abaqus treats UD lamina as homogeneous orthotropic or transversely isotropic material. In Abaqus manual (Dassault Systèmes Simulia 2014) there are specific locations to input material properties in the fiber direction or transverse to the fiber direction. In this section, by using a user-defined material subroutine, the locations of material properties (strengths, fracture energies) and sequence of Hashin's criteria will be switched. For instance, in Abaqus regular procedure, 1-direction (the local in-plane material direction) is reserved for material properties in the fiber direction. Likewise, 2-direction is allocated to the properties in the direction transverse to the fiber direction.

In the new input method, called 'switch input' method, a reverse convention should be considered. Figure E.1 compares the difference between Abaqus 'regular input' convention and 'switch input' convention. By using a VUMAT subroutine, it is possible to switch all in-plane input parameters between the fiber direction and transverse to the fiber direction; moreover, Hashin's criteria can be switched to be compatible with this modification. Another version of the 'switch input' method without using material subroutine will be considered here. In this case, all material properties, elastic moduli, fracture energies, and strengths, will be switched between fiber direction and transverse to the fiber direction. However, Hashin's criteria remained unchanged. Abaqus uses the same post-damaged softening for all four failure modes with using a linear energy degradation scheme. Thus, there will be no problem with the new input method from this point of view.

Figure E.1 - Description of 'switch input' procedure by using a VUMAT.

**Elastic parameters input**

	E1	E2	E3	Nu12	Nu13	Nu23	G12	G13	G23
'Regular input'	$E_f$	$E_m$	$E_m$	$Nu_{12}$	$Nu_{13}$	$Nu_{23}$	$G_{12}$	$G_{12}$	$G_{23}$
'Switch input'	$E_m$	$E_f$	$E_m$	$Nu_{21}$	$Nu_{23}$	$Nu_{12}$	$G_{12}$	$G_{23}$	$G_{12}$

**Strength parameters input**

	Longitudinal Tensile Strength	Longitudinal Compressive Strength	Transverse Tensile Strength	Transverse Compressive Strength	Longitudinal Shear Strength	Transverse Shear Strength
'Regular input'	$X_T$	$X_C$	$Y_T$	$Y_C$	$S$	$S$
'Switch input'	$Y_T$	$Y_C$	$X_T$	$X_C$	$S$	$S$

	Longitudinal Tensile Fracture Energy	Longitudinal Compressive Fracture Energy	Transverse Tensile Fracture Energy	Transverse Compressive Fracture Energy
'Regular input'	$G_{ft}$	$G_{fc}$	$G_{mt}$	$G_{mc}$
'Switch input'	$G_{mt}$	$G_{mc}$	$G_{ft}$	$G_{fc}$

**Hashin's criteria**

	1-direction tensile	1-direction compression	2-direction tensile	2-direction compression
'Regular input'	$\left(\frac{\hat{\sigma}_{11}}{X^T}\right)^2 + \left(\frac{\hat{\tau}_{12}}{S^L}\right)^2 = 1$	$\left(\frac{\hat{\sigma}_{11}}{X^C}\right)^2 = 1$	$\left(\frac{\hat{\sigma}_{22}}{Y^T}\right)^2 + \left(\frac{\hat{\tau}_{12}}{S^L}\right)^2 = 1$	$\left(\frac{\hat{\sigma}_{22}}{2S^T}\right)^2 + \left[\left(\frac{Y^C}{2S_{23}}\right)^2 - 1\right] \left(\frac{\hat{\sigma}_{22}}{Y^C}\right)^2 + \left(\frac{\hat{\tau}_{12}}{S_{12}}\right)^2 = 1$
'Switch input'	$\left(\frac{\hat{\sigma}_{22}}{Y^T}\right)^2 + \left(\frac{\hat{\tau}_{12}}{S^L}\right)^2 = 1$	$\left(\frac{\hat{\sigma}_{22}}{2S^T}\right)^2 + \left[\left(\frac{Y^C}{2S_{23}}\right)^2 - 1\right] \left(\frac{\hat{\sigma}_{22}}{Y^C}\right)^2 + \left(\frac{\hat{\tau}_{12}}{S_{12}}\right)^2 = 1$	$\left(\frac{\hat{\sigma}_{11}}{X^T}\right)^2 + \left(\frac{\hat{\tau}_{12}}{S^L}\right)^2 = 1$	$\left(\frac{\hat{\sigma}_{11}}{X^C}\right)^2 = 1$

Source: The author.

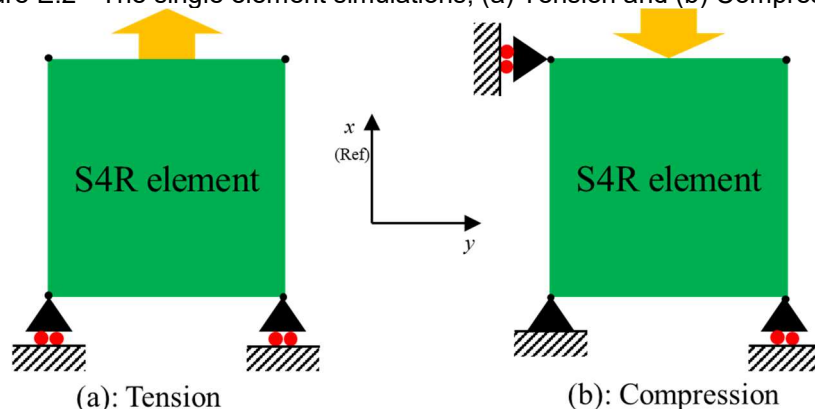
Therefore, when Hashin's criteria are not switched between fiber and transverse to the fiber directions, the following situations occur about damage initiation.

- Hashin's failure theory has similar damage initiations criteria under tension, for both directions; fiber and transverse direction to the fiber. Thus, no conflict will arise.
- Damage initiations criteria under compression are not similar in Hashin's failure theory.

- Maximum stress failure theory ( $\left(\frac{\hat{\sigma}_{11}}{Y^C}\right)^2 = 1$ ) in the new model will be used for matrix failure. This maximum stress failure has been utilized in the literature to predict failure in the matrix.
- Using  $\left(\frac{\hat{\sigma}_{22}}{2S^T}\right)^2 + \left[\left(\frac{Y^C}{2S_{23}}\right)^2 - 1\right] \left(\frac{\hat{\sigma}_{22}}{Y^C}\right) + \left(\frac{\hat{\tau}_{12}}{S_{12}}\right)^2 = 1$  to predict the damage initiation in the fiber direction of UD lamina can be incorrect.

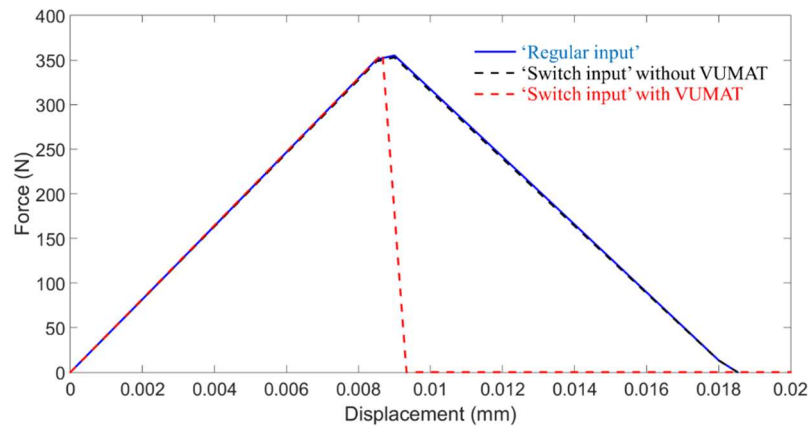
In order to verify the new input method, 'switch input', several uniaxial tensile and compression simulations have been done on a single S4R element and results were compared to the 'regular input' based on Abaqus documentation. Figure E.2 shows the boundary condition for single-shell element under tension and compression. Single-element was subjected to uniaxial tension or compression for various angles (off-axis angles) between the fiber direction and the direction of load application (off-axis angles were measured in respect to the x-direction in Figure E.2). Figures E.3- E.15 present the force-displacement curves for the three input methods; (I) 'Regular input' in Abaqus, (II) 'switch input' using VUMAT and (II) 'switch input' without VUMAT. The explicit solver was used for all simulations.

Figure E.2 - The single element simulations; (a) Tension and (b) Compression.



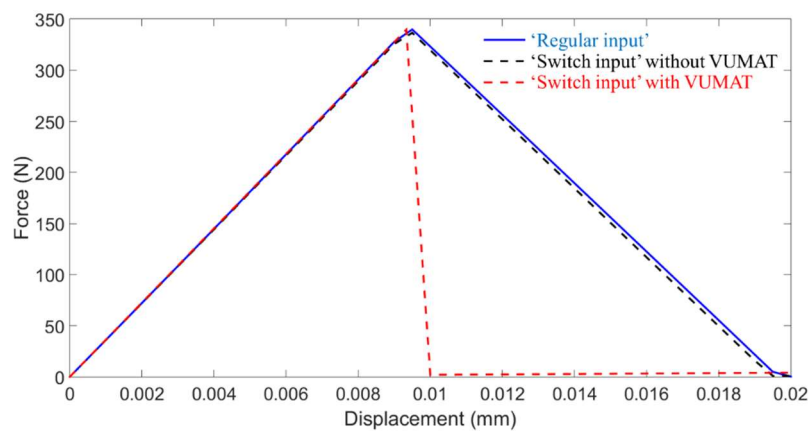
Source: The author.

Figure E.3 - The force-displacement curve for single-shell element under compression, 0° off-axis angle.



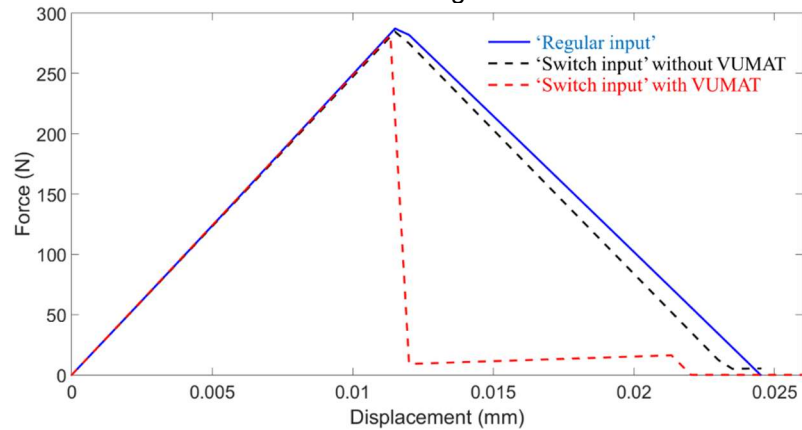
Source: The author.

Figure E.4 - The force-displacement curve for single-shell element under compression, 15° off-axis angle.



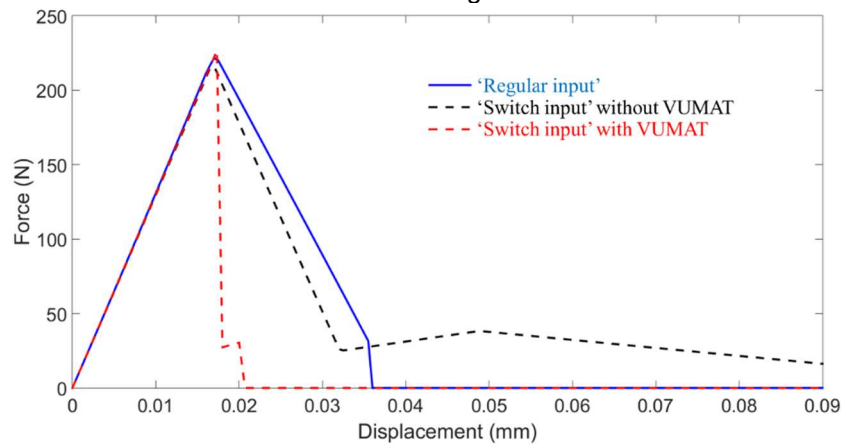
Source: The author.

Figure E.5 - The force-displacement curve for single-shell element under compression, 30° off-axis angle.



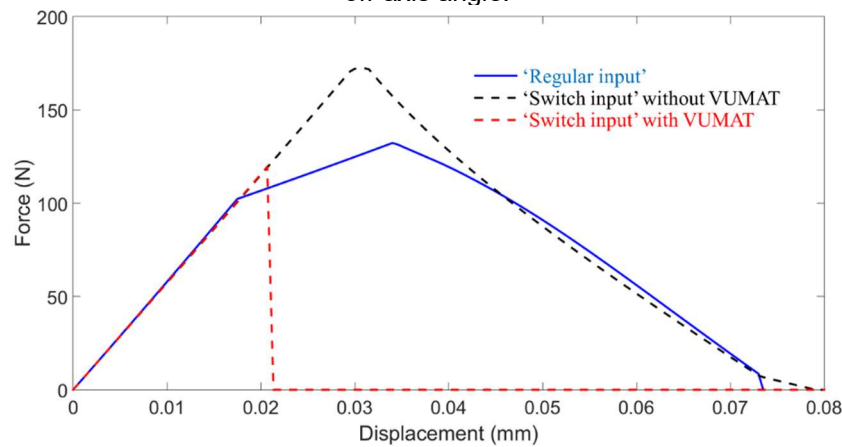
Source: The author.

Figure E.6 - The force-displacement curve for single-shell element under compression, 45° off-axis angle.



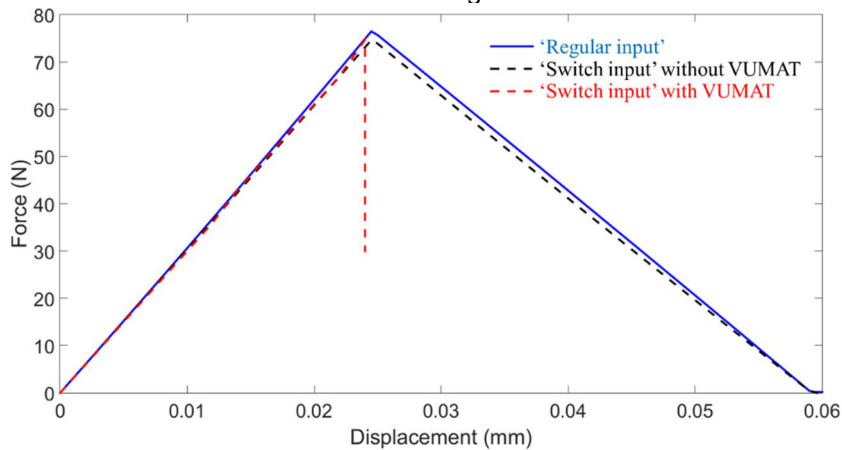
Source: The author.

Figure E.7- The force-displacement curve for single-shell element under compression, 60° off-axis angle.



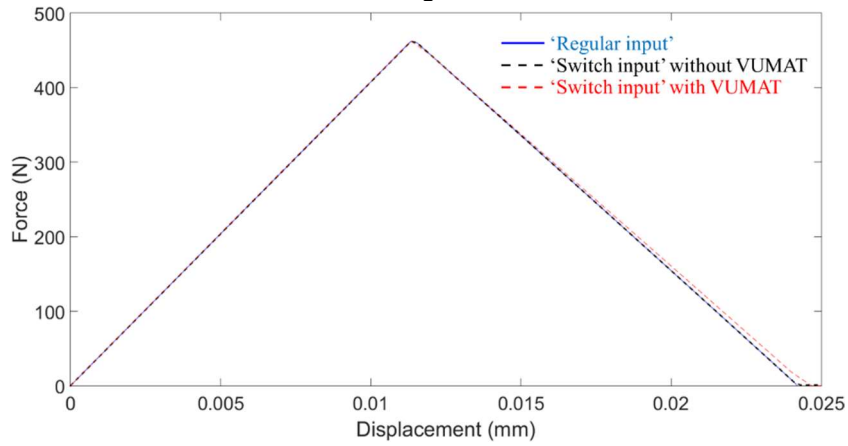
Source: The author.

Figure E.8 - The force-displacement curve for single-shell element under compression, 90° off-axis angle.



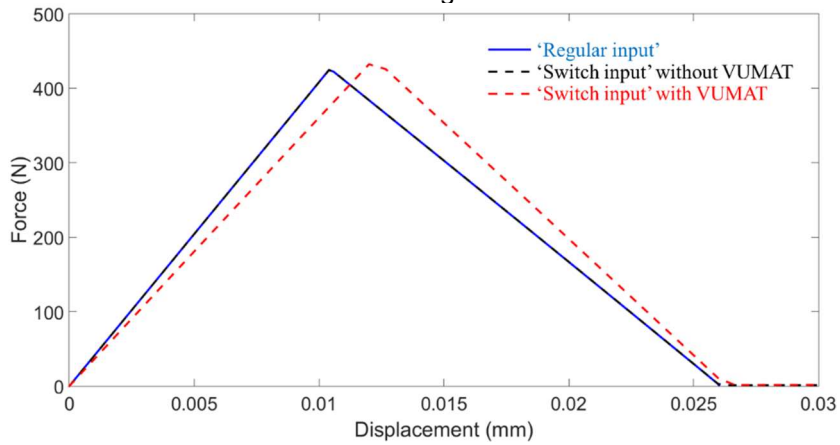
Source: The author.

Figure E.9 - The force-displacement curve for single-shell element under tension, 0° off-axis angle.



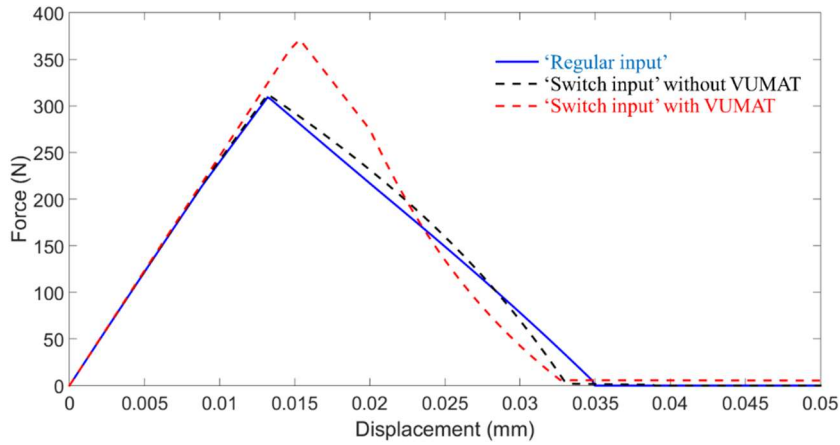
Source: The author.

Figure E.10 - The force-displacement curve for single-shell element under tension, 15° off-axis angle.



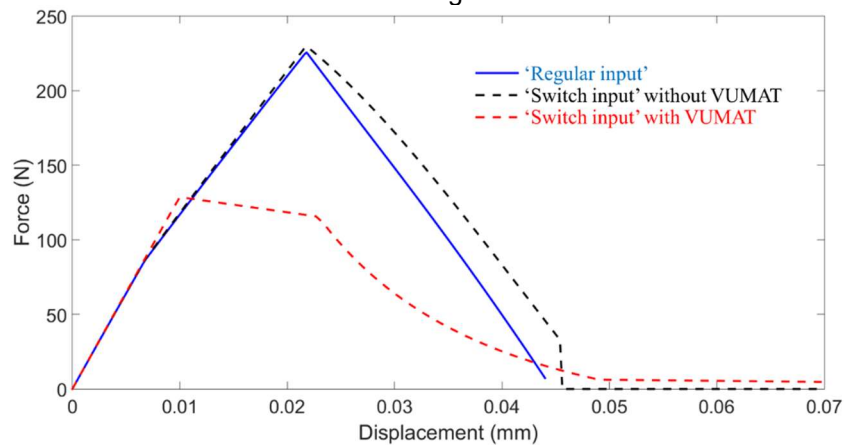
Source: The author.

Figure E.11 - The force-displacement curve for single-shell element under tension, 30° off-axis angle.



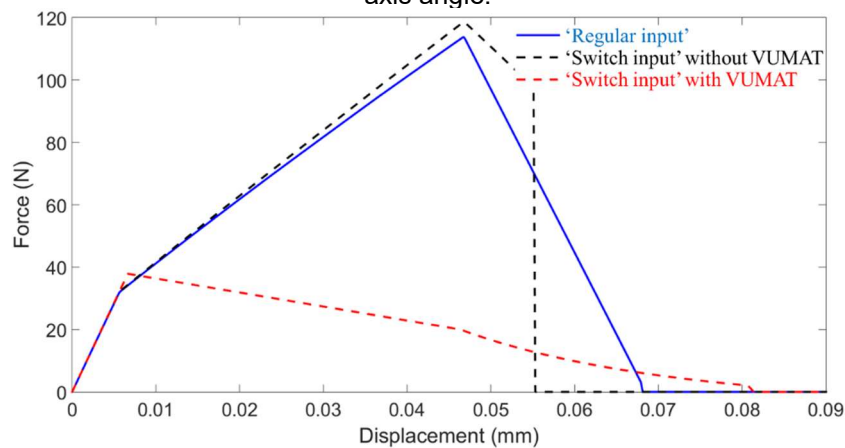
Source: The author.

Figure E.12 - The force-displacement curve for single-shell element under tension, 45° off-axis angle.



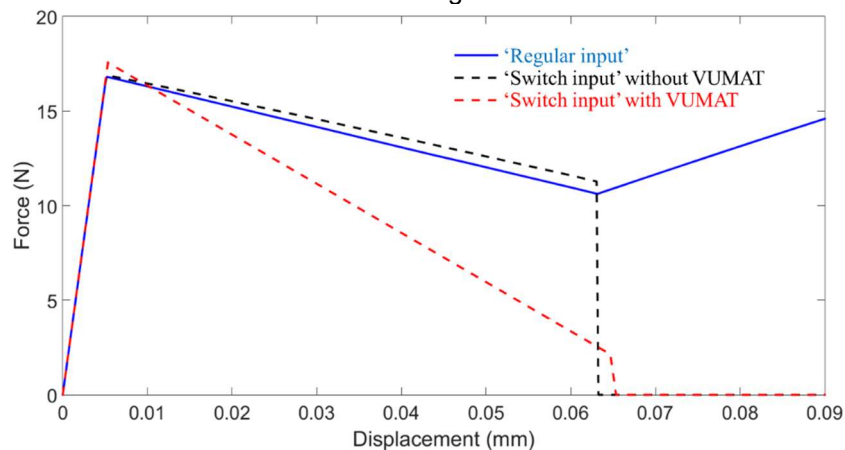
Source: The author.

Figure E.13 - The force-displacement curve for single-shell element under tension, 60° off-axis angle.



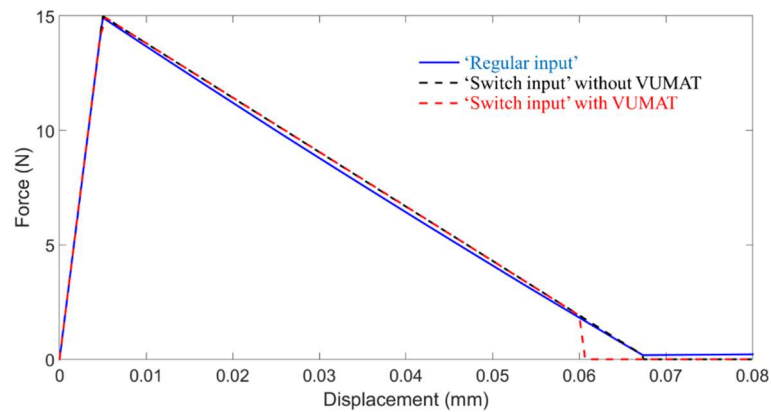
Source: The author.

Figure E.14 - The force-displacement curve for single-shell element under tension, 75° off-axis angle.



Source: The author.

Figure E.15 - The force-displacement curve for single-shell element under tension, 90° off-axis angle.

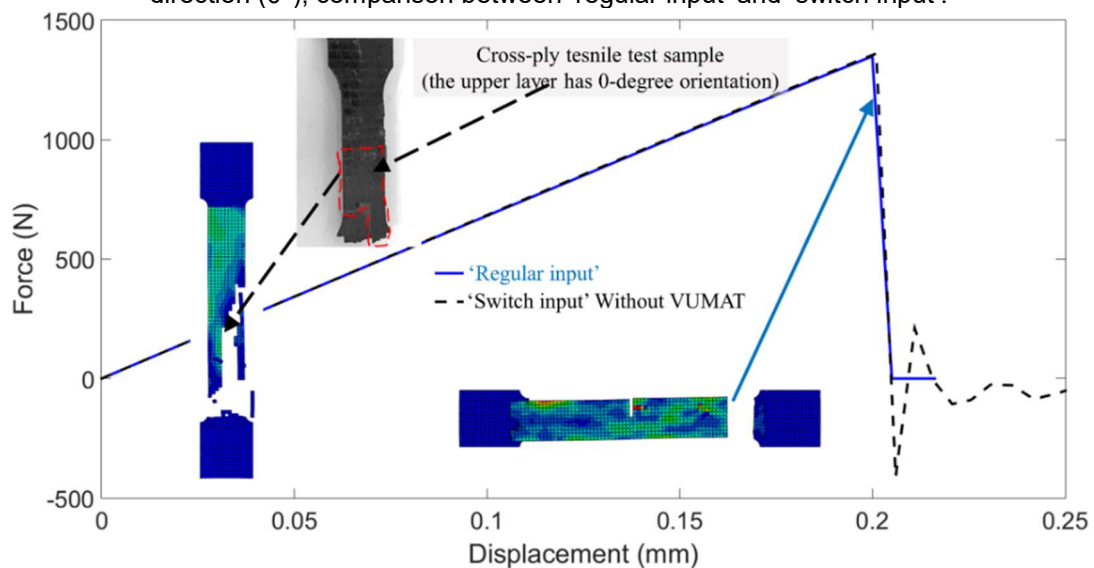


Source: The author.

Reasonable correlation between force-displacement curves of 'regular input' and 'switch input' without VUMAT has been observed for the majority of the loading conditions. Since the VUMAT results are not good enough, 'switch input' without VUMAT will be considered in the following.

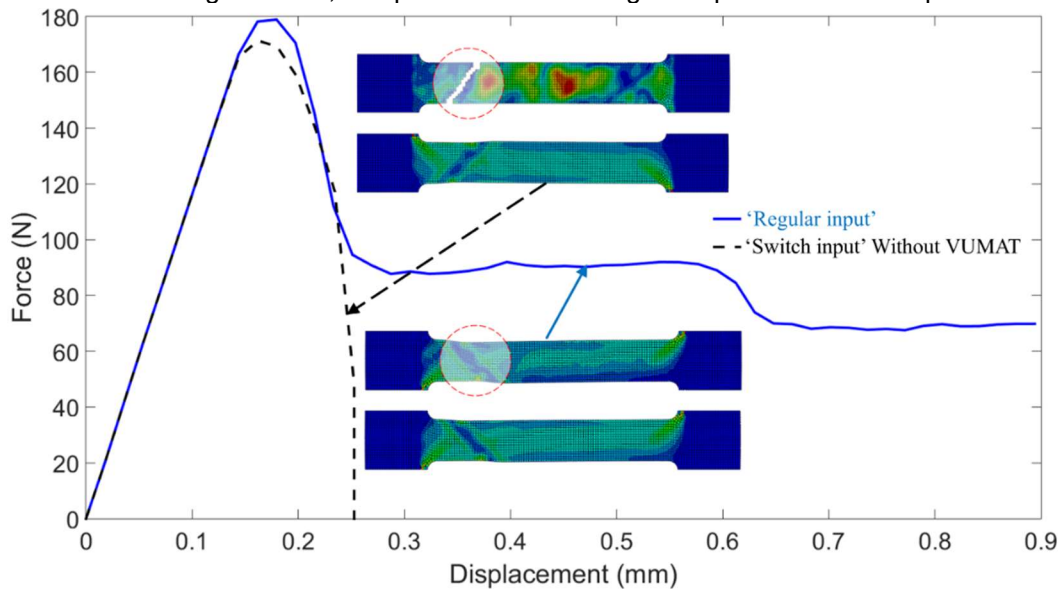
Three tensile test simulations were conducted to compare the results of 'regular input' and 'switch input' without VUMAT methods; results are presented in Figures E.16 – E.18. Each sample has only one layer of the shell with only one specific fibers orientation, 0°, 90°, and  $\pm 45^\circ$ . Here also the explicit solver was used to speed up the simulations.

Figure E.16 - Tensile test simulation on a single layer having fibers aligned with loading direction (0°); comparison between 'regular input' and 'switch input'.



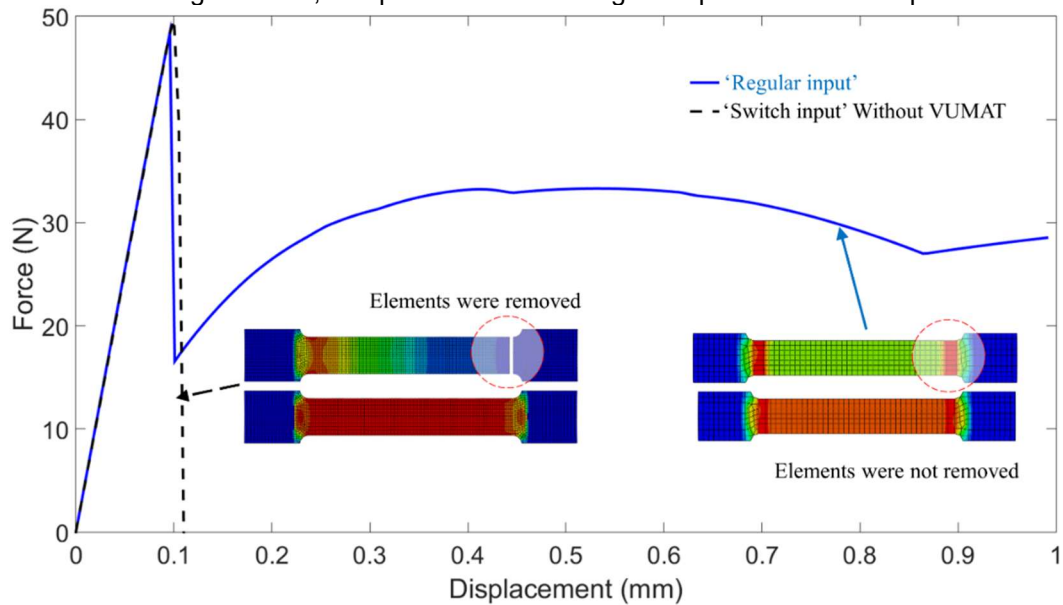
Source: The author.

Figure E.17 - Tensile test simulation on a single layer having fibers  $\pm 45^\circ$  off-axis angle against the loading direction; comparison between 'regular input' and 'switch input'.



Source: The author.

Figure E.18 - Tensile test simulation on a single layer having fibers perpendicular to the loading direction; comparison between 'regular input' and 'switch input'.



Source: The author.

Figures E.16- E.18 show that the new input method produced reasonable force-displacement curves in comparison to Abaqus regular input procedure. However, more realistic fracture morphology has been generated by using the new method, since

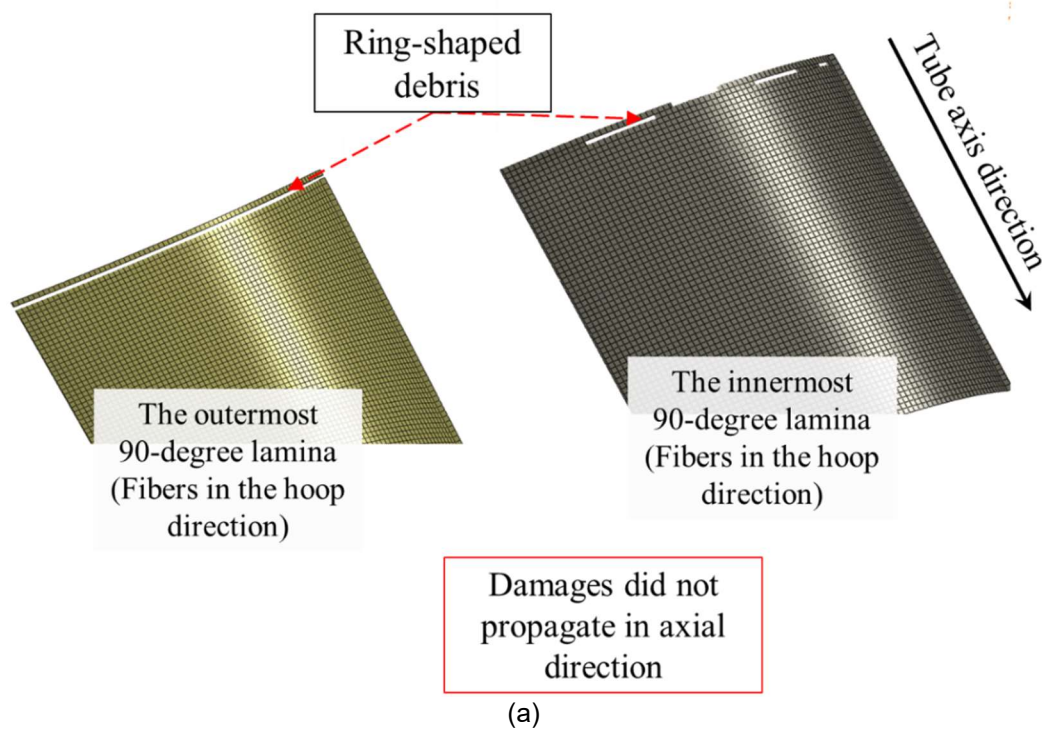
Abaqus, with regular input method, did not delete the failed elements in  $\pm 45^\circ$  and  $90^\circ$  off-axis tensile tests.

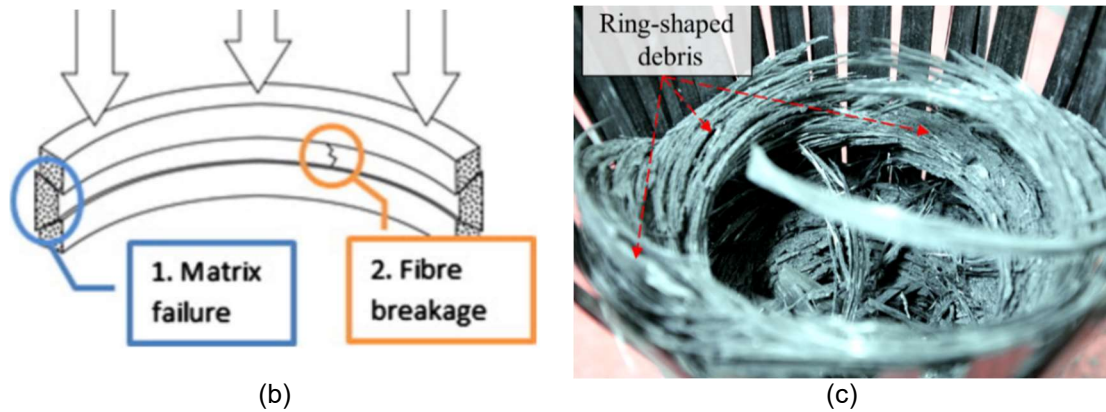
## E.2 Simulation results of the axial impact on the cross-ply specimen with the new model

The FE model of axial impact on the tube is the same; however, instead of regular material input in Abaqus, the new method ('switch input') was used in this section. The in-plane rotation angle of  $0^\circ$  and  $90^\circ$  layers has been changed to comply with new input technique. Figure E.19 shows the  $90^\circ$  layers in the cross-ply tube under axial dynamic impact just after the first contact between the tube and the impactor. The damage mechanism, generation of ring-shaped debris (Figure E.19(a)) is very similar to the schematic damaging behavior of tubular layers having fibers in the hoop direction (Figure E.19(b)) and experimental observation (Figure E.19(c)).

Figure E.19 - Damage in  $90^\circ$  layers of the cross-ply tube; (a) Ring-shaped debris in the FE model; (b) Damage mechanism in the  $90^\circ$  plies; (c) Ring-shaped debris after axial impact.

Stacking sequence of the cross-ply tube : [0/90/0/90/0]

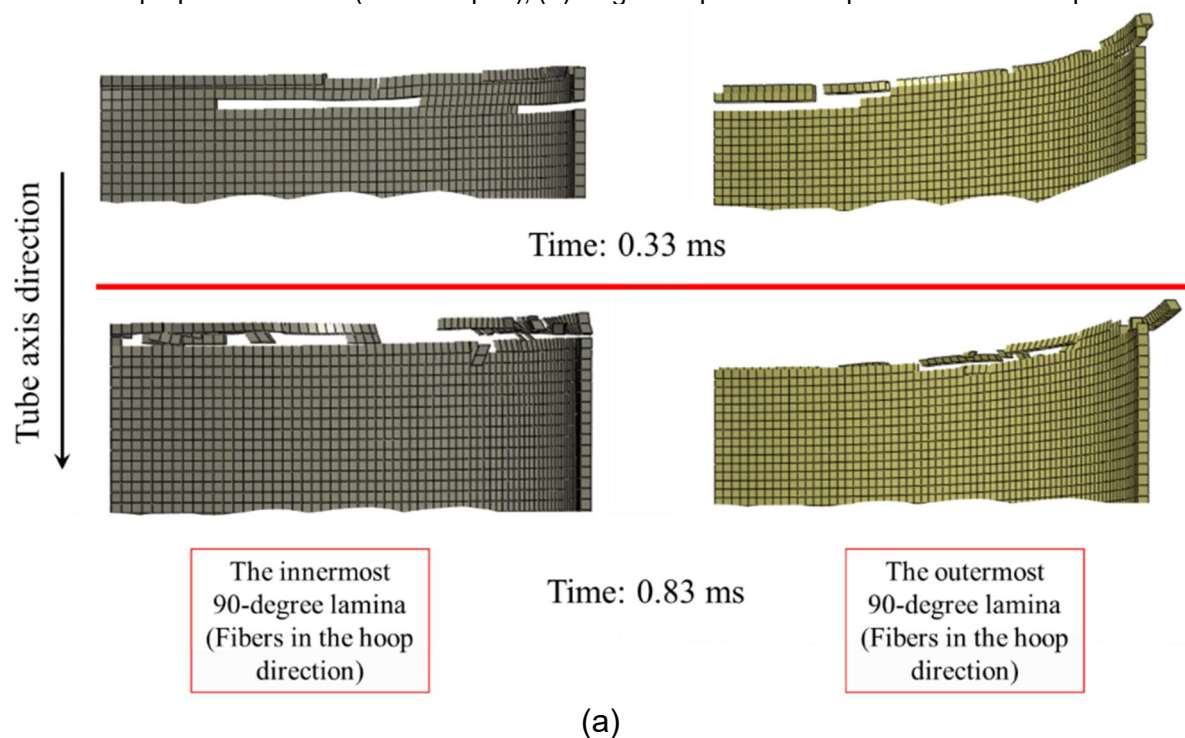




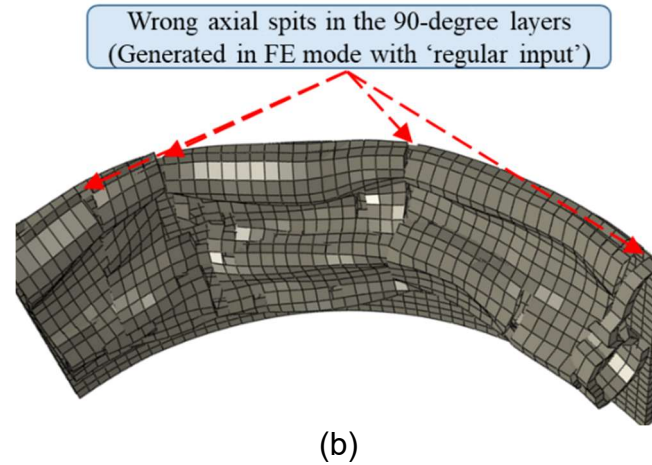
Source: (a,c): The author; (b): (Chiu et al. 2015)

Figure E.20 shows few steps of damaging behavior of these 90° layers during the impact event. In contrast to the FE model with 'regular input', it is evident that damages in the 90° layers of the new model did not propagate in the tube axis direction, compared to the axial damage propagation in the 90° layers of regular input (Figure E.20(b)).

Figure E.20 - Damage propagation in the 90° layers in the tubular specimens under axial impact; (a) The proposed method ('switch input'); (b) Regular input material parameters in Abaqus.



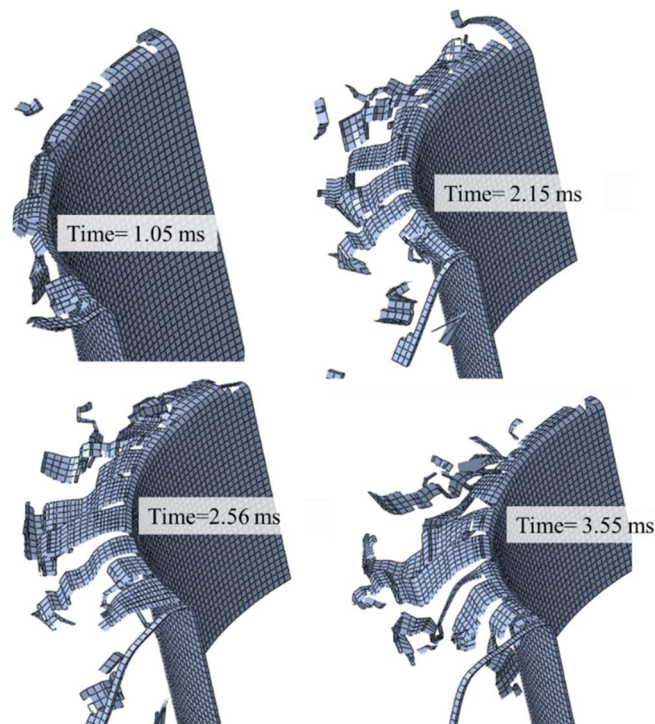
(a)



Source: The author.

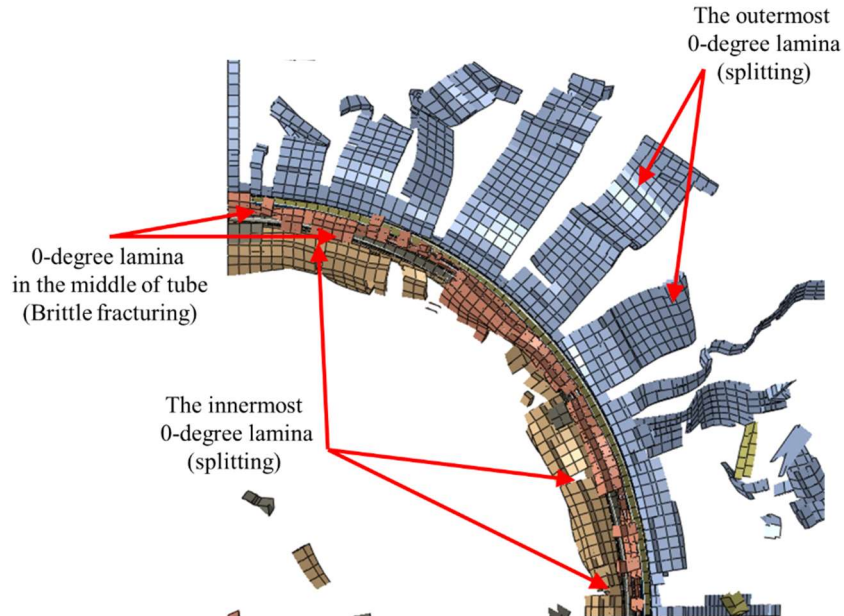
Figure E.21 shows the damaging behavior of the outermost  $0^\circ$  layer in the cross-ply tube. Similar to the experimental observations, the outermost  $0^\circ$  UD lamina split into several lamina bundles. The damages propagated parallel to the fiber direction. Figure E.22 shows the crushed morphology of the cross-ply tube (all layers). The innermost  $0^\circ$  layer splits in few lamina bundles; however, the length of these lamina bundles are shorter than the splits in the outermost  $0^\circ$  layer and experiment tests.

Figure E.21 - Damaging behavior of the outermost  $0^\circ$  layer in the cross-ply tube.



Source: The author.

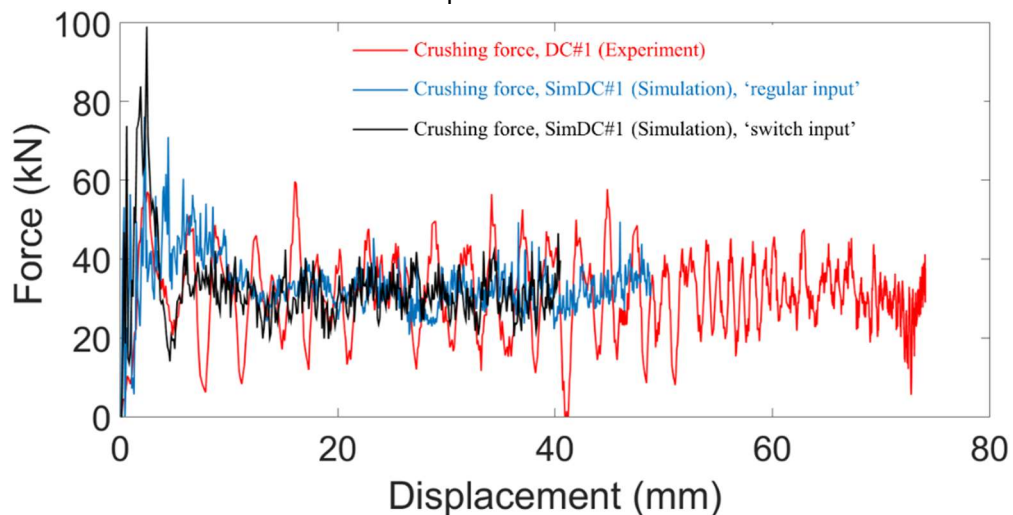
Figure E.22 - Crushed morphology of the cross-ply tube after axial dynamic impact (with new model).



Source: The author.

Figure E.23 compared the force-displacement curve of axial impact on the cross-ply tube, experimental with the FE models. The new model also produced reasonable crushing force (average crushing force equals to 31.9 kN).

Figure E.23 - The force-displacement curve for axial impact on the cross-ply tube; comparison between experiment, FE model with regular input and FE model with 'switch input' method.



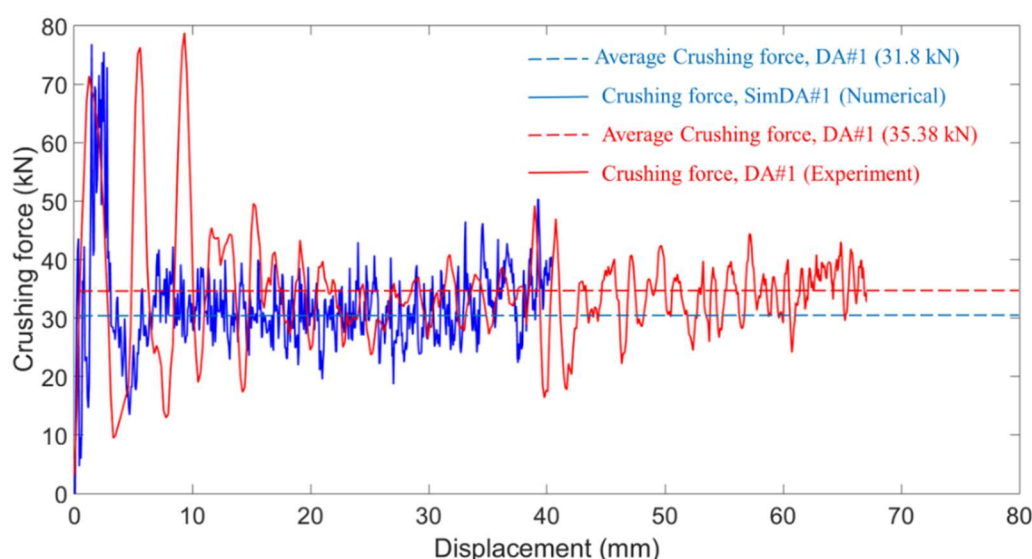
Source: The author.

### E.3 Simulation results of the axial impact on the angle-ply tube specimen with the new model

The force-displacement curve for angle-ply specimen was compared with the experimental result in Figure E.24. Likewise, by using the new input method, the average crushing force is lower than the experiment. On the contrary, with the same material properties, there was a good agreement between the reproduced force-displacement curves and the experimental one for the cross-ply models. This issue can be related to the bending behavior of  $\pm 45^\circ$  laminae. It has been observed that under axial compression on the laminate tubes,  $\pm 45^\circ$  layers experienced a higher force in the hoop direction rather than  $0^\circ$  and  $90^\circ$  layers. Due to this bending behavior, the adjacent resin layer may undergo extreme loading condition.

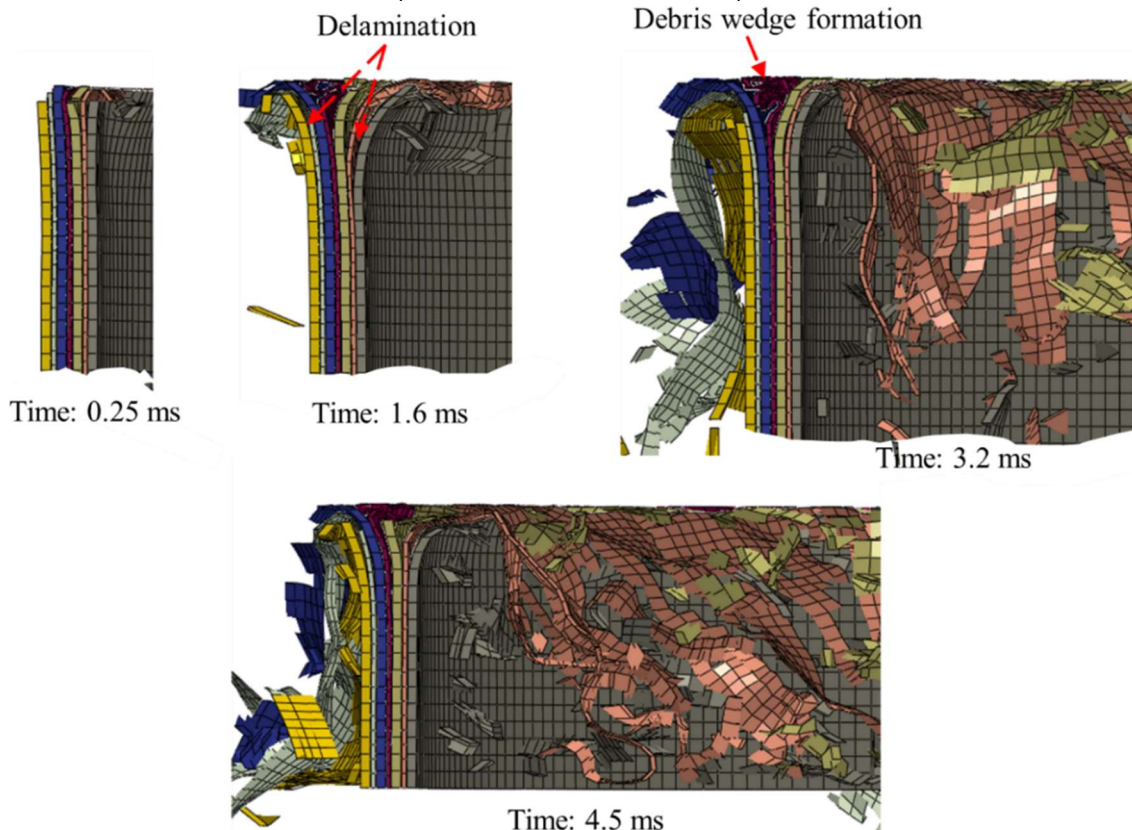
The time-lapse of deformation of the angle-ply tube under the dynamic impact is presented in Figure E.25. Bending behavior of plies is very similar to experimental results. A debris wedge was formed during the impact event between the tube and the impactor.

Figure E.24 – The force-displacement curve for axial impact on the angle-ply tube; comparison between experiment and FE model with 'switch input' method.



Source: The author.

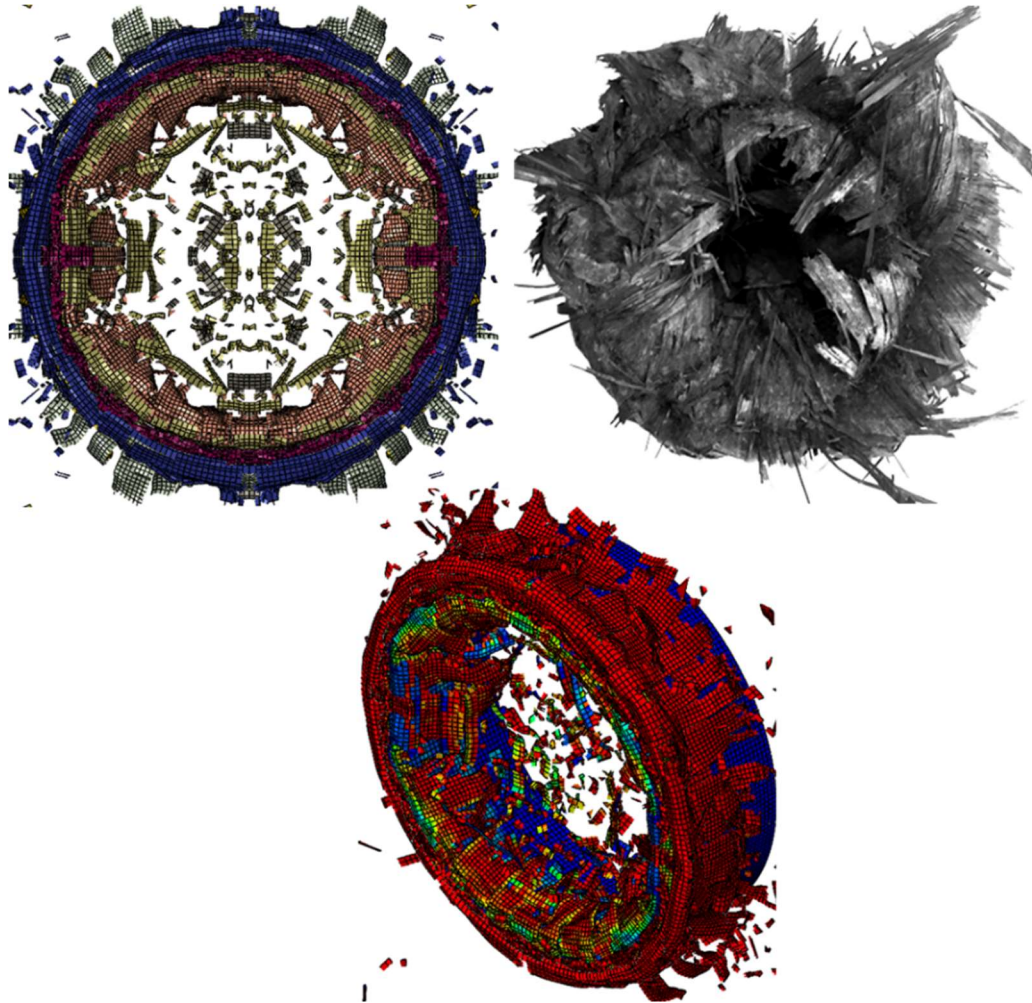
Figure E.25 - Deformation of each layer of the angle-ply specimen under the dynamic impact (shell thickness render is ON).



Source: The author.

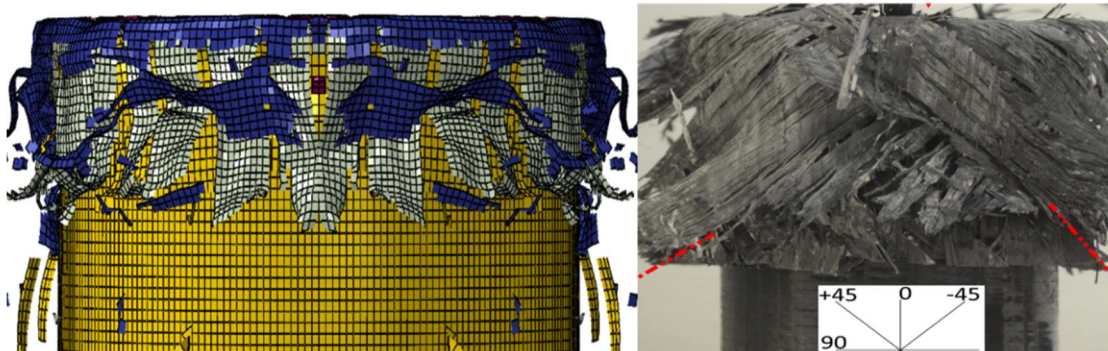
Figures E.26 and E.27 show the top-view and side-view of the angle-ply specimen, respectively, and compare them with experimental observation. Although several similarities can be observed between experiment and simulation, however, in the FE simulation, there are several broken parts after impact in contrast to the experimental test while layers usually formed long longitudinal fronds.

Figure E.26 - Comparison between damage morphology for experimental and numerical axial impact on the angle-ply specimen (top-view).



Source: The author.

Figure E.27 - Comparison between damage morphology for experimental and numerical axial impact on the angle-ply specimen (side-view).



Source: The author.